

Dissecting the photoacidity of spiropyran/merocyanine molecular switches in water.

Présentée le 27 janvier 2023

Faculté des sciences de base
Laboratoire de chimie supramoléculaire
Programme doctoral en chimie et génie chimique

pour l'obtention du grade de Docteur ès Sciences

par

Cesare BERTON

Acceptée sur proposition du jury

Prof. M. Mazzanti, présidente du jury
Prof. K. Severin, C. Pezzato, directeurs de thèse
Prof. J. Milic, rapporteuse
Prof. M. Lerch, rapporteur
Prof. X. Hu, rapporteur

Acknowledgements

I thank Dr. Cristian Pezzato and Prof. Kay Severin for giving me the invaluable opportunity to embark the adventure that have been my doctoral studies at EPFL. You have been my guidance for my growth as a scientist and as a person. Your patience, determination and discipline has been and will always be a reference point for me. I have learnt a lot and I am still learning more thanks to you; I will always be grateful and happy to share moments with you whenever the opportunity comes.

I thank Prof. Cristiano Zonta for guiding me in the first steps of my studies. Your guidance has been essential in the first phases of my career in chemistry.

I thank my Helena, who I love with all my heart and soul and who makes my life joyful every day. With you, and only you, also the most difficult moments become happy.

I thank my mother, Elsa. Thank you for being a loving mother and to have powered through any difficulty to provide me good guidance and opportunities. I am extremely thankful to you and I would never make it without your support.

I thank all my family for supporting and believing in me. Having your support and help was essential to make all of this possible.

I thank my university friends Federico and Ruggero. You are extremely good friends, you helped me in every occasion and I know that I can count on you for any situation.

I thank my childhood friend, Federico, for being my reference point whenever I needed it, no matter the time or the circumstances.

I thank Nadir, Luciano, Sylvain and José, my friends that I consider as brothers. Your company motivated me and pushed me to overcome any obstacle. I am thankful and I really hope our pathways can intertwine once again in the future.

I thank Carl, Luca, Gazza, Federico, Giacomo, Zhaowen, for being great friends both in good and in bad times. The moments we shared together will be always remembered by me as positive thanks to your presence.

I thank my friends Noga, Christeena, Mrityika, Anastasia, Bastiaan, Pavel, Tak Hin, Jean, Chaolei, Rujin, Damien for the good times we spent in and out of the lab and for the interesting discussions concerning chemistry and not only.

I thank Rosario, Euro, Farzaneh and Daniel for being good friends and helpers, no matter whether it was time to solve a chemical problem or to share a thought or a pleasant conversation.

I thank Valentin, Margarida and Yufei, the students that I supervised, for helping me in the experimental work. I dedicated much time to you and seeing you learn new things day by day has been a great satisfaction.

My time at EPFL has been full of ups and downs, nevertheless, the experience was more than positive overall. I will never forget most of the moments I spent here, and I will always be more than grateful to the people who took part to my pathway.

Abstract

Photochemistry is a discipline that studies the interaction between light and matter with the scope to induce chemical transformations. The first conjugation between light and chemistry can be dated back to the lifespan of Giacomo Luigi Ciamician, who is considered to be one of the founders and pioneers of photochemistry. In the ensemble of photochemical reactions and of photosensitive compounds discovered so far, molecular switches are compounds with such promising features to be included in the Nobel prize for chemistry assigned in 2016. Indeed, in these works, molecular machines were actioned by combinations of thermal and photochemical stimuli managing to move these machines in a defined direction. The interest in this field is expanding as well in the domain for energy conversion. As matter of fact, it is possible to find a major contribution of photochemistry in the development of semiconductor-based solar panels. These devices are widespread and are contributing to the reduction of the emission of pollutants in the atmosphere. The solar panels, for instance, are deriving from the extensive study of the interaction between light and the materials that compose the panels themselves. Another subject that is pivoting around photochemical processes is biochemistry. Converting sunlight into chemical energy is a process that plants and photosynthetic organisms perform every day for all their lifespan with great efficiency. Based on these inspirations, scientists have always demonstrated the ambition to mimic and reproduce photosynthesis, a complex yet fascinating natural process. Moreover, the abundance of solar irradiation on earth makes technologies for solar power conversion a central point around which current research is orbiting. In this key and with the inspiration mentioned above, the thesis

treats synthesis and description of benzo indolino pirano spyrans (BIPS) photoacids, compounds able to react to the presence of visible light by releasing protons. Many implications of their photoacidity have been already reported in the past as for photolithography, biochemistry and smart materials (*i.e.*, soft robotics) to mention some. These compounds represent a class of photoswitches which displays a broad set of interesting applications, nevertheless their photoacidity was never subject of extensive studies from the physico-chemical point of view. The accumulation of chemical energy in the form of acidity gradients represents an interesting potential derivation of BIPS; these bear all the chemical photochemical characteristics to be excellent candidates in this task. In the first part of this elaborate will be discussed the background, the applicability, and the most relevant studies on the chemistry of BIPS in water. The third chapter will cover the formulation of a working mechanism and the design of a generally applicable quantitative characterization protocol for the (photo)chemistry of BIPS photoacids in water using a combination of different physico-chemical techniques. The fourth chapter describes the temperature dependency of the chemistry of BIPS photoswitches in water. Altering the environmental variables for improving the performance of BIPS photoswitching is an aspect that was not described in detail in the past. In this chapter, the focus is to exploit temperature differences for maximizing the photoacidity (and the performances in general) of BIPS. The fifth chapter will cover the functionalization of BIPS with EDGs and the correspondent changes in activity of the photoswitches. This part also introduces the general concept of light-switchable buffer as a buffer solution whose pK_a value that can be switched using light irradiation. In the final chapter will be discussed the synthesis and the characterization of a novel imidazolium-functionalized BIPS photoacid. This displays very high water solubility and its properties are dramatically improved by the

encapsulation within the cavity of cucurbit-[7]-uril, a synthetic supramolecular receptor with high affinity towards organic cations. In general, in this elaborate, our project is to exploit to the maximum the potential that can be produced from these small organic molecules with the objective of maximizing the photoinduced pH excursion in water.

Keywords: photoacids, photochromism, photochemistry, photoswitches, spiropyrans, pH, water, supramolecular chemistry, light-harvesting, energy, merocyanines, cucurbiturils, host-guest, dyes.

Riassunto

La fotochimica è una scienza che studia l'interazione tra luce e materia al fine di indurre trasformazioni chimiche. Il connubio tra luce e chimica può essere datato al periodo di vita di Giacomo Luigi Ciamician, considerato il padre fondatore della fotochimica come la conosciamo oggi. Questa disciplina, è ben diversa e più evoluta rispetto a come l'immaginava Ciamician. Nell'insieme delle reazioni fotochimiche e dei composti fotosensibili scoperti finora, i molecular switches si dimostrano essere delle entità chimiche con caratteristiche così promettenti da essere inclusi nel lavoro del premio Nobel per la chimica assegnato nel 2016. In quest'ultimo, delle macchine molecolari sono state azionate attraverso una combinazione di stimoli termici e fotochimici riuscendo a muovere delle molecole in un verso definito. L'interesse in questo campo spazia anche nella produzione energetica. Un esempio si può trovare nei pannelli solari a base di semiconduttori, essi sono molto diffusi e stanno contribuendo alla riduzione delle emissioni di gas nocivi per l'ambiente. Questi dispositivi derivano dallo studio dei processi fotochimici a carico dei materiali che li costituiscono. Un'altra materia incardinata sui processi fotochimici è la biochimica, infatti, la conversione dell'energia luminosa in energia chimica è un processo che le piante e gli organismi fotosintetici effettuano durante l'arco della loro intera vita con grande efficienza. In virtù di questo fatto, gli scienziati hanno sempre dimostrato l'ambizione di mimare e riprodurre questo processo naturale così affascinante e complesso. Inoltre, l'abbondanza della radiazione solare rende le tecnologie per la conversione di questa fonte energetica un punto cardine attorno al quale la ricerca attuale sta orbitando. Questa tesi tratta la sintesi e descrizione dei fotoacidi benzo

indolino pirano spirani (BIPS) che sono composti capaci di reagire alla presenza di luce visibile rilasciando un protone in maniera reversibile. Alcune applicazioni già si trovano nei campi della fotolitografia, biochimica e dei materiali intelligenti (per esempio, nella robotica soft). Questi rappresentano una famiglia di composti studiati da molto tempo, tuttavia la loro fotoacidità non è mai stata soggetto di studi accurati sia dal punto di vista chimico-fisico che funzionale. L'accumulazione di energia chimica nella forma di gradienti di acidità rappresenta una potenziale applicazione dei BIPS; questi dimostrano di essere eccellenti candidati per questo compito viste tutte le proprietà chimiche e fotochimiche che possiedono. Nella prima parte di questa tesi verrà discussa la panoramica generale, l'applicabilità e gli studi più rilevanti sulla chimica dei BIPS in acqua. Nel terzo capitolo si discute della definizione dei meccanismi di funzionamento e del design di un protocollo generale e quantitativo di caratterizzazione della (foto)chimica acquosa dei BIPS. Questo verrà descritto usando una combinazione di studi chimico-fisici. Il quarto capitolo descrive la dipendenza dalla temperatura della chimica dei BIPS in acqua. Il cambiamento delle variabili ambientali con l'obiettivo di migliorare la performance del photoswitching dei BIPS, è un aspetto non descritto in precedenza. In questo capitolo, lo scopo è di sfruttare delle differenze di temperatura per massimizzare la fotoacidità di questi composti (e la loro performance in generale). Il quinto capitolo tratterà la funzionalizzazione dei BIPS con degli EDG ed il conseguente cambio in attività dei photoswitch. Questa parte introduce anche il concetto generale di light-switchable buffer che consiste in una soluzione tampone con pK_a variabile con l'ausilio della luce. Nel capitolo finale sarà discussa la sintesi e la caratterizzazione di un nuovo BIPS con una funzionalizzazione imidazolio. Questo BIPS dimostra un'elevata solubilità in acqua e le sue proprietà vengono amplificate una volta incapsulato nella cavità del cucurbit-[7]-urile, un recettore

sintetico supramolecolare con affinità alta per i cationi organici. In questo elaborato il nostro progetto è quello di sfruttare al massimo il potenziale che può essere erogato da queste piccole molecole organiche con l'obiettivo di massimizzare la variazione fotoindotta di pH in acqua.

Parole chiave: fotoacidi, fotocromismo, fotochimica, photoswitches, spiropirani, pH, acqua, chimica supramolecolare, light-harvesting, energia, merocianine, cucurbiturili, host-guest, coloranti.

Symbols and abbreviations

ACN	Acetonitrile
AcOH	Acetic acid
ASIC	Acid sensitive ion channel
BIPS	Benzo Indolino Pirano Spyran
cal	Calories
CB[n]	Curcurbit-[n]-uril
CB7	Cucurbit-[7]-uril
CD	Circular dichroism
<i>cis</i> -MCH	Merocyanine, <i>cis</i> -form
cm	Centimeters
DCM	Dichloromethane
DMSO	Dimethylsulfoxide
DNA	Deoxyribonucleic acid
EDG	Electron-donating group
ESI	Electrospray ionization
EtOH	Ethanol
EWG	Electron-withdrawing group
<i>h</i>	Planck constant

$i\text{-PrOH}$	Isopropanol
ITC	Isothermal titration calorimetry
ITO	Indium Tin Oxide
J	Joules
K_a	Acidity constant
K_a^{GS}	Acidity constant of the ground state
K_a^{MS}	Acidity constant of the metastable state
k_B	Boltzmann constant
K_c	MC-to-SP equilibrium constant
kcal	Kilocalories
kJ	Kilojoules
K_w	Water autoprotolysis equilibrium constant
L	Liters
LED	Light-emitting diode
LTQ	Linear triple quadrupole
M	Molar
MC	Merocyanine, deprotonated form
MCH	Merocyanine, protonated form
MeOH	Methanol

mim	1-methylimidazole
mL	Milliliters
mM	Millimolar
mm	Millimeters
mmol	Millimoles
mol	Moles
MS	Mass spectrometry
MOF	Metal-Organic Framework
N	Normal
NIR	Near infrared
nm	Nanometers
NMR	Nuclear magnetic resonance
OMe	Methoxy (-OCH ₃)
pK	Co-logarithm in base 10 of K
PMT	Photomultiplier tube
ppm	Parts per million
PTFE	poly(tetrafluoroethylene)
r.t.	Room temperature
SP	Spiropyran

T	Temperature
TFA	Trifluoroacetic acid
UCNP	Upconverting nanoparticle
UV-Vis	Ultraviolet-Visible
α	Alpha, fractional degree of neutralization
$\Delta_r G$	Gibbs free energy of reaction
$\Delta_r H$	Reaction enthalpy
$\Delta_r S$	Reaction entropy
λ	Wavelength
μL	Microliters
μM	Micromolar
μmol	Micromoles
Π	Photoacidity ($\text{pK}_{\text{aGS}}\text{-pK}_{\text{aMS}}$)

Table of contents

1. Acknowledgements	ii
2. Abstract.....	iv
3. Symbols and abbreviations	x
4. Table of contents	xiv
5. Introduction	1
1.1 In the quest for reversible photoacids	3
1.2 Applying BIPS reversible proton release in water	5
6. Aim of the thesis.....	15
7. Thermodynamics and kinetics of protonated merocyanine photoacids in water....	17
3.1 Introduction.....	17
3.2 The ground state	18
3.3 The metastable state	27
3.4 The hydrolytic stability	29
3.5 The metastability	31
3.6 Comparative evaluation	34
3.7 Reversible proton release in water.....	38
3.8 Conclusions.....	42
3.9 Experimental section	42
8. The effect of temperature on the photoacidity of merocyanine photoacids in water	114
4.1 Introduction.....	114
4.2 Room temperature chemistry.....	114

4.3 Variable-temperature effects.....	120
4.4 Conclusions.....	122
4.5 Experimental Section.....	123
9. Light-switchable buffers	140
5.1 Introduction.....	140
5.2 Preliminary screening	141
5.3 Narrowing the focus.....	146
5.4 pH photoswitching	151
5.5 Conclusions.....	154
5.6 Experimental section	155
10. Integrating photoacidity and host-guest chemistry in water	184
6.1 Introduction.....	184
6.2 Synthesis and characterization of the photoswitch.....	185
6.3 Supramolecular chemistry with cucurbit-[7]-uril.....	190
6.4 Conclusions.....	199
6.5 Experimental section	201
11. Bibliography.....	255
12. Curriculum Vitae.....	261

Chapter 1

Introduction

Spiropyran compounds are one of the most studied families of molecular switches owing to their ease of synthesis and multifaceted applications^[1]. Nowadays, the skeletal formula commonly associated with spiropyran molecular switches is the so-called “indoline-pyran” hybrid, which results from the condensation of Fischer’s bases with salicylaldehydes.^[2,3] Indolinospirobenzopyrans—abbreviated by IUPAC with the acronym “BIPS”, which stands for Benzo Indolino Pyrano Spyran^[4]—were introduced in 1940 by Wizimberg and Wenning^[5] to elucidate the temperature-dependent intramolecular ionization of spiro compounds and began to be popularized in 1952 by Hirschberg and Fischer^[6] following the discovery of their photochromic properties. BIPS are typically composed of a 1,3,3-trimethyl indoline moiety sharing the tetrahedral carbon atom in position 2 with a benzopyran (or chromene) moiety (Figure 1). They exist in a closed-ring spiro form (SP) and in an open-ring merocyanine form (MC). The former is colourless, since the two halves of the molecule are located orthogonally to each other via the spiro carbon and therefore are not conjugated, whereas the latter is coloured because the indoline and the chromene parts are coplanar and conjugated through the central ethylene bridge.^[7] Interconversion between these two forms can occur with a variety of external stimuli such as temperature^[8,9] (thermochromism), light^[10–12] (photochromism), solvent polarity^[13] (solvatochromism), acids^[14] (acidochromism), metal ions^[15] (ionochromomism), redox potential^[16,17] (electrochromism), and even mechanical stress (mechanochromism).^[3]

The photochromism of BIPS can be of two types (Figure 1.1 a). When the thermodynamically most stable state is the colourless SP form, photoexcitation with UV light (< 400 nm), which cleaves heterolytically the spiro carbon-oxygen bond, results in the formation of the MC form, this species typically (as for the examples in Figure 1.1) displays intense absorptions in the visible spectrum and results in deeply coloured solutions — *i.e.*, the system displays “positive” photochromism.^[4] On the other hand, when the thermodynamically most stable state is the coloured MC form, photoexcitation with visible light (> 400 nm) triggers a ring-closing reaction leading to

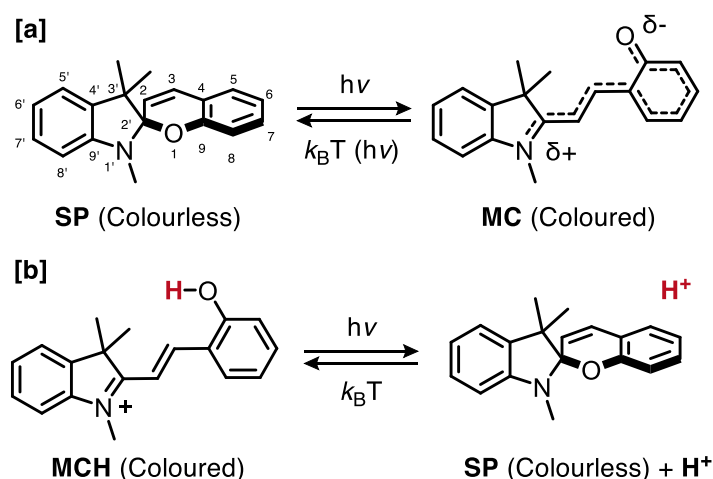


Figure 1.1. The photochromic behaviors of BIPS.

the blueshifted SP form, which typically absorbs in the ultraviolet region, thus typically (as for the examples in Figure 1.1), resulting in faint yellow solutions that are almost transparent to the naked eye — *i.e.*, the system displays “negative” (or “inverse”)

photochromism.^[3] The thermodynamic stability of MC and SP, and therefore the resulting photochromic behaviour, strongly depends on the molecular structure and the solvent polarity. Positive photochromism is common with “activated” BIPS (e.g., 6-nitro BIPS) and/or in nonpolar solvents^[7,18,19], whereas negative photochromism is mainly observed with “non-activated” BIPS^[20–22] and/or in polar solvents^[23,24]. BIPS photochromism has been extensively studied over the years, but mostly in organic solvent mixtures. In polar solvents such as water, though, population of the protonated state of MC (MCH) is also possible.^[2,3] The aqueous equilibrium of BIPS in the ground state depends on the pH of the solution and, when it is shifted in favour of MCH,

irradiation with visible light can lead to the formation of SP and the concomitant dissociation of a proton (Figure 1 b). Eventually, if the dark equilibrium is shifted in favour of SP, irradiation with UV light may lead to ring-opening accompanied by proton uptake. This thesis focuses only on the negative photochromism aspects as shown in Figure 1.1 b —*i.e.*, only on the photoacidity of BIPS in water.

1.1 In the quest for reversible photoacids

Chemical reactions driving predictable pH changes in aqueous solutions can provide easy access to the control of pH-sensitive (bio)chemical systems.^[25] The growing interest in the development of photoacids^[26,27]—which, in a broad sense, can be defined as chemical species converting into acids following light absorption—arises from the opportunity to trigger such type of reactions selectively, with high spatial and temporal precision, and without the generation of waste products. Depending on their mechanism of action, photoacids can be classified into three different types, which are: i) photoacid generators, ii) excited-state photoacids, and iii) metastable state photoacids. Photoacid generators are compounds that release Lewis or Brønsted acids upon photolysis in solution; typical examples are diazonium, diaryliodonium and triarylsulfonium salts. Their actuation is generally irreversible and found application in photolithography, light-controlled surface shaping, and cationic photopolymerizations.^[28–30] Excited-state photoacids are compounds displaying extreme acidity differences between their ground state and excited state (ΔpK_a values of up to 12)^[31]; prominent examples are phenols, naphthols and pyranine dyes. Their activation is reversible, but proton recombination is so fast that modest pH changes are difficult to be observed even using intense light sources.^[32] On the contrary, metastable state photoacids are compounds which, after photoexcitation with light of

moderate intensity, can access a dissociated state that is relatively long-lived.^[26,27,33] They are also fully reversible, as in the absence of light they spontaneously revert to their original undissociated state. Important examples include *ortho*-hydroxy azobenzenes^[34], tetra-*ortho*-methoxy azonium ions^[35], tricyanofuran-based compounds^[36] and BIPS in their open protonated form (MCH, see above). In azobenzene-based systems, the difference in acidity is due to dissimilar hydrogen bonding interactions in the corresponding trans and cis isomers, whereas in BIPS it emerges from the occurrence of an intramolecular cyclization reaction between the (electrophilic) indolium moiety and the (weakly acidic and nucleophilic) phenol moiety accompanied by the release of a proton (Figure 1 b). The acidity difference between the ground state and metastable state of BIPS in water can attain 4 p*K* units and the photo-induced proton dissociation can last for minutes. If proton dissociation does not occur—as, for example, in acetonitrile solutions^[37–40]—molecules with compatible basicity can reversibly uptake the proton to assist the ring-closure. In other words, any BIPS can be used to reversibly control acid-base equilibria featuring an equilibrium constant that is higher than that of its ground state, but lower than that of its metastable state.^[39,41] But what is the reason for proton dissociation to occur when using BIPS in water? What are the prerequisites necessary for BIPS to induce reversible pH changes? If we assume that i) the ground state equilibrium of a given BIPS is quantitatively shifted to its MCH form and ii) visible light absorption leads to quantitative isomerization of MCH into SP and H⁺, the resulting pH change can be approximated as:

$$\Delta\text{pH} \approx \sqrt{\frac{C}{K_a^{GS}}} \quad \text{Eq. 1.1}$$

Where ΔpH correspond to the pH difference accessible during light irradiation (*i.e.*, $\text{pH}_{\text{dark}} - \text{pH}_{\text{light}}$), whereas C indicates the concentration of the MCH form and K_{a}^{GS} the corresponding ground state acidity constant (see appendix below for more details). It follows that reversible proton dissociation in water can be observed only when C is higher than K_{a}^{GS} —*i.e.*, ΔpH can be non-zero and positive only in the case $C \geq K_{\text{a}}^{\text{GS}}$. It should be noted that solubilization of BIPS starting from their SP form may lead to ring-opening and proton uptake, resulting in aqueous equilibrium distributions where MCH is not quantitatively populated. In this case, C should be higher than the proton concentration in the dark for observing acidification upon light irradiation. In general, however, the water-solubility of BIPS is poor, and the conditions above can be satisfied by making BIPS derivatives that are highly water-soluble and/or weakly acidic in the dark.

1.2 Applying BIPS reversible proton release in water

Evidence that BIPS can display reversible proton dissociation in solution emerged as early as 1967 when Shimizu and co-workers^[11] reported on the light-triggered proton relay between 6-nitro BIPS and malonic acid in acetone. They showed that the addition of malonic acid to a solution of 6-nitro BIPS produces the corresponding MCH form (as malonate salt) in the dark, and that the system can be driven back to the SP form (and malonic acid) by light irradiation. At the turn of the 21st century, similar results were obtained in water as well by either Braslavsky^[42], who studied the ring closure of MCH in the presence of malonic acid by laser-induced optoacoustic spectroscopy, and Willner^[43], who showed that MCH moieties anchored onto monolayer surfaces can directly isomerize to SP following visible light absorption. Direct proof of the reversible proton dissociation of BIPS in water, however, did not appear before 2004, when

Sumaru and co-workers^[44] first demonstrated, with pH measurements, that BIPS-functionalized poly(*N*-isopropylacrylamide) polymers can be used to lower the pH of their aqueous solutions by approximately 1 pH unit. Later on in 2011, these results were consolidated by the seminal work of Liao and co-workers^[33], who showed that a specific non-activated BIPS—bearing a propyl-sulfonate group in position 1' and lacking the nitro group in position 6—can be used to drive reversible pH changes in water as high as ca. 2 pH units following blue light absorption. Looking more closely at these two seminal examples, it is interesting to note how BIPS concentration was almost the same (ca. 0.2 mM), whilst the corresponding pK_a^{GS} values were estimated to be both close to neutrality (ca. 6-7)—*i.e.*, the prerequisite for having pH jumps outlined above ($C \gg K_a^{GS}$) was satisfied. Since Liao's contribution, the use of BIPS to control acid-base reactions remotely and reversibly has gained momentum.^[27] In the following sections we try to give, to the best of our knowledge, an overview of what has been achieved using BIPS as metastable state photoacids in water.

1.2.1 Control over bio-related systems

Water-soluble BIPS are biocompatible compounds, and their pH switch can be used as tool for tweaking and controlling the properties of various bio-related proton-sensitive systems. In the group of Sleiman^[45] BIPS photoacids were used as proton source for reorganization and error-correction of polyadenine coagulates (Figure 1.2 a). Visible light irradiation resulted in protonation of the polyadenines and so in their disassembly. The disassembled structures can subsequently undergo reorganization in a highly ordered aggregation state once the light is switched off. In other words, the system is pushed away from equilibrium (defected triplex) to form a protonated

intermediate (duplex); once the light source is stopped, the duplex state decays yielding a more ordered final state (ordered triplex).

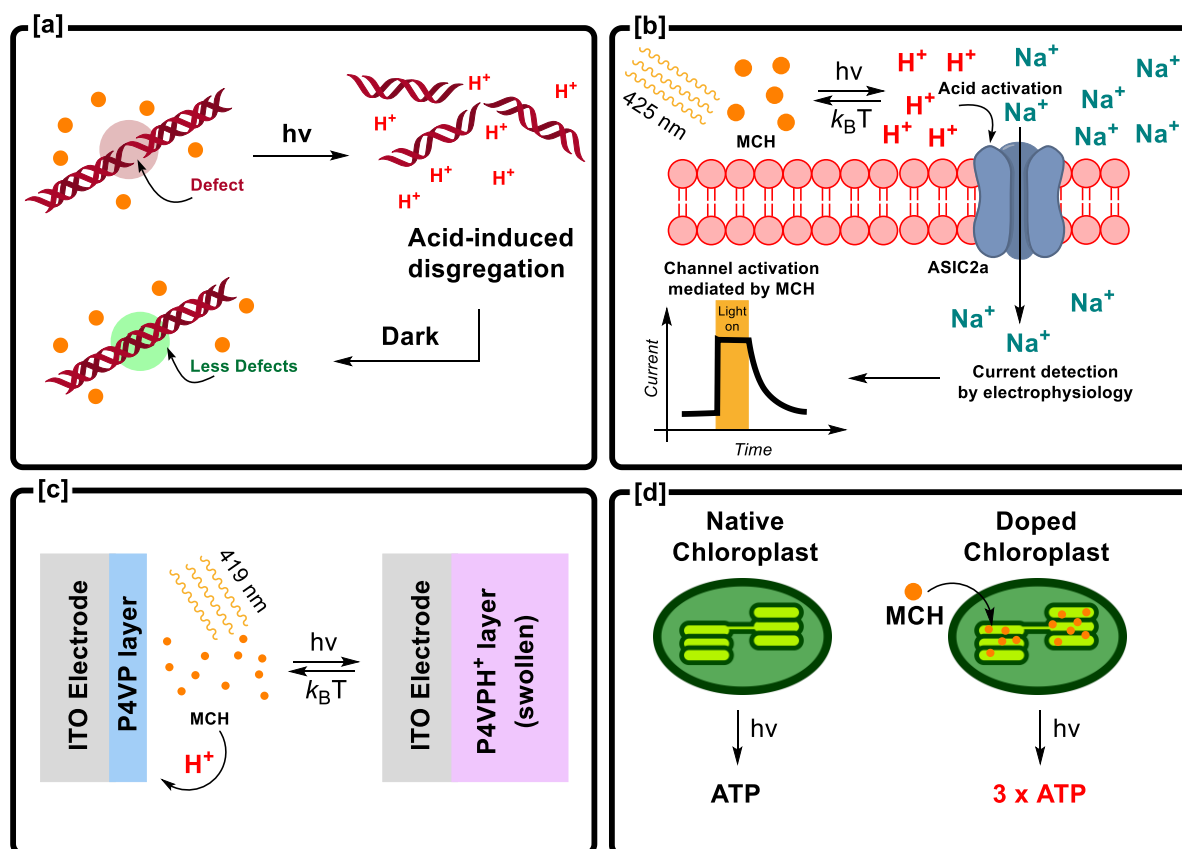


Figure 1.2. Selection of applications for BIPS in bio-related systems. In [a] poly-adenine assembly and disassembly using the photoacidity of MCH, [b] photoacid-induced activation of the ASIC2a sodium channel, [c] modulation of the activity of a microbial fuel-cell by photoacid-induced swelling of the material fabricated on the ITO electrode, [d] chloroplast doping with MCH yields higher ATP productions from light exposure.

BIPS photoacidity can be coupled also with transmembrane ion channels (Figure 1.2 b). Similarly to what was done by Feringa^[46] and co-workers, the group of Dougherty^[47], for example, used BIPS to control the activation of an ASIC2a acid-sensitive ligand-gated ion channel (GLIC). They employed a sulfonated BIPS displaying exceptional water-solubility and that was not interfering with the biochemistry associated to the GLIC. To prove the effective triggering of the channel upon irradiation, the experiments were designed so to force oocytes from *Xenopus laevis* to express the GLICs and to these cells was applied a solution of photoacid.

The electrophysiology traces showed no current in the dark, while under 455 nm irradiation there was a strong and immediate response due to the protonation and the opening of the ion-channels, which could easily be reverted under dark conditions. BIPS have found use also in the reversible actuation of microbial fuel cells (Figure 1.2 c).^[48] In the work of Z. Li and co-workers, the visible light-triggered release of protons by BIPS interfere with the surface chemistry of an ITO electrode bearing a pH-sensitive poly(4-vinyl pyridine)-modified interface, resulting in fast and effective current modulation. This study showcases the opportunity to switch the activity of microbial fuel cells in a fully reversible manner without the need for stepwise addition of acids or bases, which can lead to the accumulation of waste products in the power cell. The possibility to use BIPS *in-vivo* has been demonstrated also by Junbai Li and co-workers^[49], who showed that BIPS can be easily actuated inside chloroplasts (Figure 1.2 d). Chloroplasts convert light into a proton-motive force, which in turn is used to produce ATP, thus fixating the energy of light into phosphoanhydride bonds. The extent of this conversion depends on the size of the proton gradient across the thylakoid membrane. Incorporation of BIPS inside chloroplasts resulted in enhanced ATP synthesis following visible light irradiation (around 400 nmol/mg for the native and 1200 nmol/mg for the doped chloroplasts).

1.2.2 Opportunities for BIPS in photomedicine

Visible and NIR light-sensitive systems capable of promoting selective chemical transformations are viable for targeted drug delivery, disinfection and for addressing solubility or aggregation issues. Right after their seminal work in 2011, Liao and co-workers^[50] reported on the possibility of exploiting BIPS for inactivating the growth of multidrug-resistant bacteria (Figure 1.3 a). They showed that reversible pH jumps from

pH 5.8 to pH 3.3 can be used to kill different strains of *Pseudomonas Aeruginosa*—which are bacteria responsible for many hospital-related infections—by inhibiting the synthesis of intracellular proteins at low pH. It was also shown that combination of BIPS photoacidity with colistin (a peptide antibiotic) decreased the minimum inhibition concentration of the latter by more than one order of magnitude (ca. 30 times).

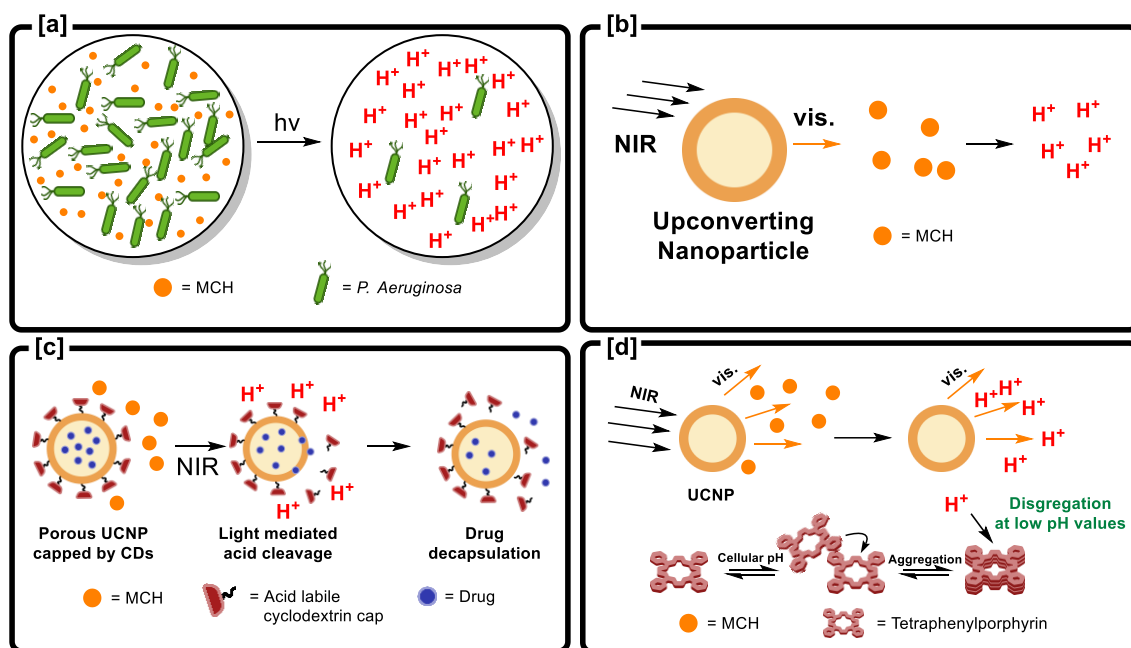


Figure 1.3. Selection of applications for BIPS in the photomedicine world. In [a] MCH is used to kill *P. Aeruginosa* by means of its photoacidity, [b] the strategy for using MCH *in-vivo* by means of UCNP's activation and subsequent proton release, [c] drug delivery application of MCH that can trigger the acidic cleavage of the cyclodextrin caps on an UCNP carrying the drug load, this can be released on-demand by means of NIR irradiation, [d] UCNP-mediated photoacidity of MCH used as a strategy for keeping TPPs in the non-aggregated state, thus, increasing the 1O_2 production.

Utilizing BIPS *in vivo* is a challenging task because the optical density of living tissues limits the penetration of visible light – *i.e.*, 440 nm light is completely extinguished at around 1 mm of depth from the surface of the skin.^[51] Upconverting nanoparticles (UCNPs), however, have been shown to successfully mediate the activation of BIPS *in vivo*. UCNPs are nanoparticles that can absorb multiple low-frequency photons and convert them into one high-frequency photon—e.g., two NIR photons into one visible photon (Figure 1.3 b). An interesting example has been reported by Hou and co-

workers^[52], who showed that porous cyclodextrin-capped UCNPs and BIPS can be used in the targeted release of doxorubicin—a well-known DNA intercalating agent (Figure 1.3 c). Irradiation of UCNPs with NIR photons generated light of suitable wavelength to trigger the photoreaction of MCH, which in turn caused the cleavage of the cyclodextrin capping groups and the subsequent release of doxorubicin molecules. A similar strategy was adopted by Bu and coworkers^[53], who used a combination of UCNPs and BIPS for the reversible generation of protons by using NIR light in biologically relevant conditions (Figure 1.3 d). Typically, tetraphenylporphyrins (TPPs) suffer from low solubility at physiological pH and their aggregates have low activity in $^1\text{O}_2$ generation. Introduction of alkylamino sidechains on the phenyl rings of TPPs made the system acid-sensitive, thus hindering their aggregation at low pH following protonation of the amino groups. It turned out that NIR-generated protons can be used to prevent the aggregation of TPPs to keep $^1\text{O}_2$ generation at peak performance in biologically relevant conditions. Cytotoxicity assays have shown a 10-fold tumor growth inhibition as compared to the same untreated cell culture.

1.2.3 BIPS photoacidity and materials

Direct incorporation of BIPS into materials has been shown to allow for tuning a variety of acid-base sensitive systems. BIPS photoacids can easily be adsorbed within MOFs (metal-organic frameworks) to regulate their proton sensitivity.^[54] For example, Zhang and coworkers have shown that introduction of BIPS in Zinc oxalate-based MOFs enabled the reversible switching of proton conductivity of this composite material (Figure 1.4 a). Under visible light irradiation, the material featured higher conductivity and the process could be reverted simply by stopping the light irradiation.

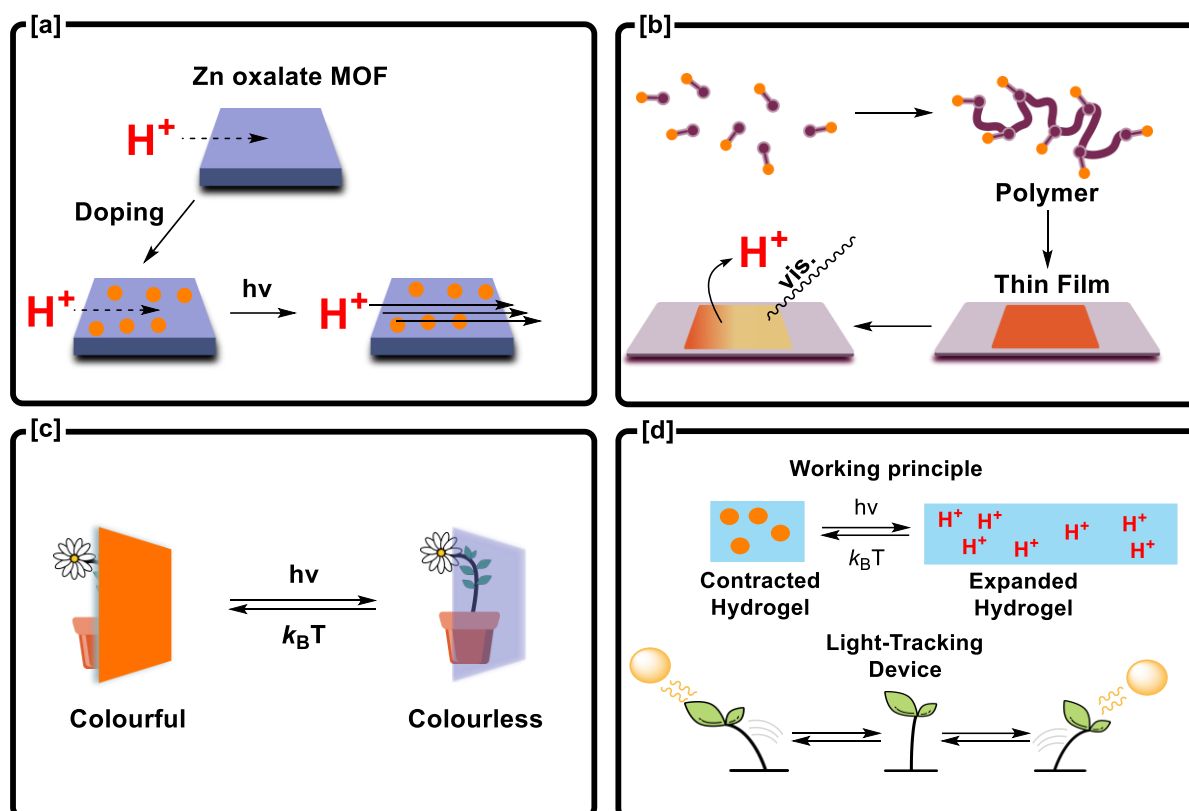


Figure 1.4. Selection of applications form BIPS in the material science world. In [a] MOF doped with MCH increases the proton conductivity of the material once exposed to visible light irradiation, [b] MCH-functionalized monomers are polymerized and fabricated in a thin-film form providing photoacidic and photochromic properties to the material, [c] in general materials can be doped with MCH to confer photochromic properties, [d] MCH is used to change the properties of soft materials between the dark and light state; in this example MCH is used to mimic the sun-tracking behavior of the plant named Cornish mallow.

Solid-state photoacid-doped materials have also been reported by Liao and co-workers^[55], who prepared BIPS-functionalized methacrylate polymers (Figure 1.4 b). Such polymeric materials were characterized in PBS aqueous buffer solutions by means of optical spectroscopy and potentiometry. They found that micrometric films of these polymers can induce pH changes of the supernatant of about 1.9 pH units. The observed proton release revealed to be extremely fast and reversible. The same group has shown the possibility to exploit BIPS in the development of photochromic materials (Figure 1.4 c).^[10] Incorporation of BIPS together with bromocresol green in a thin film of polycaprolactone resulted in a very optically dense material which became almost transparent following visible light irradiation. BIPS visible-light

mediated photoacidity can also be used to regulate gelation and aggregation processes. The group of Kuehne^[56], for example, has prepared a colloidal microgel which could respond to acid-base stimuli, melting into its building blocks at acidic pH values. This material was described as a dissipative self-assembling system, since the energy delivered by photons is then slowly released as heat during proton reuptake, which led to the re-constitution of the colloidal state. In the context of nanomaterials, Ikkala and co-workers^[57] prepared hydrogels capable of responding to either temperature and light stimuli in a programmable fashion. Temperature changes or light-induced pH changes can confer different forms to the hydrogel due to different reactive pathways. Similarly, Li and co-workers used BIPS for changing the aggregation state of proton-sensitive materials, like chitosan^[58]. In this case, the light-induced pH change was exploited for protonating the amino groups on the polysaccharide, which in turn act as ionic groups for scavenging the resulting SP anions. This resulted in the formation of many single-strands of SP-chitosan ion pairs which assemble into supramolecular nanoparticles. The system disassembles spontaneously to the initial state in the dark, thus allowing cyclability. BIPS reversible proton release have been shown to provide a means for biomimetic photoactuation (Figure 1.4 d). For example, Faul and co-workers^[59] engineered a device capable of replicating the behavior of the Cornish mallow – a plant that reorients its leaves according to the position of the light source. Their device features a BIPS-containing hydrogel matrix which contracts/expands depending on light-induced pH changes. The geometry of the device was designed such that only the light-exposed part contracts due to the shrinking of the hydrogel matrix. Upon reaching the maximum exposure position, the force exerted by the opposite side of the gel matrix blocks the movement.

1.2.4 Control over chemical systems

The chemistry of BIPS can be exploited for controlling chemical systems in water. The group of Liu^[60] reported on the reversible disassembly of supramolecular nanothreads constituted by subunits of Zn coordinated to 4,4'-bipyridine included in β -cyclodextrins (Figure 1.5 a). Protonation of the bipyridine basic sites decreases the affinity for the metal ion and the supramolecular structure collapses into its building blocks. Once the irradiation is stopped, the system slowly reverts back to the nanothread-shaped state.

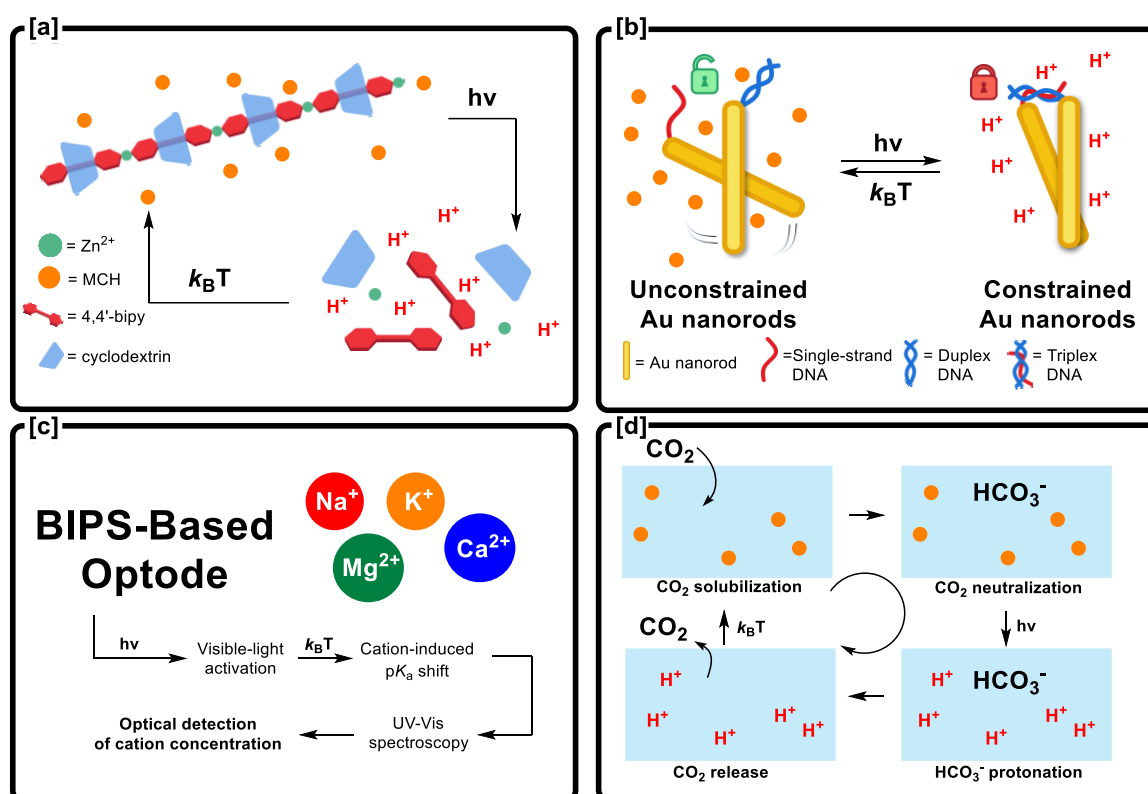


Figure 1.5. Selection of applications from BIPS in the chemistry world. In [a] the reversible disassembly of proton-sensitive supramolecular structures mediated by the light-activation of MCH, [b] threaded gold nanorods are constrained by the aggregation of a DNA duplex (left) into DNA triplex (right). This strategy is used to lock the relative rotation of the nanorods about their pivot point located in the center, [c] the use of BIPS photoacids as optical detectors for alkali metal ions can be employed seen the pK_a shift that they undergo due to the presence of the metal ions in solution, [d] CO₂ pump designed to operate thanks to the presence of MCH in solution that acts as reversible proton source available for the on-demand release of CO₂.

Kuzyk and co-workers^[61] used BIPS photoswitches to control the shape of DNA-origami (Figure 1.5 b). In this example pairs of gold nanorods were threaded together

and functionalized on one end with a pH responsive DNA lock. While resting at pH close to neutrality these assemblies show weak CD signals indicating low concentration of chiral chromophores. Upon irradiation, the system gets locked in a highly asymmetric state as indicated by an intense CD signal. In the context of supramolecular chemistry, Aprahamian and co-workers^[62] reported a hydrazone switch which can be activated by protonation using a BIPS-type photoacid. In his work, the reported hydrazone switch is found in a *E/Z* ratio of approximately 6:4 according to NMR studies. Upon BIPS-mediated protonation the switch gets locked in the *Z* isomer and slowly decays back to the original equilibrium distribution in the dark. BIPS photoacidity can contribute also to the development of novel analytical methods. The group of Chumbimuni-Torres, for example, developed BIPS-based systems for ion-sensing (Figure 1.5 c).^[15,63] Specifically, they embedded BIPS into a polymeric matrix which is capable of releasing protons under light irradiation creating room for accommodating Ca^{2+} ions. The material showed differences in optical spectra which can be ascribed to the presence of the cation, thus enabling its detection. Remarkably, BIPS reversible proton release may find use in novel eco-friendly solutions in chemical scavenging and energy harvesting systems. For example, the group of Puxty (Figure 1.5 d)^[64] has shown that, even if to a small extent, carbon dioxide can be desorbed reversibly from aqueous solutions containing BIPS. The proton release induced by the photoactivity of BIPS lowered the pH value, thus promoting the controlled release of carbon dioxide upon irradiation. Very recently, Bae and co-workers^[65] have also shown the possibility of using BIPS in the development of simple and cost-effective solar energy harvesting system.

Chapter 2

Aim of the thesis

Notwithstanding the ever-growing interest in BIPS and the important impact they are having as metastable state photoacids across multiple research fields, evaluating their (photo)chemistry—including their photoacidic properties—still remains fragmentary. An accurate description of BIPS equilibrium distributions and photostationary states in water is missing, and the mechanisms of hydrolysis and relaxation from the metastable state are all still subjects of debate. As matter of fact, for example, there is a lack of analytical methods for determining unambiguously the acidity constant of both their ground state and metastable state. **To compensate for this absence, this thesis aims at rationalizing BIPS thermodynamics and kinetics through the development of new characterization protocols. With better knowledge over the fundamental processes of BIPS, it will be possible to augment their performance as photoacids in water by taking advantage of precise structural modifications and by using supramolecular chemistry.** In particular, Chapter 3 describes physical organic chemistry approaches aimed for gaining a firm grasp of BIPS working principles in water and for formulating a series of new interpretations spanning both their ground state and metastable state chemistries. These approaches develop further in Chapter 4, where the dependency of BIPS photoacidity on temperature is studied in more detail. Chapter 5 deals with structure-function relationships on a library of four different BIPS with the objective of increasing the hydrolytic stability and to better characterize their solubility equilibria towards enhanced pH jumps. Chapter 6

tackles the challenge of increasing the fatigue-resistance over multiple pH jumps by exploiting a precisely designed and selective supramolecular host-guest system. Overall, the aim of this Thesis is to obtain soluble and robust systems able to at least double the pH jumps so far achievable by BIPS in water following visible light irradiation – *i.e.*, ΔpH from 2 to 4.

Chapter 3

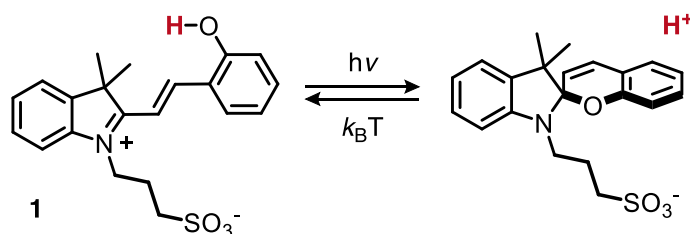
Thermodynamics and kinetics of protonated merocyanine photoacids in water

Parts of this chapter have been taken from:

C. Berton, D.,M. Busiello, S. Zamuner, E. Solari, R. Scopelliti, F. Fadei-Tirani, K. Severin, C. Pezzato, *Chemical Science*, **2020**, 11, 8457-68.

3.1 Introduction

Liao's photoacid^[33] – referred to here as compound **1** – represents the archetype of metastable state photoacids. Under dark conditions, **1** behaves as weak acid whereas, following visible light absorption, it undergoes photoisomerization leading to the corresponding SP form and the release of a proton (Scheme 3.1).



Scheme 3.1. Reversible photoreactivity of Liao's merocyanine **1**.

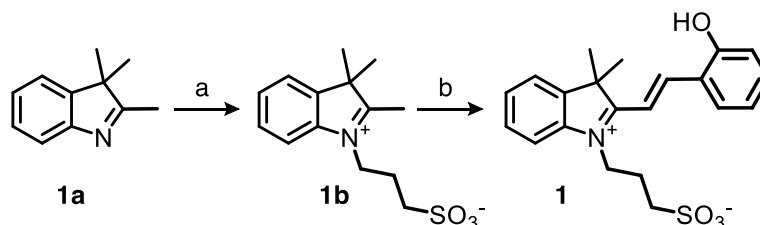
The reason behind this negative photochromism resides for the most part to the lack of electron-withdrawing (EWG) substituents (e.g., $p\text{-NO}_2$)^[12] on the phenol side, which in turn decrease the stability of the open deprotonated form (MC) in favor of MCH.^[66] Generally, the acidity difference existing between the ground state (pK_a^{GS}) and the metastable state (pK_a^{MS}), along with a moderately long lifetime of proton photo-dissociation, makes **1** and BIPS in their open protonated forms – referred hereafter to

as MCHs – suitable for controlling remotely any chemical system relying on acidic inputs. MCHs have been used as light-responsive regulators of molecular machines,^[37,67,68] gelation^[57,69,70] and self-assembly processes^[71,72], photochromic systems,^[38,73] and many more already mentioned in the introductory chapter. MCHs have also been employed in the remote control of acid-catalyzed reactions such as the hydrolysis of acetals,^[36] and the polymerization of cyclic lactones,^[74] whereas diverse polymer scaffolds^[15,75–78] are recently emerging for tuning the switching properties of MCHs in general. Notwithstanding the tremendous impact that **1** has had and is having across multiple research fields, evaluation of its thermodynamics and kinetics in water so far remained inconclusive. The lack of experimental protocols for defining accurately both pK_a^{GS} and pK_a^{MS} has led to diverse re-interpretations over the past years, and the mechanisms of both hydrolysis and relaxation are still subject to debate. Herein, we rationalize the behaviors of **1** in water through cross-validation of ¹H NMR, UV-Vis and pH measurements, and modelling. The developed methodology is general and can be easily applied to other MCHs.

3.2 The ground state

Compound **1** was synthesized starting from the Fisher's base 2,3,3-trimethylindoleine **1a** which reacts with 1,3-propanesultone yielding the indolium salt **1b**. Knoevenagel condensation of **1b** with salicylaldehyde yields **1** as a orange and air stable solid which is fully characterized by high-resolution mass spectrometry (HR-MS), ¹H and ¹³C-NMR spectroscopy, as well as X-ray analysis. Our investigations on the ground state started from a simple observation: aqueous solutions of compound **1**, under dark conditions and at known concentration, exhibited pH values diverging substantially from those

expected considering previously reported pK_a estimates.^[26,33,79] Initially, we ascribed this outcome to possible differences in (i) temperature and (ii) ionic strength of the sample, as well as (iii) equilibration time before data collection, which are all common parameters to which direct pH readings are sensitive to.



Scheme 3.2. Synthesis of Liao's merocyanine; a: 1,3-propanesultone, MeCN, reflux, 24 h (98%); b: salicylaldehyde, EtOH, reflux, 12h (95%).

Motivated by these results, we decided to employ ^1H NMR spectroscopy for quantifying the dissociation behavior of **1** in the ground state. Contrary to common UV-Vis spectroscopic studies, where the absorption of multiple species can overlap, ^1H NMR spectroscopy offers the possibility to have a rather wide and more resolved response window, possibly allowing for direct structural characterization and the monitoring of multiple phenomena without mutual interferences. Samples for ^1H NMR analysis were prepared by adding an aqueous solution of **1** to 20 mM potassium phosphate buffers solutions ranging from pH 3 to 10, and subsequently analyzed after an equilibration time of 15 minutes in the dark and at a constant temperature of 25 °C. The ^1H NMR spectra obtained for **1** are reported in Figure 3.1. At first glance, it appears evident how all the resonances found at low pH progressively shift and weaken in favor of a third species. The doublet centered at around 8.7 ppm – displaying a coupling constant typical of vicinal, *trans*-alkenyl hydrogens ($^3J_{\text{trans,a}} = 16.3$ Hz) – confirms that the predominant species at low pH is the open protonated form MCH (represented in black), whereas the chemical shift perturbations associated

to it and all the other signals reflect a change of the equilibrium position towards the open deprotonated form MC (represented in blue). Concomitantly, however, the new doublet emerging at around 5.9 ppm – displaying a coupling constant typical of vicinal, *cis*-alkenyl hydrogens ($^3J_{\text{cis},b^*} = 10.3 \text{ Hz}$) – indicates a progressive displacement towards a configurational isomer: the closed spiropyran form SP (highlighted in red). The fact that the resonances associated to the methylene protons of the propyl-1-sulfonate bridge, as well as those of the methyl groups, undergo splitting into diastereotopic patterns confirms the installment of a chiral center – *i.e.*, the spiro carbon (labeled as *). Taken together, these observations suggest that $\text{p}K_{\text{a}}^{\text{GS}}$ should not account merely on a single dissociation event, but rather on a three-component equilibrium, as proposed first by Coudret^[80] and Liao thereafter.^[81]

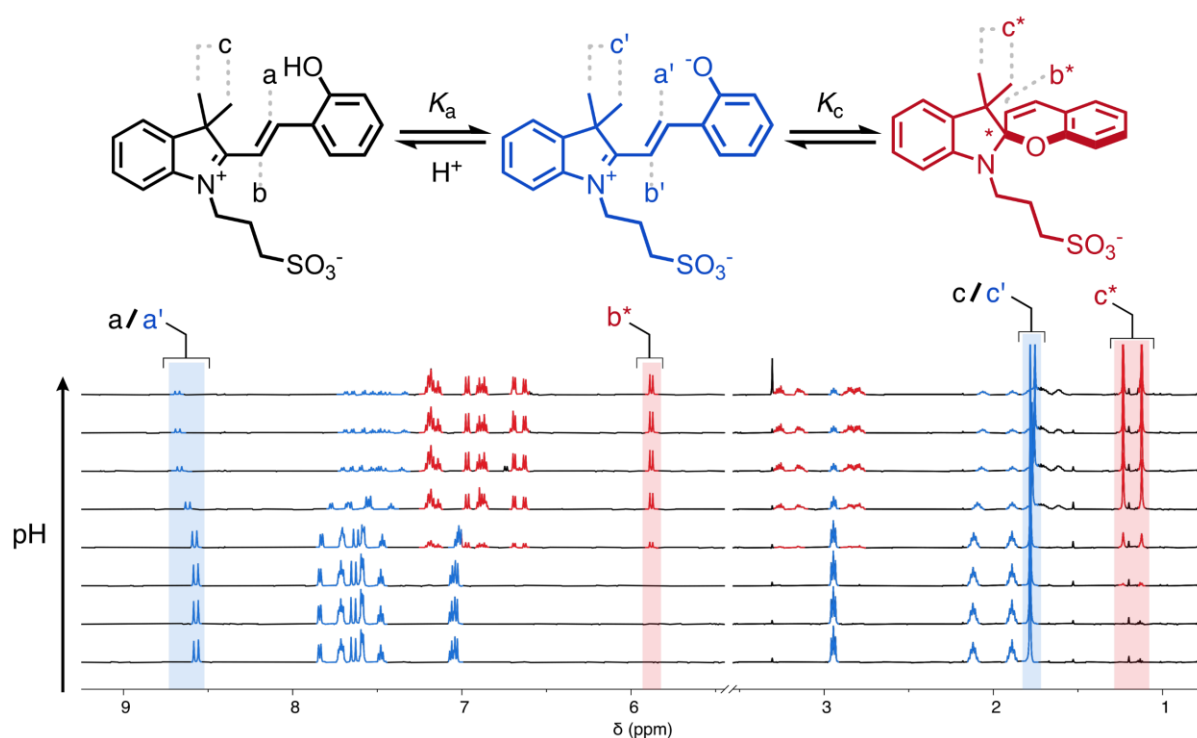


Figure 3.1. ^1H -NMR spectra (600 MHz, 298K, $\text{H}_2\text{O}/\text{D}_2\text{O}$ 6:4) at increasing pH values (potassium phosphate buffers 20 mM, pH 3.0-9.5 every 1.0 units). The colors indicate signals belonging to the MCH/MC couple (blue) or to the SP form (red).

The chemical shift perturbations observed for all the resonances associated to the MCH/MC couple reflect a decreasing extent of protonation from low to high pH values and can be considered as the weighted average of the two open forms in equilibrium. This is typical for events happening faster than the NMR timescale and gives the possibility to determine unambiguously the acidity constant of the phenoxy group – hereafter referred to as K_a . The K_a of **1** was calculated from the chemical shift profiles of suitable well-resolved resonances (*e.g.*, the one associated to the methyl groups c/c' , Figure 3.2 a) as a function of the pH by least-squares curve fitting to Eq. 3.1.

$$\delta_{\text{obs}} = \frac{[\text{H}^+] \delta_{\text{MCH}} + K_a \delta_{\text{MC}}}{[\text{H}^+] K_a} \quad \text{Eq. 3.1}$$

where δ_{obs} is the observed chemical shift, while δ_{MCH} and δ_{MC} are the chemical shifts associated to MCH and MC, respectively.

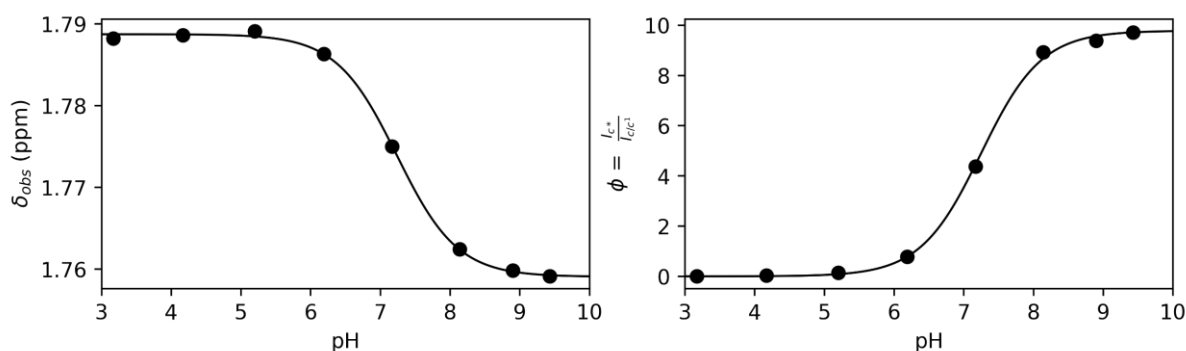


Figure 3.2. In [a] Chemical shift perturbation against pH value of protons c/c' for compound **1**. In [b] integral ratio between the SP (proton c^*) and the MCH/MC couple (protons c/c').

The model fits with very good confidence ($R^2 > 0.99$) the experimental data and gave a pK_a value of 7.2 ± 0.1 . This value is lower than the one predicted numerically by Coudret (7.75)^[23], yet very close to that of *o*-nitrophenol^[82] in water and gives a hint of the EWG effect of the indolium moiety on the acidity of the phenoxyl group. Analysis

of the integral perturbation in favor of SP offers the possibility to assess simultaneously K_a and the equilibrium constant of the $MC \rightleftharpoons SP$ isomerization – hereafter referred to as K_c . Indeed, both K_a and K_c can be calculated from the profile of suitable integrals ratio (e.g., that between the integrals of c^* and c/c' , Figure 3.2 b) as a function of the pH by least-squares curve fitting to Eq. 3.2.

$$\varphi = \frac{[SP]}{[MCH] + [MC]} = \frac{K_c}{\left(1 + \frac{[H^+]}{K_a}\right)} \quad \text{Eq. 3.2}$$

where ϕ represents the ratio between the concentration of the closed form and the total concentration of the open forms. This simple model equation suits the three-component equilibrium system depicted in Figure 3.1 and fits with good confidence the experimental data yielding a similar pK_a (7.2 ± 0.1) and a pK_c value of -0.99 ± 0.04 (Figure 3.2 b). Having quantified, for the first time experimentally, the equilibria taking part in solution and considering that the proton concentration at equilibrium should satisfy the charge balance – *i.e.*, $[H^+] = [SP] + [MC]$ – it follows that K_a^{GS} can be expressed as follows:

$$K_a^{GS} = K_a(1 + K_c) \quad \text{Eq. 3.3}$$

It should be noticed at this point, the contribution of K_c to the overall extent of proton dissociation in the ground state: for $K_c \ll 1$ ($[MC] \gg [SP]$) K_a^{GS} reduces to K_a , whereas for $K_c \gg 1$ ($[MC] \ll [SP]$) K_a^{GS} can be approximated to $K_a K_c$ (see the Experimental Section for more details). In the case of **1**, none of these two cases apply and by using Eq. 3.3 we obtain a pK_a^{GS} value of 6.2 ± 0.1 . This value is significantly lower than any of those so far estimated for **1** through simple pH readings in the dark (7.8 ,^[21] 7.5 ,^[18]

$<7.4^{[20]}$) and numerical analysis (ca. 7) $^{[23]}$, yet fairly in line with some reports on polymers functionalized with SPs lacking the *para*-NO₂ group (6–7) $^{[44]}$. To complement the NMR data, we decided to study the equilibration of MC towards SP by UV-Vis spectroscopy. In general, samples for UV-Vis analysis were prepared starting from stock solutions in dry MeOH, as we found these solutions (ca. 5 mM) underwent negligible $^{[67]}$ degradation over two months when stored at 4 °C. The concentration of each stock was determined from a series of three independent potentiometric titrations, using the corresponding second derivative curve for calculating the endpoint (see Experimental Section).

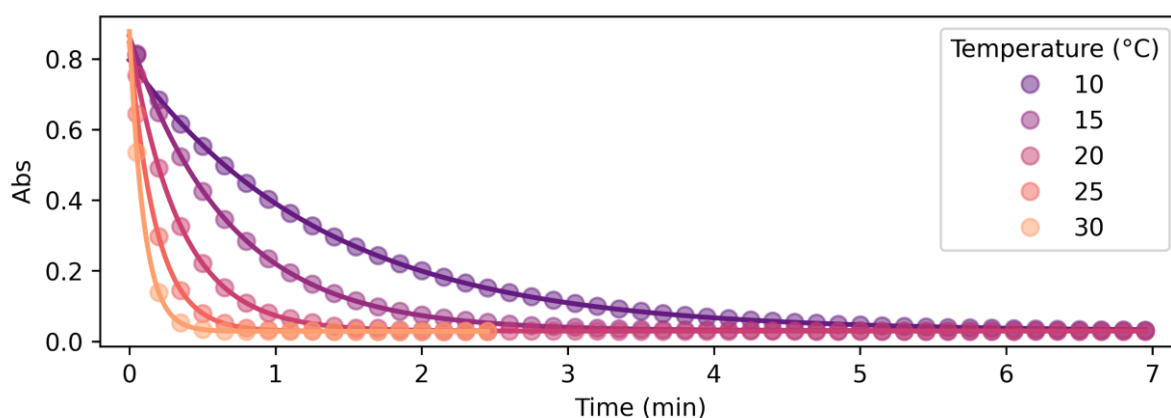


Figure 3.3. Kinetics profiles for the decay of MC into SP at 532 nm. Solid lines represent the best-fit to a first-order decay.

In a typical experiment, aliquots of an aqueous solution of photoacid – 10% MeOH v/v, freshly prepared by dilution of one of the stocks above – were added to 20 mM potassium phosphate buffers solutions at the desired pH and subsequently analysed. In order to investigate the $MC \rightleftharpoons SP$ isomerization, we decided to operate at pH 9.5 ($pH \gg pK_a$), where the presence of MCH is negligible and the equilibrium reduces to MC and SP only. Kinetic analyses were carried out monitoring the decay of the absorption band of the corresponding MC form at temperatures varying from 10 to 30 °C (Figure 3.3). In all cases, data fit well to a first-order decay kinetics as in Eq. 3.4.

$$A_t = A_0(A_{eq} - A_0) \exp(-k_{obs,eq} t) \quad \text{Eq. 3.4}$$

Where A_t , A_0 and A_{eq} are the absorbances (in this case of MC) at any time t , $t = 0$ and at equilibrium, respectively, while $k_{obs,eq}$ is the apparent first-order rate constant of isomerization. At any temperature, K_c was calculated as:

$$K_c = \frac{[SP]}{[MC]} = \frac{A_0 - A_{eq}}{A_0} \quad \text{Eq. 3.5}$$

and subsequently used for breaking down the corresponding $k_{obs,eq}$ into the forward (MC-to-SP, k_2) and backward (SP-to-MC, k_{-2}) rate constants of isomerization as follows:

$$k_2 = \frac{K_c}{1 + K_c} k_{obs,eq} \quad \text{Eq. 3.6}$$

$$k_{-2} = \frac{1}{1 + K_c} k_{obs,eq} \quad \text{Eq. 3.7}$$

Consequently, energy diagrams for the $MC \rightleftharpoons SP$ isomerization of **1** were obtained by means of van't Hoff analyses and Eyring plots (see Experimental section) – all thermodynamic and kinetic parameters obtained in this way are listed in Table S 3.2 found in the Experimental section. First, we noticed that the MC-to-SP isomerization is endothermic, with a standard enthalpy ($\Delta_r H$) of $2.1 \pm 0.7 \text{ kJ mol}^{-1}$. In the case of SPs, it has been shown previously^[83] that the ground state energy of MC becomes lower than that of SP on account of hydrogen bonding interaction with water molecules – *i.e.*, the isomerization of SPs in water is enthalpically-driven, with an equilibrium distribution shifted towards MC. Contrary to SPs, however, here we found that the isomerization of **1** is entropically dominated, resulting in a standard free energy of

isomerization ($\Delta_r G$) of $-5.3 \pm 1.4 \text{ kJ mol}^{-1}$ at 25°C – *i.e.*, in an equilibrium distribution shifted in favour of SP. The resulting equilibrium constant is in agreement with the one obtained by ^1H NMR. The values found for the enthalpy (ΔH^\ddagger) and the entropy (ΔS^\ddagger) of activation are $92 \pm 1 \text{ kJ mol}^{-1}$ and $37 \pm 2 \text{ J K}^{-1} \text{ mol}^{-1}$, and both are in line with the activation parameters reported^[83] so far for SPs in polar protic solvents. The interpretation of the ground state thermodynamics of **1** emerging from ^1H NMR analyses was subsequently validated by UV-Vis titrations. Samples were prepared as described above with potassium phosphate buffer solutions ranging from pH 3 to 10, and subsequently analysed in the same way as the NMR titrations – one should note at this point the importance of equilibration time in the dark prior to data acquisition (Figure 3.3). The UV-Vis spectra of compound **1** at increasing pH values (Figure 3.4 a) were recorded after an equilibration time of 15 minutes at 25°C . The band centered at 424 nm, which progressively decreases as the pH increases, is assigned to the π – π^* transition of MCH, whereas the two new bands emerging at 535 and 297 nm are assigned to π – π^* of MC and the π – π^* transition of the chromene moiety of SP, respectively.^[3]

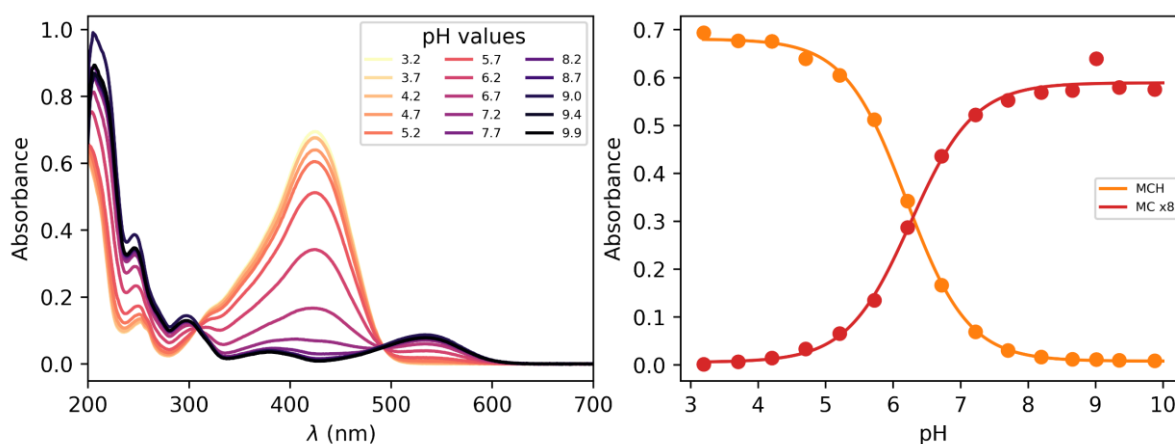


Figure 3.4. In [a] UV-Vis titration of compound **1** at different pH values (298 K, potassium phosphates 20 mM). In [b] intensities for the bands of MCH (orange) and MC (red, multiplied x8 for the sake of clarity) with the respective best-fit curves to Eq. 3.8.

Compared to SPs, the large hypsochromic shift observed for the band associated to MC (<550 nm) suggests that the phenolate resonance form of MC dominates over the quinoidal one, which indeed is typically favoured in non-polar media.^[84] The pK_a^{GS} was calculated from the profiles of the absorbance of either MCH and MC (Figure 3.4 b) as a function of the pH by least-squares curve fitting to Boltzmann equation:

$$A_{pH} = A_{OH} + \frac{A_H - A_{OH}}{1 + \exp\left(\frac{pH - pK_a^{GS}}{P}\right)} \quad \text{Eq. 3.8}$$

where A_H and A_{OH} are absorbances detected respectively at low and high pH, respectively, whereas P represent a fitting factor. The pK_a^{GS} thus obtained (6.20 ± 0.03) is nicely in agreement with that determined above with Eq. 3.3 and, importantly, with the one (6.23) obtained similarly in a recent study by Zhang and co-workers.^[85] Alternatively, knowing the molar extinction coefficients of all the species taking part in the equilibrium, UV-Vis data can be processed so as to obtain ϕ . The molar extinction coefficients of the MCH form were obtained by quantitative calibrations at pH 3 ($pH \ll pK_a^{GS}$) in the dark, whereas that of the SP form through calibrations at neutral pH ($pH \gg pK_a^{MS}$) under continuous LED-light irradiation (425 nm, 100 mW). Due to the transient nature of the MC form, molar extinctions were computed knowing the equilibrium composition at pH 9.5 (vide supra) and the optical readout of the corresponding SP form (see Experimental Section). Thus, the speciation diagram of 1 was obtained, for the first time experimentally, from the same UV-Vis titration (Figure 3.4) knowing the optical readout of SP, MCH and MC at all the corresponding λ_{max} (see Experimental Section). The absorption data allowed us to calculate the parameter ϕ as a function of the pH, by which both K_a and K_c were determined from fitting to Eq. 3.2. We were pleased to see that, despite a larger uncertainty due to error propagation,

all the equilibrium constants were fully consistent with those obtained by ^1H -NMR (see Table S 3.3). Overall, the evidences gained so far highlight the importance of the $\text{MC} \rightleftharpoons \text{SP}$ isomerization in determining $\text{p}K_{\text{a}}^{\text{GS}}$, unravelling a new design rationale for possibly decreasing the ground state acidity and amplifying the operational pH window of MCHs.

3.3 The metastable state

Having assessed the thermodynamics of the ground state by comparative ^1H NMR and UV-Vis analyses in the dark, we then moved on investigating the metastable state (Figure 3.5). So far, probing the metastable acid–base equilibrium of **1** in water was claimed to be challenging due to its low solubility and fast reverse reaction, and the corresponding $\text{p}K_{\text{a}}^{\text{MS}}$ was proposed to lay within 1.7–3.2 based on indirect measurements in MeOH.^[26] Numerical analyses by Coudret and co-workers, however, predicted the $\text{p}K_{\text{a}}^{\text{MS}}$ value of **1** to be 4.3.^[80] Motivated by these straying results, we opted for UV-Vis titrations under powerful and continuous LED-light irradiation for probing the photostationary state of **1**. Samples were prepared as described above, but using aliquots of standard HCl for fixing the pH below 4; the LED-light beam (425 nm, 100 mW) was delivered directly from the top of sample cuvettes by a 3-meter-long optical fibre. The UV-Vis spectra obtained exploiting the “room light immunity” feature of our spectrometer which, in brief, is the capability to exclude the contribution of external light sources to the absorption spectrum. The two overlapping bands centred at 330 and 385 nm, which progressively decrease as the pH increases, are assigned respectively to the π – π^* transition of the indolium and the chromene parts of the protonated form. Compared to the π – π^* transition of MCH (424 nm) in the dark, the observed blue shift and splitting can be ascribed to the decreased electronic

delocalization of a twisted conformation – *i.e.*, *cis*-MCH. In the case of SP, electronic delocalization is broken by the spiro carbon, and the same two transitions become distinct^[28] and narrow at 244 and 297 nm, respectively. The clear isosbestic point found at 300 nm confirms that the two forms constitute a photostationary state. The pK_a^{MS} of **1** was determined from the profiles of the absorbance of either *cis*-MCH and SP (Figure 3.5 b) as a function of the pH by least-squares curve fitting to Eq. 3.8 of metastable form of **1** (green and red traces Figure 3.5 b).

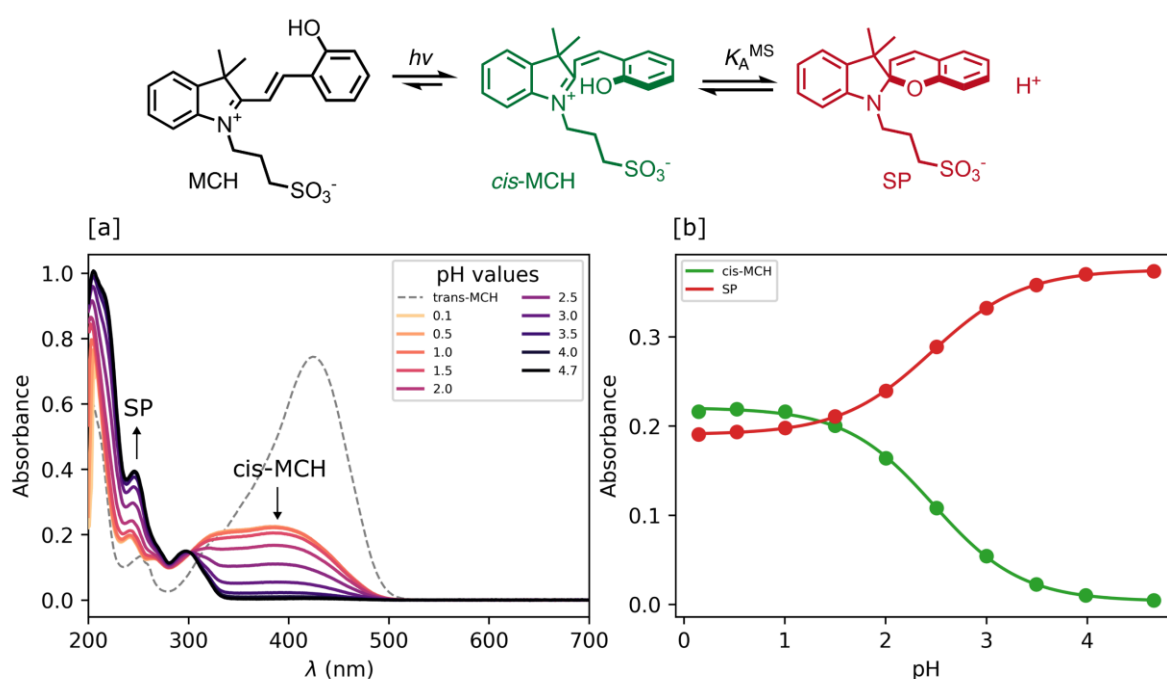


Figure 3.5. In [a] UV-Vis titration of compound **1** at different pH values (298 K, potassium phosphates 20 mM) under 425 nm light irradiation. In [b] intensities for the bands of *cis*-MCH at 415 nm (green) and SP at 244 nm (red) with the respective best-fit curves to Eq. 3.8.

The pK_a^{MS} thus obtained (2.47 ± 0.04) fall exactly between 1.7 and 3.2^[26] as proposed by Liao. At this point, in an analogy with excited-state photoacids,^[25] we propose to define the photoacidity of MCHs (referred to here as Π) as the difference between the acidity constants of the ground state and the metastable state:

$$\Pi = \text{p}K_{\text{a}}^{\text{GS}} - \text{p}K_{\text{a}}^{\text{MS}} \quad \text{Eq. 3.9}$$

This definition allows for rapid comparison of different MCHs and can be used to easily quantify their capability of changing the acidity of a solution after light irradiation (see below). The photoacidity of **1** was found to be $\Pi = 3.7 \pm 0.1$.

3.4 The hydrolytic stability

A delicate aspect to consider when using MCHs in water is their propensity to hydrolyze irreversibly. In the case of SPs, it has been shown previously^[86] that hydrolysis is initiated by addition of water to the ene-iminium moiety of their MC form, followed by a retro-aldol condensation reaction yielding the products. Water is the major nucleophile involved in the reaction below pH 9, but the MCH form is considered to be not susceptible to hydrolysis.^[87] On the other hand, compound **1** displays an half-life of decomposition of 16 hours at pH 5.4 – *i.e.*, at a pH where MCH dominates over MC.^[79] Also, it has been proposed that electron-donating groups conjugated to ene-iminium moiety may enhance the hydrolytic stability of MCHs in aqueous environments, and that hydrolysis of **1** would be catalyzed by OH⁻.^[79] The mechanism by which **1** undergoes hydrolysis, however, remains unclear, and we believed studying it in detail would be of interest in terms of practical applications. Thus, we decided to study the hydrolysis of **1** over the entire pH window ranging from 3 to 9. Kinetic analyses were carried out at 40 °C, monitoring the decay of the absorption band of the MC(H) form. The kinetic profiles were linearized, and apparent first-order rate constants of hydrolysis ($k_{\text{obs,hydr}}$) obtained as the slope of the corresponding linear fit (Figure 3.6 a). We found that the rate of hydrolysis gradually increases until around

pH 6, after that it starts to decrease for becoming progressively independent of pH (right of Figure 3.6 b). This bell-shaped profile is reminiscent of those observed for Schiff bases^[88] and, similarly, we think it could be due to a change in the rate-determining step from decomposition of tetrahedral intermediate X (II) to nucleophilic addition of water (I) at higher pH values (Fig. 5a). Inspired by the seminal work of Jencks and co-workers^[89] on the hydrolysis of substituted benzylidene-1,1-dimethylethylamines, and applying steady-state conditions in respect to the intermediate species X, we formulate the rate expression for the hydrolysis reaction as follows:

$$k_{\text{obs,hydro}} = \frac{k_w[\text{H}^+] + k_{\text{OH}}K_w}{([\text{H}^+] + K_a^{\text{GS}}) \left(\frac{k_{-w}}{k_h} [\text{H}^+] + 1 \right)} \quad \text{Eq. 3.10}$$

where k_w is the rate constant for the attack of water and k_{-w} that for the corresponding reverse reaction, k_{OH} is the rate constant for the nucleophilic attack of hydroxide ion and k_h that for the decomposition of X, whereas K_w is the autoprotolysis constant of water (see Experimental Section). Each kinetic contribution was at first estimated independently: (i) k_w from the maximum observed rate constant (for which $k_w[\text{H}^+] \gg k_{\text{OH}}K_w$ and $k_{-w}[\text{H}^+] \approx k_h$) or alternatively from that at neutral pH (where $k_w[\text{H}^+] \gg k_{\text{OH}}K_w$, $[\text{H}^+] < K_a^{\text{GS}}$ and $k_{-w}[\text{H}^+]/k_h < 1$), (ii) k_{OH} from the observed rate constant at pH 9 (where $k_w[\text{H}^+] \ll k_{\text{OH}}K_w$, $[\text{H}^+] \ll K_a^{\text{GS}}$ and $k_{-w}[\text{H}^+]/k_h \ll 1$), whereas (iii) k_{-w}/k_h from the observed rate constant at pH 3 (where $k_w[\text{H}^+] \gg k_{\text{OH}}K_w$, $[\text{H}^+] \gg K_a^{\text{GS}}$ and $k_{-w}[\text{H}^+]/k_h \gg 1$). Thus, least-squares curve fitting to Eq. 3.10 was performed using these guess parameters as initial values. The model fits with good confidence ($R^2 > 0.99$) the experimental data (Figure 3.6 b) and supports the change in rate-determining step proposed above. The

same experiment was repeated at 25 °C from pH 3 to 9 (see Experimental Section). In this case, data fitting to Eq. 3.10 (solid black line) allowed us to estimate all the forward rate constants involved in the hydrolytic pathway as $k_w = (2.8 \pm 0.4) \times 10^{-3} \text{ min}^{-1}$, $k_{OH} = (9.5 \pm 0.4) \times 10^3 \text{ M}^{-1} \text{ min}^{-1}$ and $k_h = (2.0 \pm 0.2) \times 10^{-2} \text{ min}^{-1}$ (see Experimental Section), which all in all show that the hydrolysis of **1** is significantly slower than the corresponding MC-to-SP equilibration (e.g., min^{-1} vs. s^{-1}).

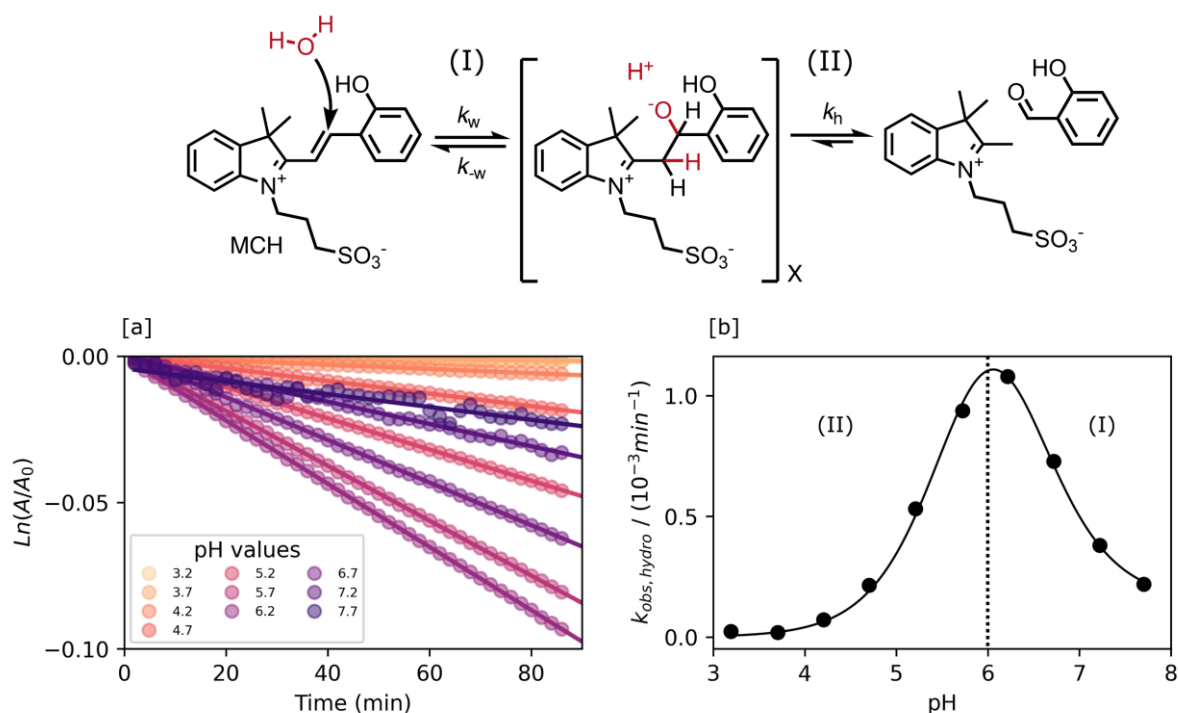


Figure 3.6. a) Linearized kinetic traces for the decay of MCH/MC in aqueous potassium phosphate buffers (298 K, 20 mM) b) values of hydrolysis rate constant (bullets) vs pH and the respective best-fit curve to Eq. 3.10. The dissecting line represents the change of rate-determining step from (II) to (I).

3.5 The metastability

The relative long lifetime of proton-photodissociation is the key feature distinguishing MCHs from other types of photoacids. As for compound **1**, Liao and co-workers^[33] have shown that the relaxation of SP towards MCH obeys first-order kinetics,

displaying a half-life of 76 s in water. Later on, however, the same group showed that the behavior of **1** strongly depends upon solvent effects: the relaxation kinetics was found to be particularly fast in water as compared to that in ethanol, which in turn was found to be faster than that in dimethylsulfoxide (DMSO).^[66] This observation set the foundation for the now commonly accepted hypothesis of having protonation involved in the rate determining step, by which second-order rate constants were calculated. The observed marked decrease in rate constant (from 73 to 0.034 M⁻¹ s⁻¹) was ascribed to the hydrogen bond donor acidity of the solvent, which in fact gradually decrease from water to DMSO.^[66] Recent studies^[85] in methanol appears to be consistent with this interpretation. Despite the properties of the solvent certainly play a role in determining kinetics in general,^[84] solvent effects alone do not necessarily indicate a rate determining step of bimolecular nature. Therefore, in order to investigate whether the proton takes part in the rate determining step, we decided to examine the relaxation kinetics of **1** over the entire pH window ranging from 0 to 10 (Figure 3.7).

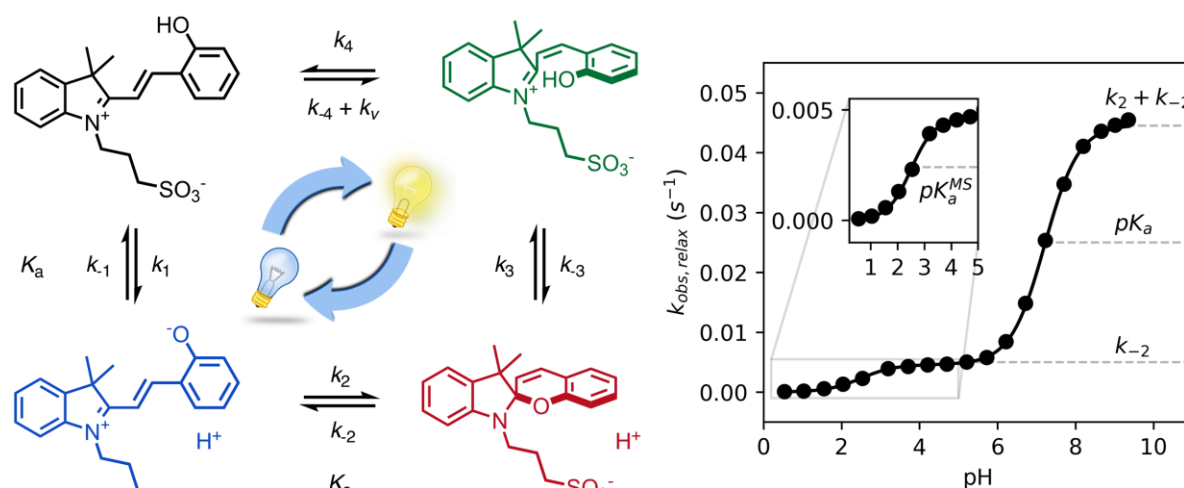


Figure 3.7. Full kinetic model for the description of the aqueous (photo)chemistry of merocyanine photoacids (left). On the right experimental values of $k_{obs,relax}$ (bullets) with the corresponding best-fit to Eq. 3.11 (solid line). The inset highlights the inflection point appearing at pH close to pK_a^{MS} .

In addition, considering all evidences emerging in the above sections, we propose the four-component cycle depicted in Figure 3.7 as kinetic model, where $k_1/k_{-1} = K_a$, $k_2/k_{-2} = K_c$, $k_{-3}/k_3 = K_a^{MS}$, while k_{-4} and k_4 are the kinetic constants associated to the *trans*-to-*cis* isomerization of MCH and to the corresponding reverse reaction, respectively, in the dark – *i.e.*, with $k_v = 0$. Kinetic analyses were carried out at 25 °C, monitoring the recovery of the absorption band of the corresponding MC(H) form. Apparent pseudo first-order rate constants of relaxation ($k_{obs,relax}$) were obtained using Eq. 3.11, the corresponding profile as a function the pH are reported in Figure 3.7. We found that the $k_{obs,relax}$ of **1** progressively increase with pH following a double-sigmoidal behavior, displaying two inflection points close to the corresponding pK_a^{MS} and pK_a . Despite excluding a concerted bimolecular reaction between SP and H^+ yielding MCH,^[3,90,90] the kinetic model is fully consistent, with numerical fitting curves approaching nicely the experimental profile with good confidence. A general way to estimate relaxation rates is to study the non-zero eigenvalues of the rate matrix. In this case, it can be shown that the apparent rate constant of relaxation corresponds to the opposite of the largest non-zero eigenvalue (see Experimental Section for more details). At extremely acidic pH values ($pH < pK_a^{MS}$), the observed rate constants are all very low, suggesting that the *cis*-MCH form is thermally stable. This is in line with previous reports on the acidochromism of SPs, though the observed low rates were ascribed to existence of an SP form protonated at the indole nitrogen atom^[26,78,87] acting as “unreactive sink”^[84] – *i.e.*, SPH. Recent computational studies by Browne^[91] and co-workers have shown that, even considering the existence of SPH, proton transfer coupled with C–O cleavage is barrierless and results in the formation of *cis*-MCH. Thus, given the apparent thermal stability of *cis*-MCH, one may assume SP the

only species undergoing relaxation, so as to use the pre-equilibrium approximation^[92] for deriving the rate expression of relaxation as follows:

$$k_{obs,relax} = k_{-2} \left(\frac{K_a^{MS}}{[H^+] + K_a^{MS}} \right) \left(\frac{K_a(1 + K_c) + [H^+]}{[H^+] + K_a} \right) \quad \text{Eq. 3.11}$$

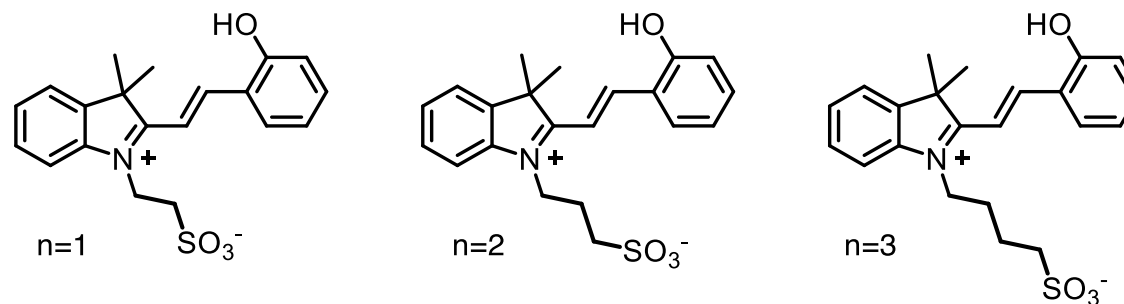
Fitting was initialized with the corresponding thermodynamic and kinetic constants obtained above, using the errors associated to each equilibrium constant as constraints and leaving k_{-2} free to vary. The value obtained for k_{-2} is in accordance with that found independently at 25 °C from equilibration studies (Table S 3.2). The model function suits with very good confidence ($R^2 > 0.99$) the experimental profiles (Figure 3.7 solid line) and strongly suggests a situation where thermal ring opening of SP (k_{-2}) remains rate-determining throughout the entire pH window,^[87] with *cis*-to-*trans* isomerization of *cis*-MCH (slow) competing significantly only at low pH values. This emerges in a clear manner by looking at the profiles of $k_{obs,relax}$ scaled for the effective concentration of species undergoing isomerization, which increase for becoming independent of pH after pK_a^{MS} , with a plateau corresponding to k_{-2} . This interpretation explains why the relaxation of **1**, in a pH window well above pK_a^{MS} , could be fitted well to a first order rate equation^[33] also in the absence of buffers holding $[H^+]$ constant.

3.6 Comparative evaluation

Previously, structural modifications of either the chromene^[74,93–95] and/or the indolium^[47,85,93,94] moieties of **1** have been introduced for tuning its photochemistry in both aqueous and organic environments. Little attention, however, has been devoted towards modifying the propyl-1-sulfonate group connected to the iminium nitrogen

atom, which is considered to be important for preserving the thermodynamics of MCHs – *i.e.*, stabilizing the open forms MCH and MC.^[33] Here, we decided to explore the role of the sulfonate group with a series of MCHs bearing an increasingly long alkyl-1-sulfonate bridge (see Experimental Section). Thus, two compounds featuring respectively an ethyl- (**2**, $n = 1$) and a butyl-1-sulfonate group^[22,96] (**3**, $n = 3$) were synthesized similarly to Liao's photoacid (**1**, $n = 2$), and fully characterized by HR-MS, ^1H and ^{13}C NMR spectroscopy, as well as X-ray analysis (see Experimental Section for more details). The methods presented above are general and both compounds **2** and **3** were analyzed in the same way, all results are summarized in Table 1 to aid comparative evaluation as function of n . First, comparison of **1–3** revealed that $\text{p}K_{\text{a}}$ remains constant within the experimental error, whereas $\text{p}K_{\text{c}}$ linearly increase with increasing n . This effect correlates with the distance of the sulfonate group from the positive charge localized on the indolium nitrogen: passing two to four carbon atoms, the EWG effect of the sulfonate group attenuates, making the iminium site less and less polarized and prone to react intramolecularly. This was further confirmed by comparative van't Hoff analysis, which showed that the $\Delta_{\text{r}}G$ of MC-to-SP isomerization linearly decrease as function of n . With regards to the activation parameters for the MC-to-SP reaction, we found that the ΔH^{\ddagger} slightly increase with increasing n (Table S 3.2). We tentatively ascribed this to higher degrees of freedom of the butyl bridge in compound **3**, which in turn might take part in increasing the through-space electrostatic repulsions^[84] between the sulfonate group and the phenolate group, and so the barrier for conversion of *trans*-MC to *cis*-MC. On the other hand, the values found for ΔS^{\ddagger} are all consistent with those reported so far^[27] for SPs in polar protic solvents, indicating comparable solvent–solute dipolar orientational correlations.^[24] The solubility (S) of each compound refers to aqueous potassium chloride solutions (see below). S values

were determined by both UV-Vis and NMR analysis at 25 °C (see Experimental Section) and are reported in Table 3.1 as the average of multiple experiments. We found that S dramatically increase in the order: $1 < 2 < 3$. The superior water solubility of compound **3** allowed us to carry out successfully photo-NMR^[97] investigations by in situ illumination, which, for $\text{pH} < \text{p}K_{\text{a}}^{\text{MS}}$, corroborated the nearly quantitative conversion of MCH into an achiral species displaying a *cis*-non-coplanar conformation (*cis*-MCH) (see Experimental Section for a more detailed discussion). Interestingly, UV-Vis studies revealed that all $\text{p}K_{\text{a}}^{\text{MS}}$ values fall within the range 1.7–3.2 as proposed by Liao^[26] and, as observed for $\text{p}K_{\text{c}}$, progressively increase as a function of n . These results further confirm the interplay between the EWG effect of the sulfonate group and the length of the alkyl bridge in determining the thermodynamics. Hence, subsequent comparison of **1–3** through Eq. 3.9 showed that ΔH remains fairly constant within the experimental error (3.6 ± 0.2), but gradually shift towards more neutral regions with increasing n (ca. +1 pH unit). Comparative kinetics analysis of **1–3** was carried out at 25 °C. In the case of hydrolysis, we decided to investigate the pH range from pH 3 to 8. Importantly, all fitting were satisfactory, confirming the mechanism of hydrolysis evoked above is valid for all compounds. Notably, we found that k_{w} , k_{OH} and k_{h} linearly decrease with increasing n , highlighting the role of the proximity of the sulfonate group in dictating the reactivity: the hydrolytic stability of MCHs in water gradually increases with n . With regards to thermal relaxation, experiments were repeated for **2** and **3** covering the full pH window as in the case of **1**. Also in this case, we found all fitting were satisfactory: thermal ring-opening of SP is always rate-determining regardless of pH, with k_{-2} linearly increasing as a function of n . Taken together, these results show that the four-component cycle depicted in Figure 3.7 has general applicability.



<i>n</i>	pK_a	pK_c	pK_a^{GS}	pK_a^{MS}	Π	S	k_w	k_{OH}	k_h	k_{-2}^a	Φ
<i>Units</i>						mM	10^{-3} min^{-1}	$10^3 \text{ M}^{-1} \text{ min}^{-1}$	10^{-2} min^{-1}	10^{-2} s^{-1}	
1	7.23 ± 0.06	-1.48 ± 0.02	5.74 ± 0.08	2.14 ± 0.04	3.6 ± 0.1	0.56 ± 0.05	4.2 ± 0.1	13 ± 2	5.0 ± 0.5	0.31	0.73 ± 0.09
2	7.20 ± 0.03	-0.96 ± 0.03	6.19 ± 0.06	2.47 ± 0.04	3.7 ± 0.1	0.19 ± 0.03	2.8 ± 0.4	9.5 ± 0.4	2.0 ± 0.2	0.45	0.37 ± 0.04
3	7.25 ± 0.05	-0.59 ± 0.02	6.56 ± 0.07	3.07 ± 0.04	3.5 ± 0.1	2.66 ± 0.28	1.7 ± 0.3	4.5 ± 0.4	0.26 ± 0.03	0.59	0.22 ± 0.03

Table 3.1. Thermodynamic and kinetic parameters for compounds **1-3**. ^a Check experimental section for more details.

3.7 Reversible proton release in water

We finally focused on studying the proton release/uptake of **1–3** in water by means of direct pH measurements. Saturated solutions of **1–3** were prepared by sonication (10 min), adding an excess amount of crystalline material into aqueous potassium chloride (30 mL, 20 mM). We chose this for reproducing the same ionic strength in the experiments above and for optimal response of the glass electrode. In a typical experiment, the solution was microfiltered and transferred in our in-house designed photochemical vessel and the pH measurements started after 5 minutes of equilibration at 25 °C and under gentle nitrogen bubbling through a cannula which was temporarily introduced in the system.

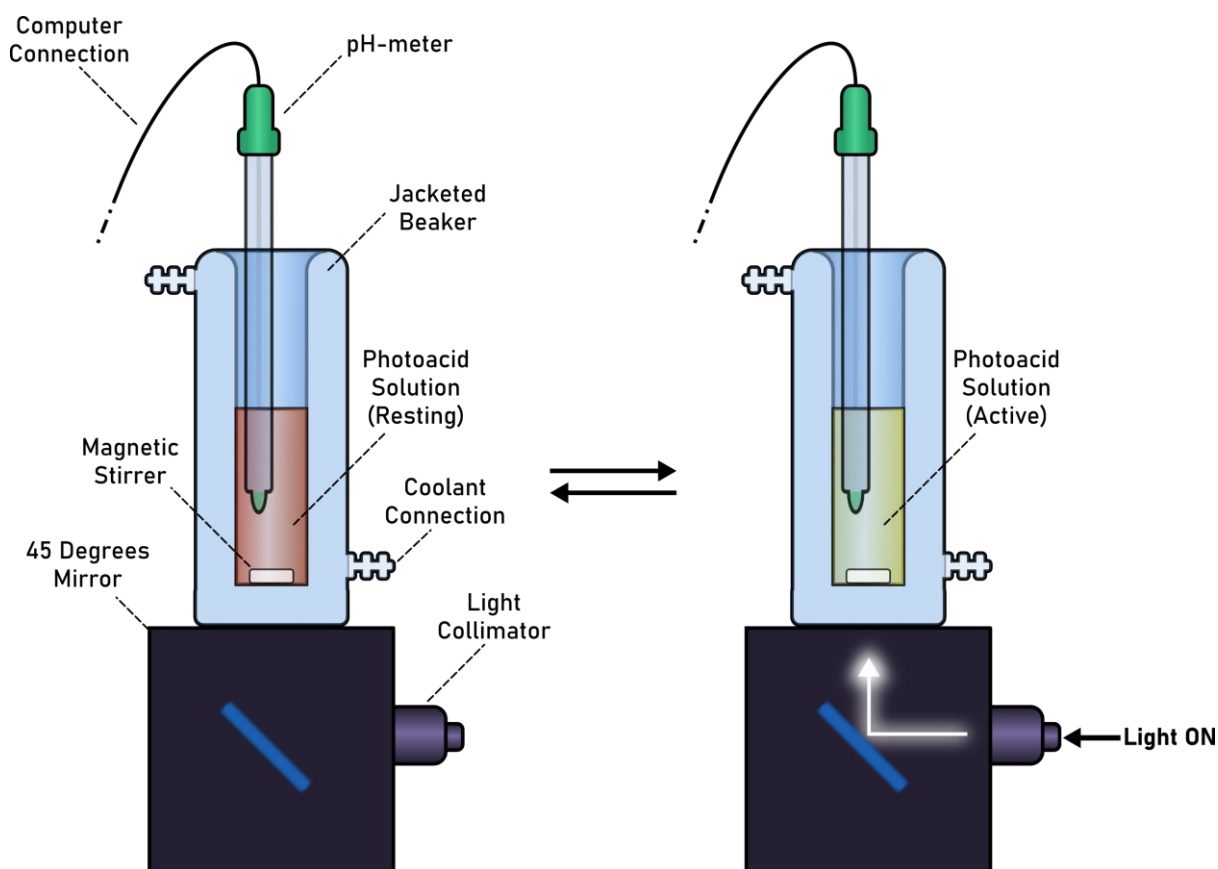


Figure 3.8. Experimental setup for the monitoring of the photochemical pH jumps.

We found that pH readings in the dark were all consistent with the pH value predicted by the weak acid approximation and the corresponding pK_a^{GS} . Subsequently, light irradiation induced pH drops down to a stationary value close to $-\log S$, indicating nearly quantitative proton photo-dissociation;^[33] in the case of **3** (Figure 3.9 c) the final pH settled to a value very close to its pK_a^{MS} – *i.e.*, the maximum possible level of proton release for **3**. Inspection of the obtained pH profiles revealed that the pH recovery after light irradiation follows first-order kinetics, with $k_{obs,relax}$ consistent with the corresponding k_{-2} (see Experimental Section). As for **3**, the explored pH window is such that $k_{obs,relax} \approx k_{-2}/2$ (see Eq. 3.11), in line with the fact the final pH obtained under irradiation (ca. 3.1) equals its pK_a^{MS} (3.07 ± 0.04). These observations show that proton release is fully reversible and, again, that the mechanism proposed above for **1** is general. Thus, we decided to investigate whether the four-component kinetic cycle depicted in Figure 3.7 is also compatible with the observed full dynamics of proton release/uptake. Simultaneous data fit were performed considering the three distinct data sets of three independent experiments, namely: (i) pH jump, (ii) $k_{obs,hydrolysis}$ vs. pH and (iii) $k_{obs,relax}$ vs. pH. Combined data fit were initialized with the thermodynamic and kinetic parameters listed in Table 3.1, and the resulting outcome subjected to Monte Carlo cross validation (see Experimental Section). We were very pleased to see that computed dynamics are fully consistent with the experimental profiles (Figure 3.9 a-c). In addition, this numerical procedure allowed us to estimate k_v , which represents the rate constant of MCH's photo-isomerization and can be used to directly estimate the quantum yield (Φ) as follows:

$$\Phi = \frac{N}{N_{\lambda}} k_v \quad \text{Eq. 3.12}$$

where N is the number of molecules undergoing isomerization, and N_{λ} is the photon flux – *i.e.*, the number of photons per unit time (see Experimental Section for more details). Interestingly, we found that Φ gradually decrease with increasing n . We ascribed this to the electrophilicity of the spiro carbon, which decreases as a function of n (see above). Independent variable-power pH jumps revealed linear relationships between k_v and N_{λ} , meaning that Φ does not depend on the power of the LED light source within the range 50–350 mW – quantum yields of **1–3** are thus reported in Table 3.1 as the trimmed mean resulting from multiple pH jump profiles and relative fitting. It is worth noting that the quantum yield we obtained in this way for **1** (0.37 ± 0.04) is in good agreement with that (0.38 ± 0.03) previously reported^[80] for the same compound in water.

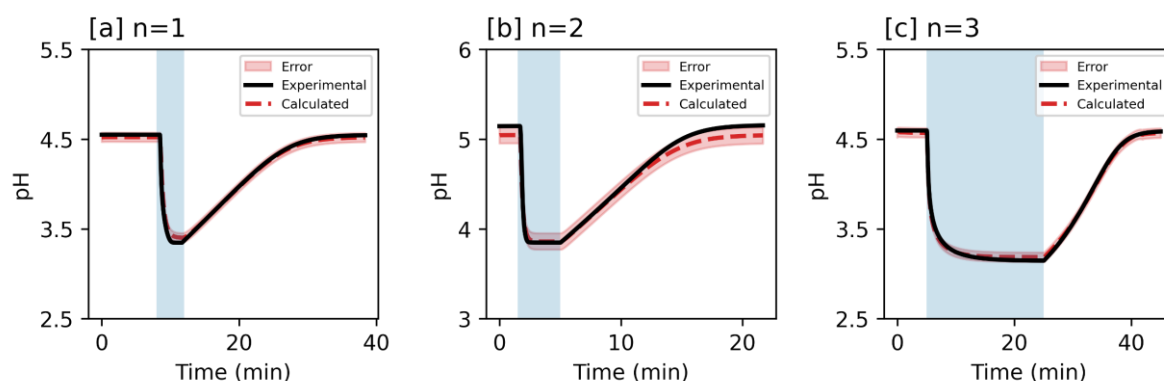


Figure 3.9. pH jump experiments with 425 nm light irradiation for compounds a) **2** ($n=1$), b) **1** ($n=2$), c) **3** ($n=3$). The blue area represents the effective irradiation time.

In general, the amplitude of the pH jump – and so the potential application of a given MCH – is regulated not only by the complete set of thermodynamic and kinetic constants we have unraveled here but also simply by S . At this point, given the

superior hydrolytic stability and water solubility of the new compound **3**, along with its relatively high pK_a^{GS} , we decided to explore the possibility of amplifying its pH jump by partially neutralizing the solution with a base. Even if this would sacrifice part of the protons available initially, the system will still exhibit pH drops because of the remaining MCH in solution. On these regards, we repeated the same experiment above, but with in situ addition of sodium bicarbonate (0.25 equivalents), the corresponding pH profile is reported in Figure 3.10. We were very pleased to see that (i) the pH jump passed from ca. 1.5 to 2.5 pH units, (ii) it can be repeated for at least 6 hours without significant loss and, most importantly, (iii) the full dynamics can be simulated nicely adopting the thermodynamic and kinetic parameters obtained above. This result shows that the cyclic model implemented here is robust and can be used to fully predict the behavior of MCHs in water.

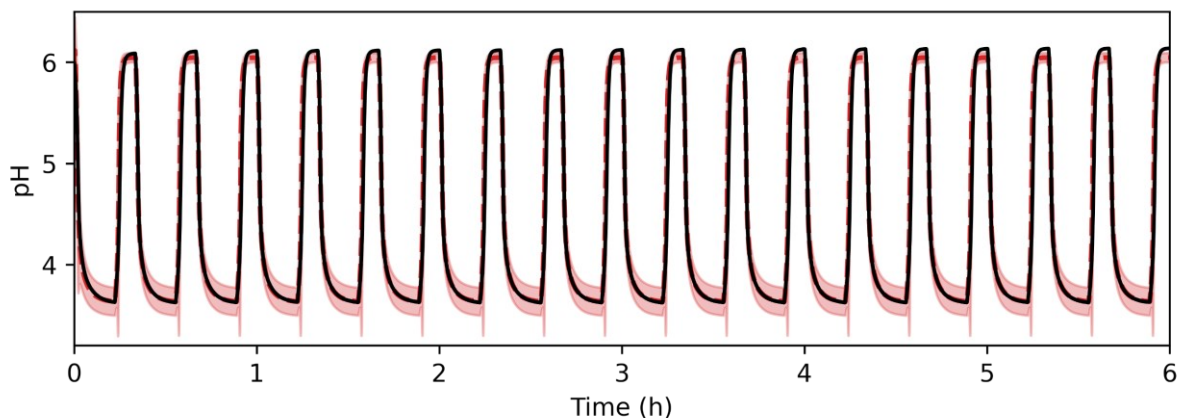


Figure 3.10. pH jump experiments with 425 nm light irradiation for compound **3** after partial neutralization with sodium bicarbonate.

3.8 Conclusions

In conclusion, we have rationalized the behavior of MCHs in water through a series of ^1H NMR and UV-Vis studies and relative modelling. We have provided straightforward methodologies for assessing the acidity constant of both the ground state and the metastable state. In particular, we were able to quantify experimentally the equilibrium of MCHs under dark conditions, and so the effects of the $\text{MC} \rightleftharpoons \text{SP}$ isomerization on proton dissociation – *i.e.*, $K_a^{\text{GS}} = K_a(1 + K_c)$. In addition, we have shown that the protonated metastable state is an achiral species with a *cis*-non-coplanar conformation (*cis*-MCH). We have analyzed the mechanism of both hydrolysis and relaxation kinetics as a function of the pH and found that (i) MCHs hydrolyze similarly to Schiff bases and (ii) re-protonation is not involved in the rate determining step of relaxation. Direct pH measurements are fully consistent with the obtained thermodynamic constants, and the four-component cycle proposed here as model suits very well the observed reversible proton release/uptake dynamics of MCHs in water.

3.9 Experimental section

3.9.1 General remarks

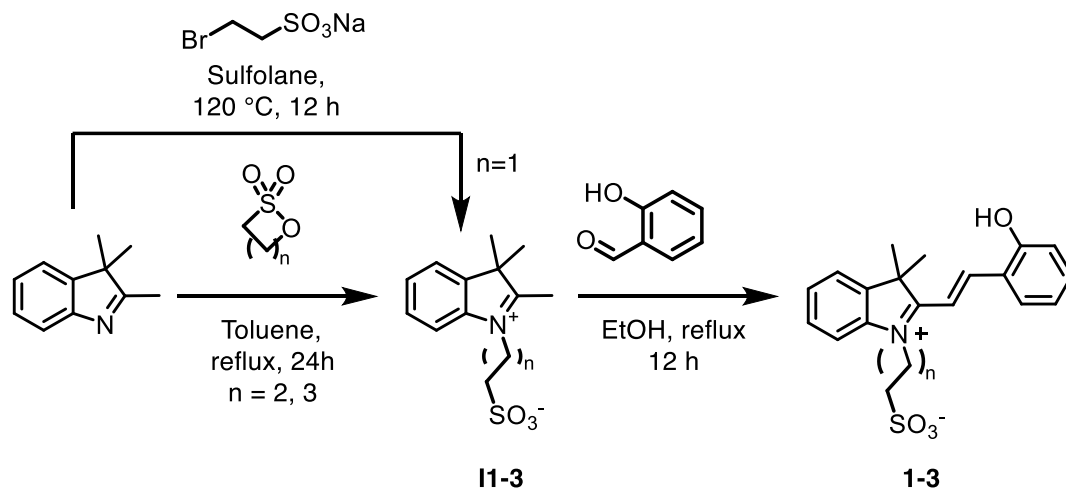
2,3,3-Trimethylindolenine (98%), sodium 2-bromoethanesulfonate (98%) and standard NaOH 0.1 N were purchased from Acros Organics. 1,3-Propane sultone (99%) and 1,4-butane sultone (99%) were purchased from Fluorochem and Sigma Aldrich, respectively. Salicylaldehyde (99%) was purchased from Abcr. H_3PO_4 85% and standard HCl 1 N from Merck, while KOH was purchased from Reactolab. All reagents and solvents were used without further purification, whereas H_2O used in all

preparations was filtered with a MilliQ-Integral5 purification system, degassed by N₂ bubbling (1h under vigorous stirring) and stored at 4 °C. NMR spectra were recorded on a Bruker Avance III spectrometer (¹H: 400 MHz; ¹³C: 101 MHz) equipped with a 5 mm BBFOz ATMA probe (characterization), and on a Bruker Avance III HD spectrometer (¹H: 600 MHz) equipped with a 5 mm CPPBBOz ATMA probe (pH titrations). Chemical shifts (δ) are reported in parts per million (ppm), while coupling constants (J) are given in Hertz (Hz). Solvent residual signals are used as internal reference for spectra alignment (DMSO-*d*₆: δ = 2.50 ppm, D₂O: δ = 4.87 ppm). Electrospray-ionization HRMS analyses were run (positive mode/direct injection) on a Waters XEVO G2-S GTOF spectrometer interfaced with Acquity UPLC pumps and sample manager system. UV-Vis spectra and kinetics were acquired on an Agilent Cary 60 spectrometer equipped with an 18-cell holder coupled to a Huber thermostat, using Suprasil quartz cuvettes (114-QS) from Hellma Analytics. pH measurements were performed using Metrohm pH module 867 or Titrando 888 coupled with Unitrode Pt1000 or Biotrode glass electrodes; pH data were processed using the software Metrohm Tiamo Light. Samples photoirradiation was carried out using a Prizmatix FC-LED-425Z high-power LED light source (λ = 425 nm). Unless stated otherwise, the light beam was delivered by polymer optical fibers (core 1500 μ M) i) positioned orthogonally to and just below the liquid/air interface of sample solutions (UV-Vis) or ii) connected to an FCM1-06 collimator coupled with a 45° mirror cage, resulting in a 25 mm light beam tilted by 90° (pH jumps). Power measurements of the fiber-coupled LED output were made with Thorlabs S142C integrating sphere photodiode power sensor; the uncertainty is within 3-5%. Potassium phosphate buffers from pH 3 to 10 were prepared titrating a solution of H₃PO₄ (100 mM, 1L) with KOH 10 M. Diluted stocks of standard HCl 0.1 N were used below pH 4. All buffer stocks were stored at

room temperature. In order to account for the pH change in sample preparations, the pH of each buffer stock is measured again after dilution (1/5, 20 mM) in mQ water. In the case of ^1H NMR titrations, we account for the presence of D_2O with an uncertainty of ± 0.1 pH units^[98], whereas in the UV-Vis experiments the error on pH values results from multiple readings before and after the experiments ($\leq \pm 0.04$). Unless stated otherwise, curve fitting is performed in Excel, using the Solver add-in for minimizing the sum of the square deviations from the corresponding model curve.

3.9.2 Synthetic procedures

Synthesis of 2,3,3-trimethylindolium – alkyl – 1 – sulfonates **11-3**



Scheme S 3.1. Synthesis of compounds **1-3**.

11 ($n = 2$): was synthesized as described previously^[33,74] and recrystallized^[85] from hot MeCN. Spectra agree with literature values.

^1H NMR (400 MHz, $\text{DMSO}-d_6$) δ 8.11–7.99 (m, 1H), 7.89–7.77 (m, 1H), 7.70–7.54 (m, 2H), 4.66 (t, $J = 8.0$ Hz, 2H), 2.83 (s, 3H), 2.62 (t, 6.4 Hz, 2H), 1.53 (s, 6H).

^{13}C NMR (101 MHz, $\text{DMSO}-d_6$) δ 196.56, 141.95, 141.21, 129.33, 128.96, 123.44, 115.47, 54.14, 47.38, 46.59, 40.15, 39.94, 39.73, 39.52, 39.31, 39.10, 38.89, 23.76, 22.06, 13.81. HRMS (ESI/QTOF) m/z : $[\text{M} + \text{H}]^+$ Calcd for $\text{C}_{14}\text{H}_{20}\text{NO}_3\text{S}^+$ 282.1158; Found 282.1162.

12 ($n = 1$): In a 100-mL round-bottom flask 2,3,3-trimethylindolenine (2.01 g, 12.4 mmol) and sodium 2-bromoethanesulfonate (2.64 g, 12.3 mmol) were dissolved in sulfolane (20 mL). The flask was sealed with a septum and the solution degassed by gentle N_2 bubbling (10 min) prior to heating it up to $120\text{ }^\circ\text{C}$ under stirring for 6 days.

The resulting dark purple mixture was cooled down to room temperature and added dropwise to EtOAc (800 mL) under vigorous stirring. The precipitate was filtered and washed with EtOAc (2 × 400 mL). The residue was treated with MeCN (20 mL) followed by sonication (2 min). The insoluble material (mainly NaBr and unreacted sodium 2-bromoethanesulfonate) was filtered off and the resulting clear red solution added dropwise to EtOAc (800 mL) under vigorous stirring. The precipitate was filtered, washed with EtOAc (2 × 100 mL) and dried under vacuum. This MeCN/EtOAc trituration procedure was repeated once again, affording **I2** as a pink solid (0.85 g, 26%).

¹H NMR (400 MHz, DMSO-*d*₆) δ 7.92–7.86 (m, 1H), 7.83–7.78 (m, 1H), 7.64–7.56 (m, 2H), 4.72–4.66 (m, 2H), 3.03–2.96 (m, 2H), 2.90 (s, 3H), 1.50 (s, 6H).

¹³C NMR (101 MHz, DMSO-*d*₆) δ 198.19, 141.77, 140.67, 129.00, 128.76, 123.38, 115.34, 54.04, 46.30, 44.55, 40.15, 39.94, 39.73, 39.52, 39.31, 39.10, 38.89, 21.50, 14.38.

HRMS (ESI/QTOF) *m/z*: [M + H]⁺ Calcd for C₁₃H₁₈NO₃S⁺ 268.1002; Found 268.1007.

I3 (*n* = 3): In a 100-mL round-bottom flask 2,3,3-trimethylindolenine (6.00 g, 36.9 mmol) and 1,4-butane sultone (5.16 g, 37.5 mmol) were dissolved in PhMe (30 mL). The flask was sealed with a septum and the solution degassed by gentle N₂ bubbling (10 min) prior to heating it up to 120 °C under stirring for 48 h. The resulting dark purple mixture was cooled down to room temperature and the precipitate filtered, washed with PhMe (4 × 50 mL), grinded and dried under vacuum to afford **I3** as a purple crystalline powder (4.12 g, 38%).

^1H NMR (400 MHz, DMSO- d_6) δ 8.09–7.97 (m, 1H), 7.89–7.77 (m, 1H), 7.67–7.54 (m, 2H), 4.86 (t, J = 7.8 Hz, 2H), 2.85 (s, 3H), 2.51 (t, 7.2 Hz, 2H), 2.02–1.91 (m, 2H), 1.79–1.68 (m, 2H), 1.53 (s, 6H). ^{13}C NMR (101 MHz, DMSO- d_6) δ 196.50, 141.85, 141.19, 129.36, 128.95, 123.43, 115.63, 54.12, 50.14, 47.29, 40.15, 39.94, 39.73, 39.52, 39.31, 39.10, 38.89, 26.04, 22.15, 22.01, 13.83. HRMS (ESI/QTOF) m/z : $[\text{M} + \text{H}]^+$ Calcd for $\text{C}_{15}\text{H}_{22}\text{NO}_3\text{S}^+$ 296.1315; Found 296.1318.

General procedure for the synthesis of 1-3

In a 50-mL round-bottom flask the corresponding indolium alkyl-1-sulfonate (**11-3**) was dissolved in absolute EtOH (ca. 20 mL/g). Salicylaldehyde (2 equivalents) was added, the flask sealed with a septum and the solution degassed by gentle N_2 bubbling (10 min) prior to heating it up to 90 °C under stirring for 24 h. The resulting orange precipitate was filtered, washed thoroughly with EtOH to remove unreacted materials and recrystallized from hot MeOH. In all cases, crystals grow by slow cooling, down to -20 °C, over a couple of days. Crystals were collected, washed with cold MeOH and dried under vacuum (isolated yield 50-60%). Crystals are then grinded, transferred in amber glass vials and stored in a desiccator at room temperature.

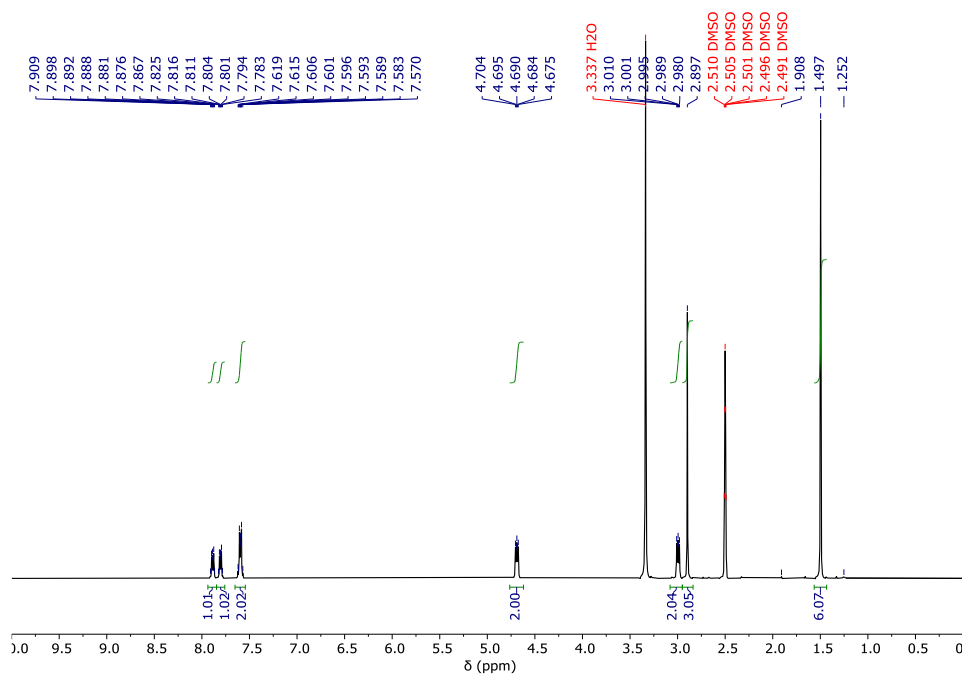
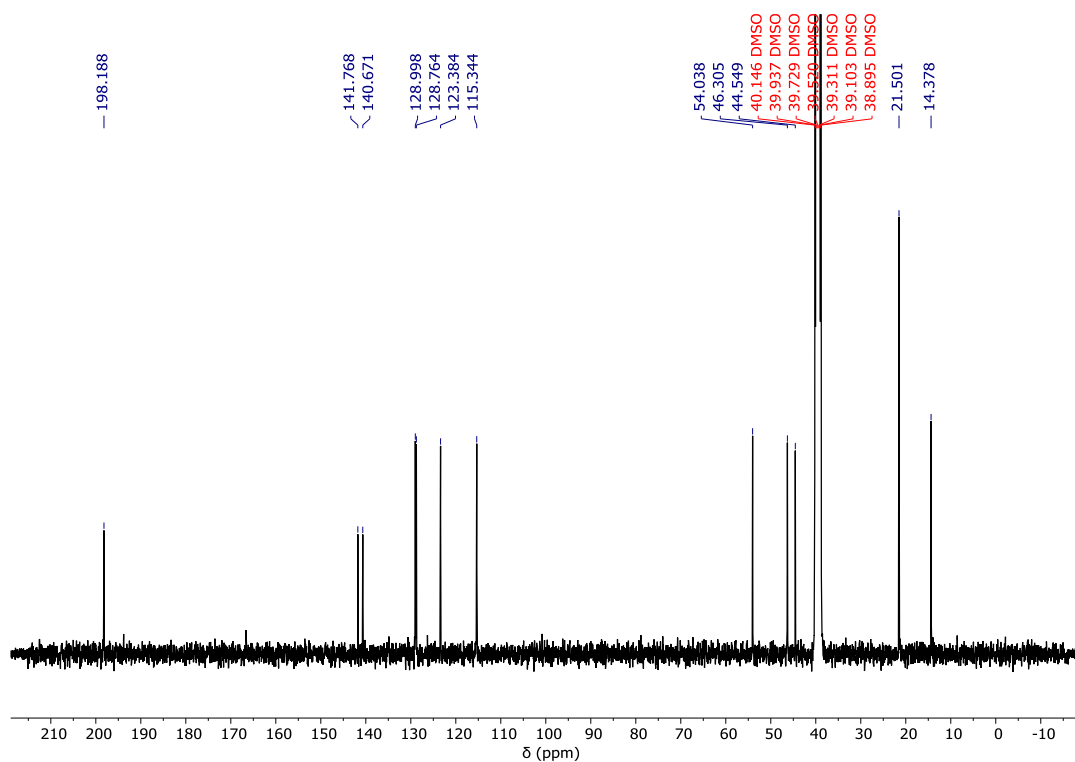
1. ^1H NMR (400 MHz, DMSO- d_6) δ 11.03 (s, 1H), 8.60 (d, J_{trans} = 16.4 Hz, 1H), 8.28 (d, J = 7.6 Hz, 1H), 8.02 (d, J = 7.2 Hz, 1H), 7.94–7.81 (m, 2H), 7.68–7.56 (m, 2H), 7.51–7.43 (m, 1H), 7.04 (d, J = 8.4 Hz, 1H), 6.99 (t, J = 7.6 Hz, 1H), 4.81 (t, J = 7.8 Hz, 2H), 2.65 (t, J = 6.4 Hz, 2H), 2.25–2.11 (m, 2H), 1.77 (s, 6H).

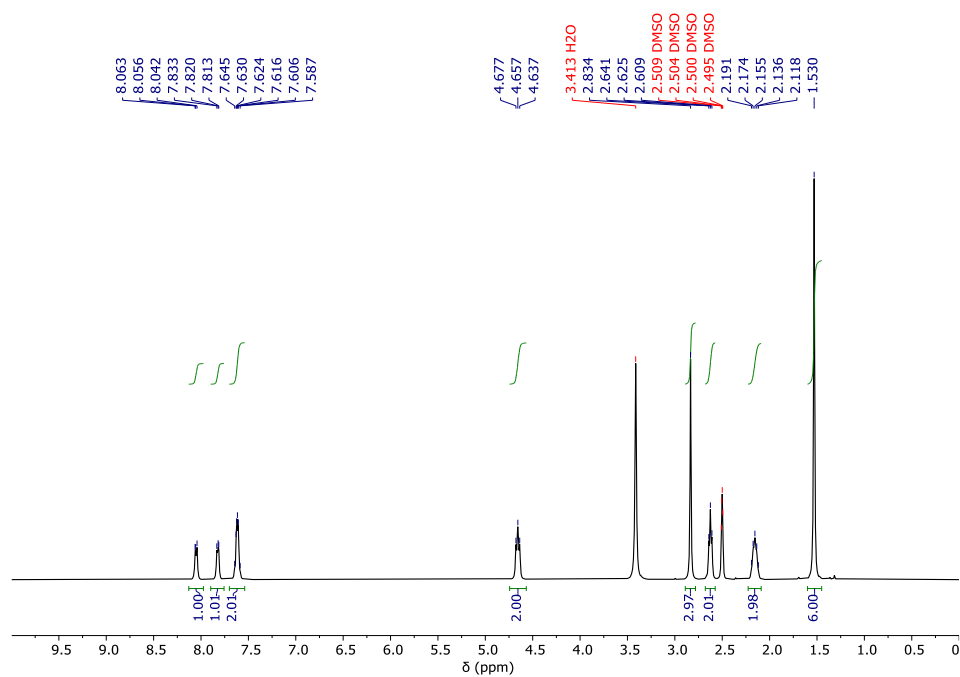
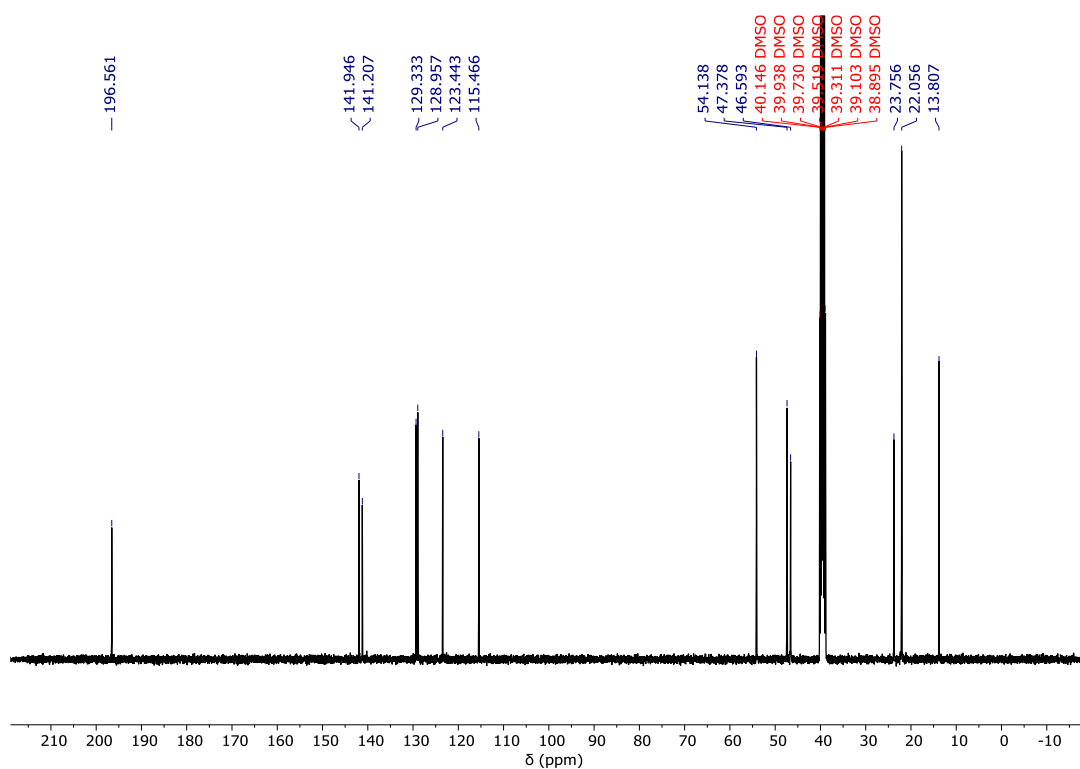
^{13}C NMR (101 MHz, DMSO- d_6) δ 181.75, 159.01, 148.67, 143.48, 140.93, 135.74, 129.77, 129.14, 129.12, 122.98, 121.34, 120.06, 116.61, 115.09, 111.46, 51.90,

47.33, 45.53, 40.15, 39.94, 39.73, 39.52, 39.31, 39.10, 38.89, 26.44, 24.59. HRMS (ESI/QTOF) m/z : $[M + H]^+$ Calcd for $C_{21}H_{24}NO_4S^+$ 386.1421; Found 386.1425.

2. 1H NMR (400 MHz, DMSO- d_6) δ 10.96 (s, 1H), 8.49 (d, $J_{trans} = 16.4$ Hz, 1H), 8.05 (d, $J = 7.6$ Hz, 1H), 7.97 (d, $J_{trans} = 16.4$ Hz, 1H), 7.92–7.86 (m, 1H), 7.86–7.80 (m, 1H), 7.65–7.55 (m, 2H), 7.49–7.41 (m, 1H), 7.03 (d, $J = 8.4$ Hz, 1H), 6.98 (t, $J = 7.6$ Hz, 1H), 4.82 (t, $J = 6.4$ Hz, 2H), 3.07 (t, $J = 6.4$ Hz, 2H), 1.75 (s, 6H). ^{13}C NMR (101 MHz, DMSO- d_6) δ 182.75, 158.71, 147.27, 143.35, 140.72, 135.15, 129.54, 128.95, 128.89, 122.84, 121.61, 119.94, 116.61, 115.20, 113.41, 51.93, 47.56, 43.82, 40.15, 39.94, 39.73, 39.52, 39.31, 39.10, 38.90, 26.12. HRMS (ESI/QTOF) m/z : $[M + Na]^+$ Calcd for $C_{20}H_{21}NNaO_4S^+$ 394.1084; Found 394.1085.

3. 1H NMR (400 MHz, DMSO- d_6) δ 11.13 (s, 1H), 8.56 (d, $J_{trans} = 16.4$ Hz, 1H), 8.20 (d, $J = 8.0$ Hz, 1H), 8.03–7.96 (m, 1H), 7.90–7.84 (m, 1H), 7.82 (d, $J_{trans} = 16.4$ Hz, 1H), 7.67–7.56 (m, 2H), 7.52–7.43 (m, 1H), 7.04 (d, $J = 8.4$ Hz, 1H), 7.00 (t, $J = 7.6$ Hz, 1H), 4.63 (t, $J = 7.8$ Hz, 2H), 2.53 (t, $J = 7.2$ Hz, 2H), 2.04–1.92 (m, 2H), 1.87–1.72 (m + s, 8H). ^{13}C NMR (101 MHz, DMSO- d_6) δ 181.74, 159.15, 149.17, 143.45, 140.86, 135.65, 130.46, 129.16, 122.97, 121.29, 119.98, 116.70, 115.28, 111.66, 51.91, 50.24, 46.50, 40.15, 39.94, 39.73, 39.52, 39.31, 39.10, 38.89, 26.96, 26.38, 22.36. HRMS (ESI/QTOF) m/z : $[M + H]^+$ Calcd for $C_{22}H_{26}NO_4S^+$ 400.1577; Found 400.1580.

3.9.3 ^{13}C and ^1H NMR characterization spectraFigure S 3.1. ^1H -NMR (400 MHz, $\text{DMSO}-d_6$) of compound **12**Figure S 3.2. ^{13}C -NMR (101 MHz, $\text{DMSO}-d_6$) of compound **12**

Figure S 3.3. ¹H-NMR (400 MHz, DMSO-*d*₆) of compound I1Figure S 3.4. ¹³C-NMR (101 MHz, DMSO-*d*₆) of compound I2

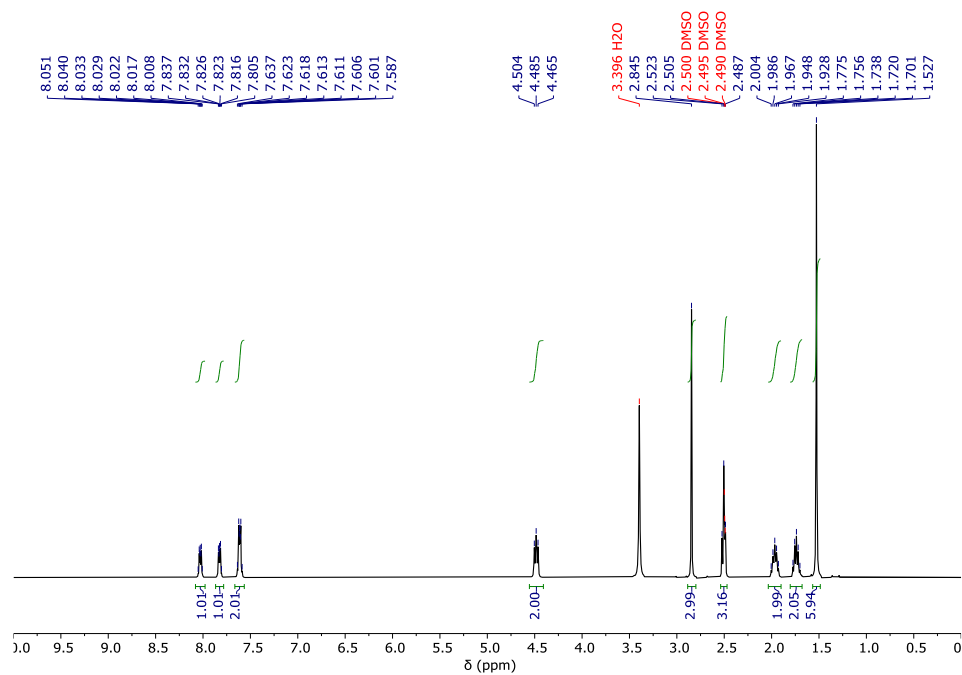


Figure S 3.5. ¹H-NMR (400 MHz, DMSO-*d*₆) of compound **I3**

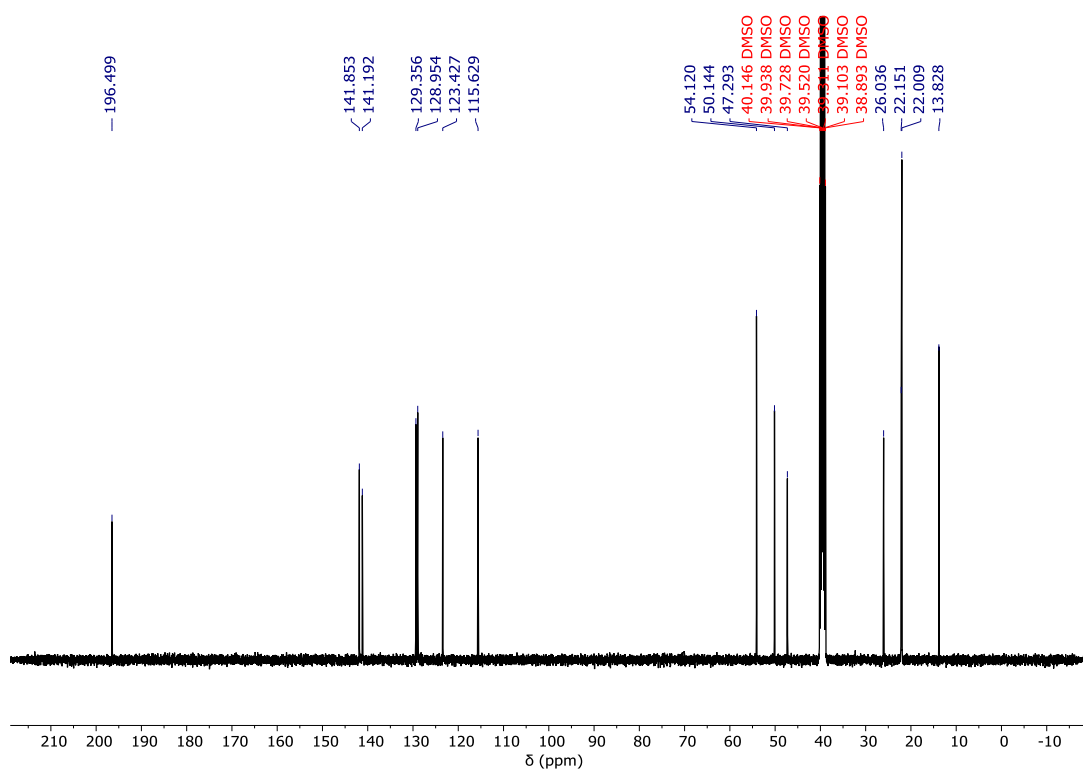
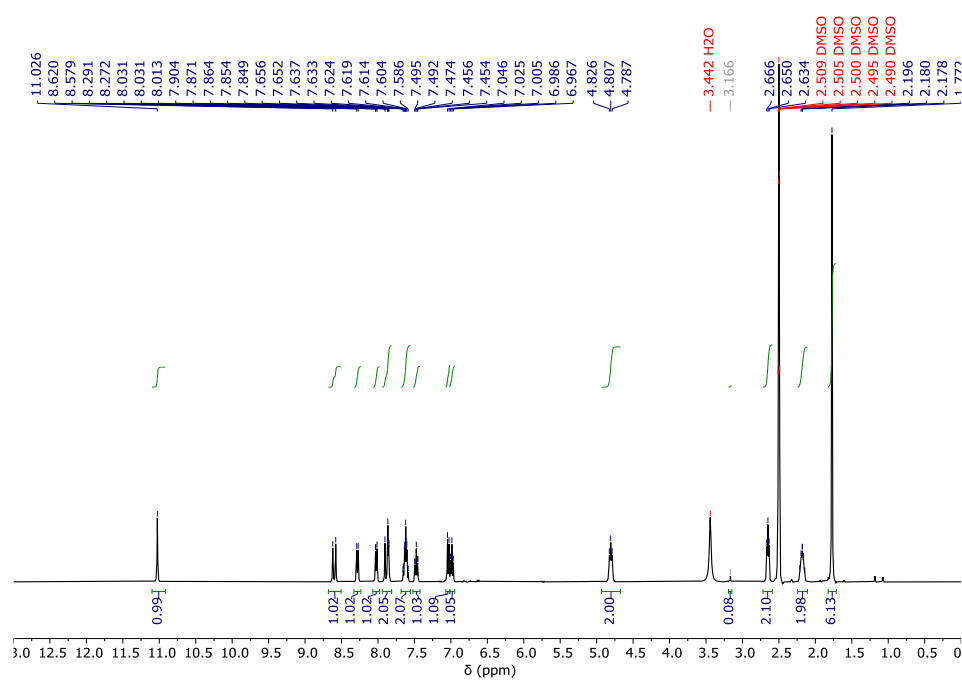
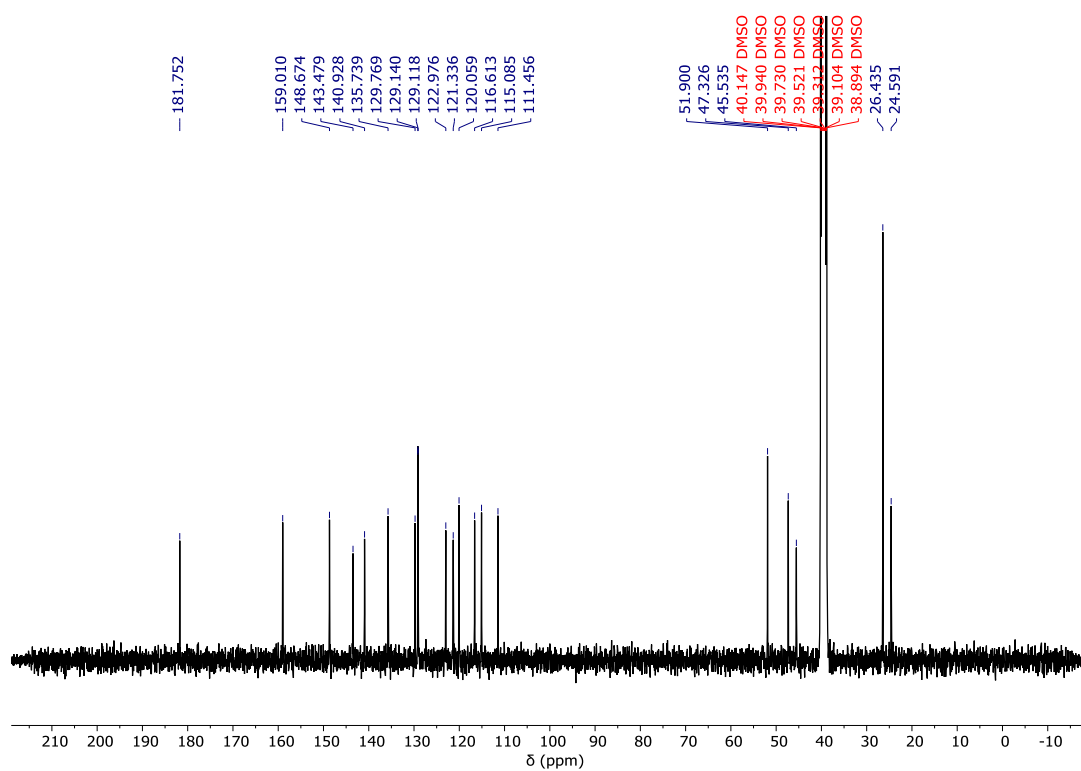
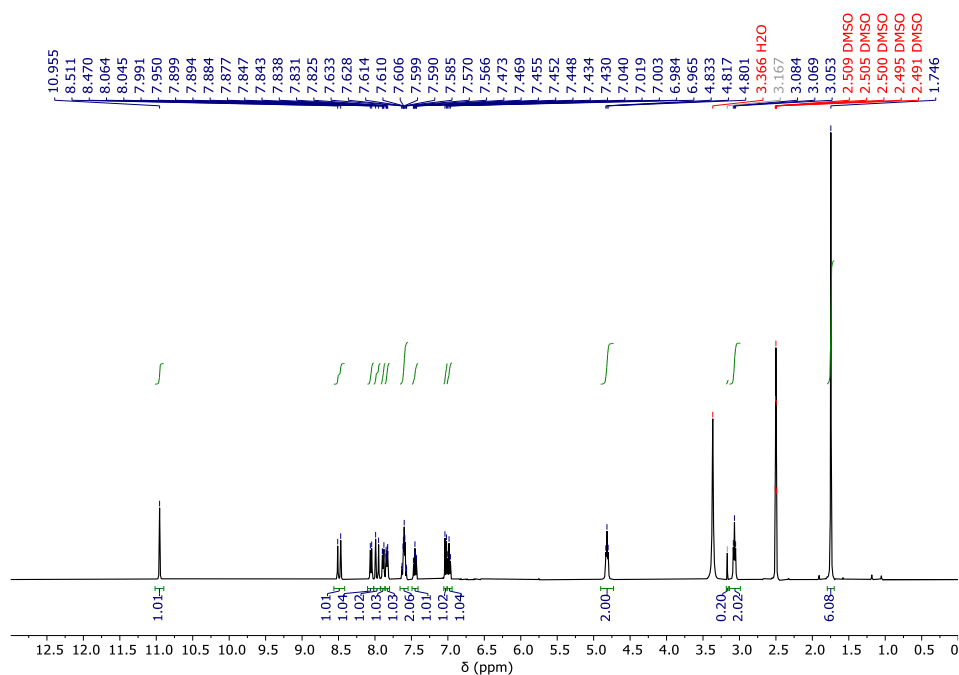
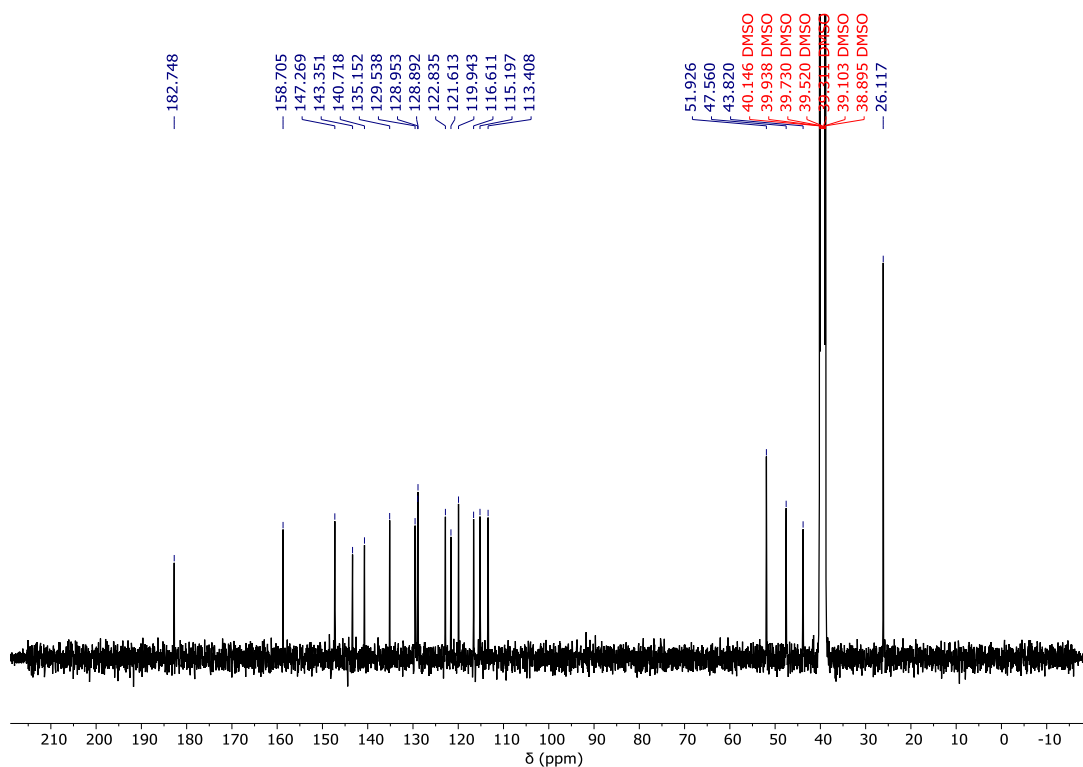
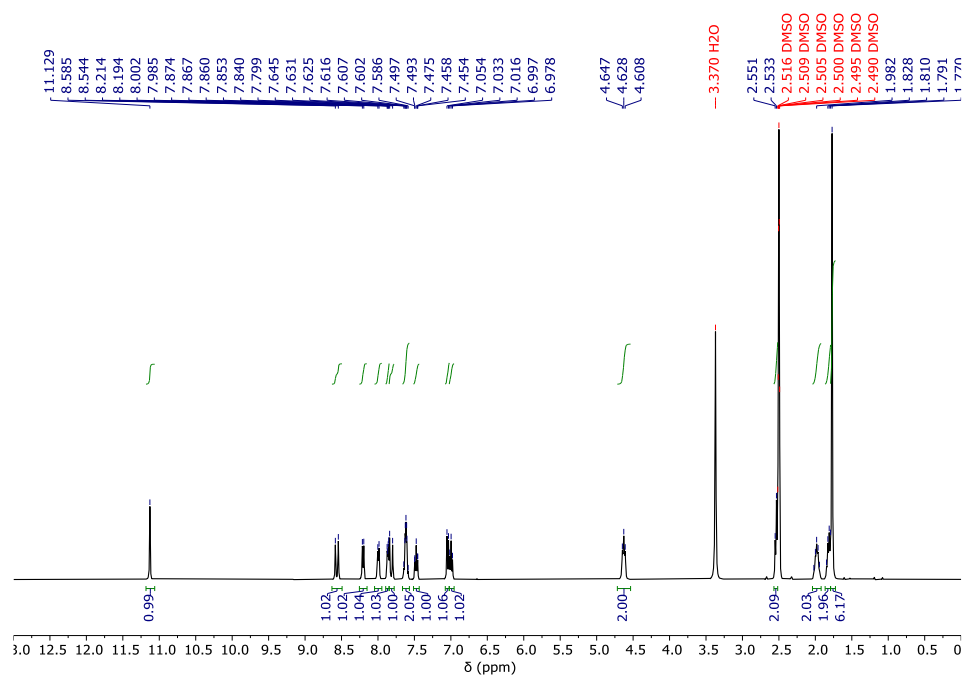
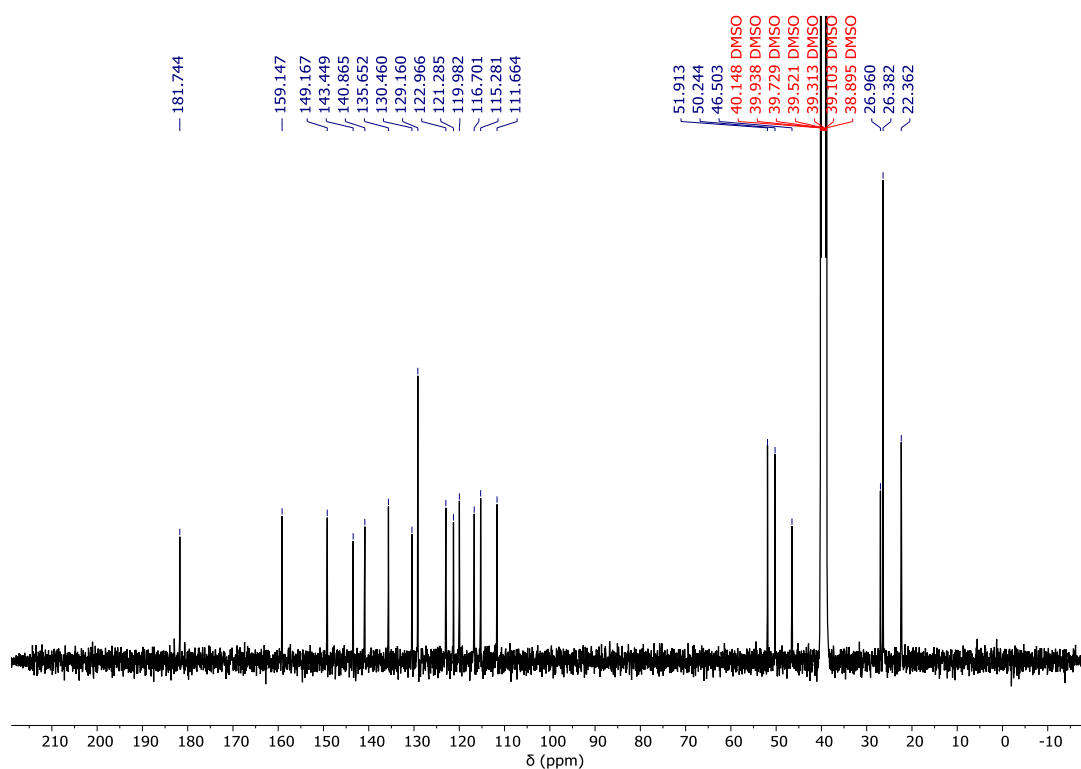


Figure S 3.6. ¹³C-NMR (101 MHz, DMSO-*d*₆) of compound **I3**

Figure S 3.7. ¹H-NMR (400 MHz, DMSO-*d*₆) of compound **1**Figure S 3.8. ¹³C-NMR (101 MHz, DMSO-*d*₆) of compound **1**

Figure S 3.9. ¹H-NMR (400 MHz, DMSO-*d*₆) of compound **2**Figure S 3.10. ¹³C-NMR (101 MHz, DMSO-*d*₆) of compound **2**

Figure S 3.11. ¹H-NMR (400 MHz, DMSO-*d*₆) of compound **3**Figure S 3.12. ¹³C-NMR (101 MHz, DMSO-*d*₆) of compound **3**

3.9.4 Crystallography

Bragg-intensities of **2** and **3** were collected at 140 K using CuK α radiation on a Rigaku SuperNova dual system diffractometer equipped with an Atlas S2 CCD detector. The datasets were reduced and corrected for absorption, with the help of a set of faces enclosing the crystal as snugly as possible, with CrysAlisPro.^[1] Bragg intensities of **1** were collected at room temperature and using MoK α radiation on a Bruker APEX II CCD diffractometer equipped with a κ -geometry goniometer. The data set was reduced by EvalCCD^[2] and then corrected for absorption^[3]. The solution and refinement of the structures were performed by the latest available version of ShelXT^[4] and ShelXL.^[5] The obtained crystallographic and refinement data are summarized below.

References for paragraph 3.9.4

- [1] CrysAlisPro Software System, Rigaku Oxford Diffraction, (2015).
- [2] Duisenberg, A. J. M.; Kroon-Batenburg, L. M. J.; Schreurs, A. M. M. *J. Appl. Crystallogr.* **2003**, 36, 220–229.
- [3] Blessing, R. H. *Acta Crystallogr. A* **1995**, 51, 33–38.
- [4] Sheldrick, G.M., ShelXT-Integrated space-group and crystal-structure determination, *Acta Cryst.*, (2015), **A71**, 3-8.
- [5] Sheldrick, G.M., Crystal structure refinement with ShelXL, *Acta Cryst.*, (2015), **C71**, 3-8.

Table S 3.1. Crystallographic data summary

Compound	1 (n=2)	2 (n=1)	3 (n=3)
CCDC code	1910833	2005264	2005262
Empirical formula	C ₂₁ H ₂₃ NO ₄ S	C ₂₀ H ₂₁ NO ₄ S	C ₂₂ H ₂₅ NO ₄ S
Formula weight	385.46	371.44	399.49
Temperature/K	296(2)	140.00(10)	139.99(10)
Crystal system	monoclinic	monoclinic	orthorhombic
Space group	P2 ₁ /c	P2 ₁ /n	Pna2 ₁
a/Å	11.282(6)	8.33916(6)	17.1075(3)
b/Å	15.881(7)	19.51555(15)	6.98647(10)
c/Å	11.591(6)	11.56961(9)	19.6635(2)
α /°	90	90	90
β /°	111.756(12)	102.2199(8)	90
γ /°	90	90	90
Volume/Å ³	1928.7(17)	1840.21(2)	2350.20(6)
Z	4	4	4
ρ_{calc} /g/cm ³	1.327	1.341	1.129
μ /mm ⁻¹	0.194	1.776	1.422
F(000)	816.0	784.0	848.0
Crystal size/mm ³	0.220 × 0.200 × 0.180	0.602 × 0.153 × 0.098	0.233 × 0.215 × 0.161
Radiation	MoK α (λ = 0.71073)	Cu K α (λ = 1.54184)	Cu K α (λ = 1.54184)
2 θ range for data collection/°	3.888 to 51.198	9.038 to 152.202	10.342 to 145.136
Index ranges	-13 ≤ h ≤ 13, -18 ≤ k ≤ 19, -14 ≤ l ≤ 13	-6 ≤ h ≤ 10, -24 ≤ k ≤ 24, -14 ≤ l ≤ 14	-21 ≤ h ≤ 19, -8 ≤ k ≤ 8, -24 ≤ l ≤ 23
Reflections collected	11443	17018	19755
Independent reflections	3544 [R _{int} = 0.1443, R _{sigma} = 0.1474]	3828 [R _{int} = 0.0126, R _{sigma} = 0.0098]	4466 [R _{int} = 0.0193, R _{sigma} = 0.0140]
Data/restraints/parameters	3544/1/249	3828/0/320	4466/1/261
Goodness-of-fit on F ²	0.958	1.052	1.036
Final R indexes [$ I \geq 2\sigma(I)$]	R ₁ = 0.0748, wR ₂ = 0.1676	R ₁ = 0.0298, wR ₂ = 0.0763	R ₁ = 0.0302, wR ₂ = 0.0827
Final R indexes [all data]	R ₁ = 0.1508, wR ₂ = 0.2100	R ₁ = 0.0303, wR ₂ = 0.0769	R ₁ = 0.0307, wR ₂ = 0.0832
Largest diff. peak/hole / e Å ⁻³	0.28/-0.59	0.38/-0.39	0.19/-0.19
Flack parameter	na	na	0.04(2)

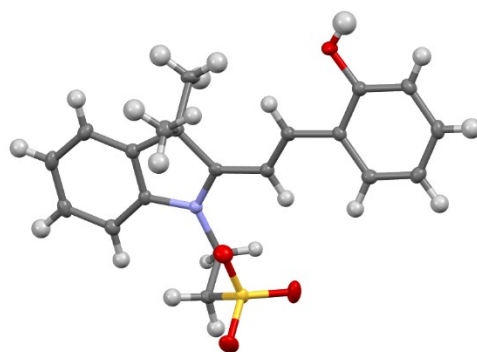


Figure S 3.13. Molecular crystal structure of compound **2**, thermal ellipsoids at 50% probability.

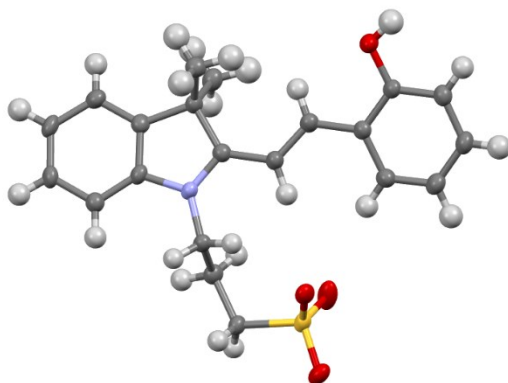


Figure S 3.14. Molecular crystal structure of compound **1**, thermal ellipsoids at 50% probability.

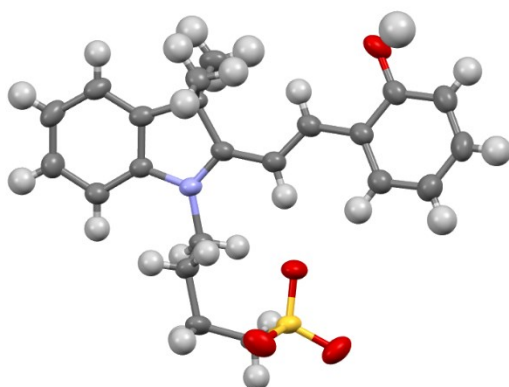


Figure S 3.15. Molecular crystal structure of compound **3**, thermal ellipsoids at 50% probability.

3.9.5 ^1H NMR analyses

pH Titrations

A solution of compound **1-3** (0.8 mL, 0.125 mM) in $\text{H}_2\text{O}/\text{D}_2\text{O}$ 1:1 is added to potassium phosphate buffer stocks (0.2 mL, 0.1 M), and the resulting sample solutions (1.0 mL) stored in amber-glass vials at 4°C prior to NMR analysis. Each sample is transferred (0.6 mL) into an NMR-tube and allowed to warm up to room temperature over a period of 5 minutes. After setting up of all the parameters for acquisition (5 min), the corresponding ^1H NMR spectrum is acquired after further 5 min at 25 °C (total equilibration time ca. 5 + 10 min in the dark and at 25 °C). This timing represents a viable compromise for allowing each sample to equilibrate at 25 °C without hydrolyzing significantly (< 3%).

All spectra are acquired using the Bruker pulse-program *noesygprr1d*. The optimized parameters for *mixing time*, *recycle delay*, *dummy scans* and *number of acquisitions* are 12.5 μs , 3 s, 4 and 128, respectively. Spectra are processed in MestreNova by applying i) an exponential apodization with a line broadening of 1.0 Hz, ii) a linear prediction to 32 *k* points starting from 19 *k*, iii) a manual phase correction and iv) an automated baseline correction (Whittaker Smoother algorithm). Chemical shifts and integrals for elaboration are obtained directly from the stacked spectra with the “*Max. Peak Pos.*” and “*Integral*” graph-functions available in the Data Analysis tab. Curve fitting is performed in Excel, using the Solver add-in for minimizing the sum of the square deviations from the corresponding model curve.

Photo-NMR investigations

In order to quest for the structural features of the metastable states we opted for photo-NMR^[97] investigations by *in situ* illumination. Samples for ¹H NMR analyses are prepared by adding a potassium phosphate buffer solution (pH 7) or deuterated trifluoroacetic acid (TFA-*d*) to a saturated solution of **3** in D₂O, and subsequently analyzed at 25 °C; photoirradiation is performed with a LED-light source (425 nm, 30 mW) coupled with a 6-meter-long optical fiber ending with 5-cm scratched tip wedged into a coaxial insert for NMR tubes (Figure S 3.19 a). The ¹H NMR spectra under continuous light irradiation obtained for compound **3** are reported in Figure S 3.19 b, along with the corresponding spectrum of MCH for comparison (black trace). At neutral pH (red trace), the metastable state is fully dissociated and it is found to exist in the form of SP. This finding is corroborated by the dramatic change observed for the coupling constant of the alkenyl hydrogens (from ³*J*_{trans, a} = 16.3 Hz to ³*J*_{cis, b*} = 10.3 Hz) and, importantly, by all the aliphatic protons featuring diastereotopic splitting patterns (see above), which all in all support the quantitative conversion of MCH into SP under photostationary conditions – the photostationary state (PSS) is found to be MCH:SP = 3:97 as determined by NMR integration. On the other hand, at extremely acidic conditions (TFA-*d* 10% v/v, pH ca. 0) (green trace), the metastable state is fully protonated and we believe it exists as the *cis*-isomer of MCH (*cis*-MCH). The value found for ³*J*_{cis, b''} (13.0 Hz) fall exactly between those observed for the MCH and SP forms, and in fact is in good agreement with that observed earlier by Li^[99] (13.5 Hz) and recently by Browne^[2] (12.8 Hz) for SPs after reaction with strong acids. Notably, is also very similar to the coupling constant found by Andréasson^[100] (12.8-13.2 Hz) for O-substituted merocyanines after light irradiation. Furthermore, contrary to the

dissociated state, we see in this case that the upfield shift of all the resonances is not accompanied by any diastereotopic splitting. An observation which contrasts firmly with the hypothesis of having SP protonated at the indole nitrogen atom (*i.e.*, SPH^[26,87,101]). If that would have been the case, clear diastereotopic splitting patterns should have been observed as in the case of the SP form. Taken together, our experiments strongly suggest the nearly quantitative conversion of MCH into an achiral species displaying a *cis*-non-coplanar conformation (PSS = 8:92). When performing titrations in the pH range 0-5, however, we were not able to develop any quantitative analysis on account of significant peak broadening, which we ascribed to coalescence of the two forms in rapid exchange at intermediate pH values and 25 °C. Thus, pK_a^{MS} are calculated by UV-Vis measurements under continuous light irradiation.

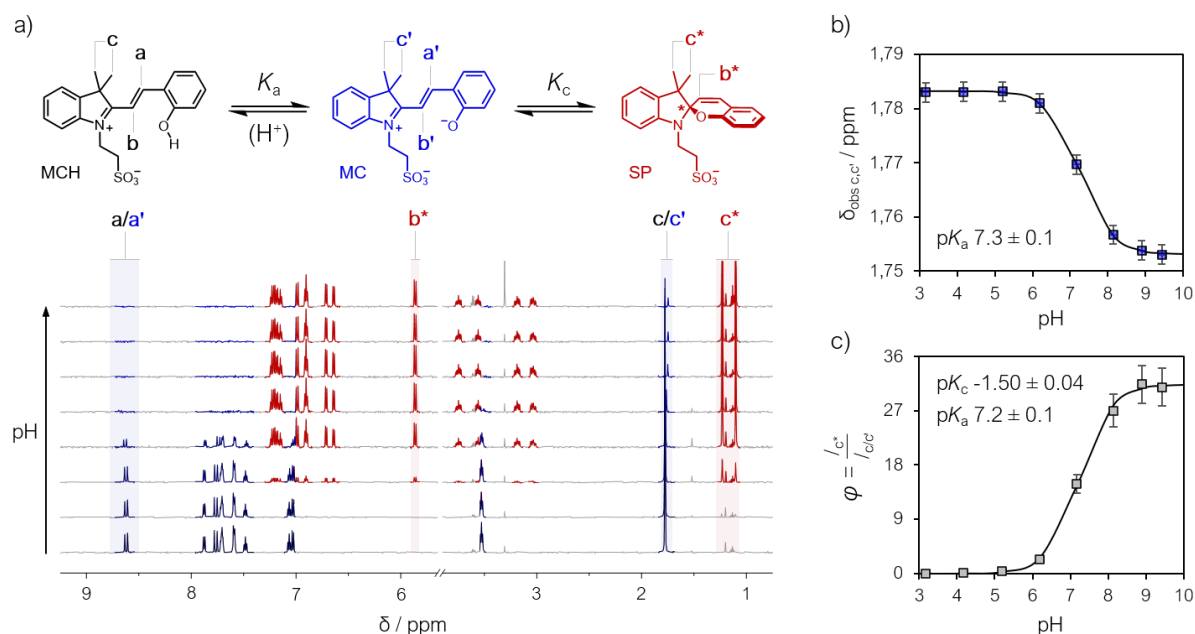


Figure S 3.16. a) ^1H -NMR (600 MHz, $\text{D}_2\text{O}:\text{H}_2\text{O}$ 6:4], 298 K) titration of compound **2** at variable pH, b) chemical shift calculation of the pK_a value, the solid line represents the best-fit model, c) integral ratio between protons c^* and c/c' for the calculation of pK_a and K_c . In the spectra, the water peak has been suppressed and omitted for clarity.

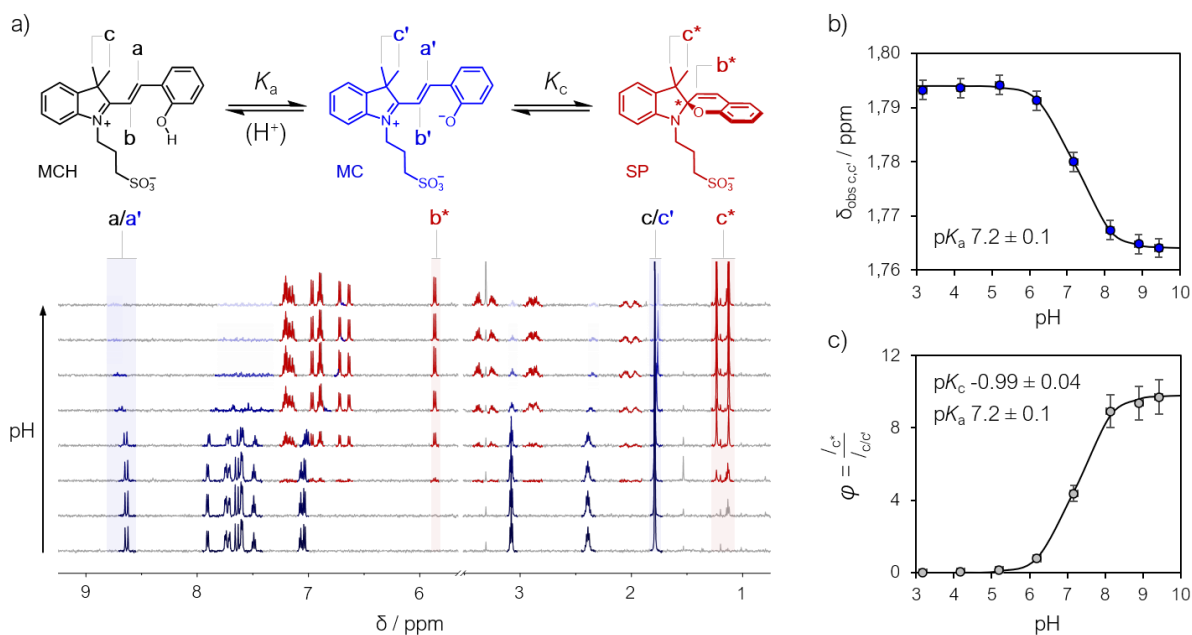


Figure S 3.17. a) ^1H -NMR (600 MHz, $\text{D}_2\text{O}:\text{H}_2\text{O}$ 6:4], 298 K) titration of compound **1** at variable pH, b) chemical shift calculation of the pK_a value, the solid line represents the best-fit model, c) integral ratio between protons c^* and c/c' for the calculation of pK_a and K_c . In the spectra, the water peak has been suppressed and omitted for clarity.

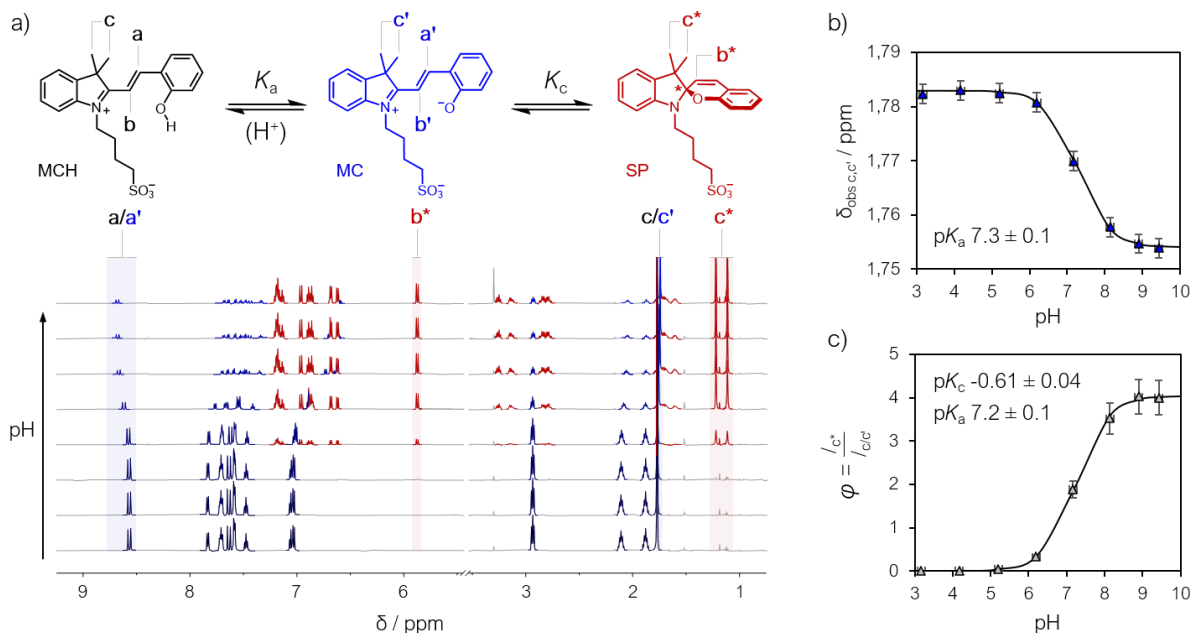


Figure S 3.18. a) ^1H -NMR (600 MHz, $\text{D}_2\text{O}:\text{H}_2\text{O}$ 6:4], 298 K) titration of compound **3** at variable pH, b) chemical shift calculation of the pK_a value, the solid line represents the best-fit model, c) integral ratio between protons c^* and c/c' for the calculation of pK_a and K_c . In the spectra, the water peak has been suppressed and omitted for clarity.

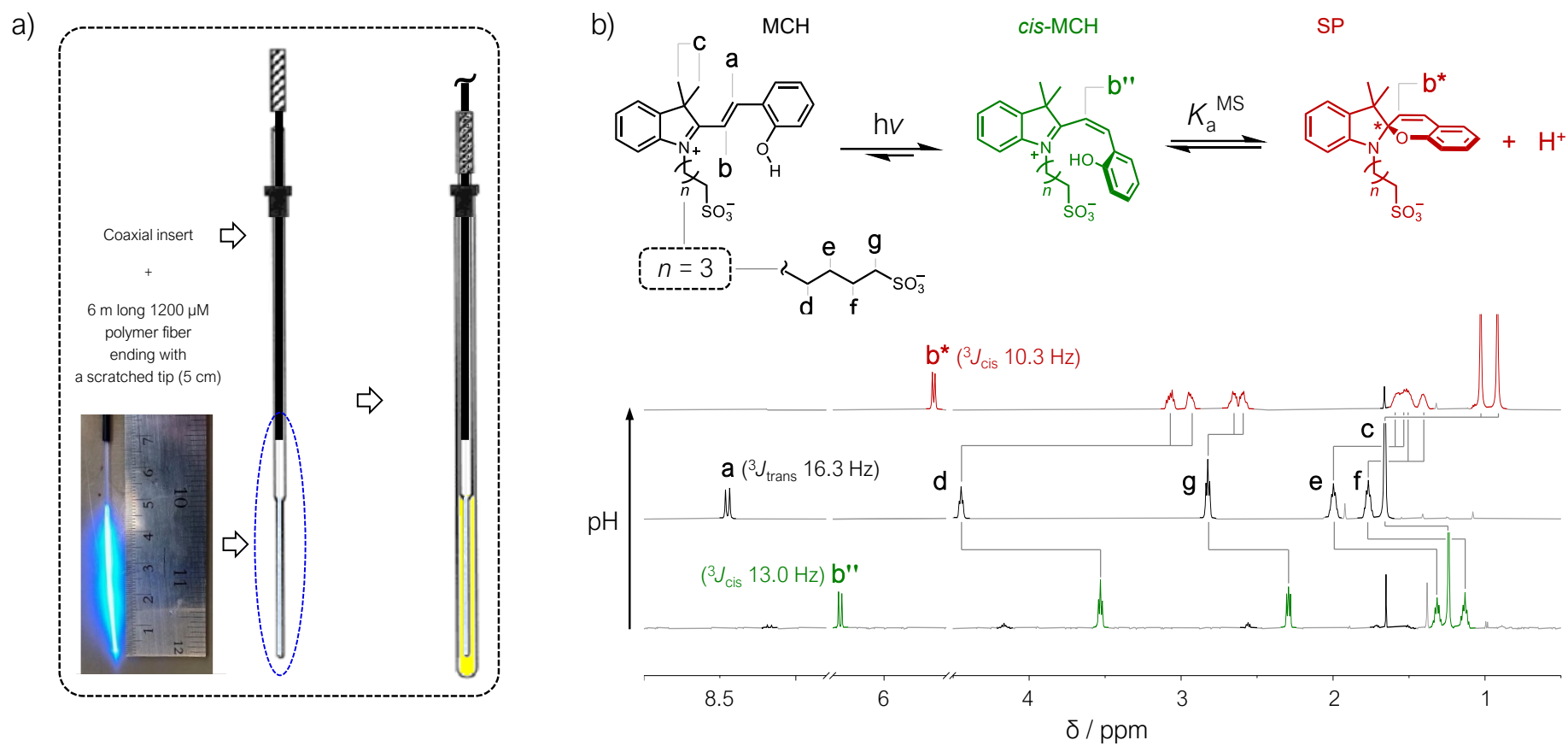


Figure S 3.19. ^1H -NMR (600 MHz, $\text{D}_2\text{O}:\text{H}_2\text{O}$ 6:4], 298 K) a) experimental setup for the Photo-NMR experiments, b) the three species detected in the experiment MCH (black), SP (red) and *cis*-MCH (green) the correspondingly coloured spectra are reported below.

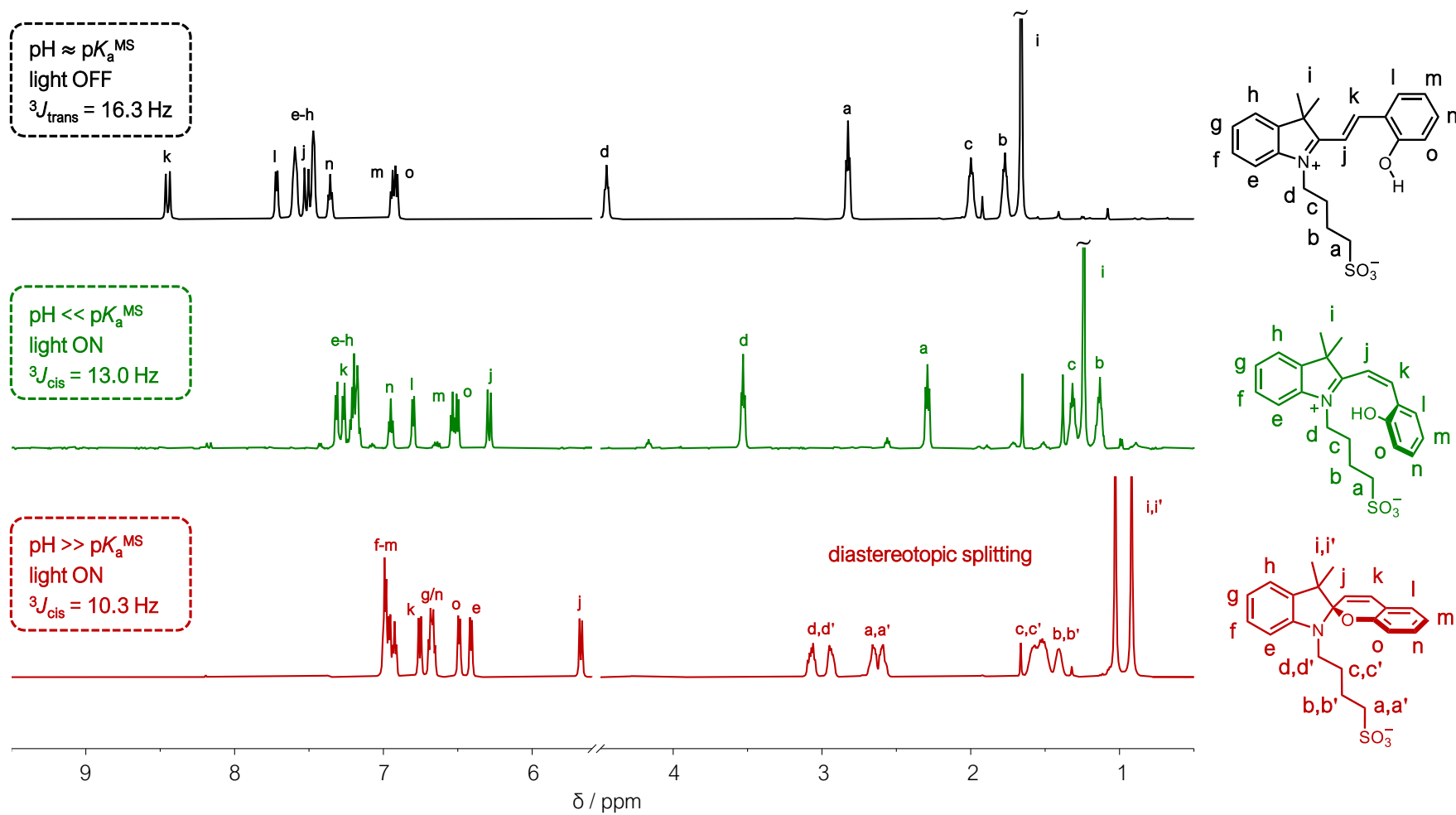


Figure S 3.20. ^1H -NMR (600 MHz, $\text{D}_2\text{O}:\text{H}_2\text{O}$ 6:4], 298 K) full spectra of compound **3** in the resting state (in black), under light irradiation at $\text{pH} \ll \text{p}K_a^{\text{MS}}$ (in green) and at $\text{pH} \gg \text{p}K_a^{\text{MS}}$.

3.9.6 UV-Vis analyses

Mother stocks of compound **1-3** (ca. 5.0 mM) are prepared in dry MeOH, micro-filtered with PTFE syringe filters and stored in 10-mL amber-glass vials at 4 °C. These solutions are stable for at least a couple of months.

The exact concentration of each stock solution is determined by three independent potentiometric titrations with standard NaOH 0.1 N. Typically, in a 20-mL amber-glass vial, the photoacid stock in MeOH (2.0 mL) is added to an aqueous solution of KCl (20 mM, 18.0 mL). After inserting a pre-calibrated Unitrode Pt1000 glass electrode and the Titrand burette tip, the titration is started, after an equilibration time of 5 minutes, under gentle stirring and nitrogen bubbling. The resulting profiles of pH vs V_{NaOH} are processed calculating the second derivative curve, from which the equivalent point (V_{eq}) is extrapolated as V_{NaOH} at $d^2\text{pH}/dV_{\text{NaOH}}^2 = 0$ (Figure S 3.21, right side).

Typically, prior to any experiment, a fresh aqueous solution of compound **1-3** is prepared by dilution (1/10) of the corresponding MeOH stock above. This solution (10% MeOH v/v) is immediately used for preparing, directly into quartz cuvettes, 1-mL aqueous samples at the desired pH and concentration. In all the experiment, the buffer concentration is 20 mM. In the case of MC-to-SP kinetics, each sample is run singularly: first, a cuvette filled with phosphate buffer at pH 9.5 (100 mM, 200 μL) and mQ-water (600 μL) is equilibrated at the desired temperature by putting it in the thermostatted cell holder of the UV-Vis spectrometer for 5 minutes. The acquisition is started and 50 μL of the previous stock are pre-mixed with mQ-water (150 μL). Subsequently, this 200 μL aliquot is added to the cuvette *in situ*, and the sample mixed (gently pipetting) for 6 seconds.

Except for the MC-to-SP kinetics, where sample preparation occurs concomitantly with acquisition, all other spectra/kinetic traces are acquired after an equilibration time of 15 minutes at 25 °C and, when indicated, during or after 30 s of photoirradiation (425 nm, 100 mW). Kinetics are carried out monitoring the absorbance at the maximum absorption (λ_{max}) of MC or MCH.

MC \rightleftharpoons SP isomerization: The time period spanning from the start of the acquisition to the mixing of the sample is discharged, and the obtained kinetic profiles (Figure S 3.22, left) analysed as described in the main text, all results are illustrated in Figure S 3.22. At the end of each experiment, an UV-Vis spectrum is acquired and used together with K_c and the optical readout of SP to calculate ε_{MC} at all λ_{max} (see below). In general, $\Delta_r H$ and $\Delta_r S$ are obtained respectively from the slope and the intercept of the corresponding van't Hoff plot (Figure S 3.22, middle). In the case of **1**, however, data fit better to a second-order polynomial ($\ln K_c = a + b/T + c/T^2$) and both $\Delta_r H$ and $\Delta_r S$ are extrapolated at 25 °C as described previously.^[102] K_c values (Table S1) are calculated from the corresponding $\Delta_r G$ at $T = 25^\circ\text{C}$. In all cases, activation parameters ΔH^\ddagger and ΔS^\ddagger are obtained respectively from the slope and the intercept of the corresponding Eyring plot (Figure S 3.22, right) assuming $\kappa = 1$ and $T = 25^\circ\text{C}$.

Molar absorptivities: ε_{MCH} and ε_{SP} are the slopes obtained from quantitative calibrations (performed in triplicate) at pH 3 and in mQ-water, where spectra are acquired in the dark and under continuous light irradiation, respectively (Figure S 3.24). Quantitative calibrations of MCH **1-3** at $T = 25^\circ\text{C}$. Solid black lines represent the best linear fit, whereas dotted red lines indicate the upper/lower boundaries based on the error associated to the x- and y-axis (triplicate experiments).). On the other hand, ε_{MC} are calculated knowing the UV-Vis spectra at

equilibrium and the corresponding composition: the molar fractions of MC (χ_{MC}) and SP (χ_{SP}) at equilibrium are easily derived from K_c and are equal to $1/(1+K_c)$ and $K_c/(1+K_c)$, respectively. Molar absorptivities are obtained as:

$$\varepsilon_{MC, \lambda_{max}} = \frac{A_{eq} - \varepsilon_{SP, \lambda_{max}} \chi_{SP} C}{\chi_{MC} C}$$

where A_{eq} is the absorbance at any λ_{max} detected at equilibrium and C is the total concentration of photoacid in the dark (optical path is 1 cm). Note that at λ_{max} of both MCH and MC there are no optical interferences ($\varepsilon_{SP} = 0$), whereas below 350 nm optical interferences are significant. Accordingly, the full UV-Vis spectrum of MC **1-3** is computed as follows, knowing the one of SP at the same concentration:

$$A_{MC} = \frac{A_{eq} - A_{SP} \chi_{SP}}{\chi_{MC}}$$

pH titrations: all the absorbances used for elaboration are the average value resulting from two independent experiments. As described in the main text, both pK_a^{GS} and pK_a^{MS} are obtained from the profiles of two distinct absorbances as a function of the pH by non-least square curve fitting to Boltzmann function, and both are reported as the average value of the two distinct outcomes. Under dark conditions and at any given pH, the absorbances detected at the three different λ_{max} are converted into concentrations knowing all the corresponding molar extinction coefficients as follows (the concentration of *cis*-MCH is considered negligible, see below):

$$[MC]^{eq} = \frac{A_{eq, \lambda_{MC}}}{\varepsilon_{MC, \lambda_{MC}}}$$

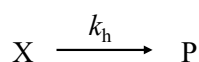
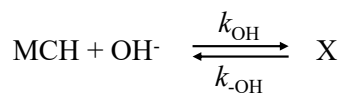
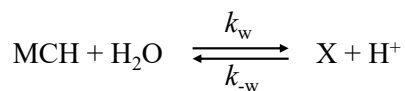
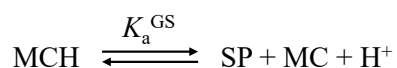
$$[MCH]^{eq} = \frac{A_{eq, \lambda_{MCH}} - \varepsilon_{MC, \lambda_{MCH}} [MC]^{eq}}{\varepsilon_{MCH, \lambda_{MCH}}}$$

$$[\text{SP}]^{eq} = \frac{A_{eq,\lambda_{SP}} - \varepsilon_{MC,\lambda_{SP}}[\text{MC}]^{eq} - \varepsilon_{MCH,\lambda_{SP}}[\text{MCH}]^{eq}}{\varepsilon_{SP,\lambda_{SP}}}$$

$$C \approx [\text{MCH}]^{eq} + [\text{MC}]^{eq} + [\text{SP}]^{eq}$$

which are used for calculating the corresponding speciation diagram (χ vs pH) and the parameter ϕ as described previously in the chapter.

Hydrolysis: the obtained kinetic profiles are analysed as described previously in the chapter. The model is derived as follows. Assuming: i) MCH dissociating into MC, SP and H^+ according to the corresponding ground state acidity constant ($\text{p}K_a^{\text{GS}}$), ii) MCH undergoing reaction with either H_2O or the hydroxide ion and iii) X the tetrahedral intermediated leading to products:



And considering steady-state conditions in respect to intermediate X:

$$\frac{d[\text{X}]}{dt} \approx 0 = k_w[\text{MCH}] - k_{-w}[\text{X}][\text{H}^+] + k_{OH}[\text{MCH}][\text{OH}^-] - k_{-OH}[\text{X}] - k_h[\text{X}]$$

It follows that:

$$[\text{X}] = \frac{[\text{MCH}](k_w + k_{OH}[\text{OH}^-])}{k_{-w}[\text{H}^+] + k_{-OH} + k_h}$$

Given the initial rate equal to $v_0 = k_h[X]$ and expressing $[MCH]$ as a function of C and pK_a^{GS} :

$$[MCH] = \frac{C [H^+]}{[H^+] + K_a^{GS}}$$

We finally obtain:

$$v_0 = k_h[X] = \frac{k_h C [H^+](k_w + k_{OH}[OH^-])}{([H^+] + K_a^{GS})(k_{-w}[H^+] + k_{-OH} + k_h)} = \frac{C (k_w[H^+] + k_{OH}K_w)}{([H^+] + K_a^{GS})\left(\frac{k_{-w}}{k_h}[H^+] + \frac{k_{-OH}}{k_h} + 1\right)}$$

And so (realizing that $k_{-OH}/k_h \ll 1$):

$$k_{obs,hydr} \approx \frac{v_0}{C} = \frac{k_w[H^+] + k_{OH}K_w}{([H^+] + K_a^{GS})\left(\frac{k_{-w}}{k_h}[H^+] + 1\right)}$$

Thermal relaxation: the obtained kinetic profiles are analysed as described in the main text. The model is derived as follow. The total concentration of photoacid is always expressed by the sum of all the four species in solution:

$$C = [cMCH] + [MCH] + [MC] + [SP]$$

Considering *cis*-MCH (indicated in equations with the short label cMCH for simplicity) produced exclusively by photoirradiation it follows that the total concentration in the dark can be reasonably approximated as:

$$C = C^{dark} \approx [MCH]^{eq} + [MC]^{eq} + [SP]^{eq}$$

Instead, under light irradiation (with both MCH and MC converted into *cis*-MCH and SP), the expression for C becomes:

$$C = C^{hv} = [cMCH]^{hv} + [SP]^{hv} + [SP]^{eq} = [cMCH]_0 + [SP]_0$$

This can be reformulated in terms of [SP] considering the acid-base equilibrium existing between *cis*-MCH and SP:

$$C = C^{hv} = [\text{SP}]_0 \left(1 + \frac{[\text{H}^+]}{K_a^{MS}} \right)$$

On the other hand, the effective concentration of photochemically-populated metastable species (C_0^{hv}) can be obtained as:

$$C^{hv} - C^{dark} = [\text{cMCH}]^{hv} + [\text{SP}]^{hv} - [\text{MCH}]^{eq} - [\text{MC}]^{eq} = 0$$

$$C_0^{hv} = [\text{cMCH}]^{hv} + [\text{SP}]^{hv} = [\text{MCH}]^{eq} + [\text{MC}]^{eq} = C(1 - \chi_{SP})$$

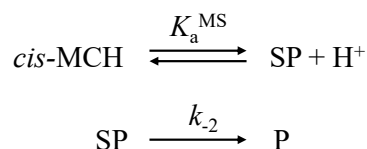
Where χ_{SP} is the molar fraction of SP at equilibrium under dark conditions. On multiplying both sides of the equation above for C^{hv} by $(1 - \chi_{SP})$, C_0^{hv} can be reformulated as:

$$C_0^{hv} = C(1 - \chi_{SP}) = [\text{SP}]_0 \left(1 + \frac{[\text{H}^+]}{K_a^{MS}} \right) (1 - \chi_{SP})$$

This equation directly relates with the pre-equilibrium between *cis*-MCH and SP – i.e., with the total concentration of the species after light irradiation – and allows for extrapolating the concentration of SP at $t = 0$ and any pH as:

$$[\text{SP}]_0 = \frac{C_0^{hv}}{(1 - \chi_{SP})} \left(\frac{K_a^{MS}}{[\text{H}^+] + K_a^{MS}} \right)$$

Considering now the ring-opening of SP towards MC the rate-determining step throughout the entire range of pH:



It follows that:

$$v_0 \approx k_{-2} [\text{SP}]_0 = k_{-2} \frac{c_0^{hv}}{(1-\chi_{SP})} \left(\frac{K_a^{MS}}{[\text{H}^+] + K_a^{MS}} \right)$$

And so:

$$k_{obs,relax} \approx \frac{v_0}{c_0^{hv}} = \frac{k_{-2}}{(1-\chi_{SP})} \left(\frac{K_a^{MS}}{1 + K_a^{MS}} \right)$$

Finally, expressing $(1 - \chi_{SP})$ as a function of all equilibrium constants in the dark, we obtain the rate expression for the thermal relaxation as:

$$k_{obs,relax} = k_{-2} \left(\frac{K_a^{MS}}{[\text{H}^+] + K_a^{MS}} \right) \left(\frac{K_a(1+K_c) + [\text{H}^+]}{[\text{H}^+] + K_a} \right)$$

This equation suits the double sigmoidal profiles obtained experimentally, with conditions for plateau and inflections extrapolated as follow:

$$K_a^{MS} \ll [\text{H}^+] \gg K_a \quad \rightarrow \quad k_{obs,relax} = k_{-2} \left(\frac{K_a^{MS}}{[\text{H}^+]} \right)$$

$$K_a^{MS} = [\text{H}^+] \gg K_a \quad \rightarrow \quad k_{obs,relax} = \frac{k_{-2}}{2}$$

$$K_a^{MS} \gg [\text{H}^+] \gg K_a \quad \rightarrow \quad k_{obs,relax} = k_{-2}$$

$$K_a^{MS} \gg [\text{H}^+] = K_a \quad \rightarrow \quad k_{obs,relax} = k_{-2} \left(\frac{2+K_c}{2} \right)$$

$$K_a^{MS} \gg [\text{H}^+] \ll K_a \quad \rightarrow \quad k_{obs,relax} = k_{-2}(1 + K_c) = k_{-2} + k_2$$

In all cases, curve fitting is performed in Excel, using the Solver add-in for minimizing the sum of the square deviations from the corresponding model function.

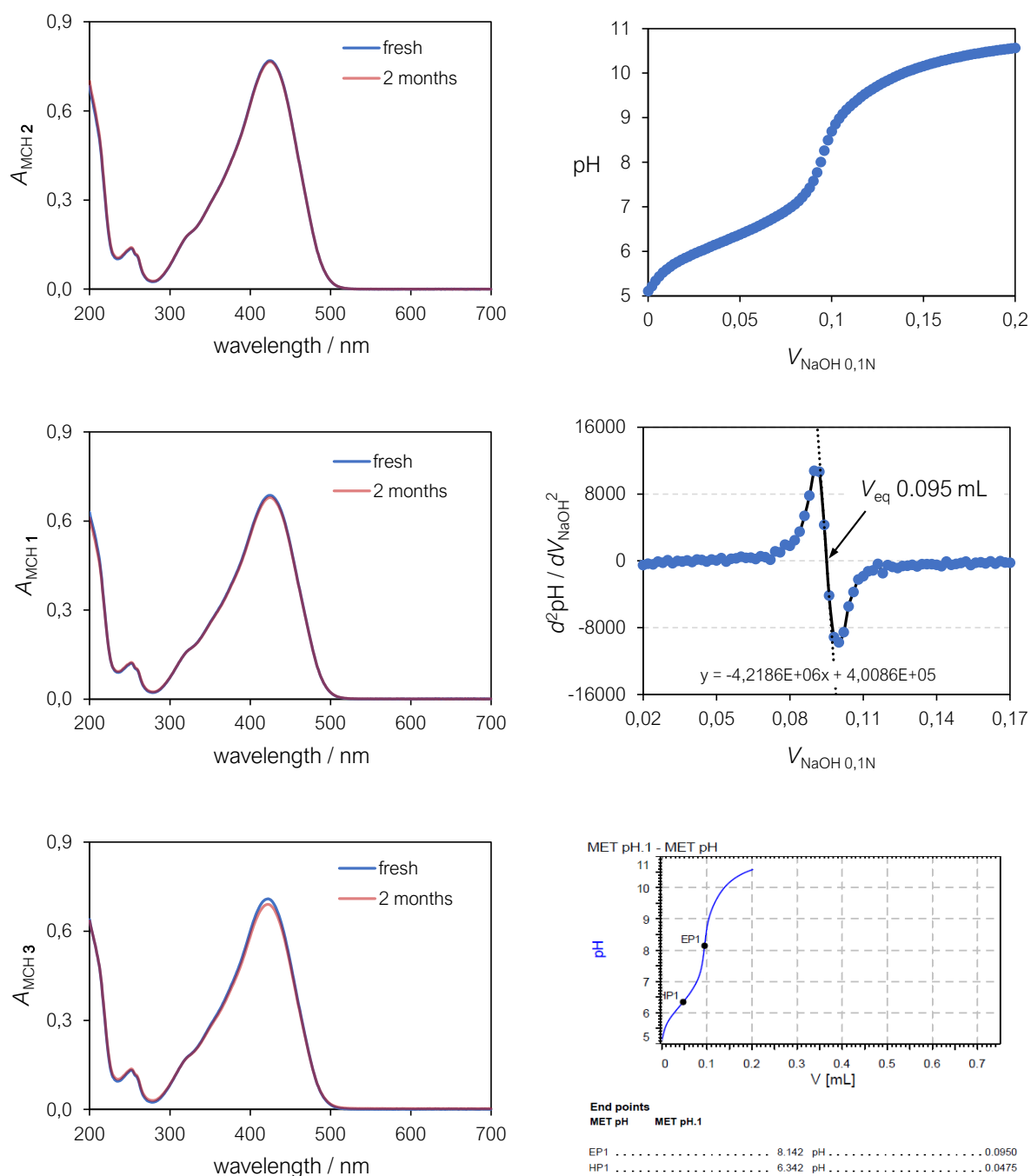


Figure S 3.21 Left side: spectra of compound 1-3 recorder at pH 3 and $T = 25$ °C immediately after preparation and after two months of usage ($\Delta\% < 3\%$). Right side: representative example of a potentiometric titration and corresponding elaboration. The equivalent point determined with the second derivative method matches the one generated automatically by the Metrohm TiamoTM software.

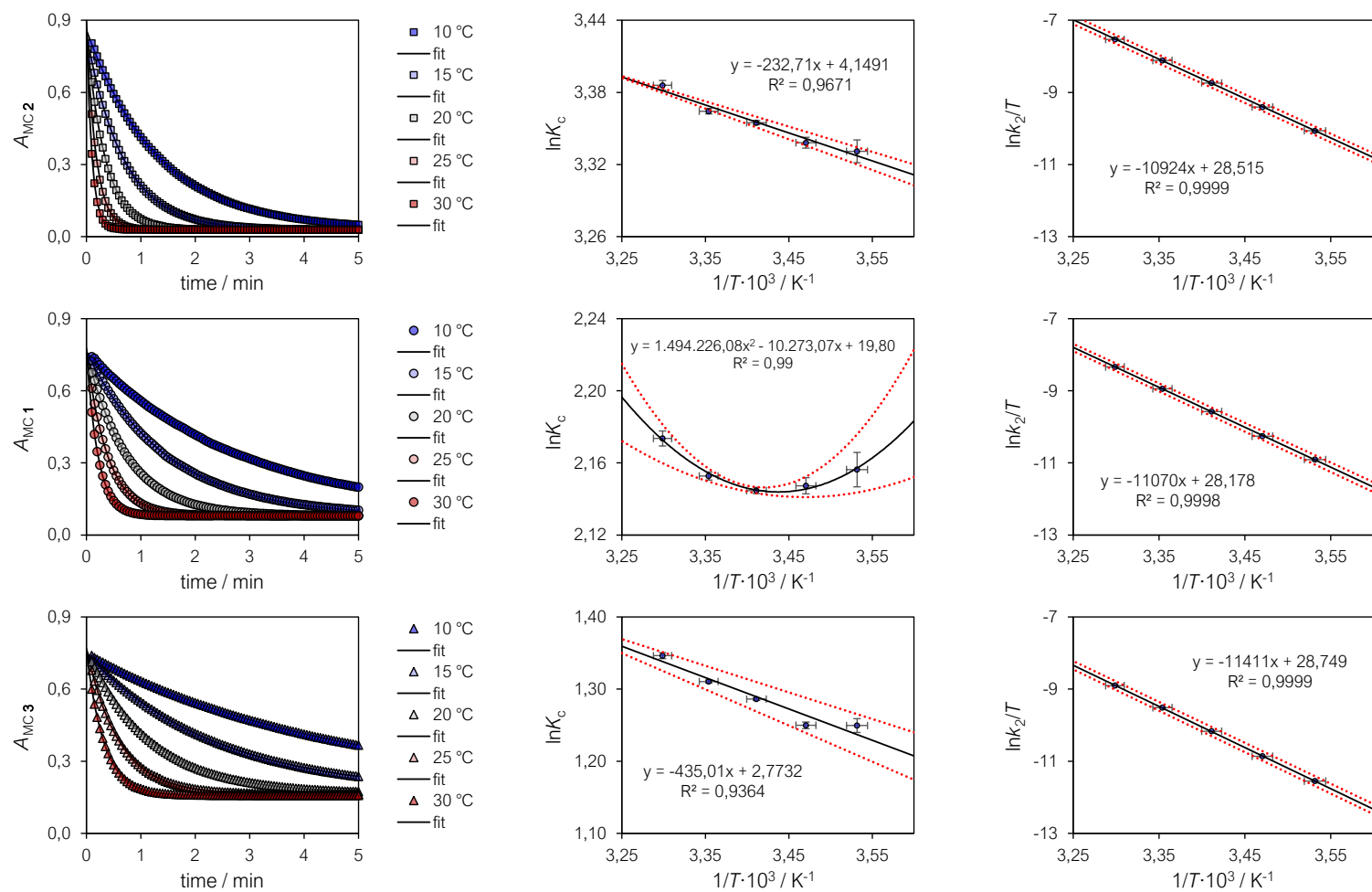


Figure S.3.22. From left to right: kinetic profiles, Van't Hoff plot, and Eyring plot, obtained for **2** ($n = 1$) (\blacksquare), **1** ($n = 2$) (\bullet) and **3** ($n = 3$) (\blacktriangle). Experimental conditions: $[2] = 25 \pm 1 \mu M$, $[1] = 21 \pm 1 \mu M$, $[3] = 23 \pm 1 \mu M$, [phosphate buffers] = 20 mM, pH 9.5, $T = 10\text{--}30 \text{ }^\circ\text{C}$ in the dark. Solid black lines represent the best fit to the corresponding model function, whereas dotted red lines indicate the upper/lower boundaries based on the error associated to the x- and y-axis (duplicate experiments).

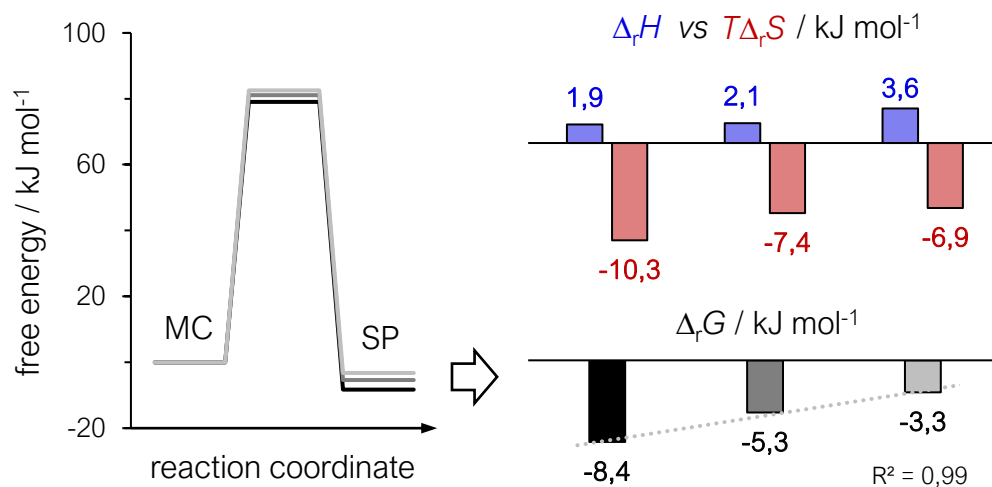


Figure S 3.23. Energy diagram for the MC ⇌ SP isomerization of **2** ($n=1$, black), **1** ($n=2$, grey) and **3** ($n=3$, light grey) obtained from the corresponding van't Hoff and Eyring plots (left), and trend of the thermodynamic parameters for the MC-to-SP reaction a function of n (right).

Table S 3.2. Thermodynamic and kinetic parameters for the MC ⇌ SP isomerization of 1-3.

n	T (°C)	$k_{\text{obs, eq}}$ (10 ⁻² s ⁻¹)	k_2 (10 ⁻² s ⁻¹)	k_{-2} (10 ⁻² s ⁻¹)	$\Delta_r H$ (kJ mol ⁻¹)	$\Delta_r S$ (J K ⁻¹ mol ⁻¹)	$\Delta_r G^a$ (kJ mol ⁻¹)	K_c^a	ΔH^\ddagger^a (kJ mol ⁻¹)	ΔS^\ddagger^a (J K ⁻¹ mol ⁻¹)
1	10	1.25	1.21	0.04	1.9 ± 0.2	34.5 ± 0.6	- 8.4 ± 0.6	29.0 ± 4.7	90.8 ± 0.1	39.5 ± 0.8
	15	2.46	2.37	0.08						
	20	4.87	4.70	0.16						
	25	9.24	8.93	0.31 (0.31 ^b)						
	30	16.83	16.28	0.55						
2	10	0.58	0.52	0.06	2.1 ± 0.7 ^a	24.9 ± 2.4 ^a	- 5.3 ± 1.4	8.6 ± 4.9	92.0 ± 0.9	36.7 ± 2.0
	15	1.13	1.01	0.12						
	20	2.27	2.04	0.24						
	25	4.34	3.89	0.45 (0.46 ^b)						
	30	8.06	7.24	0.82						
3	10	0.35	0.27	0.08	3.6 ± 0.5	23.1 ± 1.7	- 3.3 ± 1.0	3.7 ± 0.5	94.9 ± 0.6	41.5 ± 0.8
	15	0.71	0.55	0.16						
	20	1.43	1.12	0.31						
	25	2.79	2.20	0.59 (0.60 ^b)						
	30	5.20	4.12	1.07						

The superscript *a* denotes data extrapolated from the corresponding van't Hoff or Eyring plot at 25 °C. In the case of **1** we found a non-linear correlation between $\ln K_c$ and $1/T$: data fit well to a second-order polynomial, either suggesting that MC and SP may possess different heat capacities or a change in the mechanism of isomerization; more details in this regard go beyond the scope of the current work. Superscript *b* denotes values obtained from relaxation kinetics with eq. 11 in the main text.

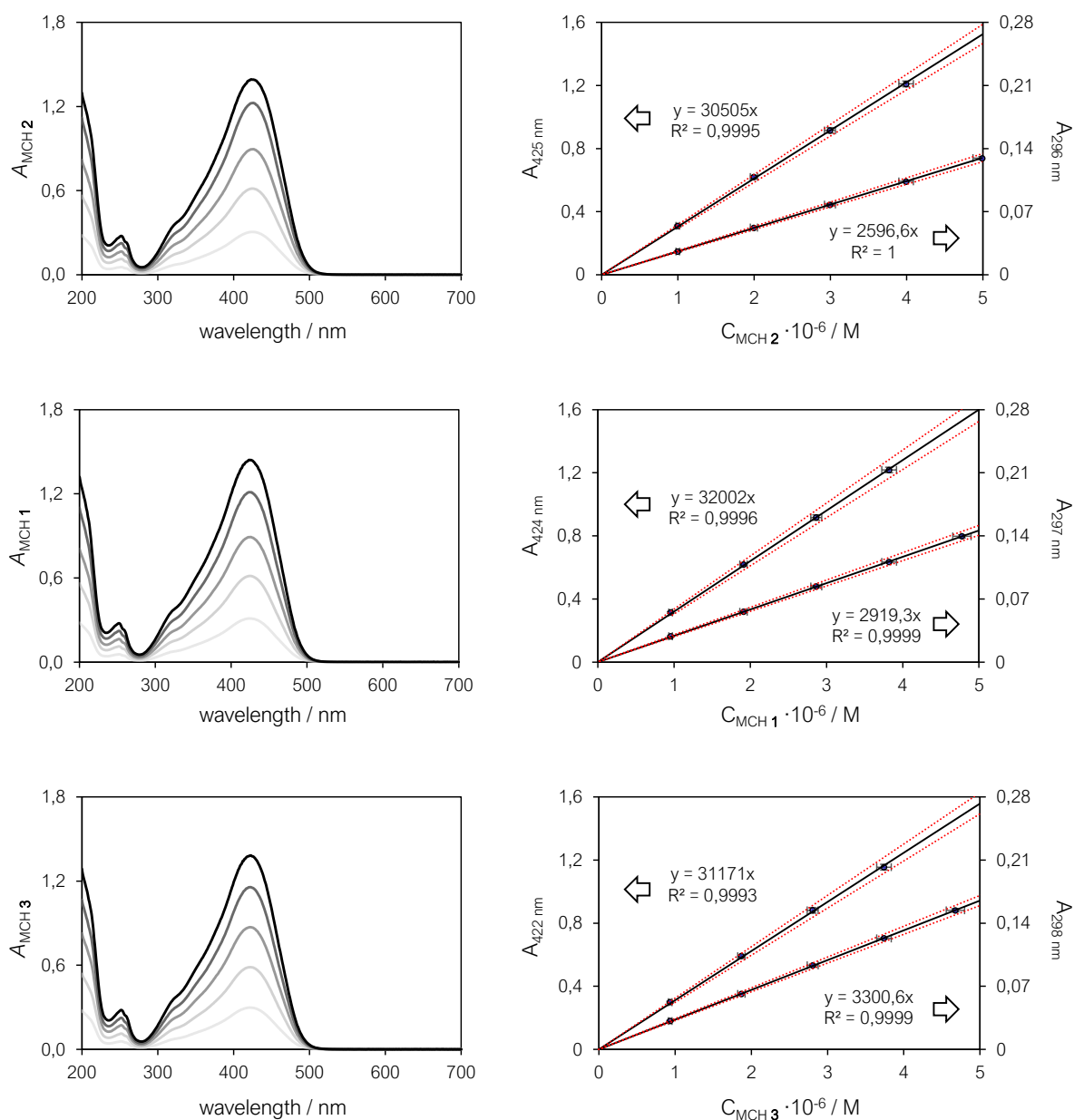


Figure S 3.24. Quantitative calibrations of MCH 1-3 at $T = 25\text{ }^{\circ}\text{C}$. Solid black lines represent the best linear fit, whereas dotted red lines indicate the upper/lower boundaries based on the error associated to the x- and y-axis (triplicate experiments).

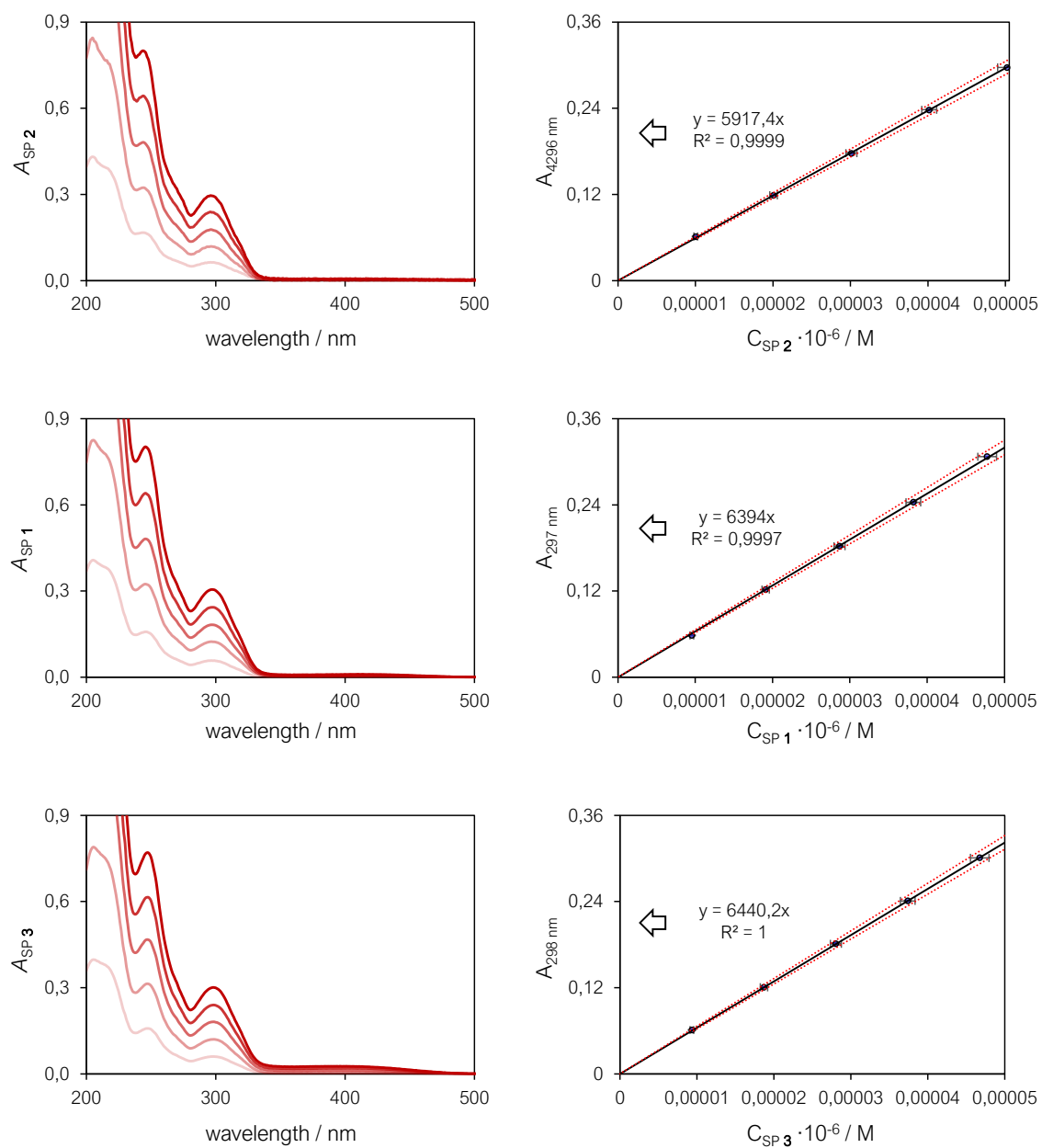
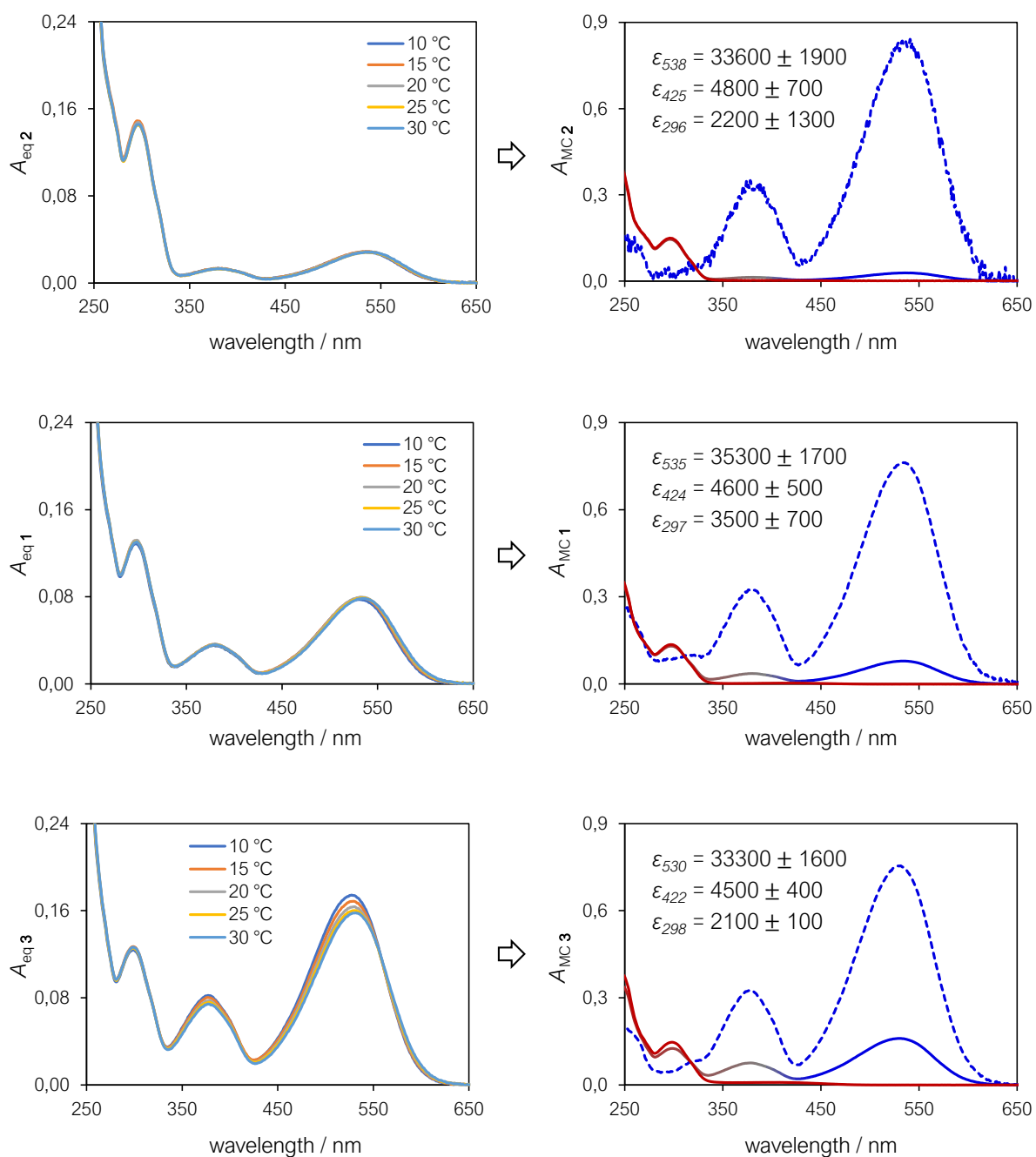


Figure S 3.25. Quantitative calibrations of SP 1-3 at $T = 25\text{ }^{\circ}\text{C}$. Solid black lines represent the best linear fit, whereas dotted red lines indicate the upper/lower boundaries based on the error associated to the x- and y-axis (triplicate experiments).



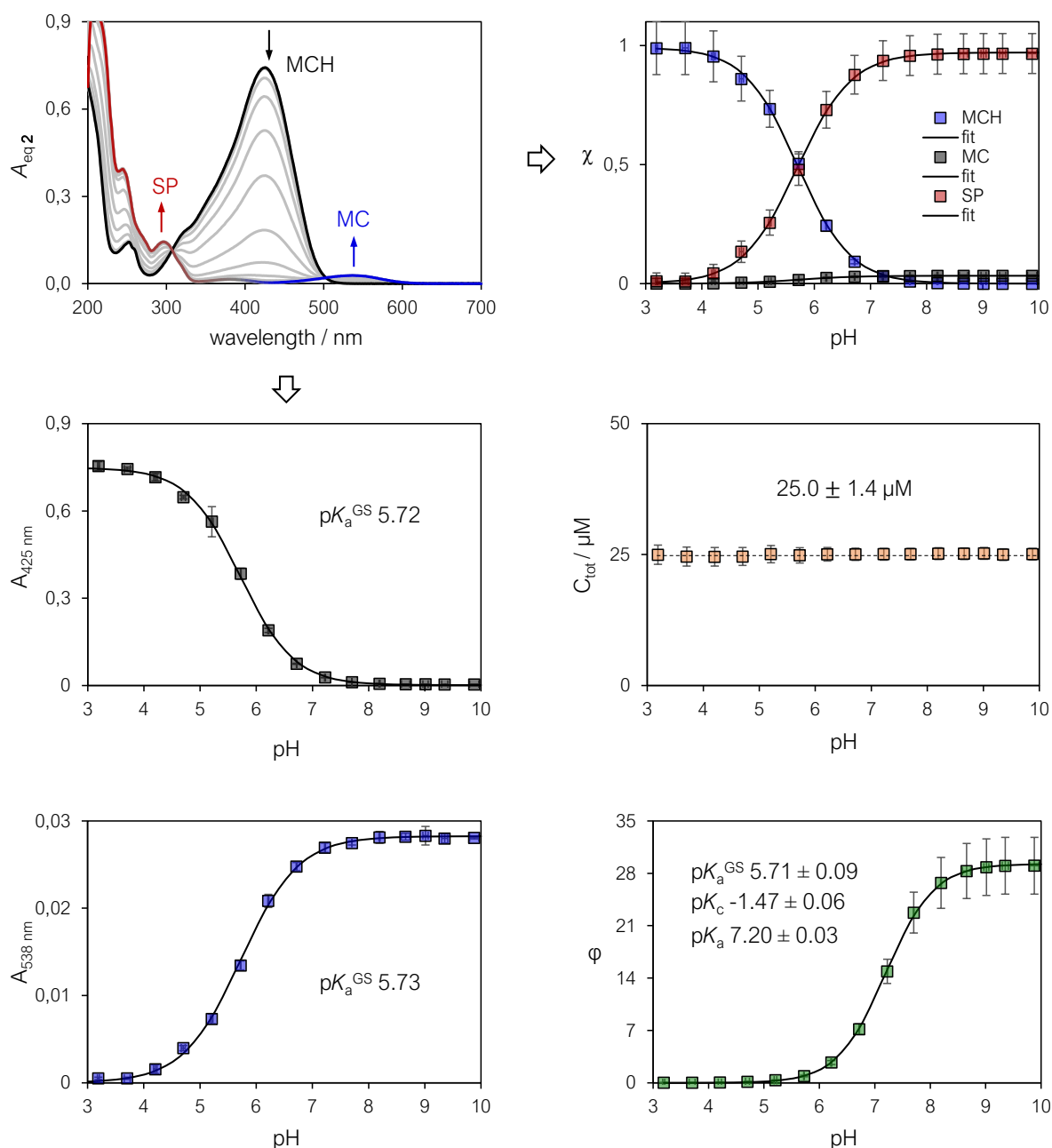


Figure S 3.27. UV-Vis titration (top left) and corresponding elaborations obtained for **2** ($n = 1$). Experimental conditions: [phosphate buffers] = 20 mM ($3 < \text{pH} < 10$), $T = 25^\circ\text{C}$ in the dark. Speciation diagrams are reported on the upright corner. Solid black lines represent the best fit to the corresponding model function, whereas error bars indicate the error associated to the x- and y-axis (duplicate experiments). In the case of the ϕ plot (bottom right corner), error bars include error propagation of all variables.

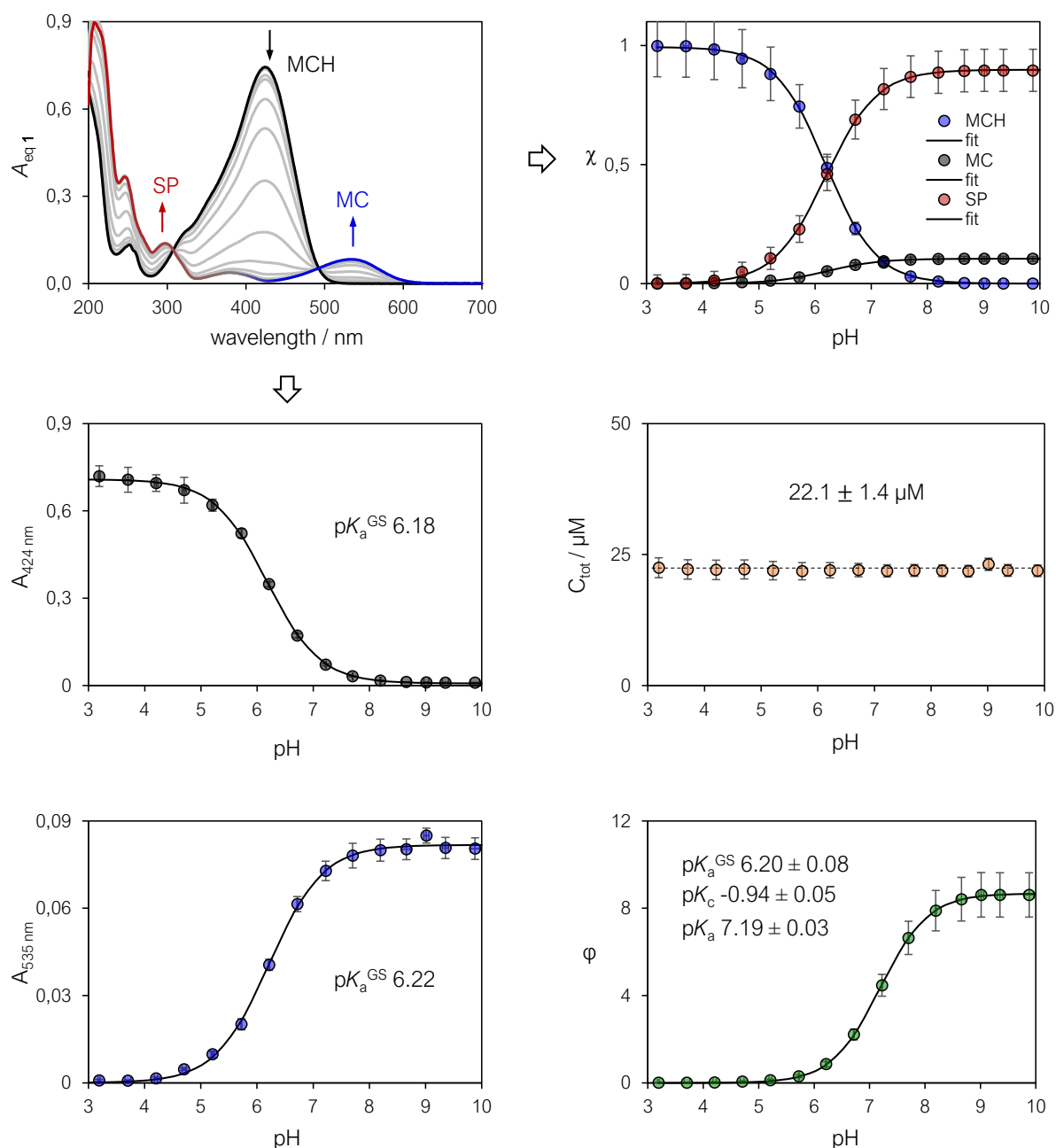


Figure S 3.28. UV-Vis titration (top left) and corresponding elaborations obtained for **1** ($n = 2$). Experimental conditions: [phosphate buffers] = 20 mM ($3 < \text{pH} < 10$), $T = 25\text{ }^\circ\text{C}$ in the dark. Speciation diagrams are reported on the upright corner. Solid black lines represent the best fit to the corresponding model function, whereas error bars indicate the error associated to the x- and y-axis (duplicate experiments). In the case of the ϕ plot (bottom right corner), error bars include error propagation of all variables.

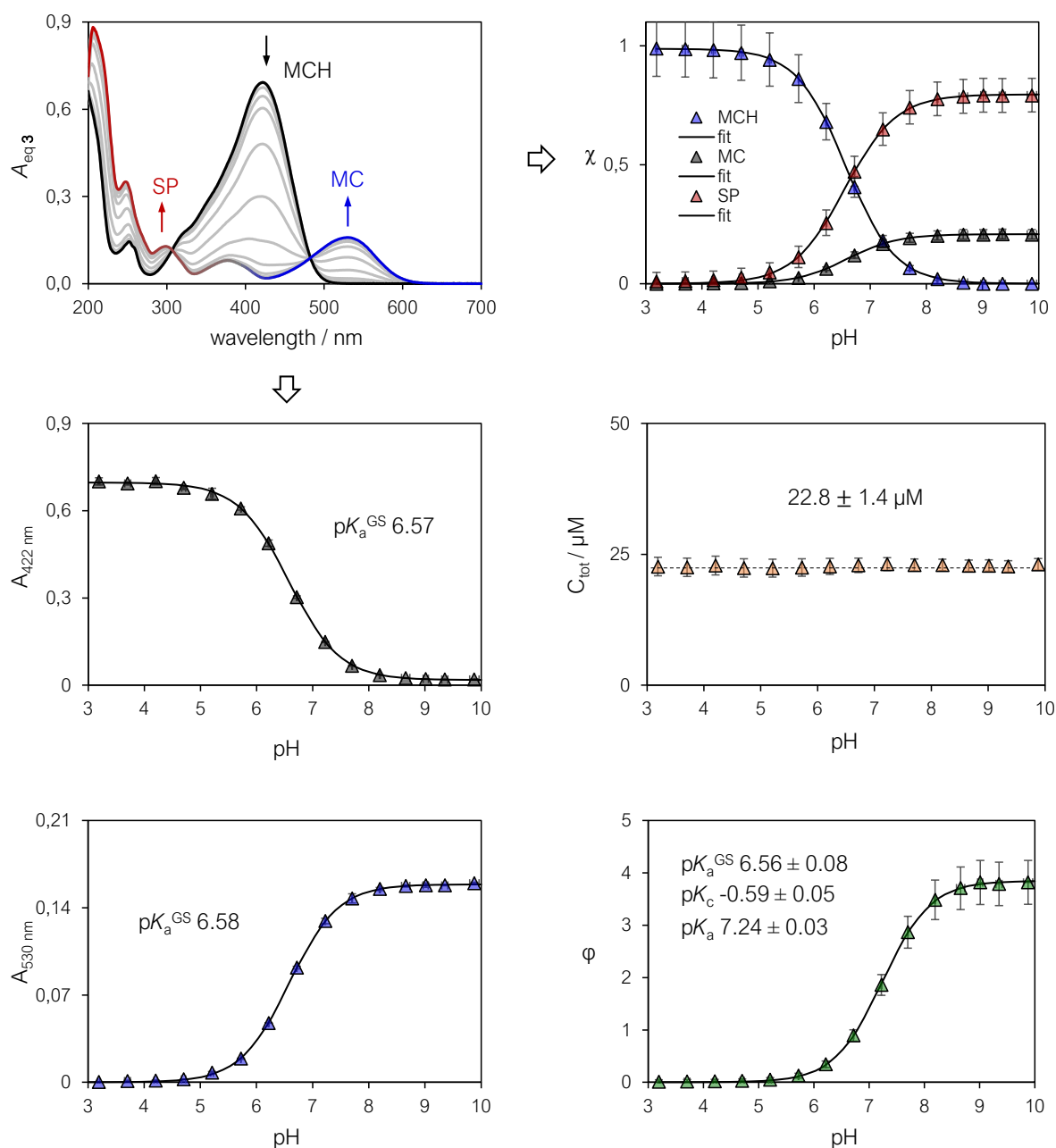


Figure S 3.29. UV-Vis titration (top left) and corresponding elaborations obtained for **3** ($n = 3$). Experimental conditions: [phosphate buffers] = 20 mM ($3 < \text{pH} < 10$), $T = 25^\circ\text{C}$ in the dark. Speciation diagrams are reported on the upright corner. Solid black lines represent the best fit to the corresponding model function, whereas error bars indicate the error associated to the x- and y-axis (duplicate experiments). In the case of the Φ plot (bottom right corner), error bars include error propagation of all variables.

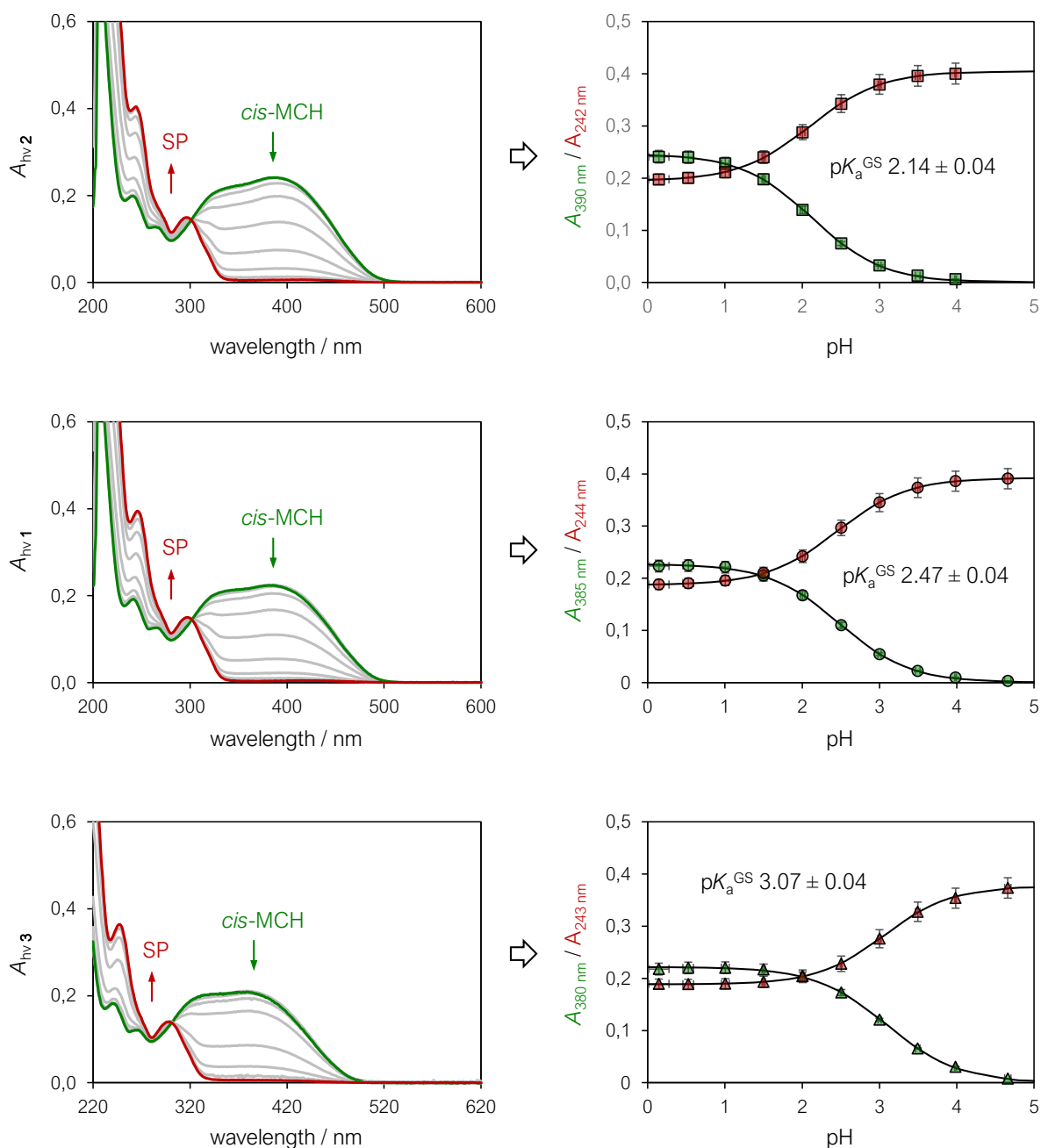


Figure S 3.30. UV-Vis titration and corresponding elaborations obtained for **1-3** under continuous light irradiation (425 nm, 100 mW). Experimental conditions: $[\text{HCl}] = 1 \text{ M}$ to 0.1 mM , $[\text{phosphate buffers}] = 20 \text{ mM}$ ($\text{pH} > 4$), $T = 25 \text{ }^\circ\text{C}$. Solid black lines represent the best fit to eq. 8, whereas error bars indicate the error associated to the x- and y-axis (duplicate experiments).

Table S 3.3. Optical readout, equilibrium constants and photoacidity of 1-3.

n	λ_{\max} (nm)	ε_{SP} (L mol ⁻¹ cm ⁻¹)	ε_{MCH} (L mol ⁻¹ cm ⁻¹)	ε_{MC} (L mol ⁻¹ cm ⁻¹)	pK_a	pK_c	pK_a^{GS}	$pK_a^{MS f}$	Π^h
1	296	5900 ± 200	2600 ± 100	2200 ± 1300	7.3 ± 0.1 ^a	-1.50 ± 0.04 ^b	5.7 ± 0.1 ^c		
	425	-	30500 ± 1200	4800 ± 700	7.2 ± 0.1 ^b	-1.47 ± 0.06 ^d	5.71 ± 0.09 ^e	2.14 ± 0.04	3.6 ± 0.1
	538	-	-	33600 ± 1900	7.20 ± 0.03 ^d	-1.46 ± 0.07 ^g	5.72 ± 0.03 ^f		
2	297	6400 ± 200	2900 ± 100	3500 ± 700	7.2 ± 0.1 ^a	-0.99 ± 0.04 ^b	6.2 ± 0.1 ^c		
	424	-	32000 ± 1500	4600 ± 500	7.2 ± 0.1 ^b	-0.94 ± 0.05 ^d	6.20 ± 0.08 ^e	2.47 ± 0.04	3.7 ± 0.1
	535	-	-	35300 ± 1700	7.19 ± 0.03 ^d	-0.94 ± 0.25 ^g	6.20 ± 0.03 ^f		
3	298	6400 ± 200	3300 ± 100	2100 ± 100	7.3 ± 0.1 ^a	-0.61 ± 0.04 ^b	6.6 ± 0.1 ^c		
	422	-	31200 ± 1300	4500 ± 400	7.2 ± 0.1 ^b	-0.59 ± 0.05 ^d	6.56 ± 0.08 ^e	3.07 ± 0.04	3.5 ± 0.1
	530	-	-	33300 ± 1600	7.24 ± 0.03 ^d	-0.57 ± 0.18 ^g	6.58 ± 0.03 ^f		

Superscripts *a*, *b* and *c* denote values obtained from ¹H NMR data with eq. 1, 2 and 3, respectively, while *d*, *e* and *f* denote values obtained from UV-Vis with eq. 2, 3 and 8, respectively. *g* indicates values extrapolated from the corresponding van't Hoff plot at 25 °C (see Table S 3.1), whereas *h* denotes the results obtained with Eq. 3.9, *i* refers to solubilities of 1-3 in KCl (20 mM) aqueous solutions, whereas *l* denotes average values obtained from multiple pH jumps experiments with eq. 12. The pK_a , pK_c , pK_a^{GS} and Π reported in Table 3.1. (main text) are reported as the average value obtained from both ¹H NMR and absorption data ± the corresponding std. deviation.

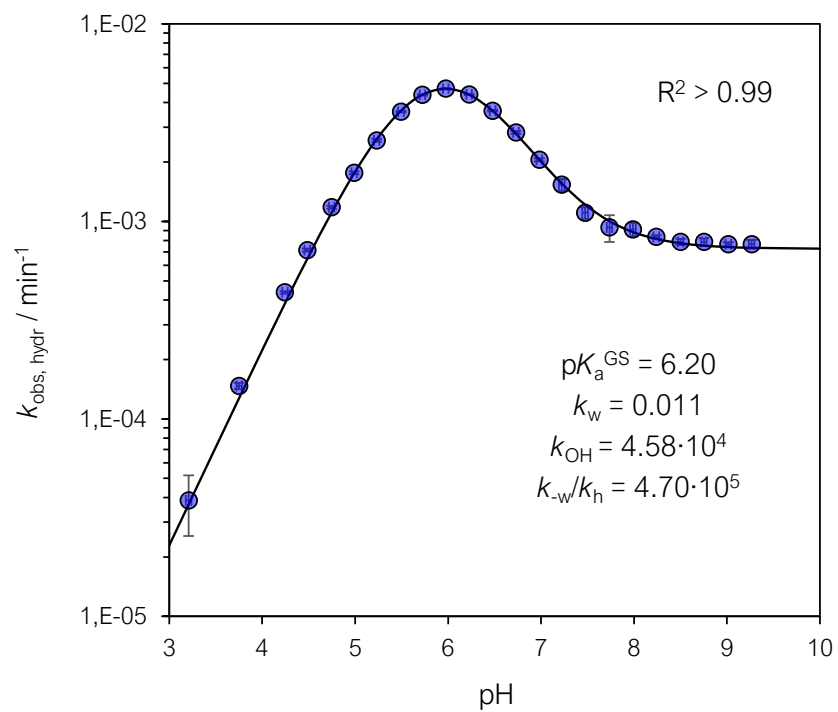
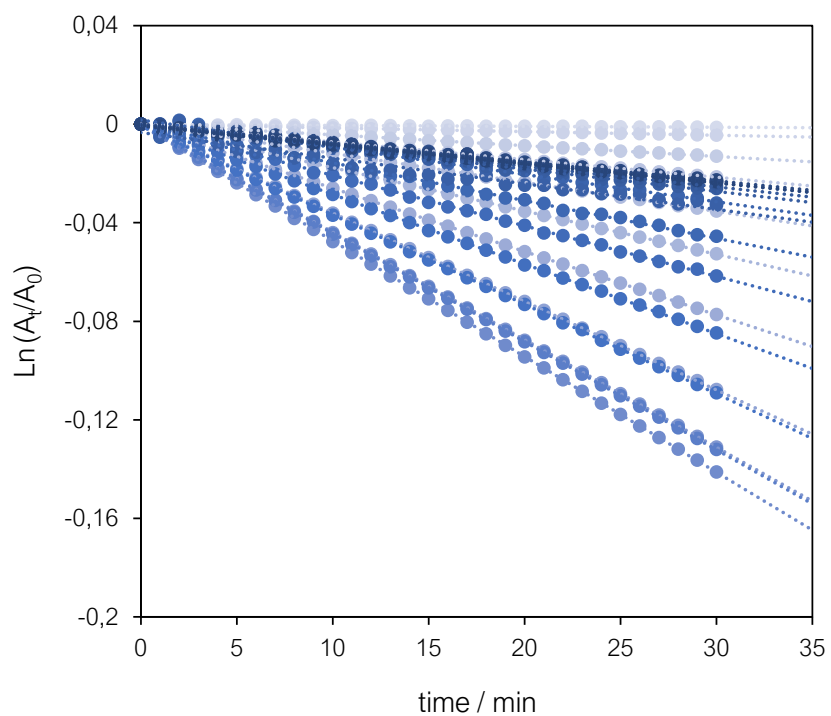


Figure S 3.31. Linearized kinetic profiles for the hydrolysis of **1** at different pH and 40 °C (left) and plot of the obtained first order apparent rate constant of hydrolysis as a function of the pH (right). Solid black lines represents the best fit, the error bars associated to the y-axis result from eight independent repetitions employing different concentration of **1** ($5 < [\mathbf{1}] < 40 \mu\text{M}$). Plots of $\text{Log}v_0$ vs $\text{Log}[\mathbf{1}]$ confirmed that reaction is first order in **1** throughout the entire range of pH. Experimental conditions: [phosphate buffers] = 20 mM ($3 < \text{pH} < 10$), $T = 25 \text{ }^\circ\text{C}$ in the dark; data collected at 425 nm ($3 < \text{pH} < 7.5$) and 535 nm ($\text{pH} > 7.5$).

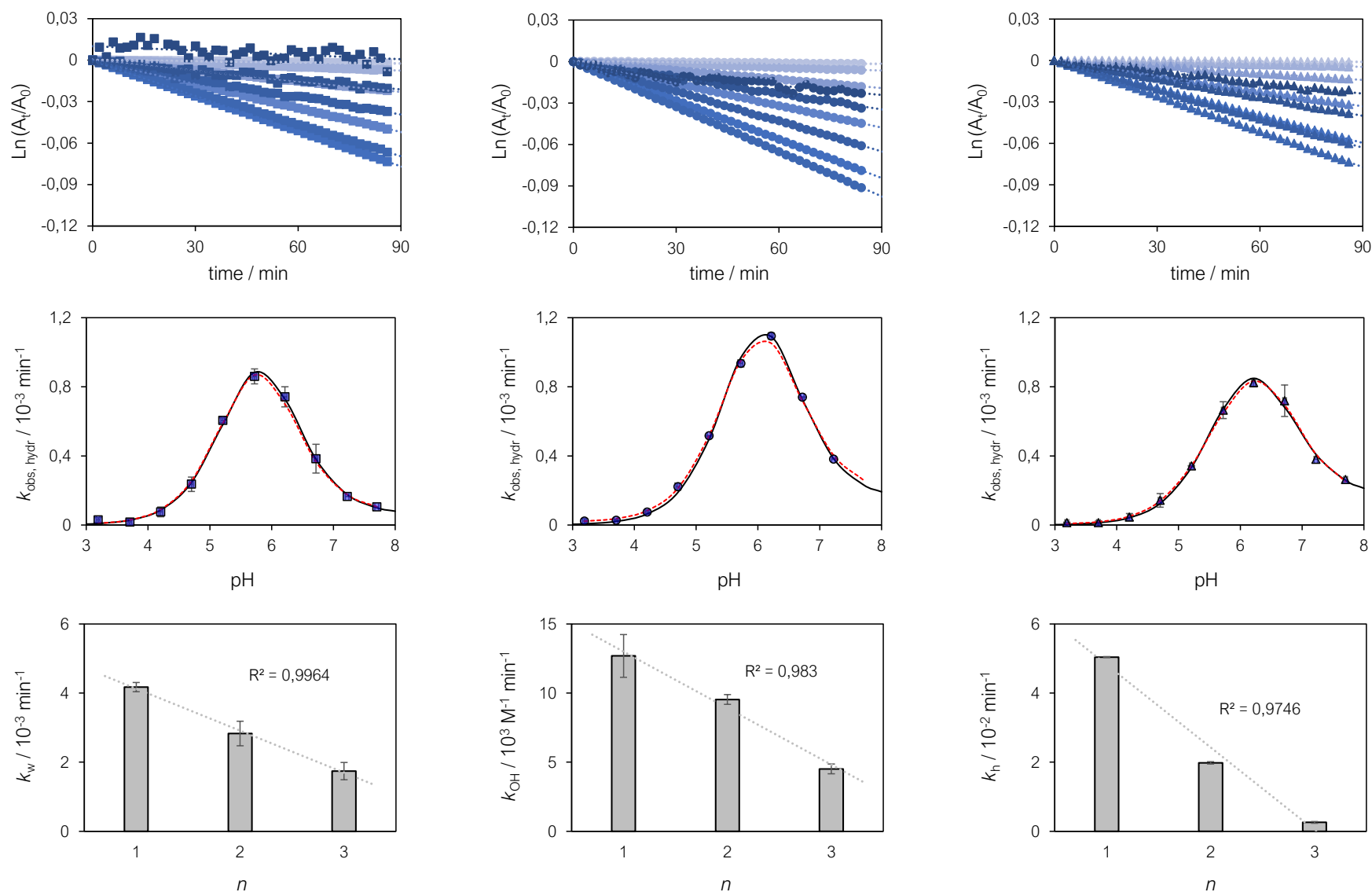


Figure S 3.32. Top: linearized kinetic profiles for the hydrolysis of **2** ($n = 1$) (■), **1** ($n = 2$) (●) and **3** ($n = 3$) (▲) at different pH and 25 °C (duplicate experiments). Middle: plots of the obtained apparent first order rate constant of hydrolysis as a function of the pH and relative fitting; solid black lines represent the best fit to eq. 10, whereas dotted red lines represent numerical fitting (see section 7 below for more details). Bottom: trends obtained for forward rate constants of hydrolysis as a function of n . Experimental conditions: $[\mathbf{1-3}] = 25 \pm 2 \mu\text{M}$, [phosphate buffers] = 20 mM ($3 < \text{pH} < 8$), $T = 25 \text{ °C}$ in the dark; data collected at 425 nm

Table S 3.4. Key parameters for the hydrolysis of 1-3 obtained from fitting.

n	T (°C)	k_w (10^{-3} min^{-1})	k_{OH} ($10^3 \text{ M}^{-1} \text{ min}^{-1}$)	k_w/k_h (10^5 M^{-1})	k_h (10^{-2} min^{-1})
1	25	4.3	11.6	7.5	-
		4.2 ± 0.1	13 ± 2	7.1 ± 0.5	5.0 ± 0.5
2	25	3.1	9.3	7.5	-
		2.8 ± 0.4	9.5 ± 0.4	6.7 ± 1.5	2.0 ± 0.2
	40	10.8	45.8	4.7	-
3	25	1.6	4.3	5.7	-
		1.7 ± 0.3	4.5 ± 0.4	5.8 ± 0.1	0.26 ± 0.03

Forward rate constants k_w , k_{OH} and k_w/k_h are first estimated from experimental data as described in the main text and subsequently optimized from fitting to eq. 10 (data highlighted in blue). These values are then used to initialize numerical fitting, which allow for estimating all the other kinetic components (*e.g.*, k_h) (see section 7 below for more details). The resulting kinetic constants (data highlighted in black) are listed as the average value obtained before and after numerical refinement \pm std. deviation; the uncertainty associated to k_h is estimated to lay within 10%.

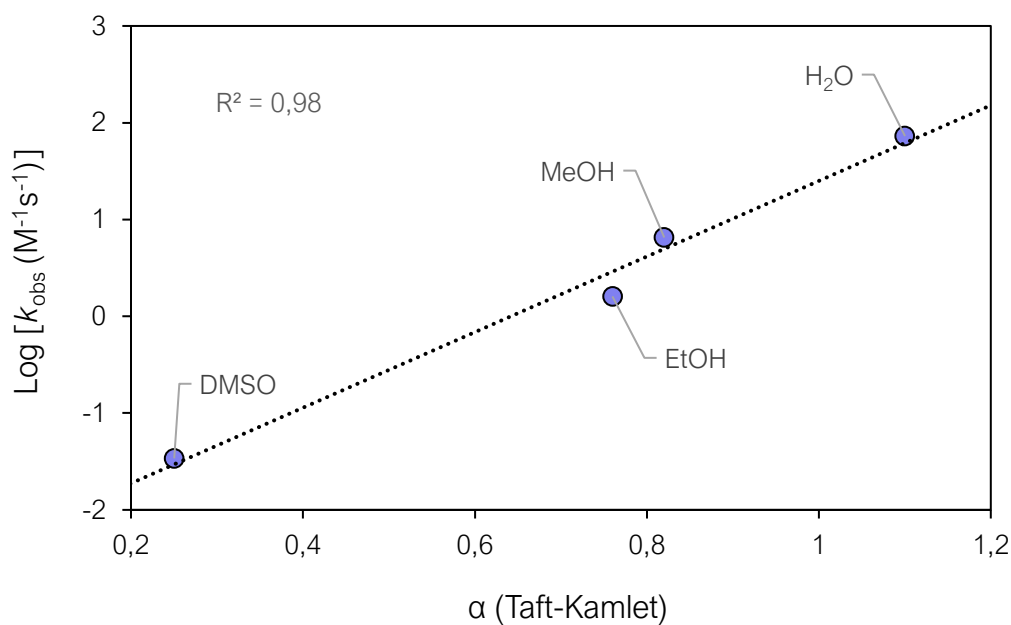


Figure S 3.33. Correlation between apparent second-order rate constants of relaxation of **1** and hydrogen bond donor acidity of the solvent.

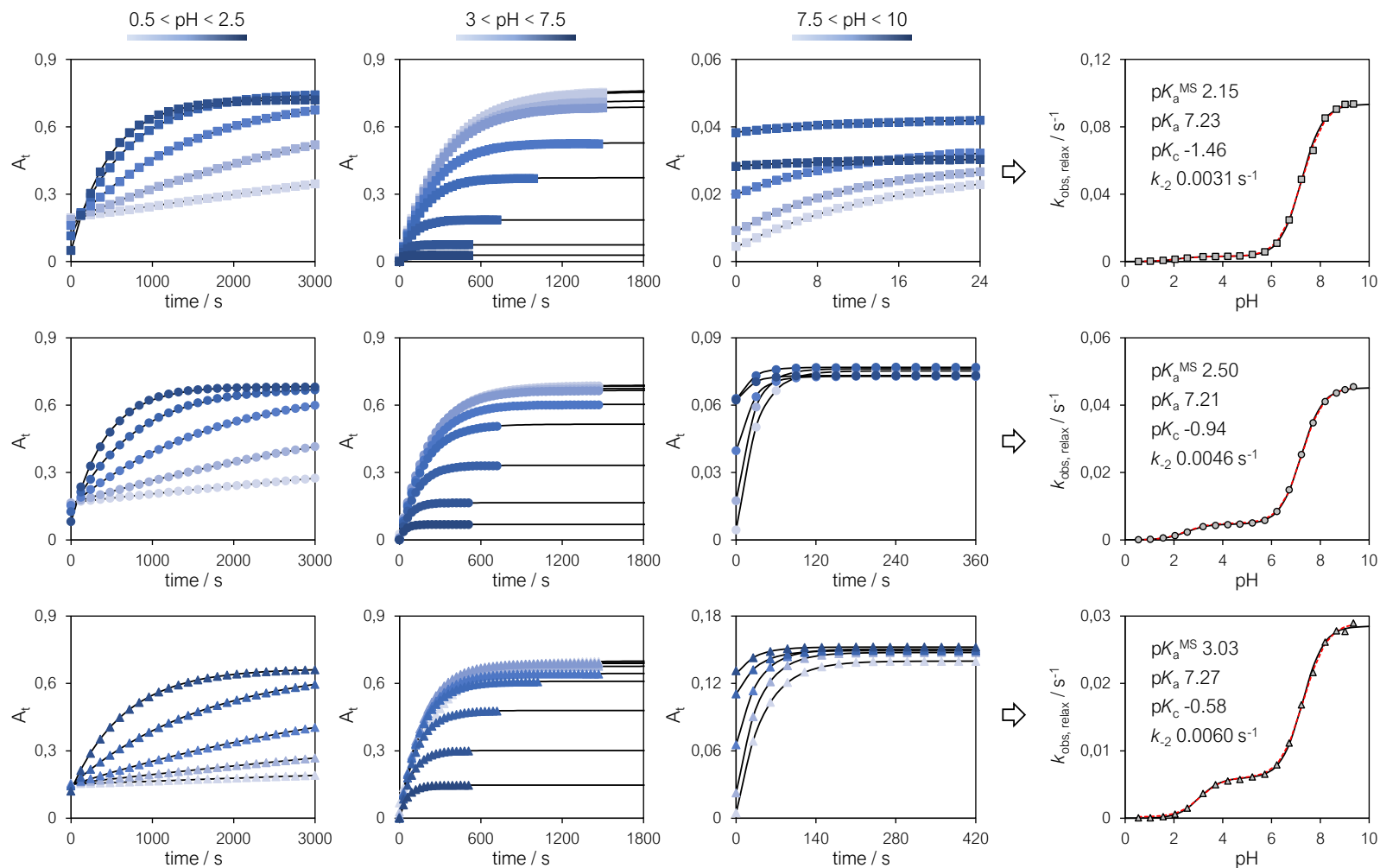
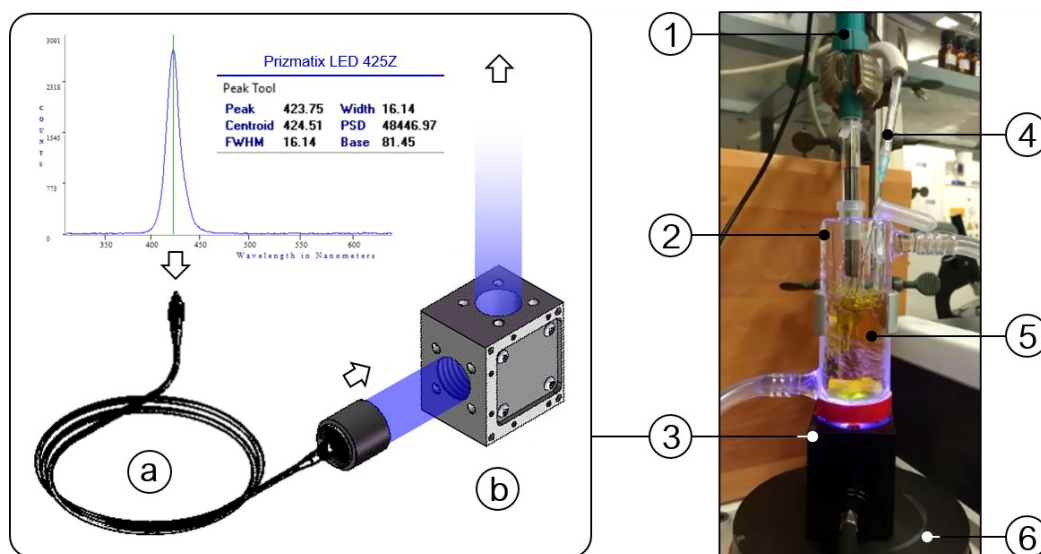


Figure S 3.34. From top to bottom: kinetic profiles for the relaxation of **2** ($n=1$) (■), **1** ($n=2$) (●) and **3** ($n=3$) (▲) at different pH and 25 °C (left), and plots of the obtained apparent pseudo-first order rate constant of relaxation as a function of the pH (right). Solid black lines represents respectively the best fits, whereas dotted red lines represent numerical fitting. The parameters sets listed on the right are those obtained from fitting. Experimental conditions: **[1-3]** = $25 \pm 2 \mu\text{M}$, $[\text{HCl}] = 0.32 \text{ M}$ to 3.2 mM , $[\text{phosphate buffers}] = 20 \text{ mM}$ ($3 < \text{pH} < 10$), $T = 25 \text{ }^\circ\text{C}$; absorption data at 425 nm ($0 < \text{pH} < 7.5$) and 535 nm ($7.5 < \text{pH} < 10$) were collected in the dark right after irradiation (30 s).

3.9.7 pH jumps studies

A saturated solution of **1-3** in aqueous KCl (30 mL, 20 mM)) is prepared by sonication for ca. 10 minutes, while degassing it by gentle N₂ bubbling. Contrary to previous reports⁴, we avoid sonication over prolonged time periods (*e.g.*, overnight) for minimizing hydrolysis. Each experiment is run independently, transferring the resulting solution into a 50-mL jacketed beaker kept at 25 °C, equipped with a 2.5 cm cross-shaped stir bar and mounted above a 45° mirror cage. pH data acquisition is started after 5 minutes of equilibration in the dark and is carried out under stirring (200 rpm) and inert atmosphere (gentle N₂ bubbling) with a pre-calibrated Unitrode Pt1000 glass electrode (Scheme S 3.2).



Scheme S 3.2. Our photochemical apparatus designed for performing pH jump studies. (1) Metrohm Unitrode Pt1000 glass electrode, (2) 50-mL jacketed beaker connected to a thermostat, (3) fiber-coupled LED-light source ending with a 2.5 cm collimator (a) mounted on a 45° mirror cage (b), (4) nitrogen inlet (needle), (5) satd. solution of photoacid equipped with a cross-shaped stir bar and (6) stir plate. During measurements, an aluminum foil is wrapped around the apparatus for preventing the loss of irradiation.

Concomitantly, the concentration of each satd. Solution (S) is determined either from optical readings at pH 3 and ϵ_{MCH} or by quantitative ^1H NMR analysis with dimethyl sulfone as internal standard.

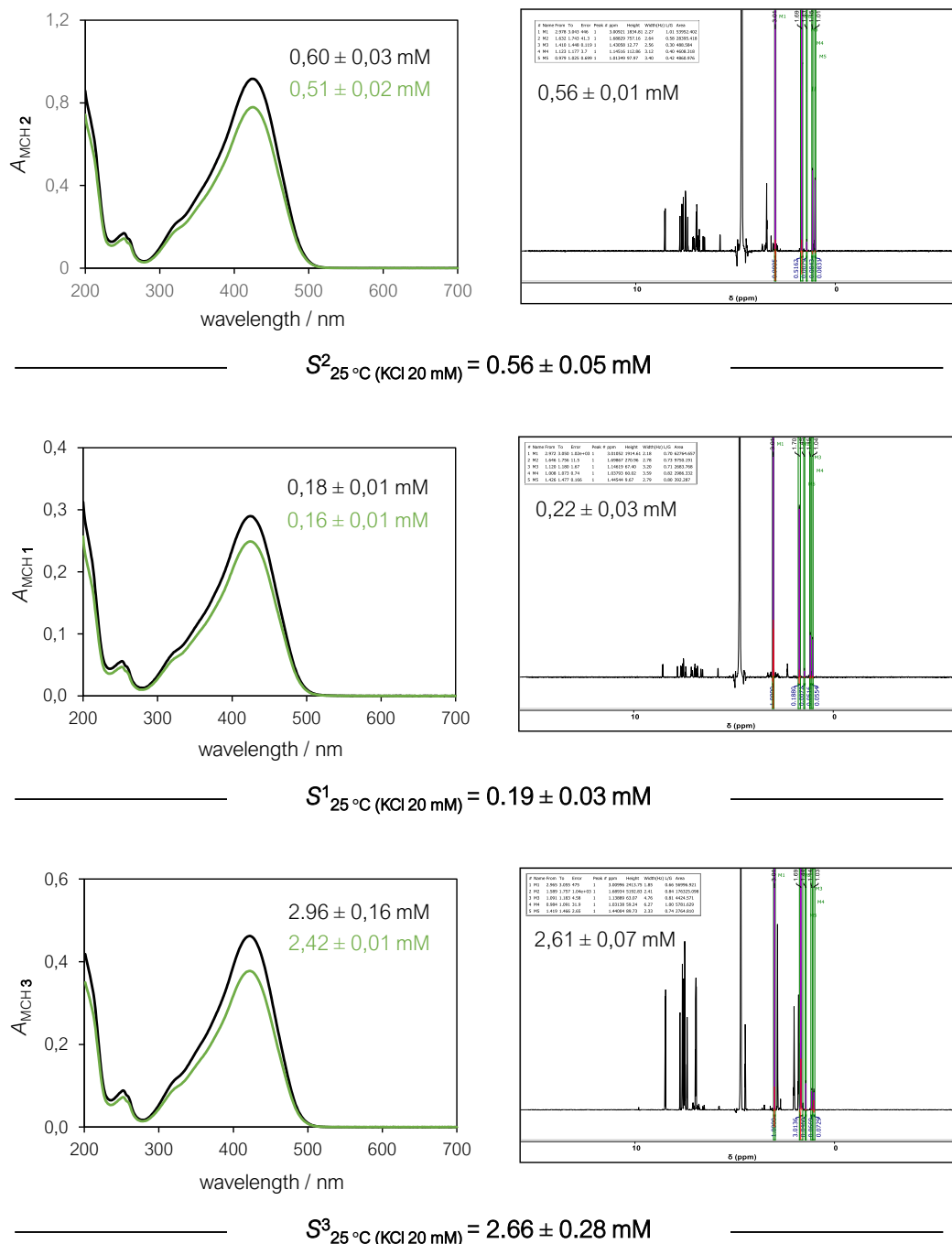


Figure S 3.35.. Left side: spectra recorder at pH 3 and $T = 25^\circ\text{C}$ immediately after sonication (10 min) of excess amount of crystals of **1-3** in aqueous KCl (30 mL, 20 mM); dilution factor is 20, 20 and 200 for **2**, **1** and **3**, respectively. Spectra refer to two independent experiments and each spectrum is the average of three independent acquisitions. Right side: ^1H NMR spectra of the same sample (black UV-Vis traces) with dimethyl sulfone as internal standard (1.2 mM). Each concentration is obtained considering the respective ϵ_{MCH} (Figure S 3.24 and Table S 3.3) or the integral of the internal standard as reference. Solubilities (S) are reported as the average \pm standard deviation of the three data points.

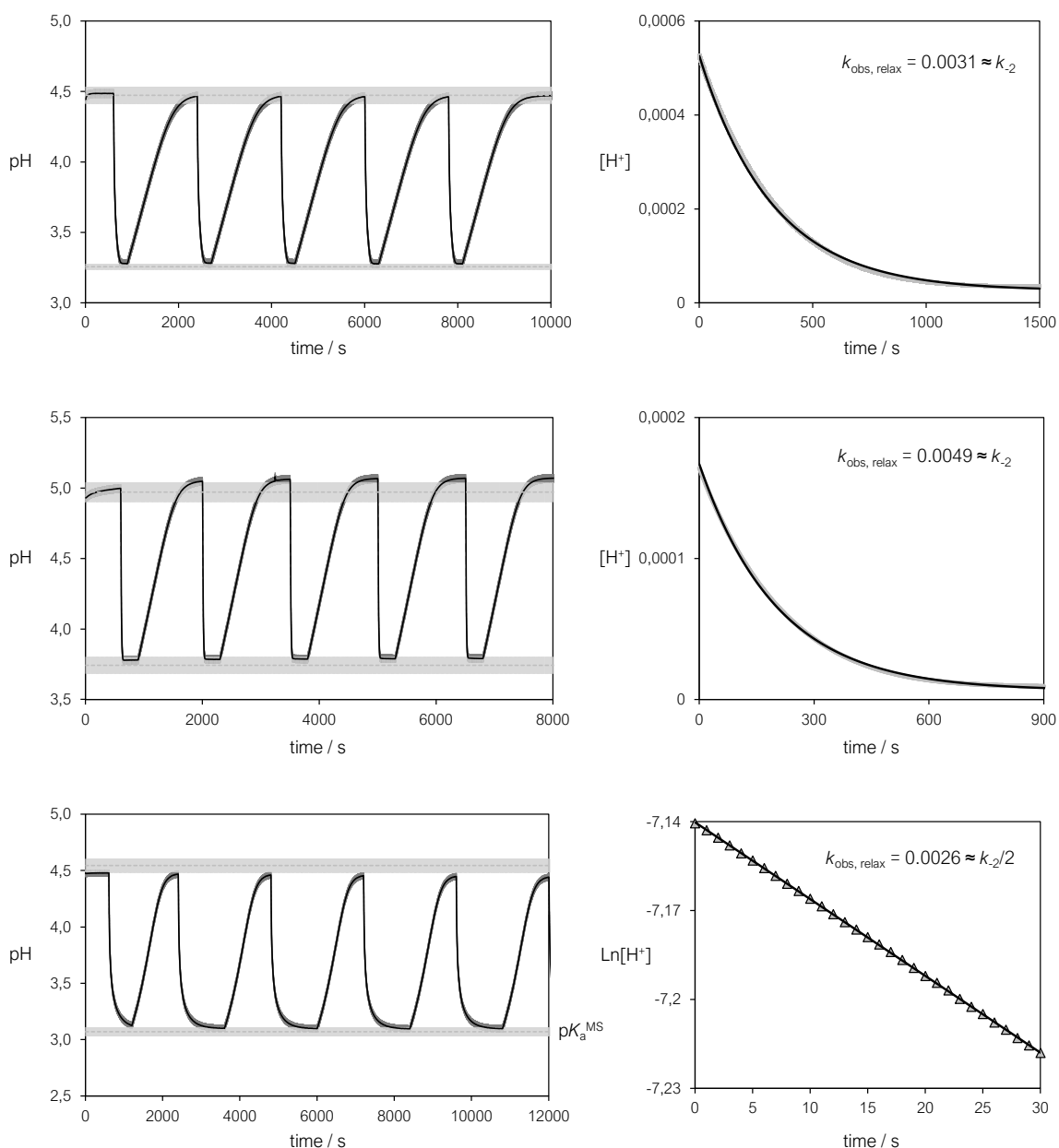


Figure S 3.36. Left side: pH-jump experiments: light irradiation (425 nm, 340 mW) triggers reversible proton release. Upper bounds represents the expected pH values based on the weak acid approximation: $[H^+] = (K_a^{\text{GS}} \cdot S)^{1/2}$, whereas lower bounds are the expected pH values considering full proton dissociation $[H^+] = S$; in the case of compound **3** the lower bound correspond to its pK_a^{MS} . Error on pH readings is ± 0.03 , whereas those associated to each pH bound results from error propagation. In the case of compound **1** we ascribed the observed drift over time to hydrolysis (see Figure S 3.33 and Figure S 3.34); A similar drift was observed previously. Right side: representative profiles of $[H^+]$ recovery in the dark showing good agreement with k_{-2} . Solid black lines represent the best fit to first order rate equation (e.g., Eq. 3.4).

3.9.8 Full model description and fitting

The model

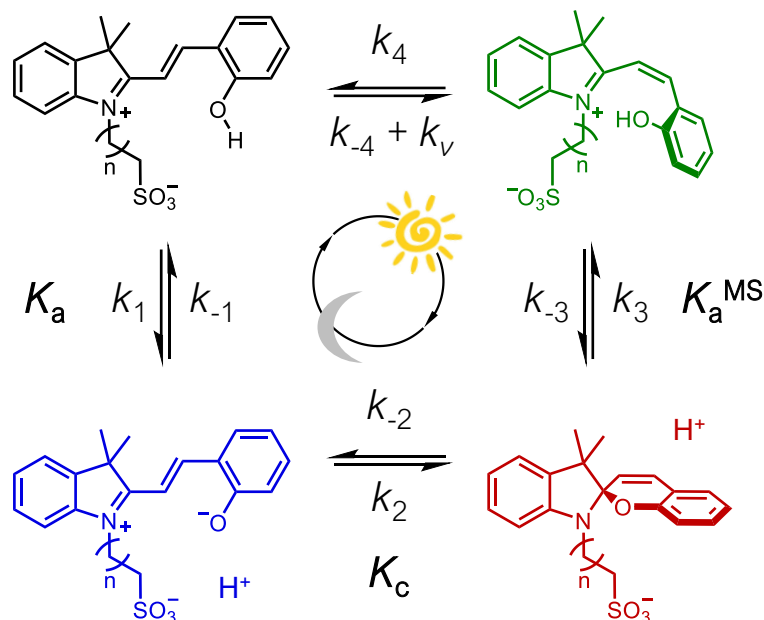
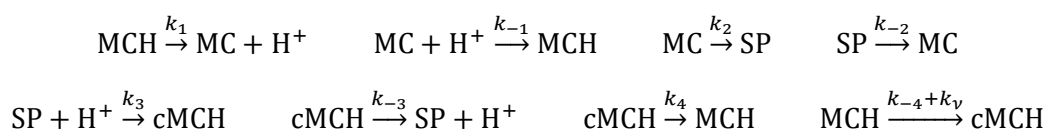


Figure S 3.37. 4-state chemical system with all possible transitions. K_a , K_a^{MS} and K_c are the equilibrium constants between states. The fourth one, not shown, is uniquely determined by thermodynamic equilibrium constraint. The chemical rate from MCH to *cis*-MCH is enhanced upon absorption of light – *i.e.*, $k_v > 0$.

The system can be described in terms of four possible states, each one corresponding to a different chemical species, MCH, SP, MC, and *cis*-MCH. To fully characterize the system, we need to specify all possible chemical transitions:



where cMCH is a short notation for *cis*-MCH, and k_v is the additional term to the rate from MCH to *cis*-MCH which is present only upon light irradiation. We also define the equilibrium constants K_a , K_c and K_a^{MS} as follows:

$$K_a = \frac{k_1}{k_{-1}} = \frac{[\text{MC}]^{eq} [\text{H}^+]^{eq}}{[\text{MCH}]^{eq}} \quad K_c = \frac{k_2}{k_{-2}} = \frac{[\text{SP}]^{eq}}{[\text{MC}]^{eq}} \quad K_a^{MS} = \frac{k_{-3}}{k_3} = \frac{[\text{SP}]^{eq} [\text{H}^+]^{eq}}{[\text{cMCH}]^{eq}}$$

The superscript \cdot^{eq} indicates equilibrium concentrations. The last equality for each line is immediately obtained employing the detailed balance condition. As an additional note, let us remark that we are neglecting the effect of hydrolysis on the time-scale in which all the measures are performed, both with and without *photo-irradiation*. We will later provide more in-depth analysis as an endorsement of this *sufficiently slow* hydrolysis approximation.

3.9.9 Equilibrium condition – “Dark acidity”

When there is no photo-irradiation, $k_v = 0$, and the system relaxes towards an equilibrium state. Thermodynamics imposes a further constraint on the rates of a cycle of reactions, through which we can determine the missing equilibrium constant:

$$\frac{K_a K_c}{K_a^{MS}} \frac{k_4}{k_{-4}} = 1 \quad \Rightarrow \quad K_4 = \frac{k_{-4}}{k_4} = \frac{[\text{cMCH}]^{eq}}{[\text{MCH}]^{eq}} = \frac{K_a K_c}{K_a^{MS}}$$

The quantity of interest in the absence of light is the final pH of the solution, which can be determined from the equilibrium concentration of H^+ . In particular:

$$\text{pH}_{\text{dark}} = \log_{10}([\text{H}^+]^{eq} + [\text{H}^+]_{\text{sol}}) \approx \log_{10}[\text{H}^+]^{eq}$$

where $[\text{H}^+]_{\text{sol}}$ results from autoprotolysis of water, and it is negligible. Moreover, $[\text{H}^+]^{eq}$ can be written in terms of the concentrations of other chemical species at equilibrium (charge balance):

$$[\text{H}^+]^{eq} = [\text{MC}]^{eq} + [\text{SP}]^{eq} = [\text{MC}]^{eq}(1 + K_c)$$

Hence, inverting the relation:

$$[\text{MC}]^{eq} = \frac{[\text{H}^+]^{eq}}{1 + K_c}$$

Using the definition of K_a , we can express $[\text{MCH}]^{eq}$ as a function of $[\text{MC}]^{eq}$ and $[\text{H}^+]^{eq}$:

$$[\text{MCH}]^{eq} = \frac{[\text{MC}]^{eq} [\text{H}^+]^{eq}}{K_a} = \frac{([\text{H}^+]^{eq})^2}{K_a(1 + K_c)}$$

where the last equality has been derived using the expression of $[\text{MC}]^{eq}$ as a function of $[\text{H}^+]^{eq}$. Moreover, making use of K_4 , we can write the total concentration as:

$$C = [\text{MC}] + [\text{SP}] + [\text{MCH}] + [\text{cMCH}] = [\text{H}^+]^{eq} + [\text{MCH}]^{eq}(1 + K_4)$$

We can substitute the definition of $[\text{MCH}]^{eq}$ previously derived, and obtain, after some manipulations:

$$[\text{H}^+]^{eq} = \frac{C - [\text{H}^+]^{eq} K_a(1 + K_c)}{1 + K_4}$$

This is a second-degree equation in $[\text{H}^+]^{eq}$. It admits two solutions, but the only with physical significance is the solution with a positive sign. The latter is:

$$[\text{H}^+]^{eq} = \frac{1}{2(1 + K_4)} \left(-K_a(1 + K_c) + \sqrt{K_a(1 + K_c)} \sqrt{K_a(1 + K_c) + 4C(1 + K_4)} \right)$$

This formula is exact for *sufficiently slow* hydrolysis. However, another notable limit can be performed, which is: $K_a + K_c K_a \ll C$. Employing this latter condition, and noting that $K_4 \approx 0$, we have:

$$[\text{H}^+]^{eq} \approx \sqrt{K_a(1 + K_c)C}$$

This expression leads to the natural introduction of a new variable: $K_a^{GS} = K_a(1 + K_c)$, which appears to be relevant to estimate the dark acidity of the system.

Moreover, adding additional information, we can further distinguish two situations:

- when $K_c \ll 1$, $[H^+]^{eq} \approx \sqrt{K_a C}$, hence $\text{pH}_{dark} = -\log_{10}(\sqrt{K_a C})$. This setting corresponds to a system where $[\text{MC}]^{eq} \gg [\text{SP}]^{eq}$;
- when $K_c \gg 1$, $[H^+]^{eq} \approx \sqrt{K_a K_c C}$, hence $\text{pH}_{dark} = -\log_{10}(\sqrt{K_a K_c C})$. This represents the case in which $[\text{SP}]^{eq} \gg [\text{MC}]^{eq}$;

We remark that usually $K_c \gtrsim 1$ for the system under investigation, hence it is necessary to use K_a^{GS} , rather than only K_a , to estimate the dark acidity.

3.9.10 Relaxation towards equilibrium

Here, we study how the system approaches equilibrium. In particular, we are interested in the apparent rate constant of relaxation, $k_{obs,relax}$, which can also be observed through experiments. We recall that, again, here we are considering the absence of photo-irradiation on the system, hence $k_v = 0$. Let us start from the dynamical equation describing the temporal evolution:

$$\frac{d}{dt} \vec{c}(t) = \hat{W} \vec{c}(t)$$

where $\vec{c} = ([\text{MCH}], [\text{MC}], [\text{SP}], [\text{cMCH}])^T$ is the vector of concentrations, and \hat{W} is the so-called rate matrix:

$$\hat{W} = \begin{pmatrix} -k_1 - k_{-4} & k_{-1}[\text{H}^+] & 0 & k_4 \\ k_1 & -k_{-1}[\text{H}^+] - k_2 & k_{-2} & 0 \\ 0 & k_2 & -k_{-2} - k_3[\text{H}^+] & k_{-3} \\ k_{-4} & 0 & k_3[\text{H}^+] & -k_{-3} - k_4 \end{pmatrix}$$

This equation is nothing but a rate equation for the chemical system in the matricial form.

The rate matrix has the following properties:

- the sum of elements along each column is zero since the dynamics preserves the total concentration;
- \widehat{W} is negative semi-definite, i.e. all its eigenvalues are non-positive;
- since the only stationary state of the dynamics is the equilibrium solution \vec{c}^{eq} , \widehat{W} has only one zero eigenvalue, whose corresponding eigenvector is \vec{c}^{eq} ;
- all other eigenvalues are negative. For the sake of simplicity, we employ the following ordering:

$$0 > \lambda_1([H^+]) > \lambda_2([H^+]) > \lambda_3([H^+])$$

where we have reported explicitly the dependence on $[H^+]$.

The formal solution of the dynamical equation is:

$$\vec{c}(t) = \vec{c}^{eq} + A_1 \vec{c}_1 e^{\lambda_1([H^+])t} + A_2 \vec{c}_2 e^{\lambda_2([H^+])t} + A_3 \vec{c}_3 e^{\lambda_3([H^+])t}$$

Where $\vec{c}_1, \vec{c}_2, \vec{c}_3$ are eigenvectors of \widehat{W} of eigenvalue $\lambda_1, \lambda_2, \lambda_3$ respectively, and A_1, A_2, A_3 are constants determined by initial conditions. Let us analyze all the approximations that can be employed to the general time evolution. The first experimental measure on the system has been performed at $t = t_0 \gg |\lambda_3|^{-1}$, meaning that the third term of the summation is always negligible. Moreover, the initial conditions for all relaxation dynamics are $[SP] \approx C$, i.e. the system populates only one species, with all the others almost unpopulated. In the solution of the rate equation, this initial condition corresponds to:

$$A_2 \approx 0 \quad \text{when } \lambda_1 \gtrsim \lambda_2$$

Since when $\lambda_1 \gg \lambda_2$, the second term in the solution can be also neglected, the dynamics can be always approximated as follows:

$$\vec{c}(t) \approx \vec{c}^{eq} + A_1 \vec{c}_1 e^{\lambda_1([H^+])t}$$

Hence, the estimation for the apparent rate constant of relaxation towards equilibrium is: $k_{obs,relax} = -\lambda_1([H^+])$. It is immediate to see that the *apparent* relaxation rate depends on $[H^+]$, as observed.

3.9.11 (Sufficiently slow) Hydrolysis

Let us imagine to observe the chemical system at the timescale in which the effect of hydrolysis becomes relevant. Henceforth, the 4-state model depicted in Figure S 3.37 cannot be intended as a closed system anymore. In order to keep track of the hydrolysis explicitly, we add the following reactions to the model:



where X is an intermediate state, which transforms into the hydrolyzed state:



Considering water autoprotolysis, we estimate $[\text{OH}^-] = 10^{-14}/[\text{H}^+]$. As a consequence, the following constraint on rate constants has to be satisfied:

$$\frac{k_w}{k_{-w}} \frac{k_{-OH}}{k_{OH}} = \frac{[\text{X}]^{eq} [\text{H}^+]^{eq}}{[\text{MCH}]^{eq}} \frac{[\text{MCH}]^{eq} [\text{OH}^-]^{eq}}{[\text{X}]^{eq}} = [\text{H}^+]^{eq} [\text{OH}^-]^{eq} = 10^{-14}$$

Another consistency constraint is that k_{-h} has to be considerably small. However, since $k_h \gg k_{-h}$, in order to preserve microscopic reversibility, we cannot just set k_{-h} equal to zero. A sanity check will be to verify that $k_{-h} \ll k_h$ after the fit. Moreover, it is

also true that $k_{OH} \gg k_{-h}$, a condition to be controlled a posteriori. Note that, for the sake of simplicity, we ignored the hydrolysis from *cis*-MCH since $[cMCH]^{eq} \ll [MCH]^{eq}$ in all experimental settings (pH > 3 and dark condition). The most general approach to find a characteristic rate of a system is to study the eigenvalues of the rate matrix, as we did before. Here, we start again from the dynamical equation of the complete 6-state system:

$$\frac{d}{dt} \vec{c}_h(t) = \widehat{W}_h \vec{c}_h(t)$$

where $\vec{c}_h = ([MCH], [MC], [SP], [cMCH], [X], [HP])$ is the vector of concentrations of the chemical species involved. Hence, the rate matrix \widehat{W}_h is:

$$\widehat{W}_h = \begin{pmatrix} -k_1 - k_{-4} - k_w - k_{OH}[OH^-] & k_{-1}[H^+] & 0 & k_4 & k_{-w}[H^+] + k_{-OH} & 0 \\ k_1 & -k_{-1}[H^+] - k_2 & k_{-2} & 0 & 0 & 0 \\ 0 & k_2 & -k_{-2} - k_3[H^+] & k_{-3} & 0 & 0 \\ k_{-4} & 0 & k_3[H^+] & -k_{-3} - k_4 & 0 & 0 \\ k_w + k_{OH}[OH^-] & 0 & 0 & 0 & -k_{-w}[H^+] - k_{-OH} - k_h & k_{-h} \\ 0 & 0 & 0 & 0 & k_h & -k_{-h} \end{pmatrix}$$

The biggest non-zero eigenvalue of \widehat{W}_h , that we name λ_{hyd} , characterizes the *apparent rate constant* of the slowest process in play. We claim, in analogy to what we presented in Section 3, that the observed rate of hydrolysis $k_{obs,hydr} = -\lambda_{hydr}([H^+])$.

Interestingly, we also obtain that the second biggest non-zero eigenvalue of the rate matrix is exactly equal to $-k_{obs,relax}$ (what we named λ_1 in Section 3). This means that the relaxation rate towards equilibrium is the second slowest process taking place in the system.

3.9.12 Non-equilibrium conditions – Photo-irradiation

Let us consider the case in which the system absorbs light, thus enhancing the transition rate from MCH to *cis*-MCH, *i.e.*, $k_v > 0$. As a consequence, the acidity of the system will increase, since *cis*-MCH can release H^+ , *i.e.*, $pK_a^{MS} < pK_a^{GS}$. This corresponds to a significant decrease in the pH at stationarity. Unfortunately, closed analytical form are lengthy and cumbersome for non-equilibrium conditions, since the stationary concentrations cannot be expressed only in terms of equilibrium constants, as for the equilibrium case. In other words, the steady-state of the system is influenced by all transition rates, not just their ratios.

3.9.13 Light absorption – Quantum yield

In this section, we investigate the efficiency of the system in absorbing photons to transform molecules. The net result of this process is the release of $[H^+]$ ions in the solution, increasing the acidity. A measure of this efficiency is the quantum yield namely the probability that 1 molecule transforms when hit by 1 photon. It is worth noting that, by definition, the quantum yield, indicated as Φ , depends only on the type of molecule involved in the experiment. To provide a theoretical estimation of the quantum yield, we start with two hypotheses:

- the system is well-mixed, since the experiments upon photo-irradiation are performed while rapidly stirring the solution (see above);
- all photons are absorbed. As long as the molecules are much more abundant than photons in a given time-interval Δt this can be considered a good approximation. The optical path length of our apparatus is ca. 6 cm for a volume, V , of 30 mL.

The number of molecules in the solution, N , is:

$$N = C V N_A$$

where C is the molar concentration, V is the volume of the solution and N_A is the Avogadro's number. Let us consider a small time-interval Δt . The total number of photons hitting the system in this time-interval, P , is estimated by dividing the energy of the LED-light source by the energy of a single photon:

$$P = \frac{W}{h\nu} \Delta t = \frac{W\lambda}{hc} \Delta t = N_\lambda \Delta t$$

where W , ν and λ are power, frequency and wavelength of the LED-light source, respectively, h is the Planck's constant and N_λ is the photon flux. By definition, the probability that 1 molecule transforms when hit by 1 photon is Φ . Hence, when hit by n photons, the probability of transformation is:

$$T(n) = 1 - (1 - \Phi)^n$$

Moreover, the probability for 1 molecule to be hit by n photons is:

$$p(n) = \frac{(N-1)^{P-n}}{N^P} \binom{P}{n}$$

that is the number of ways n photons among P can be selected, times the probability to hit 1 selected molecule among N , times the probability that $(P-n)$ photons do not hit this same molecule, but one of the remaining $N-1$. Notice that the number of photons is the one emitted in a time-interval Δt . Putting all these things together, the probability that 1 molecule transforms, in a small time-interval Δt , due to the interaction with photons is:

$$K = \sum_{n=0}^P p(n)T(n) = \sum_{n=0}^P \frac{(N-1)^{P-n}}{N^P} \binom{P}{n} (1 - (1 - \Phi)^n) = 1 - \frac{1}{N^P} \sum_{n=0}^P \binom{P}{n} (N-1)^{P-n} (1 - \Phi)^n$$

By using the binomial theorem, we obtain:

$$K = 1 - \left(\frac{N - \Phi}{N} \right)^P$$

However, from the rate equation, we know that the probability that 1 molecule transforms upon photo-irradiation, in an interval Δt , is $k_v \Delta t$. Hence, we have:

$$k_v \Delta t = 1 - \left(\frac{N - \Phi}{N} \right)^{N_\lambda \Delta t}$$

By solving this equation for Φ , we have:

$$\Phi = N(1 - (1 - k_v \Delta t)^{N_\lambda \Delta t})$$

Since we want a time-independent estimation of the quantum yield, we compute its instantaneous value by performing the limit $\Delta t \rightarrow 0$. This results in:

$$\Phi = N(1 - e^{-N_\lambda k_v})$$

The formula derived above is correct. However, we notice that in our settings $N_\lambda \approx 10^{17}$ and $N \approx 10^{19}$. We introduce a new parameter $R = N/N_\lambda$, which is of order 10^2 , and perform the limit $W \rightarrow +\infty$. This leads to the following approximate expression for the quantum yield:

$$\Phi \cong R k_v = \frac{N}{N_\lambda} k_v$$

We remark that k_v is a rate, while R has the dimension of time so that Φ is a dimensionless parameter. It is worth pointing out that k_v scales almost linearly with W and so N_λ , thus the quantum yield is approximately constant for all the powers experimentally tested (see Tables 7-9).

3.9.14 Comparison between data and theory – Fixed power experiments

The experiments are carried out for three different photoacids, namely compounds **1**-

3. For each species, we collect the following data:

- apparent rate constant of hydrolysis for different values of pH, $k_{\text{obs, hydr}}$ vs pH;
- apparent rate constant of relaxation for different values of pH, $k_{\text{obs, relax}}$ vs pH (;
- dynamical evolution from equilibrium conditions to photo-stationarity, under photo-irradiation with fixed power and frequency, pH jump. The system relaxes back to equilibrium once that the light is turned off.

We associate to each dataset a *loss function* L that quantifies how far is the model from representing the data:

$$L(\vec{x}) = \sqrt{\frac{1}{N_{\text{data}}} \sum_{i \in \text{dataset}} \frac{(x_i^{(\text{model})} - x_i^{(\text{data})})^2}{\epsilon_i^{(\text{data})}}}$$

where $x_i^{(\text{model})}$ is the value of the variable x in the point i predicted by the model, while $x_i^{(\text{data})}$ is the one contained in the data. The whole set $\vec{x}^{(\text{model})}$ represents the theoretical curve for the dataset $\vec{x}^{(\text{data})}$. The experimental error is indicated as $\epsilon_i^{(\text{data})}$, and N_{data} is the number of experimental points. The loss function is nothing but the root-mean-square deviation (RMSD) divided by the error on each measure. For the sake of clarity, we denote as L_j , L_r and L_h the loss functions associated respectively to the following datasets: dynamical evolution, apparent rate of relaxation, and

apparent rate of hydrolysis. We fit the model parameters for each species by simultaneously minimizing the *loss function* associated with each dataset, L_j, L_r and L_h . Whenever two independent experiments are available, we take the average loss between the individual experiments. We remark that a successful simultaneous minimization implies that the theoretical model is compatible with all observations.

Here, we provide details of the numerical fitting procedure.

- We compute the dynamical evolution predicted by the model by numerically integrating the rate equation using Runge-Kutta's fourth-order algorithm. Since the experiments span a relatively short time-frame when compared to the hydrolysis timescale, we employ the 4-state model introduced above, i.e. neglecting the effects of hydrolysis.
 - We assume that the initial condition of the dynamics corresponds to the equilibrium solution.
- The apparent rate of relaxation towards equilibrium, k_{obs} , is numerically computed from the largest non-zero eigenvalue of the rate matrix, $\lambda_1([H^+])$, as explained above.
- In order to estimate the apparent rate of hydrolysis, $k_{obs,hyd}$, we extend the model to include the states X and HP, as detailed in Section 4. Then, we numerically compute the largest non-zero eigenvalue of the 6-state transition matrix \widehat{W}_h , λ_{hyd} , since it is equal to $-k_{obs,hyd}$.
 - This 6-state model is similar to the one introduced by Jencks et al. [ref] to study hydrolysis.

The minimization of each loss function is performed by running 100 independent Nelder-Mead procedures with slightly different initial parameters. Then, we refine the

best minima obtained by using lbfgsb-f minimization algorithm. All model parameters and initial concentrations are kept free to vary during the optimization, with the following exceptions:

- parameters and concentrations for which an experimental measure is provided are soft-constrained. We define a loss function L_{th} quantifying the discrepancy between fitted and experimental values. The latter has the same form defined above, and it is minimized along with the others during the optimization process.

Errors on estimated parameters and predicted theoretical curves are computed by running a Metropolis Monte-Carlo simulation, starting from the optimized parameters, and using the sum of all loss functions as the energy of the system. This allows us to explore the whole space of values for all parameters, provided that they are compatible with experimental data. We extract the 16th and 84th percentile of the resulting distribution of each parameter and build the predictions associated to those values for the theoretical curves. Then, we use the average over the whole dataset of the difference between the maximum and the minimum value for each point (or parameter) as an estimation of the error.

Below, we present the result of the simultaneous fitting procedure for all species. We report the predicted theoretical value and the experimental one, if available, along with the deviation between the two, σ . The latter is an indicator of the distance between predicted and experimental values, weighted by the experimental error associated with the measure:

$$\sigma_Y = \frac{Y^{(model)} - Y^{(data)}}{\varepsilon_Y^{(data)}}$$

where $Y^{(model)}$ and $Y^{(data)}$ are respectively predicted and measured values of the model parameter Y , while $\varepsilon_Y^{(data)}$ is the experimental error.

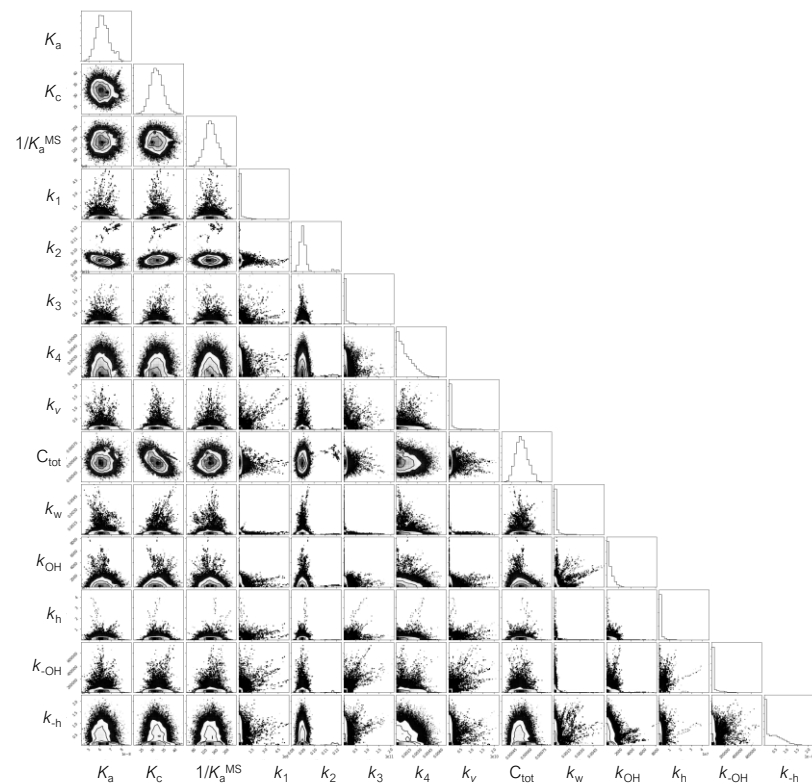
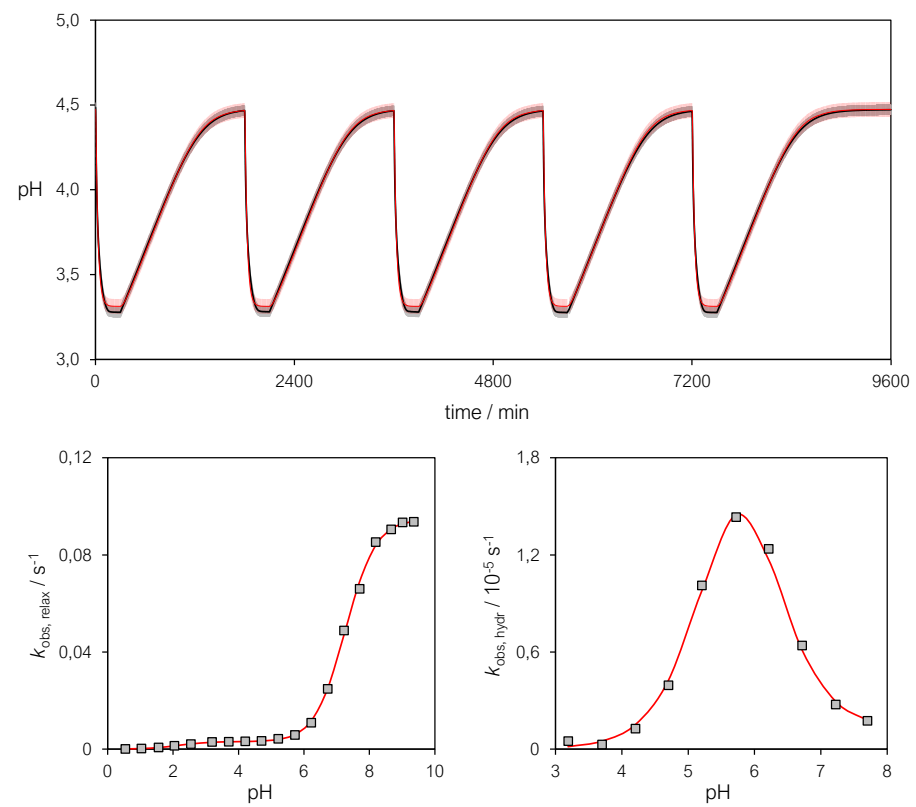


Figure S 3.38. Combined data fit and Monte-Carlo histograms obtained for compound 2 ($n = 1$).

Table S 3.5. Fitted parameters for compound 2 ($n = 1$).

Parameter	Predicted value	Experimental value ^a	Deviation (σ)
C	0.000609 M	0.000601 M (UV)	0.13
pK_a	7.19	7.23	0.8
pK_c	-1.47	-1.48	0.3
pK_a^{MS}	2.14	2.14	0
$k_1 (s^{-1})$	0.34	n/a	n/a
$k_2 (s^{-1})$	0.092	0.089	0.33
$k_3 (M^{-1}s^{-1})$	3.52	n/a	n/a
$k_4 (s^{-1})$	4.9×10^{-5}	n/a	n/a
$k_v (s^{-1})$	0.049	n/a	n/a
$k_{OH} (M^{-1}s^{-1})$	229.76	193 ^b	ok ^b
$k_{-OH} (s^{-1})$	1.9×10^{-5}	n/a	n/a
$k_h (s^{-1})$	0.00084	n/a	n/a
$k_{-h} (s^{-1})$	3.3×10^{-11}	n/a	n/a
$k_w (s^{-1})$	6.8×10^{-5}	7.1×10^{-5} ^b	ok ^b
$k_{-w} (M^{-1}s^{-1})$	566.23	n/a	n/a
$k_{-w}/k_h (M^{-1})$	674083	745139 ^b	ok ^b
pH _{dark}	4.47	4.47	0
pH _{light}	3.31	3.28	1
Φ	0.74	n/a	n/a

- a. the values of the equilibrium constants are the average obtained considering both ¹H NMR and UV-Vis data, that of k_2 results from both equilibration and relaxation studies
- b. kinetic constants for hydrolysis are optimized esteems resulting from fitting, so checked for the order of magnitude to be consistent.

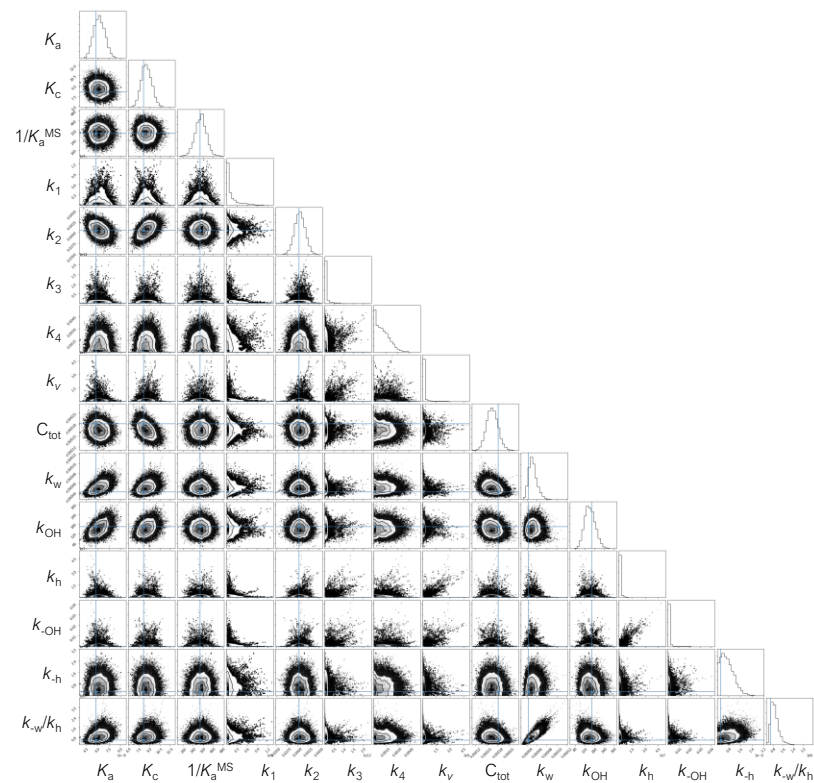
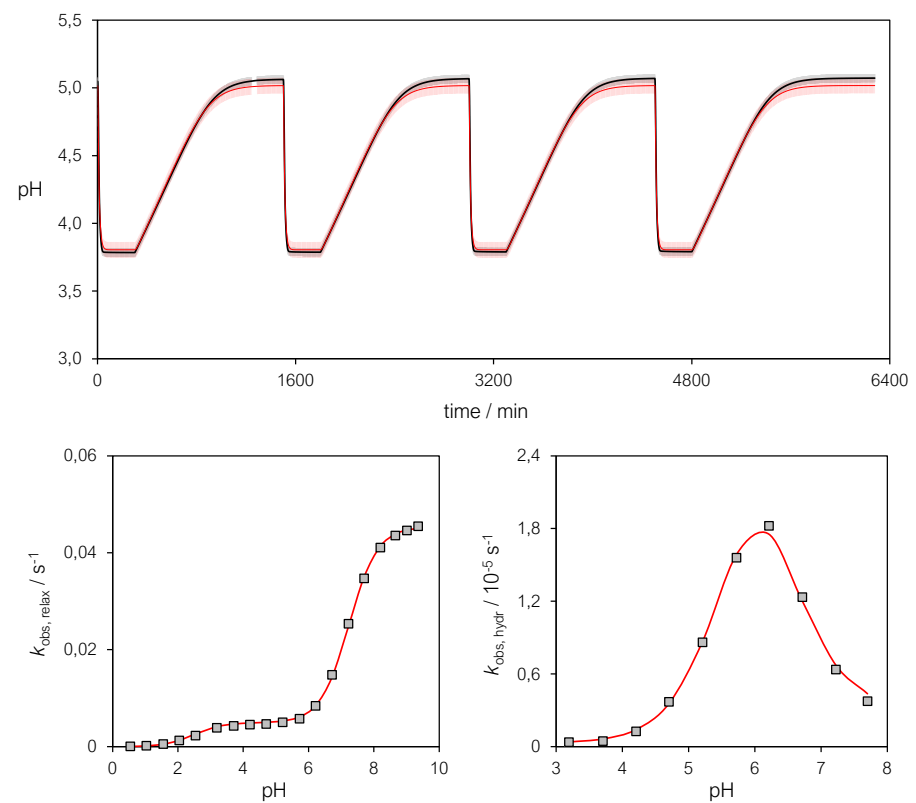


Figure S 3.39. Combined data fit and Monte-Carlo histograms obtained for compound 1 ($n = 2$).

Table S 3.6. Fitted parameters for compound 1 ($n = 2$).

Parameter	Predicted value	Experimental value ^a	Deviation (σ)
C	0.000181 M	0.000181 M (UV)	0
pK_a	7.23	7.20	0.6
pK_c	-0.91	-0.96	0.6
pK_a^{MS}	2.47	2.47	0
$k_1 (s^{-1})$	5.59	n/a	n/a
$k_2 (s^{-1})$	0.040	0.039	0.26
$k_3 (M^{-1}s^{-1})$	25.67	n/a	n/a
$k_4 (s^{-1})$	5.2×10^{-8}	n/a	n/a
$k_v (s^{-1})$	0.092	n/a	n/a
$k_{OH} (M^{-1}s^{-1})$	163.09	155 ^b	ok ^b
$k_{-OH} (s^{-1})$	7.2×10^{-6}	n/a	n/a
$k_h (s^{-1})$	0.00033	n/a	n/a
$k_{-h} (s^{-1})$	2.6×10^{-7}	n/a	n/a
$k_w (s^{-1})$	4.3×10^{-5}	5.1×10^{-5b}	ok ^b
$k_{-w} (M^{-1}s^{-1})$	191.15	n/a	n/a
$k_{-w}/k_h (M^{-1})$	579242	752280 ^b	ok ^b
pH_{dark}	5.02	5.05	1
pH_{light}	3.80	3.79	0.33
Φ	0.41	n/a	n/a

- a. the values of the equilibrium constants are the average obtained considering both ¹H NMR and UV-Vis data, that of k_2 results from both equilibration and relaxation studies
- b. kinetic constants for hydrolysis are optimized esteems resulting from fitting, so checked for the order of magnitude to be consistent.

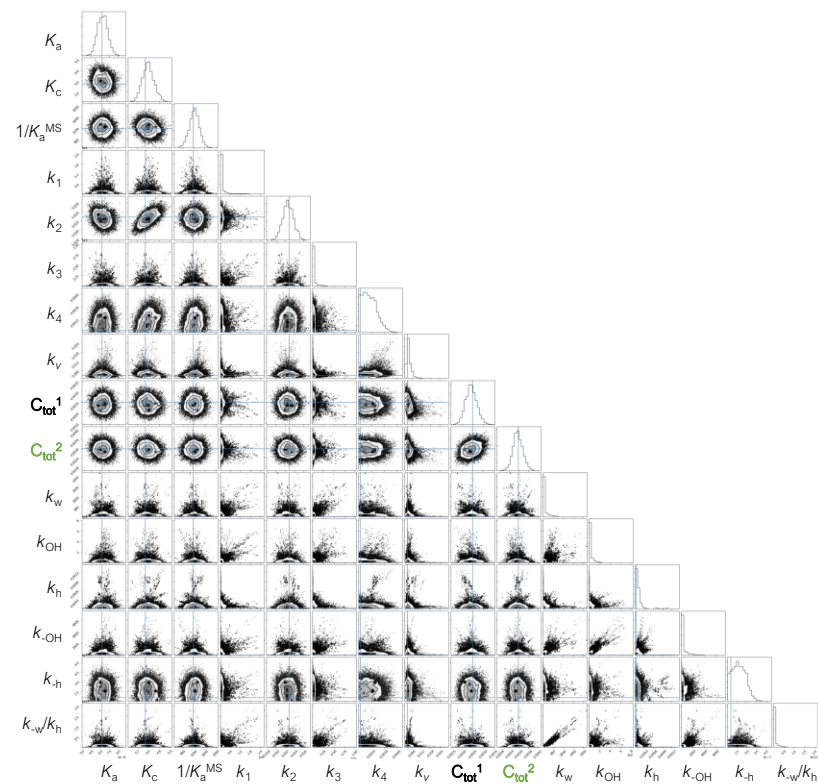
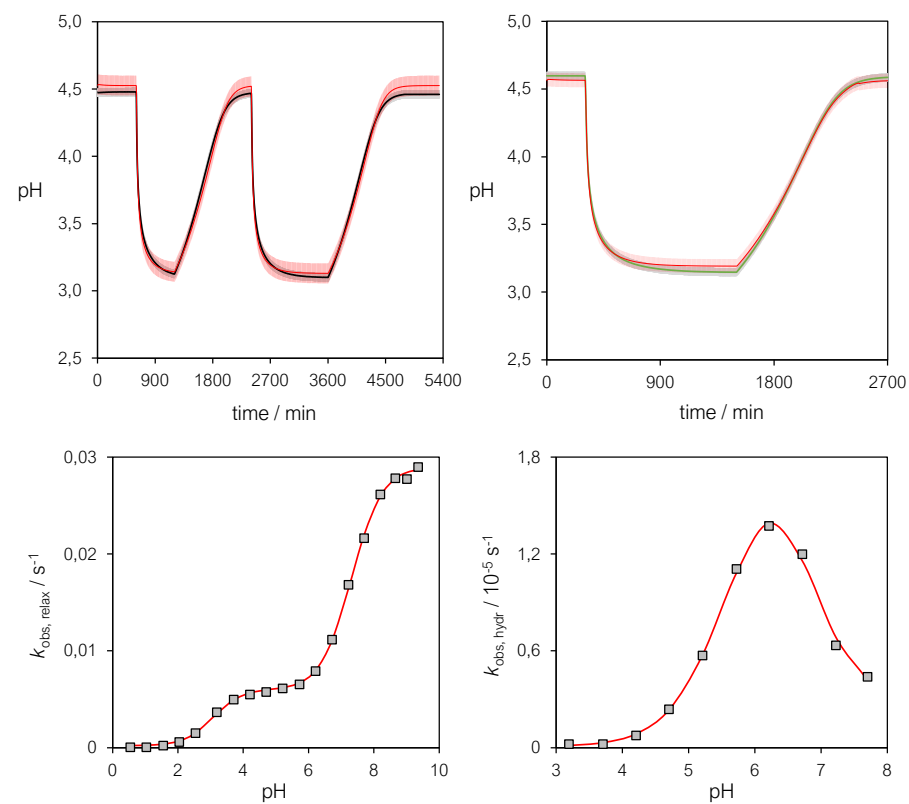


Figure S 3.40. Combined data fit and Monte-Carlo histograms obtained for compound **3** ($n = 3$).

Table S 3.7. Fitted parameters for compound 3 ($n = 3$).

In this case the fit is performed using the dynamical evolution of two experiments, with different concentrations. We denoted them as $C^{(1)}$ and $C^{(2)}$ in the table below. Notice that, since the value of pH_{dark} and pH_{light} depends on the concentrations, we report the number of the experiments which they refer to with an apex, i.e. $\text{pH}_{\text{dark/light}}^{(1)}$ and $\text{pH}_{\text{dark/light}}^{(2)}$. A similar notation is also adopted for the quantum yield. Note that, despite $\Phi^{(1)}$ and $\Phi^{(2)}$ should be equal, they are influenced by the slight difference between the predicted concentrations of the two experiments.

Parameter	Predicted value	Experimental value ^a	Deviation (σ)
$C^{(1)}$	0.00250 M	n/a	n/a
$C^{(2)}$	0.00297 M	0.00296 M (UV)	0.034
$\text{p}K_a$	7.2	7.25	1
$\text{p}K_c$	-0.58	-0.59	0.2
$\text{p}K_a^{MS}$	3.07	3.07	0
$k_1 (s^{-1})$	0.078	n/a	n/a
$k_2 (s^{-1})$	0.023	0.022	0.45
$k_3 (M^{-1}s^{-1})$	208.49	n/a	n/a
$k_4 (s^{-1})$	0.00021	n/a	n/a
$k_v (s^{-1})$	0.0030	n/a	n/a
$k_{OH} (M^{-1}s^{-1})$	79.43	71 ^b	ok ^b
$k_{-OH} (s^{-1})$	5.6×10^{-7}	n/a	n/a
$k_h (s^{-1})$	4.3×10^{-5}	n/a	n/a
$k_{-h} (s^{-1})$	5.2×10^{-8}	n/a	n/a
$k_w (s^{-1})$	3.2×10^{-5}	2.6×10^{-5} ^b	ok ^b
$k_{-w} (M^{-1}s^{-1})$	25.12	n/a	n/a
$k_{-w}/k_h (M^{-1})$	584186	569351 ^b	ok ^b
$\text{pH}_{\text{dark}}^{(1)}$	4.56	4.58	0.67
$\text{pH}_{\text{light}}^{(1)}$	3.19	3.15	1.33
$\text{pH}_{\text{dark}}^{(2)}$	4.53	4.47	2
$\text{pH}_{\text{light}}^{(2)}$	3.13	3.10	1
$\Phi^{(1)}$	0.19	n/a	n/a
$\Phi^{(2)}$	0.22	n/a	n/a

- a. the values of the equilibrium constants are the average obtained considering both ¹H NMR and UV-Vis data, that of k_2 results from both equilibration and relaxation studies
- b. kinetic constants for hydrolysis are optimized esteems resulting from fitting, so checked for the order of magnitude to be consistent.

3.9.15 Comparison between data and theory – Variable power experiments

The dynamical evolution until photo-stationarity, with consequent relaxation to the equilibrium state, is experimentally performed for every species ($n = 1, 2$ and 3), under photo-irradiation with the same frequency as above, but variable power. We fit the data with the theoretical 4-state model (neglecting the effect of hydrolysis), predicting how the value of k_v changes as a function of the power (Figure S 3.41). Quantum yields are obtained as the trimmed mean of all the values (discharging the minimum and the maximum values – highlighted in red. Table S 3.8 - Table S 3.10).

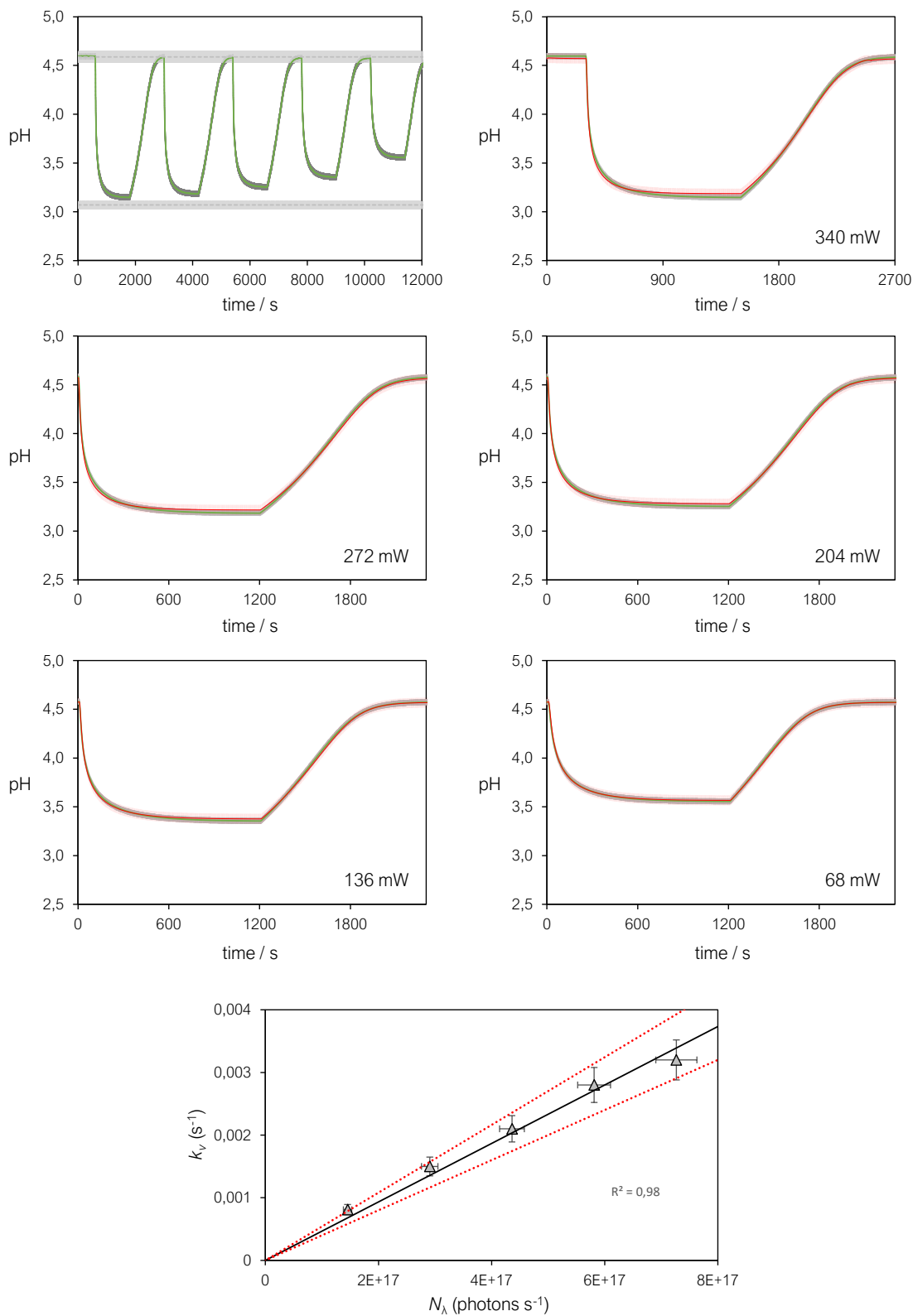


Figure S 3.41. Representative variable-power pH jump experiment obtained with compound **3** ($n = 3$). The upper and lower bounds on the top left graph are obtained as described in Figure S21. Solid red lines represent the best fit to the 4-state model from which k_v values are obtained. Bottom: plot of the obtained values of k_v against the photon flux. Similar graphs were obtained for all compounds, see the following table as summary.

Table S 3.8. Fitted parameters for compound 2 ($n = 1$) - variable power experiments

W (mW)	k_v (s^{-1})	C (mM)	Φ
340 ± 17	0.049	0.61	0.74
340 ± 17	0.053	0.49	0.65
272 ± 14	0.049	0.49	0.75
204 ± 10	0.046	0.49	0.93
136 ± 7	0.025	0.49	0.76
68 ± 3	0.011	0.49	0.67
Average Φ	n/a	n/a	0.73 ± 0.09

Table S 3.9. Fitted parameters for compound 1 ($n = 2$) - variable power experiments

In the case of compound **2** we observed a much more pronounced effect of hydrolysis with respect to other species, which results in an effective decrease of the fitted concentration with time. Since the power is changed as a function of time, lower values of power correspond to longer times and, consequently, slightly lower concentrations.

W (mW)	k_v (s^{-1})	C (mM)	Φ
340 ± 17	0.092	0.181	0.41
340 ± 17	0.088	0.159	0.34
272 ± 14	0.072	0.153	0.34
204 ± 10	0.064	0.148	0.39
136 ± 7	0.041	0.142	0.36
68 ± 3	0.023	0.136	0.39
Average Φ	n/a	n/a	0.37 ± 0.04

Table S 3.10. Fitted parameters for compound 3 ($n = 3$) - variable power experiments

W (mW)	k_v (s^{-1})	C (mM)	Φ
340 ± 17	3.0×10^{-3}	2.97	0.22
340 ± 17	3.2×10^{-3}	2.41	0.19
272 ± 14	2.8×10^{-3}	2.41	0.21
204 ± 10	2.1×10^{-3}	2.41	0.21
136 ± 7	1.5×10^{-3}	2.41	0.22
68 ± 3	8.1×10^{-4}	2.41	0.24
Average Φ	n/a	n/a	0.22 ± 0.03

3.9.16 pH jumps after partial neutralization with NaHCO_3

For compound **3**, which is the most soluble in water, we measured the dynamical evolution of the system upon photo-irradiation, with the consequent relaxation (*i.e.* pH jumps), after the neutralization of the solution with a molar concentration of NaHCO_3 equal to 0.25 (Figure S 3.42). We verified that the model predicts the same experimental curves. The error on each point of the curve is estimated, as explained above, from the 16th and 84th percentile of the parameter distribution: in this case, we consider an error of 2% only on C and $[\text{NaHCO}_3]$, keeping all the other parameters fixed to their fitted values (Table S 3.7).

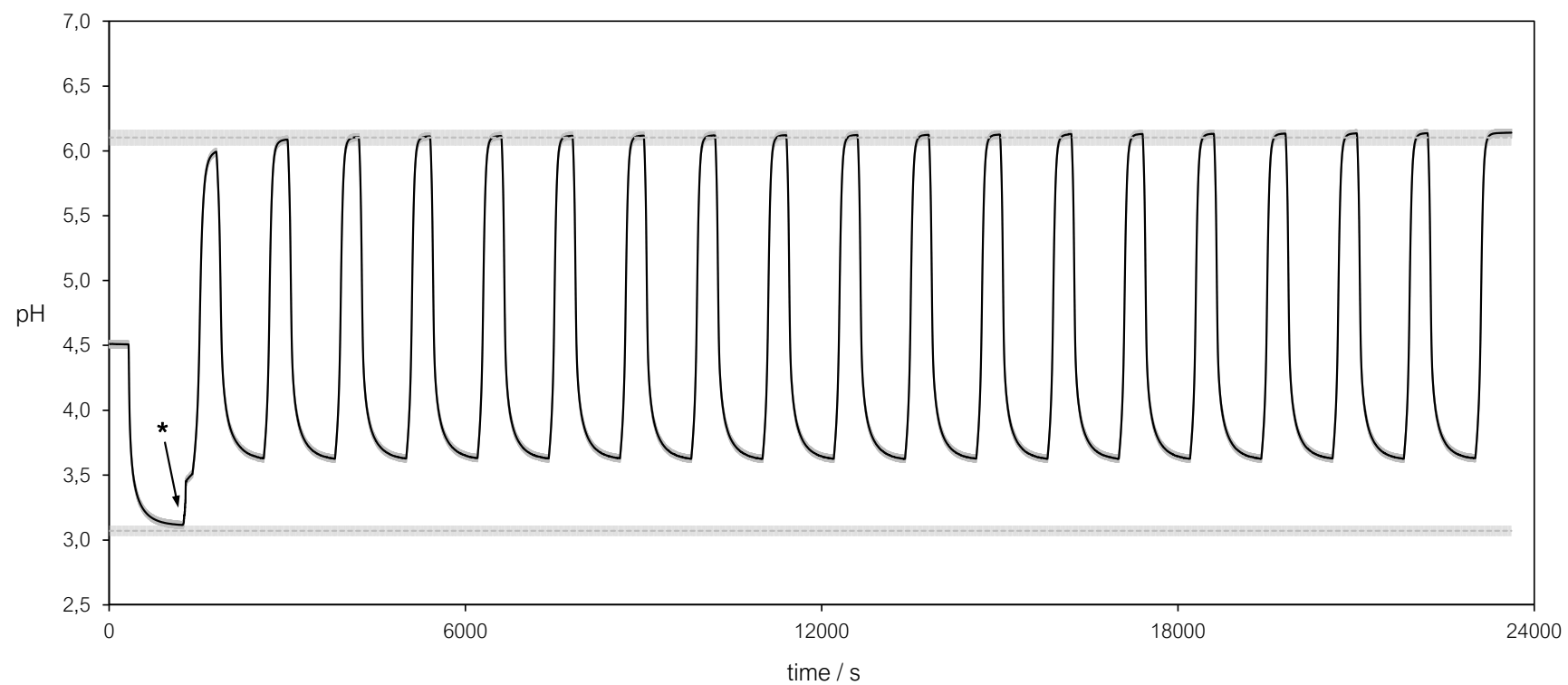


Figure S 3.42. Full dynamic of proton release/uptake obtained buffering compound **3** ($n = 3$) with *in situ* (*) addition of NaHCO₃ (0.25-2.6 mM). Upper and lower bounds are obtained as described in Figure S 3.36.

Chapter 4

The effect of temperature on the photoacidity of merocyanine photoacids in water

Parts of this chapter have been taken from:

V. J. Périllat, C. Berton, C. Pezzato, *Materials Today Chemistry*, **2022**, 25, 100918

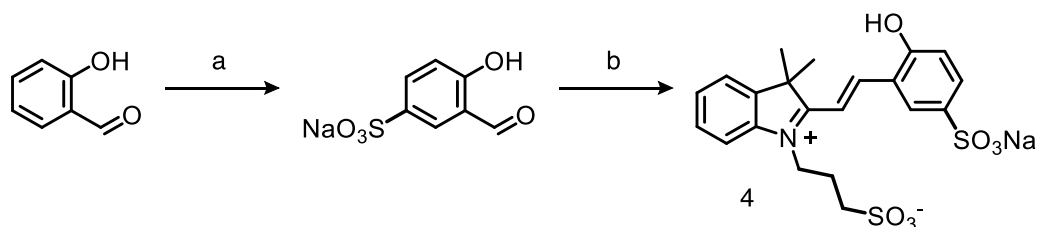
4.1 Introduction

In the context of molecular switches, temperature-dependent behaviors have extensively studied for spiropyrans^[19,83,103,104], diarylethenes^[105–108], azobenzenes^[109–111] and hydrazones.^[62,112] The effect of temperature on BIPS photoacidity in aqueous environments, however, has not yet been explored. Studying the effects of temperature of merocyanine photoacids is difficult due to their tendency to hydrolyze^[66,86,87,87,113] irreversibly, which limits the shelf-life of the samples and, at the same time, alters the equilibria taking place in solution, thus making the system dynamic and tricky to analyze. The scope of the following chapter is to prepare a biocompatible and highly water-soluble merocyanine photoacid with the aim of expanding our analytical protocols towards the accurate characterization of BIPS photoacidity as a function of the temperature.

4.2 Room temperature chemistry

Compound **4** has been prepared following literature procedures^[47] by sulfonation of salicylaldehyde followed by careful neutralization to the sodium sulfonate salt. This is

then refluxed in ethanol with the indolium propylsulfonate salt yielding the final photoswitch as an orange solid. This was characterized by ^1H , ^{13}C NMR spectroscopy, HR-MS and single crystal X-Ray diffraction.



Scheme 4.1. Synthesis of compound **4**; a: conc. H_2SO_4 , 40 °C 18 h (15%); b: EtOH, **11**, reflux 12 h (20%).

As starting point, the ground state chemistry at 298 K was investigated using the protocols described in the previous chapter. Typically, preparing samples in aqueous potassium phosphate buffers at increasing pH values and by subsequently acquiring the UV-Vis spectrum allows for the determination of the ground state acidity. Particular care has to be taken to provide sufficient equilibration time for the system to repartition fully between the MC and the SP anions following the K_c constant. Because of the previous fact, the typical waiting time is in the order of 10 minutes which allows for complete relaxation of the MCH/MC/SP triad at a fixed pH value. However, this equilibration procedure seemed incompatible with compound **4**; indeed, at pH close to neutrality the hydrolysis appeared to be very fast, thus interfering with the experiments. To overcome this problem, we decided to infer all the parameters using a chemical kinetics approach. At first, we measured the decay of the MC species at high pH values where the hydrolysis is slow and the only two species taking part to the chemistry are MC and SP (Figure 4.1 a). The data of the MC species was fit to a first-order kinetic decay as explained in the previous chapter, thus yielding the observed rate constant, k_{obs} . This was used to determine K_c as the ratio of the absorbances at time zero and

at equilibrium. For compound **4** K_c was calculated to be 2.6 ± 0.1 which is much lower compared to Liao's photoacid ($K_c = 8.6$ for compound **1**)^[113] and finds explanation in the lower nucleophilicity of the phenolate anion in the presence of an EWG in *para* position as the sulfonate in compound **4**. On the other hand, both k_2 ($1.63 \cdot 10^{-3} \text{ s}^{-1}$) and k_{-2} ($6.2 \cdot 10^{-4} \text{ s}^{-1}$) are significantly lower than those of Liao's photoacid under the same experimental conditions ($3.9 \cdot 10^{-2} \text{ s}^{-1}$ and $4.5 \cdot 10^{-3} \text{ s}^{-1}$, respectively^[113]).

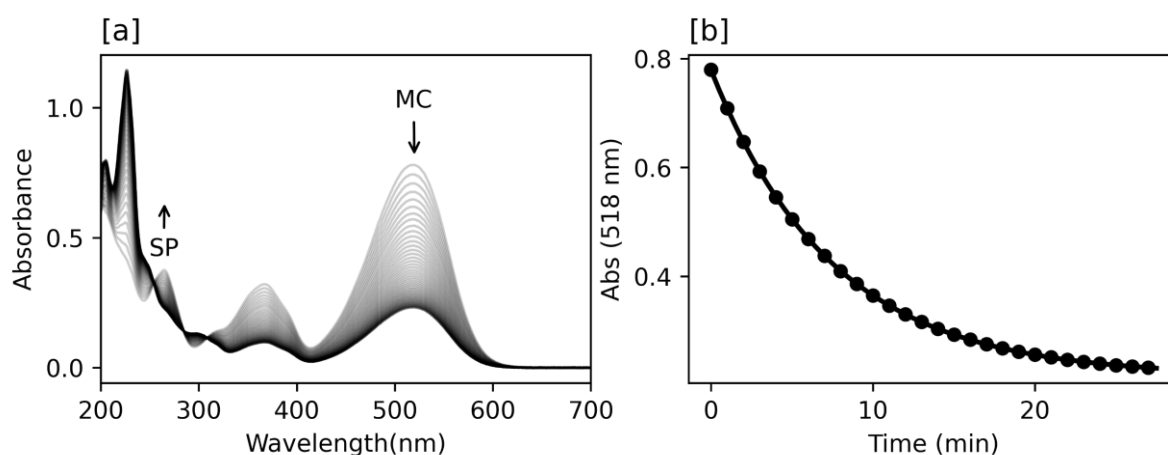


Figure 4.1. UV-Vis spectra for the MC-to-SP equilibration kinetics, in [a] the full spectra and their time evolution, in [b] the absorbance trace of the MC form. [**4**] = 25 μM , [buffer] = 20 mM, pH = 9.

Taken together, these two experimental findings give support the EWG-induced stabilization of the MC form. The dark equilibrium composition of **4** was initially examined by acquiring UV-Vis spectra as a function of pH.

$$A_t = [A_{eq} + (A_0 - A_{eq}) \exp(-k_{obs,1}t)] \exp(-k_{obs,2}t) \quad \text{Eq. 4.1}$$

At intermediate pH values, however, we observed that optical readouts were not stable. We ascribed this result to fast competing hydrolysis processes. For this reason, we decided to repeat the kinetics experiment abovementioned but as a function of the pH (Figure 4.2). In this case, all the obtained profiles (Figure 4.2 b) fit well to a double

exponential rate equation as Eq. 4.1. Where $A_{t,eq,0}$ are the absorbance at any time, equilibrium and $t=0$, respectively, $k_{obs,1}$, is the apparent rate constant of MC-to-SP equilibration, while $k_{obs,2}$ is the apparent first order rate constant of hydrolysis. This equation assumes that at any time, indicated with t , the residual amount of open form(s) subsequently undergo hydrolysis and extends the applicability of the models described in Chapter 3 to fast-hydrolyzing systems.

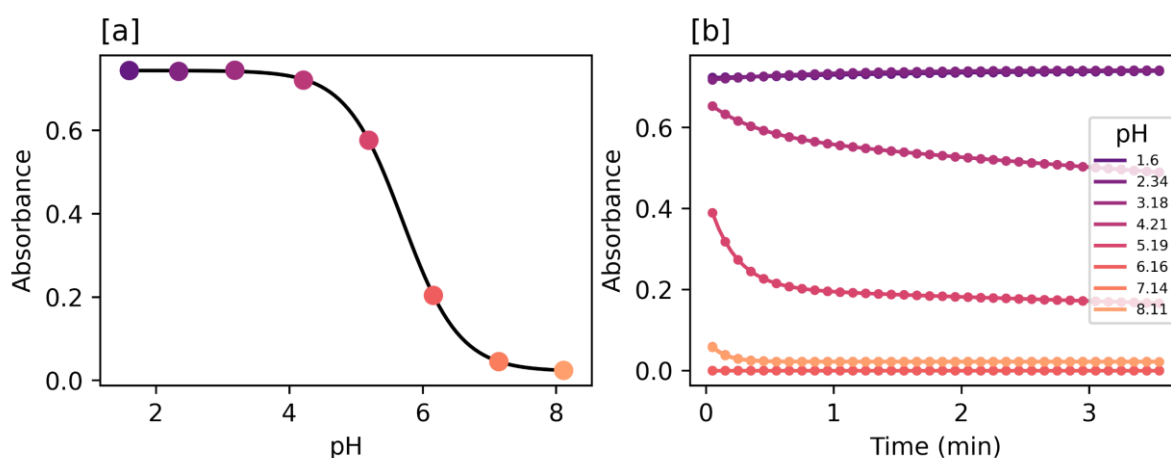


Figure 4.2. UV-Vis kinetics experiment for the determination of the pK_a^{GS} of compound **4**. In [a] the extrapolated absorbances at time-zero and in [b] the corresponding kinetic traces. The color code is maintained from panel [a] to panel [b] as visual guide.

By extrapolation of the initial absorbance (A_0) from each kinetic trace, it is possible to reconstruct the equilibrium titration curve and to fit it to a Boltzmann curve (Figure 4.2 a). The inflection point corresponds to the calculated pK_a^{GS} value 5.72 ± 0.02 , which is significantly lower than that previously determined for compound **4** (ca. 6.2).^[47] As discussed in Chapter 3 already, the acid-base equilibrium of BIPS refers to a three-component equilibrium and we believe that the value reported by Dougherty^[47] and coworkers may be instead the pK_a of **4**, as it resulted from UV-Vis spectra which were recorded without accounting for equilibration kinetics. In fact, by applying our formalism we found that compound **4** displays a pK_a value of 6.28 ± 0.04 . These results call attention to the importance of assessing equilibration kinetics prior to determining

pK_a^{GS} . Moreover, these findings support the convenience of using Eq. 4.1 instead of common biexponential equations^[114], whose pre-exponential factors are purely empirical and lack of any physical or chemical significance. Probing the acidity in the metastable state has been performed with the protocol presented in Chapter 3 without any variation. The samples were thermostatted at low pH values and subject to constant illumination prior to spectral acquisition (Figure 4.3 a). The spectra of the photosteady state are then analysed and the maximum of the band of *cis*-MCH is extracted and fit to a Boltzmann sigmoidal-type curve (Figure 4.3 b).

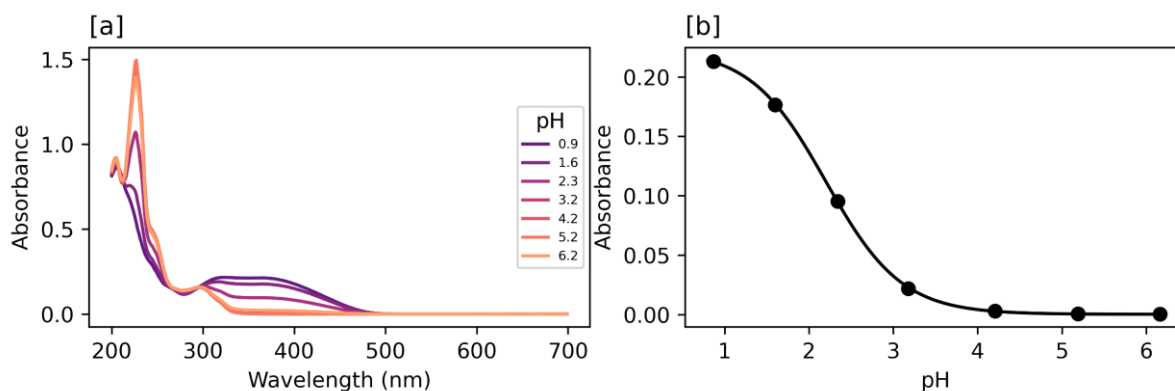


Figure 4.3. UV-Vis titration of **4** under light irradiation. In [a] the full spectra as function of pH and in [b] the absorbance trace as function of the pH.

This procedure yields the acidity constant of the metastable state - pK_a^{MS} - which was found to be 2.23 ± 0.03 ; this means that compound **4** features a photoacidity of 3.5 ± 0.1 pK units. This result is in line with our work on MCHs, which, on average, display photoacidity values around 3.6 pK units at 25 °C.^[113,115] After probing the metastable state acidity, it was time for measuring the parameters of relaxation back to the ground state. This was done by irradiation of the aqueous samples of **4** at increasing pH values and then to monitor the recovery to the ground state. Also, in this experiment hydrolysis plays an important part and results in severe interference in the

measurement. Using Eq. 4.1 proved to be, once more, the solution to this problem. Indeed, it was possible to account for the relaxation process and the hydrolysis all in a single experiment. The main difference in this case is that the $k_{\text{obs},1}$ presented in Eq. 4.1 is in this case the observed rate constant of relaxation from the metastable state as described in Chapter 3 already. The model fits well the experimental data (Figure 4.4 a) and the constants determined so-far find another confirmation with this experiment, thus, proving the generality of the four-state model presented for BIPS in chapter 3 and 4 in the specific (Figure 4.4 b).

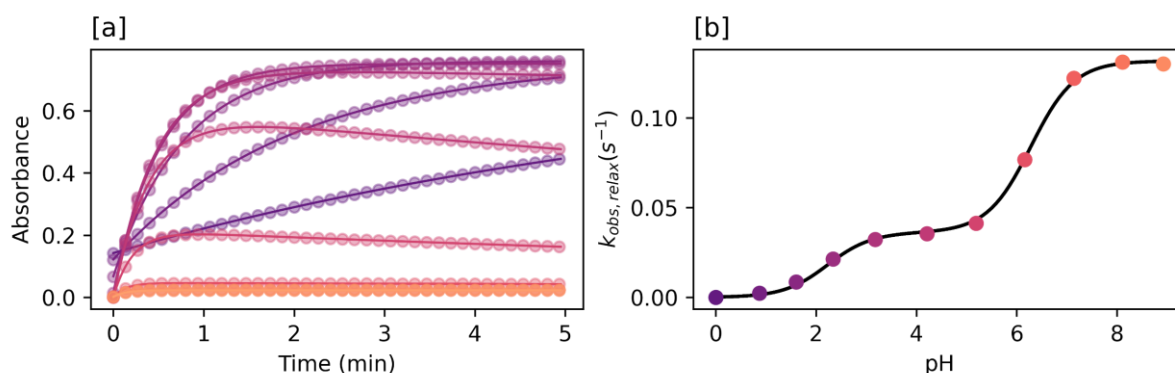


Figure 4.4. Kinetics of relaxation from the metastable state. In [a] the absorbance traces as function of the pH, in [b] the corresponding kinetic rate constants and their trend as function of the pH. The color code is maintained from panel [a] to [b] as visual guide.

However, the conjunction of Eq. 4.1 and these last experiments may be viewed as a practically convenient approach for quickly evaluating MCHs' structure-properties relationships, because it allows for assessing all the key thermodynamic and kinetic features of a given MCH – namely K_c , pK_a^{GS} , pK_a^{MS} , and the profiles of $k_{\text{obs},1}$ and $k_{\text{obs},2}$ vs. pH – all at once. Concerning the hydrolysis kinetics, we found that compound 4 hydrolyses as fast as Liao's photoacid (see Experimental Section for details). In view of a consistently slower isomerization kinetics, this last observation explains why it

was not possible to determine the pK_a^{GS} of compound **4** simply by acquiring UV-Vis spectra at equilibrium (see above).

4.3 Variable-temperature effects

Having evaluated the thermodynamics and kinetics of compound **4** at 25°C, we then studied the effects of temperature. Probing the effect of temperature on acidity constants requires an accurate correlation of pH readings with temperature. For this reason, we carefully calibrated our pH electrode prior to repeating the same experiments above at five different temperatures from 15 °C to 35 °C (see Experimental Section).

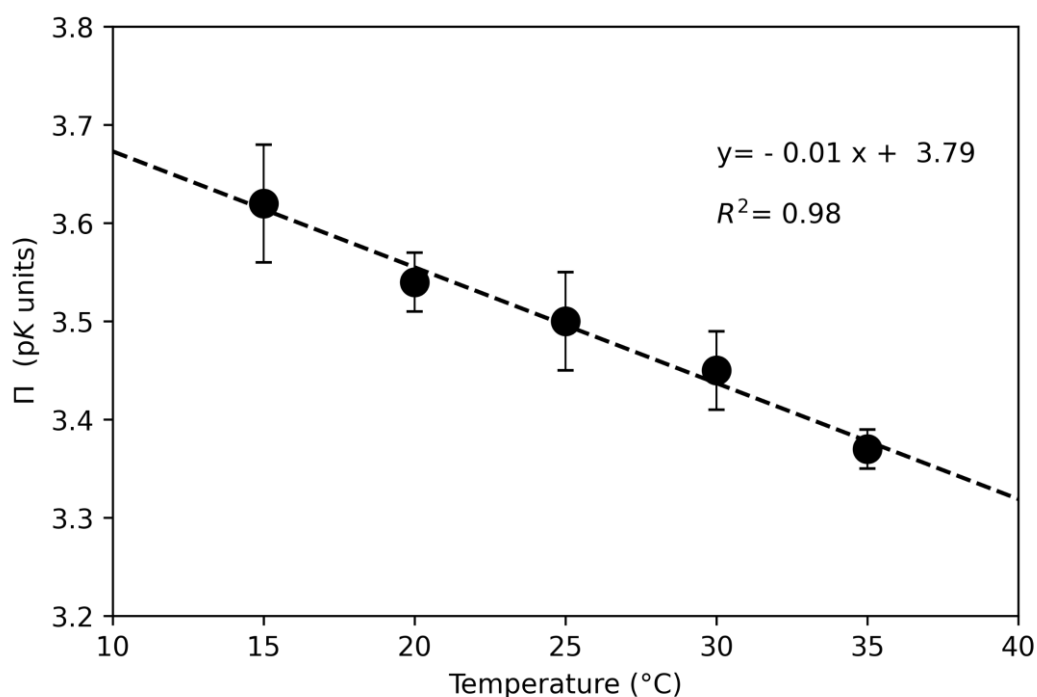


Figure 4.5. Temperature dependence of the photoacidity of compound **4**.

At every temperature, each thermodynamic constant was determined in duplicate, and van't Hoff plots computed accordingly. The obtained results are summarized in the

Experimental Section. On the one hand, we found that the acid dissociation reaction of MCH and the isomerization of MC into SP are both endothermic, with standard enthalpies ($\Delta_r H$) of 12.0 ± 0.9 , and 3.3 ± 0.6 , kJ mol^{-1} , respectively. On the other hand, the reaction from *cis*-MCH to SP and H^+ is exothermic, with $\Delta_r H$ of -5.6 ± 0.5 kJ mol^{-1} .

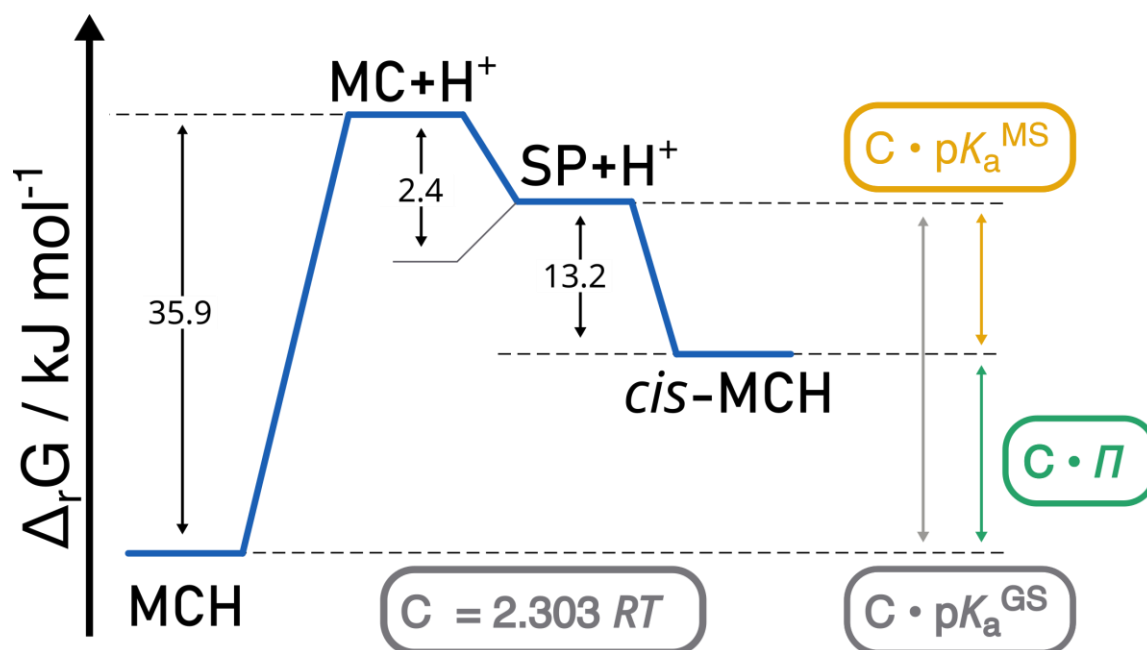


Figure 4.6. Free-energy diagram of the species deriving from **4**.

Though, in accordance with previous findings^[113], we found that the isomerization of MC into SP is entropically-driven, featuring a standard reaction entropy ($\Delta_r S$) of 19 ± 2 $\text{J mol}^{-1} \text{K}^{-1}$. The acid dissociation reactions in the dark and under light irradiation are instead entropically disfavored, with $\Delta_r S$ of -80 ± 2 and -63 ± 2 $\text{J K}^{-1} \text{mol}^{-1}$, respectively. Based on these values, free energy diagrams for the isomerization reactions of **4** in water can be subsequently determined. Within the temperature interval we examined, we found that the relative isomers' thermodynamic stability remains intact ($\text{MCH} > \text{cis-MCH} > \text{SP} > \text{MC}$), resulting in free energy diagrams as reported in Figure 4.6. However, temperature does affect the absolute free energy differences between MCH and the other isomers: that between MCH and both the deprotonated forms MC and

SP increases with temperature, while the one between MCH and *cis*-MCH decreases with temperature. The latter is associated to the photoacidity of compound **4**, which in fact decreases by ca. 0.2 p*K* units passing from 15 °C to 35 °C (Figure 4.5). These studies strongly suggest that the photoacidity of MCHs – which typically does not change that much through structural modifications – may be significantly enhanced only by selectively (de)stabilizing the (*cis*-)MCH form (e.g., through host-guest interactions).

4.4 Conclusions

In conclusion, we have synthesized compound **4** and fully characterized its (photo)chemical behaviours in water as function of the temperature. The relatively rapid hydrolysis and slow relaxation kinetics of compound **4** led us to implement Eq. 4.1 in our analyses. The conjunction of Eq. 4.1 with pH-dependent relaxation kinetic experiments provided a straightforward approach for quickly evaluating all the physicochemical properties of **4** with a single experiment, and, in general, it may be viewed as a practically convenient methodology to quickly carry out studies on new MCHs' compound libraries. In addition, van't Hoff analyses unravelled the thermodynamic parameters for the isomerization of **4** in water, showing that its photoacidity increases moderately with decreasing temperature. The present study can be generalized to other MCHs, and we believe it may be useful for expanding the applications of MCHs further.

4.5 Experimental Section

4.5.1 General Remarks

All reagents and solvents were purchased from commercial suppliers and used without further purification. 2,3,3-trimethylindolium-propyl-1-sulfonate was synthesized as described previously.^[33] Sodium 5-sulfosalicylaldehyde was also synthesized as previously^[47] described, but purified following a modified protocol. H₂O used in all preparations was filtered with a MilliQ-Integral5 purification system (mQ H₂O). NMR spectra were recorded at 298 K on a Bruker Avance III-400 equipped with a BBFO_z probe (¹H: 400 MHz; ¹³C: 101 MHz). Chemical shifts (δ) are reported in parts per million (ppm), while coupling constants (J) are given in Hertz (Hz). Solvent residual signals are used as internal reference for spectra alignment (DMSO-*d*₆: δ = 2.50 ppm). Electrospray-ionization HRMS analyses were run (negative mode) on a Waters XEVO G2-S QTOF spectrometer interfaced with Acquity UPLC pumps and sample manager system. UV-Vis spectra and kinetics were acquired on an Agilent Cary 60 spectrometer equipped with an 18-cell holder coupled to a Huber thermostat, using Suprasil quartz cuvettes (114-QS) from Hellma Analytics. pH measurements were performed using Metrohm pH module 867 coupled with a Biotrode glass electrode; pH data were processed using the software Metrohm Tiamo Light. Samples photoirradiation was carried out using a Prizmatix FC-LED-425Z high-power LED light sources (λ = 425 nm). The light beam was delivered by polymer optical fibers (core 1500 μ M) i) positioned orthogonally to and just below the liquid/air interface of sample solutions. Power measurements of the fiber-coupled LED output were made with Thorlabs S142C integrating sphere photodiode power sensor; the uncertainty is within 3-5%.

Potassium phosphate buffers from pH 3 to 10 were prepared titrating a solution of H_3PO_4 (100 mM, 1L) with KOH 10 M. Diluted stocks of H_3PO_4 were used below pH 3. All buffer stocks were stored at room temperature. In order to account for the effect of temperature on pH readings, we performed calibrations of our Biotrode glass electrode as a function of the temperature (see below). Unless stated otherwise, UV-Vis analyses were carried out and analysed as described previously (see Chapter 3).^[113]

4.5.2 Synthetic procedures

Synthesis sodium 5-sulfosalicylaldehyde

In a 50-mL round bottom flask, 95-97% sulfuric acid (41 mL, 769 mmol) was added and the flask cooled down to 0 °C with an ice bath. Salicylaldehyde (5.1 g, 41 mmol) was then slowly added dropwise under stirring. The flask was flushed with N_2 (10 min) and sealed with a septum prior to heating it up to 40 °C for 18 h. The resulting amber-orange mixture was poured in a large beaker (1 L) containing ice (200 g), and an aqueous solution of sodium carbonate (200 mL, 1.84 M) was gently added dropwise under stirring. The resulting pinkish solution was concentrated by rotary evaporation until the formation of a precipitate. The suspension was filtered, and the solid product washed with EtOH (2 × 50 mL) and Me_2CO (2 × 50 mL). 5-sulfosalicylaldehyde was further purified as follows: to remove undesired sodium (bi)sulfate salts, the obtained solid was dissolved in boiling MeOH:H₂O 5:1 (120 mL) for a few minutes. The insoluble residues were filtered off and the collected solution kept dry by rotary evaporation, yielding sodium 5-sulfosalicylaldehyde as an off-white solid (1.41 g, 15%).

^1H NMR (400 MHz, $\text{DMSO}-d_6$) δ (ppm): 10.83 (s, 1H), 10.25 (s, 1H), 7.88 (s, 1H), 7.70 (d, $J = 8.6$ Hz, 1H), 6.92 (d, $J = 8.6$ Hz, 1H).

^{13}C NMR (101 MHz, DMSO) δ (ppm): 191.39, 160.71, 140.06, 133.72, 126.22, 121.00, 116.50.

HRMS (ESI/QTOF) m/z : $[\text{M} - \text{Na}^+]^-$ Calcd for $\text{C}_7\text{H}_5\text{O}_5\text{S}^-$ 200.9863; Found 200.9856.

Synthesis of Compound 4

In a 50-mL round-bottom flask compound **11** (220 mg, 0.77 mmol) and sodium 5-sulfosalicylaldehyde (165 mg, 0.73 mmol) were dissolved in absolute EtOH (5 mL). The flask was sealed with a septum and the solution degassed by gentle N_2 bubbling (10 min) prior to heating it up to 90 °C under stirring for 18 h. The resulting orange slurry was sonicated for a few minutes, poured over a Gooch filter, and washed thoroughly with EtOH to remove unreacted materials. The crude solid was recrystallized from hot MeOH/EtOH 1:1. The product precipitated out upon slow cooling down to 4°C overnight. Compound **4** was obtained as a bright orange solid after filtration and vacuum drying (72 mg, 20%). X-ray quality crystals were obtained by slow evaporation of a satd. solution of **4** in MeOH/EtOH 1:1, which was kept in the dark for 2 months. Note: without purifying sodium 5-sulfosalicylaldehyde as described above we were not able to obtain crystals of good quality, presumably because co-precipitation of other sodium salts.

^1H NMR (400 MHz, $\text{DMSO}-d_6$) δ (ppm): 11.43 (s, 1H), 8.53 (d, $J = 16.3$ Hz, 1H), 8.28 (s, 1H), 8.07 (d, $J = 8.7$ Hz, 1H), 7.96-7.85 (m, 2H), 7.72-7.56 (m, 3H), 6.99 (d, $J = 8.7$

Hz, 1H), 4.76 (t, $J = 7.3$ Hz, 2H), 2.64 (t, $J = 7.3$ Hz, 2H), 2.19 (p, $J = 7.3$ Hz, 2H), 1.79 (s, 6H).

^{13}C NMR (201 MHz, DMSO) δ (ppm): 182.28, 159.45, 150.56, 143.66, 141.01, 140.67, 132.97, 129.33, 129.13, 129.10, 122.95, 120.18, 115.77, 115.23, 112.68, 52.06, 47.68, 45.83, 26.10, 24.46.

HRMS (ESI/QTOF) m/z : $[\text{M} - \text{Na}^+]^-$ Calcd for $\text{C}_{21}\text{H}_{22}\text{NO}_7\text{S}_2^-$ 464.0843; Found 464.0849.

4.5.3 ^1H and ^{13}C NMR spectroscopy

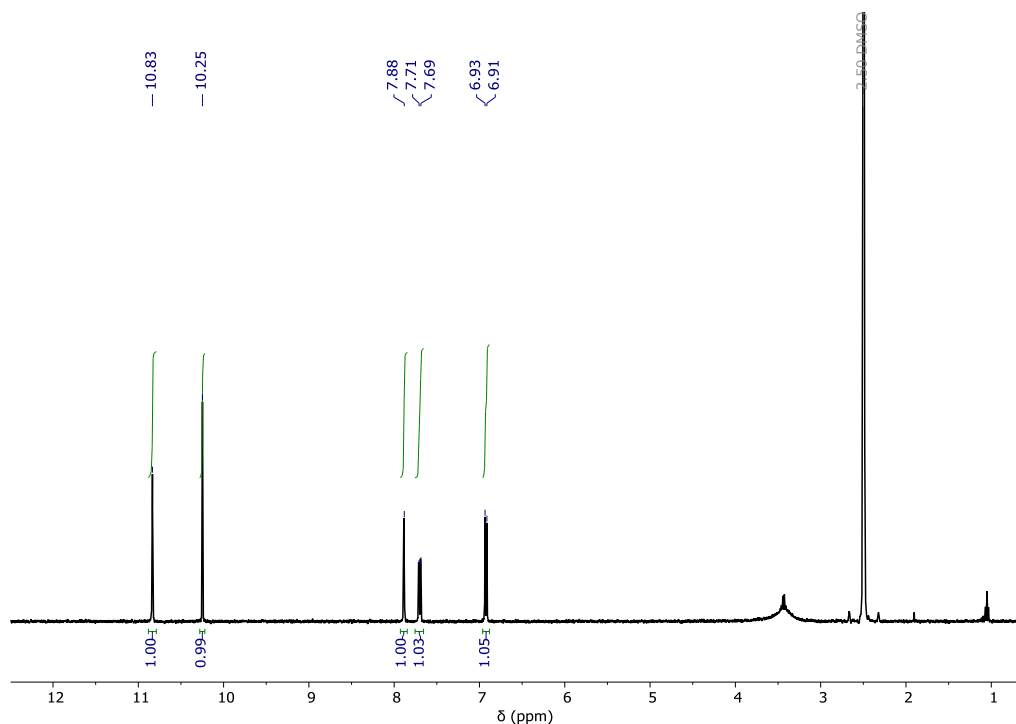


Figure S 4.1. ^1H NMR spectrum (400 MHz, $\text{DMSO}-d_6$) of sodium 5-sulfosalicylaldehyde.

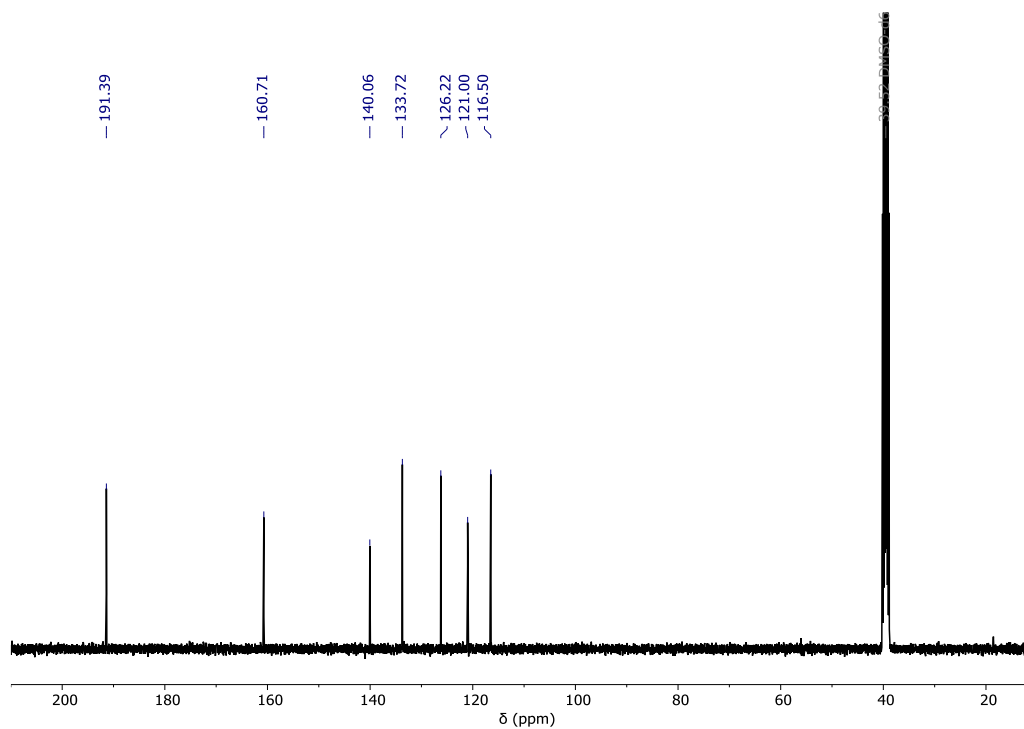


Figure S 4.2. ^{13}C NMR spectrum (101 MHz, $\text{DMSO}-d_6$) of sodium 5-sulfosalicylaldehyde.

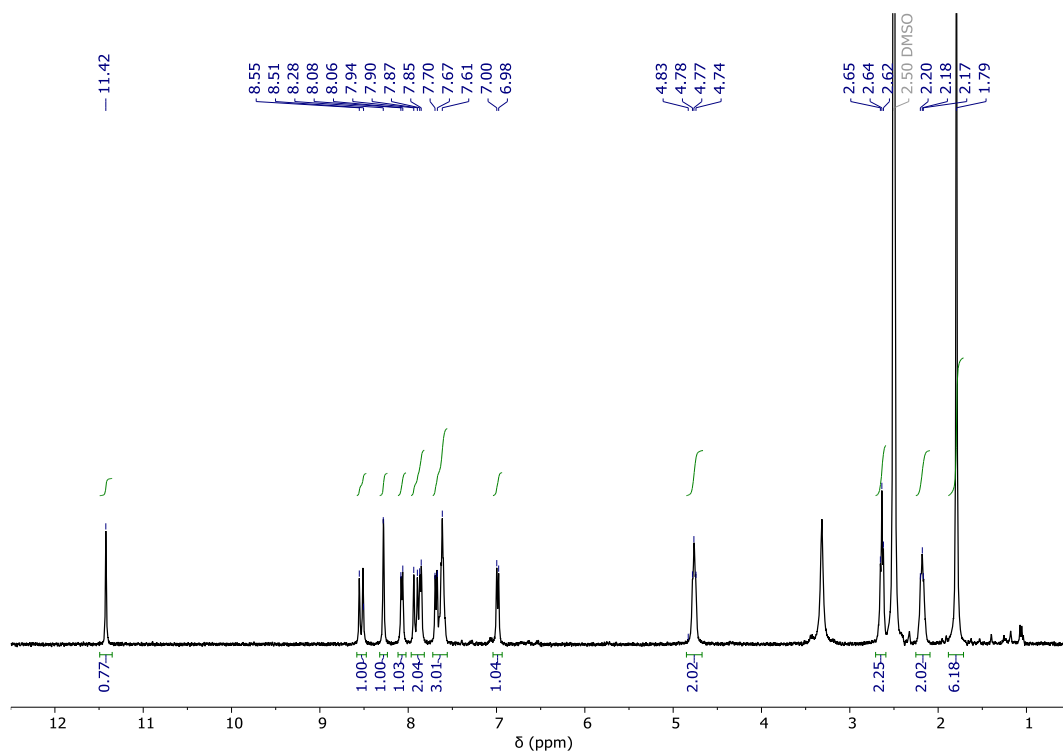


Figure S 4.3. ¹H NMR spectrum (400 MHz, DMSO-d₆) of compound 1.

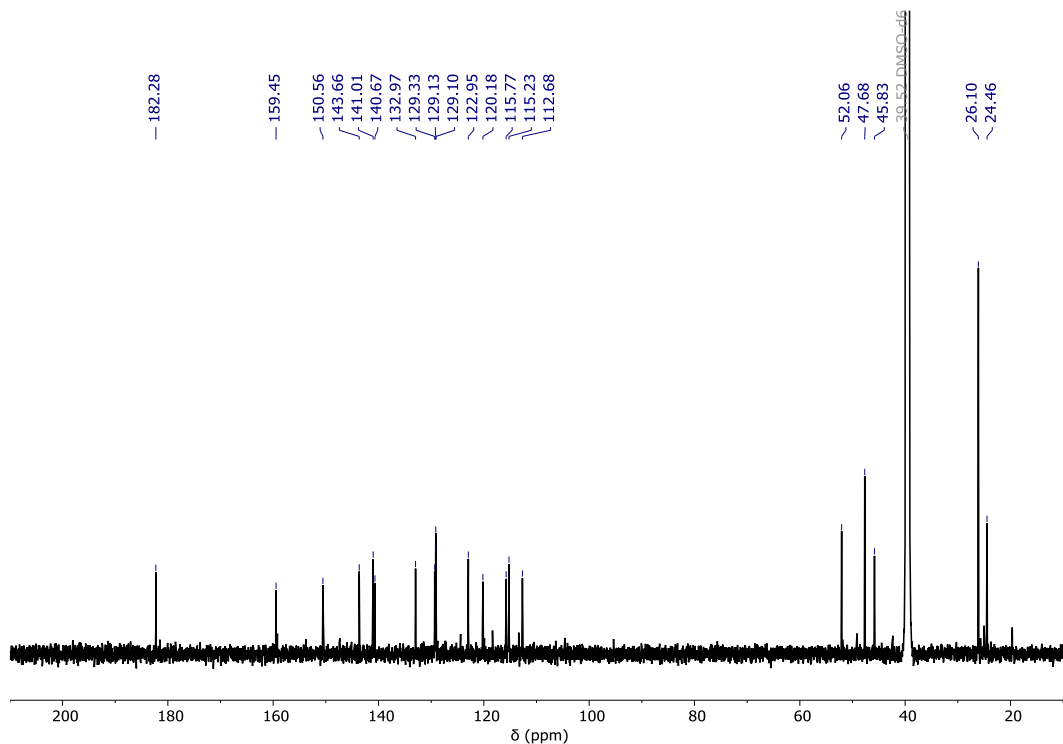


Figure S 4.4. ¹³C NMR spectrum (201 MHz, CDCl₃) of compound 1.

4.5.4 X-Ray crystallography

Table S 4.1

CCDC Deposition number	2104306
Empirical formula	C ₄₄ H ₅₂ N ₂ Na ₂ O ₁₆ S ₄
$D_{\text{calc}} / \text{g cm}^{-3}$	1.480
μ / mm^{-1}	2.690
Formula Weight	1039.09
Colour	clear intense orange
Shape	prism-shaped
Size/mm ³	0.14×0.08×0.05
Temperature/K	140.00(10)
Crystal System	monoclinic
Space Group	<i>P</i> 2 ₁ / <i>c</i>
<i>a</i> /Å	10.67871(14)
<i>b</i> /Å	21.3449(3)
<i>c</i> /Å	21.1047(3)
α°	90
β°	104.2372(13)
γ°	90
Volume/Å ³	4662.77(11)
<i>Z</i>	4
<i>Z'</i>	1
Wavelength/Å	1.54184
Radiation type	CuK α
$\theta_{\text{min}}^\circ$	2.992
$\theta_{\text{max}}^\circ$	72.536
Measured Refl's.	41444
Indep't Refl's	9153
Refl's $I \geq 2\sigma(I)$	7632
<i>R</i> _{int}	0.0356
Parameters	623
Restraints	0
Largest Peak/e Å ⁻³	1.113
Deepest Hole/e Å ⁻³	-0.520
GooF	1.030
<i>wR</i> ₂ (all data)	0.1021
<i>wR</i> ₂	0.0946
<i>R</i> ₁ (all data)	0.0478
<i>R</i> ₁	0.0369

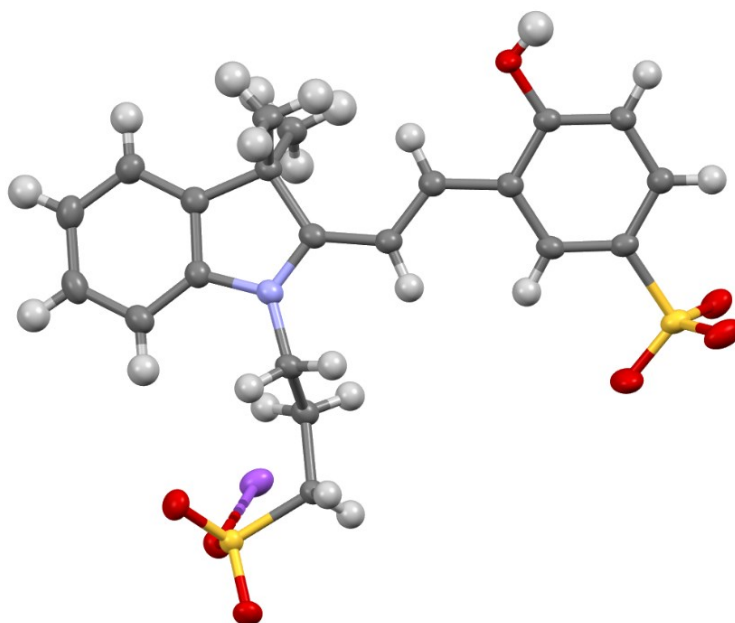
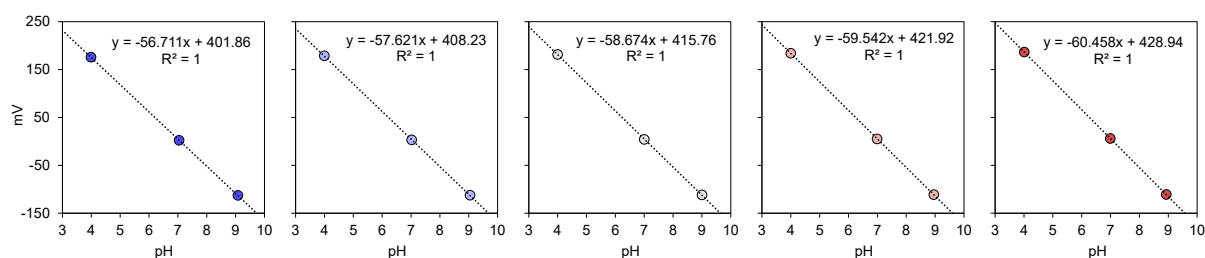


Figure S 4.5. Molecular structure of compound **4**, thermal ellipsoids at 50 % probability.

4.5.5 Calibration of the glass electrode

In order to account for the effect of temperature on pH readings we carried out electrode calibrations at different temperatures. Standard buffer solutions (Metrohm, pH 4, 7 and 9) were left equilibrating at the desired temperature in a jacketed beaker under stirring. The potential in millivolts (mV) of the solutions was read after stabilization of the electrode response, which takes a few minutes. Calibration curves were then obtained by plotting the mV readings against the actual pH of the standard buffers at a given temperature (which are known; e.g., the actual pH of Metrohm standard buffer solutions at 15 °C are 3.99, 7.04, and 9.08, respectively). The obtained calibration curves were the following:



In a typical experiment, all samples are prepared directly into cuvettes by adding mQ water, a solution of compound **1** and a phosphate buffer stock (100 mM) at a given pH. The nominal concentration of phosphate buffers in each sample is 20 mM (1/5 dilution). Thus, a series of cuvettes containing 20 mM buffer solutions were prepared, and equilibrated at the desired temperature by putting them in the thermostatted cell holder of our UV-Vis spectrometer for 10 min prior to measure the mV of each sample in situ. The actual pH of each sample is then obtained by converting the corresponding mV readout with the calibration curves above. Addition of compound **1** (μM regime) does not result in pH changes higher than the error on pH readings (± 0.03 pH units).

The results were the following:

T (°C)	15		20		25		30		35	
buffer 20 mM	mV	pH	mV	pH	mV	pH	mV	pH	mV	pH
0	354.8	0.83	358.3	0.87	364.8	0.87	370.2	0.87	375.3	0.89
1	313.0	1.57	317.2	1.58	322.0	1.60	326.9	1.60	331.2	1.62
2	270.0	2.33	274.5	2.32	278.4	2.34	282.3	2.35	285.9	2.37
3	223.6	3.14	226.2	3.16	229.3	3.18	232.0	3.19	235.0	3.21
4	164.9	4.18	167.0	4.19	169.0	4.21	170.4	4.23	173.0	4.23
5	103.9	5.25	108.9	5.19	111.2	5.19	113.4	5.19	115.4	5.19
6	49.8	6.21	52.4	6.18	54.1	6.16	55.3	6.16	56.8	6.16
7	-4.9	7.17	-3.7	7.15	-3.0	7.14	-2.5	7.13	-1.8	7.12
8	-63.5	8.21	-60.1	8.13	-59.9	8.11	-60.2	8.10	-60.2	8.09
9	-117.0	9.15	-111.8	9.03	-107.9	8.92	-106.4	8.88	-105.4	8.84
10	-173.4	10.14	-165.1	9.95	-159.5	9.80	-154.6	9.69	-149.4	9.57

4.5.6 Equilibration kinetics at high pH vs. T (K_c)

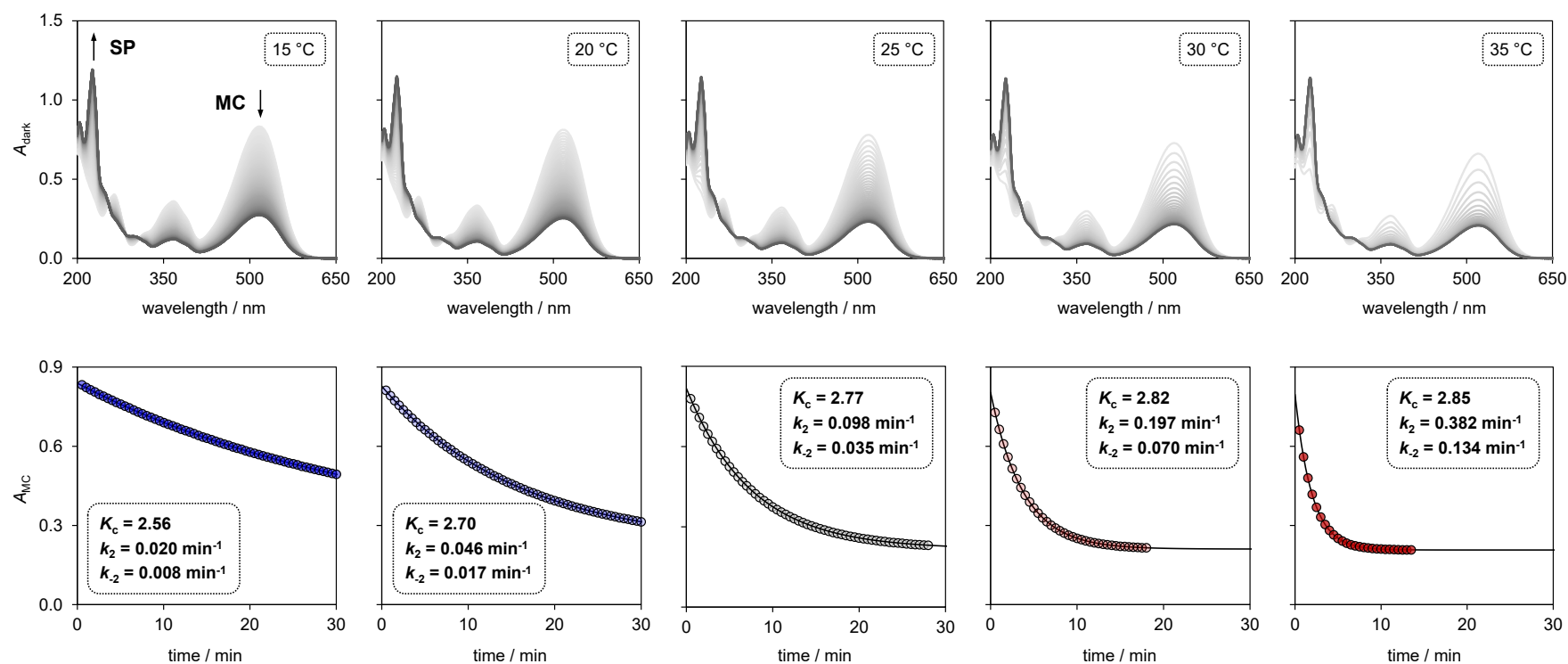


Figure S 4.6. Representative UV-Vis spectra as a function of time (top) and corresponding kinetic profile (bottom) after on-site addition and rapid mixing of an aliquot (50 μL) of a solution (0.5 mM in mQ water) of compound **1** into a cuvette containing the buffer solution (950 μL); solid black line represent the best fit to a first-order decay. Experimental conditions: $[\mathbf{4}] = 25 \pm 2 \mu\text{M}$, [phosphate buffer] = 20 mM, pH 9.5, T = from 15 to 35 °C. **These experiments provided the first dataset of K_c vs. T .**

4.5.7 Equilibration kinetics vs. pH and vs. T (K_c & pK_a^{GS})

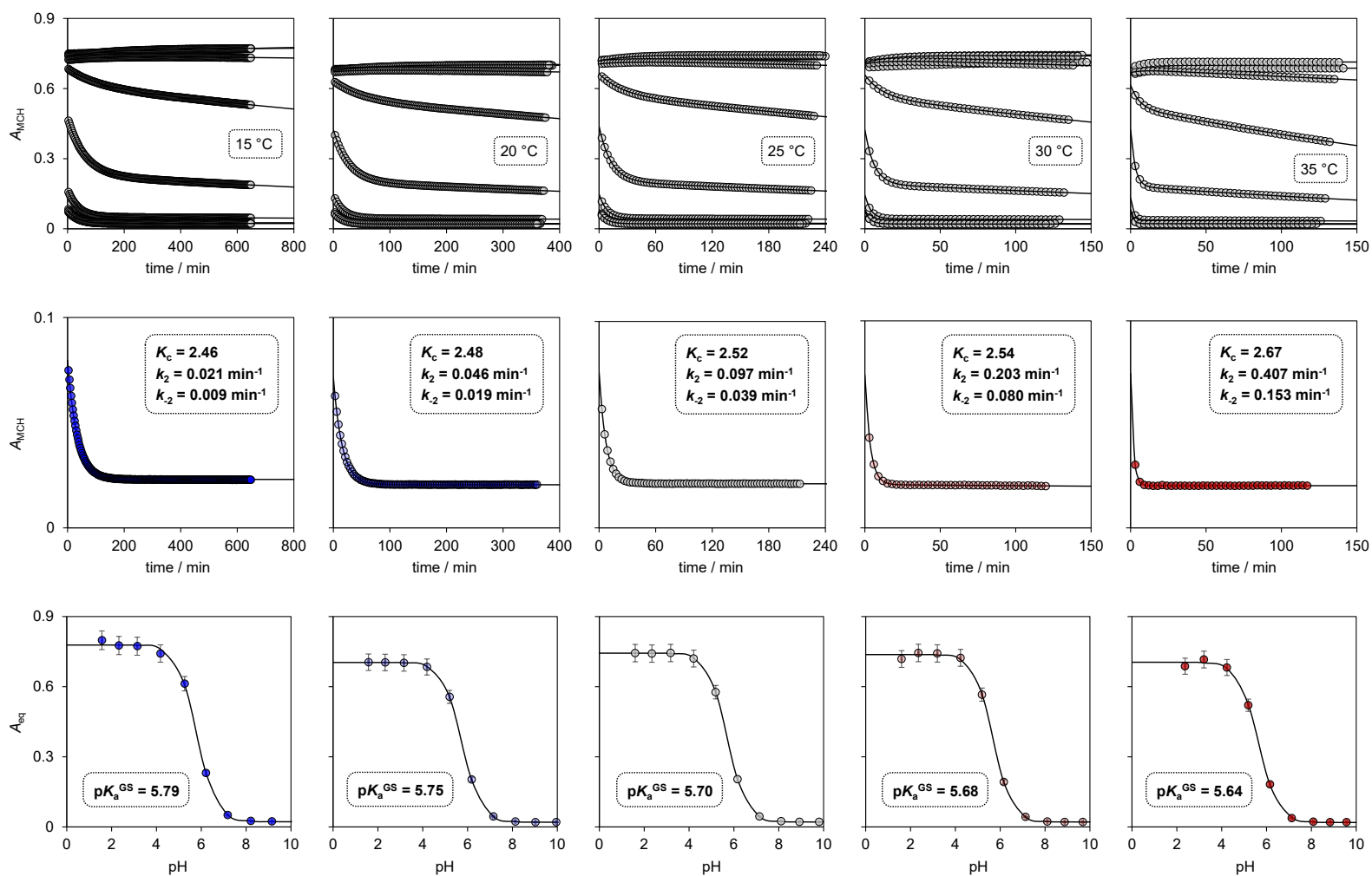


Figure S 4.7. Equilibration kinetics as a function of the pH (top) and at high pH (middle) after on-site addition and rapid mixing of an aliquot (50 μL) of a solution (0.5 mM in mQ water) of compound **1** into a cuvette containing the buffer solution (950 μL); solid black lines represent the best fit. pH-dependent profiles of the A_{eq} parameter extrapolated after fitting (bottom); solid black lines represent the best fit. Experimental conditions: $[4] = 25 \pm 2 \text{ } \mu\text{M}$, [phosphate buffer] = 20 mM, pH 1-10, $T =$ from 15 to 35 °C. **These experiments provided the second dataset of K_c vs. T , and the first dataset of pK_a^{GS} vs. T .**

4.5.8 UV-Vis pH titrations under steady light irradiation vs. T (pK_a^{MS})

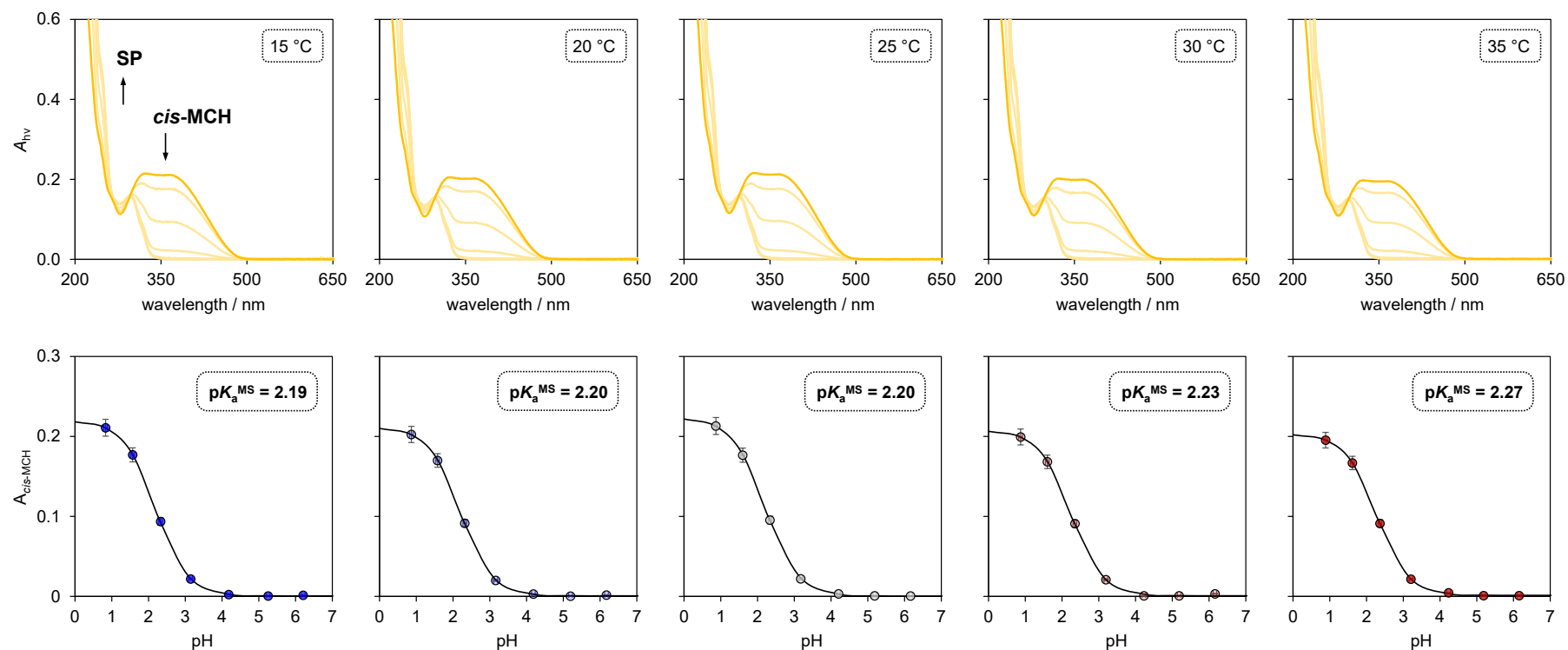


Figure S 4.8. UV-Vis pH titrations as a function of the pH (top) and corresponding pH-dependent profile of $A_{cis-MCH}$ (bottom). Experimental conditions: $[4] = 25 \pm 2 \mu\text{M}$, [phosphate buffer] = 20 mM, pH 0-7, T = from 15 to 35 °C. **These experiments provided the first dataset of pK_a^{MS} vs. T**

4.5.9 Relaxation kinetics vs. pH and vs. T (pK_a^{GS} & pK_a^{MS})

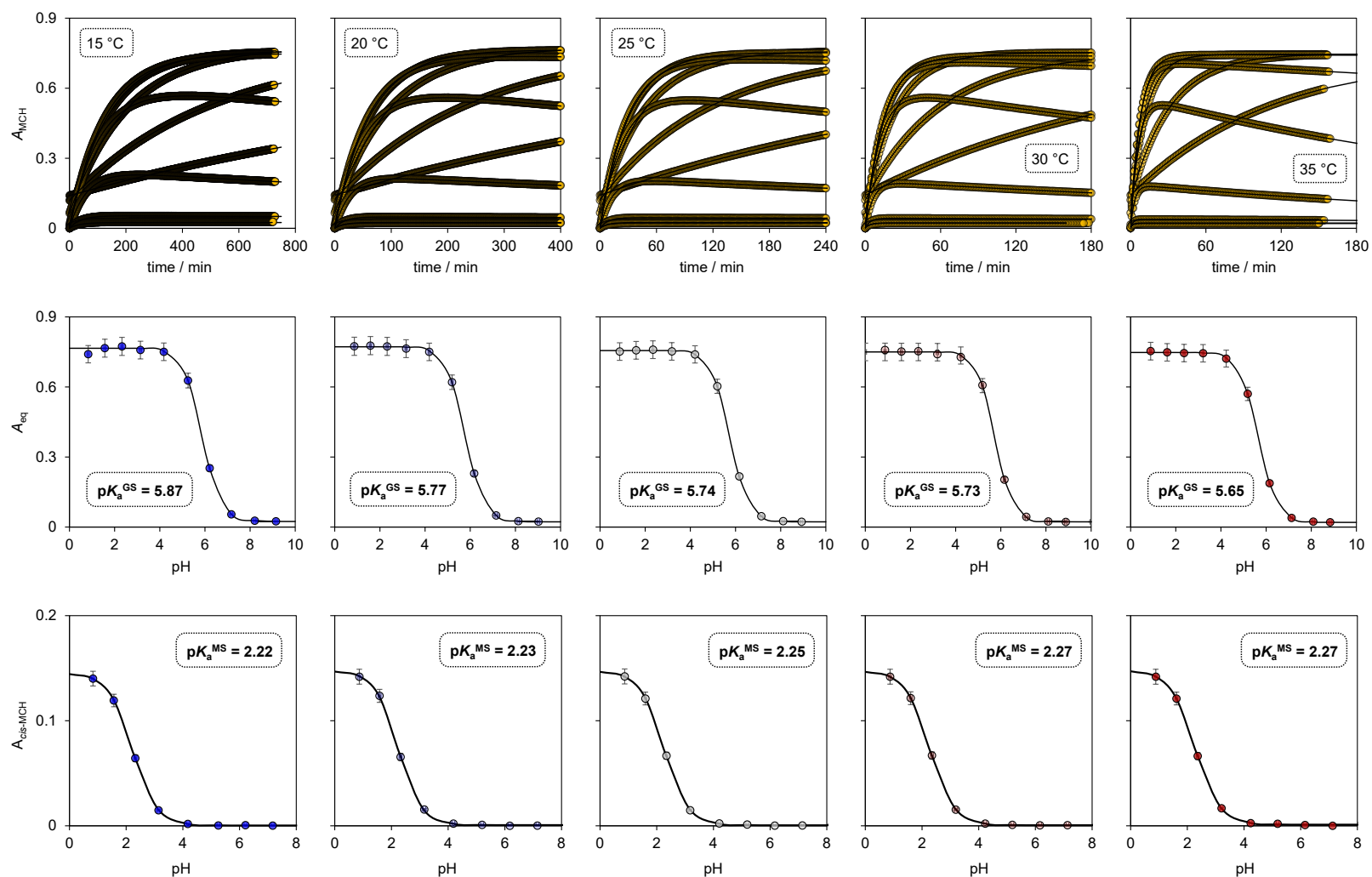


Figure S 4.9. Relaxation kinetics irradiation in situ as a function of the pH (top). pH-dependent profiles of the A_{eq} (middle) and the A_0 (bottom) parameters extrapolated after fitting; solid black line represents the best fit. Experimental conditions: $[4] = 25 \pm 2 \mu\text{M}$, [phosphate buffer] = 20 mM, pH 0-10, T = from 15 to 35 °C. **These experiments provided the second datasets of pK_a^{GS} vs. T and pK_a^{MS} vs. T .**

4.5.10 Thermodynamic constants – summary

Table S 4.2. Thermodynamic constants of compound 4 as a function of the temperature.

Reaction	Temperature / °C	Thermodynamic constant \pm error ^(a)
MC \rightarrow SP	15	$K_c = 2.51 \pm 0.05$
	20	$K_c = 2.59 \pm 0.11$
	25	$K_c = 2.64 \pm 0.13$
	30	$K_c = 2.68 \pm 0.14$
	35	$K_c = 2.76 \pm 0.09$
MCH \rightarrow MC/SP + H ⁺	15	$pK_a^{GS} = 5.83 \pm 0.04$
	20	$pK_a^{GS} = 5.76 \pm 0.01$
	25	$pK_a^{GS} = 5.72 \pm 0.02$
	30	$pK_a^{GS} = 5.70 \pm 0.03$
	35	$pK_a^{GS} = 5.65 \pm 0.01$
MCH \rightarrow MC + H ⁺	15	$pK_a = 6.38 \pm 0.05$
	20	$pK_a = 6.31 \pm 0.03$
	25	$pK_a = 6.28 \pm 0.04$
	30	$pK_a = 6.27 \pm 0.05$
	35	$pK_a = 6.22 \pm 0.02$
<i>cis</i> -MCH \rightarrow SP + H ⁺	15	$pK_a^{MS} = 2.21 \pm 0.02$
	20	$pK_a^{MS} = 2.22 \pm 0.02$
	25	$pK_a^{MS} = 2.23 \pm 0.03$
	30	$pK_a^{MS} = 2.25 \pm 0.02$
	35	$pK_a^{MS} = 2.27 \pm 0.01$

^(a) All values represent the average of two distinct datasets with relative error. Each pK_a was determined from pK_a^{GS} and K_c knowing that $K_a^{GS} = K_a(1+K_c)$. The linear trend of photoacidity vs. T presented in the main text was computed considering these avg. \pm error values.

4.5.11 Validation

To validate the values listed above we performed a quick check by examining the corresponding profiles of $k_{\text{obs},1}$ vs. pH, which, considering our four-state model interpretation, should fit to a double sigmoidal equation as explained in Chapter 3. Fitting were performed by keeping constant all the corresponding values of K_c , K_a and K_a^{MS} listed in Table S 4.2, leaving k_2 free to vary.

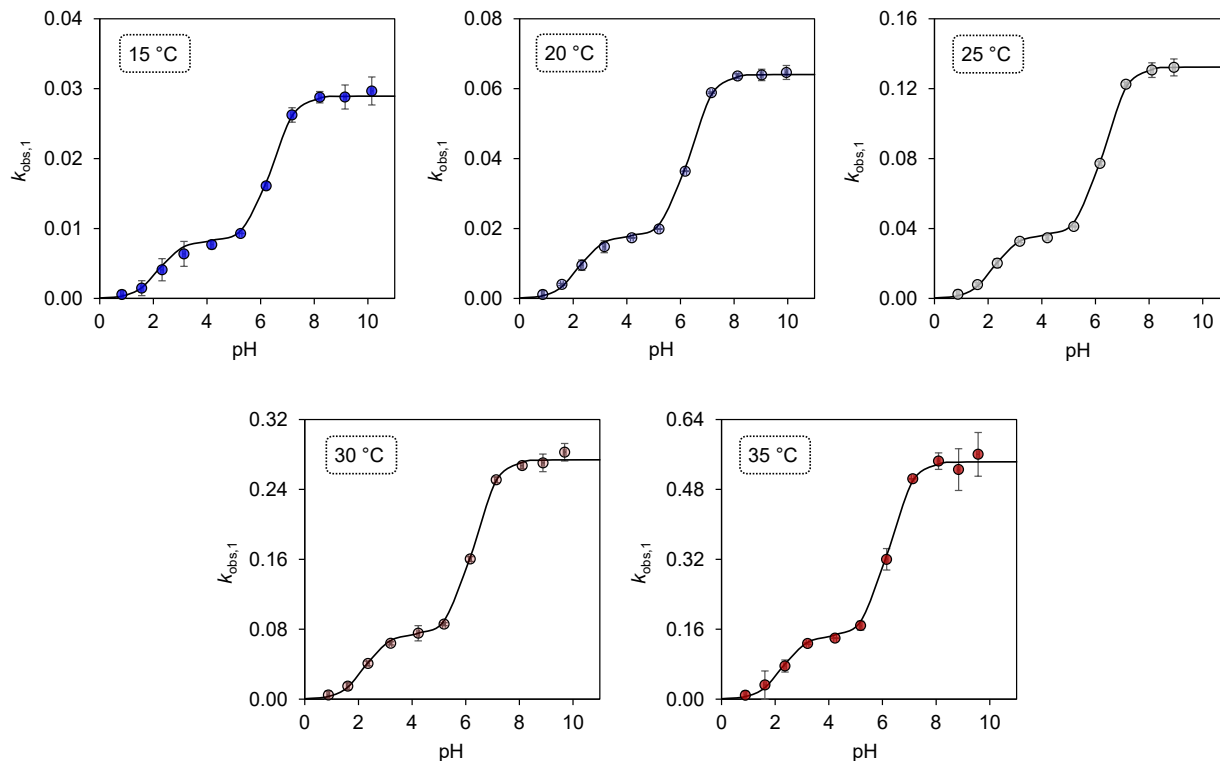


Figure S 4.10. The profiles of $k_{\text{obs},1}$ vs. pH at different temperatures. Each profile was constructed considering two datasets of $k_{\text{obs},1}$ vs. pH: the one obtained from equilibration kinetics (Figure S 4.7) and the other obtained from relaxation kinetics (Figure S 4.9).

4.5.12 Hydrolysis

The hydrolysis of compound **1** in water was evaluated by plotting $k_{\text{obs},2}$ as a function of the pH. In all cases, the obtained bell-shaped profiles are in line with the fact that the rate determining step of MCHs' hydrolysis change with pH from decomposition of a tetrahedral intermediate (k_h) to nucleophilic addition of water (k_w) at higher pH values. The detailed description can be found in the Experimental Section of Chapter 3 and the results are the following:

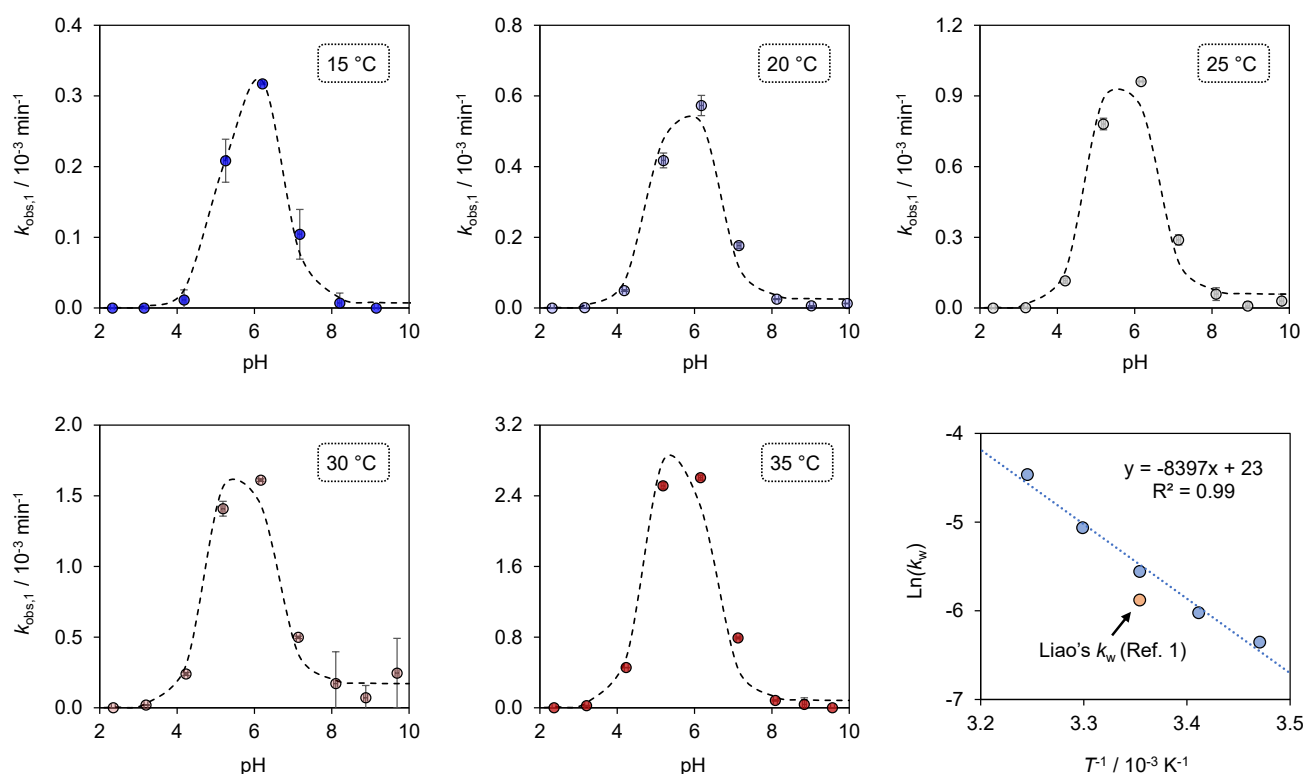


Figure S 4.11. The profiles of $k_{\text{obs},2}$ vs. pH at different temperatures. Each profile was constructed considering two datasets of $k_{\text{obs},2}$ vs. pH: the one obtained from equilibration kinetics (Figure S 4.7) and the other obtained from relaxation kinetics (Figure S 4.9). Dotted black lines represent the best fit. The resulting Eyring plot for the rate constant of water nucleophilic addition (k_w), together with a visual comparison with Liao's photoacid (compound **1**) is provided on the bottom right corner.

4.5.13 Van't Hoff analyses

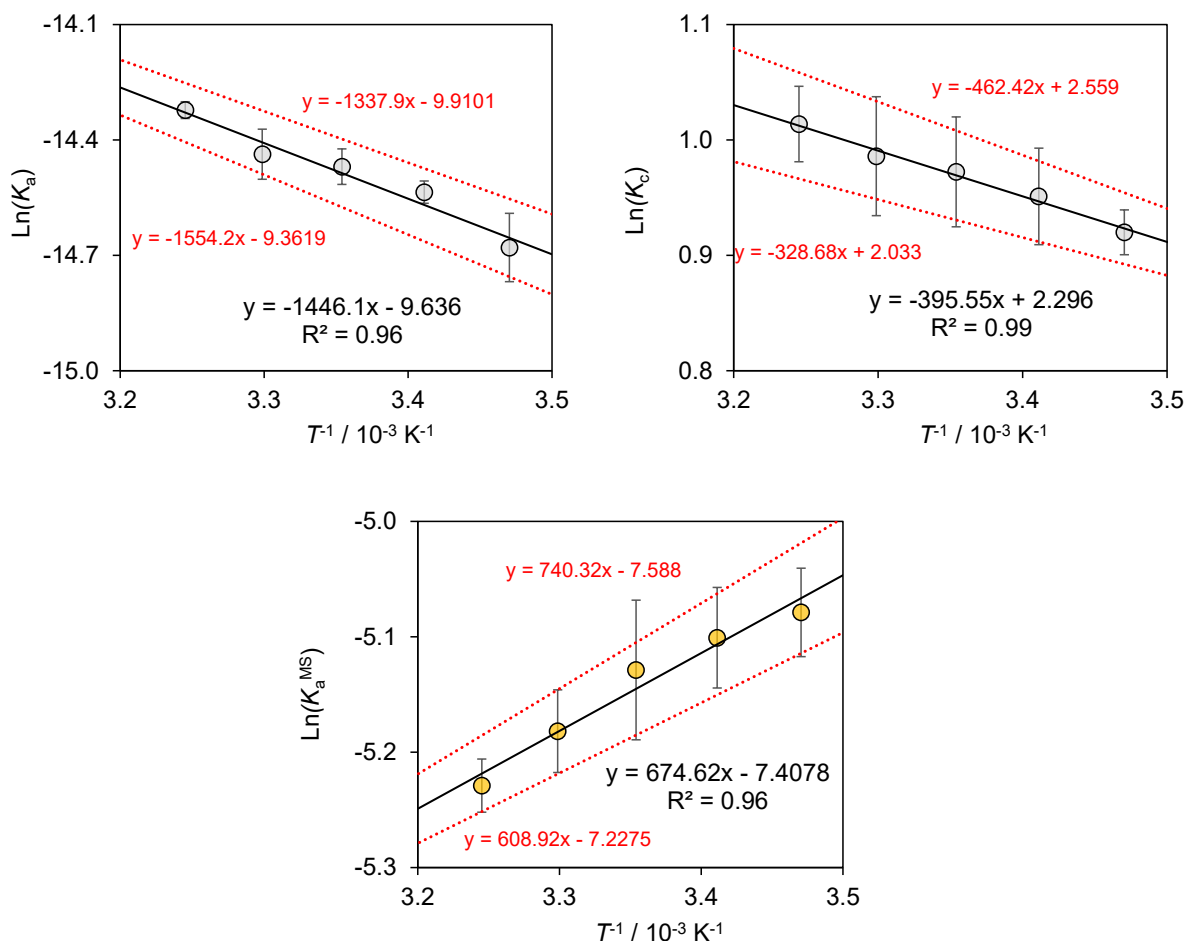
Figure S 4.12. Van't Hoff analyses. Each van't Hoff plot was computed considering the values \pm error listed in Table S 4.2.

Table S 4.3. Extrapolated thermodynamic parameters

Reaction	$\Delta_r H$ (kJ mol ⁻¹) ^(a)	$\Delta_r S$ (J K ⁻¹ mol ⁻¹) ^(b)
MCH \rightarrow MC + H ⁺	+12.0 \pm 0.9	-80.1 \pm 2.3
MC \rightarrow SP	+3.3 \pm 0.6	+19.1 \pm 2.2
<i>cis</i> -MCH \rightarrow SP + H ⁺	-5.6 \pm 0.5	-63.1 \pm 1.5

^(a) Each enthalpy of reaction was determined from the slope ($-\Delta_r H/RT$) of the corresponding van't Hoff plot. ^(b) Each entropy of reaction was determined from the intercept ($\Delta_r S/R$) of the corresponding van't Hoff plot. Errors were estimated considering upper and lower boundaries, which in turn comes from the uncertainty of each value listed in Table S 4.2. The free energy diagram at 25 °C presented in the main text was computed using the values listed here.

Chapter 5

Light-switchable buffers

Parts of this chapter have been taken from:

C. Berton, D.M. Busiello, S. Zamuner, R. Scopelliti, F. Fadei-Tirani, K. Severin, C. Pezzato, *Angewandte Chemie International Edition*, **2021**, 27, 27137

5.1 Introduction

In the previous chapters we discussed the reactivity and the influence of variables such as temperature on the chemistry of BIPS. The potential of these molecules have as photoacids is fascinating, and having the possibility to trigger large pH changes in aqueous media will open new horizons in the control of (bio)chemical acid-sensitive systems.^[116] In the quest of preparing and analyzing improved versions of BIPS photoacids, we came across the definition given by Sørensen^[117] in 1909 of buffer systems. The simplest aqueous buffer system comprises a weak monoprotic acid or base that upon partial neutralization with a strong base creates a solution capable to withstand small additions of strong acid or base without significant pH variations. The approximated equation that correlates the pH of a buffer with the acid dissociation exponent of the acid-base pair is made of (pK_a) is the so-called Henderson-Hasselbalch equation^[118]:

$$\text{pH} = \text{p}K_a + \log\left(\frac{[\text{A}]}{[\text{HA}]}\right) \quad \text{Eq. 5.1}$$

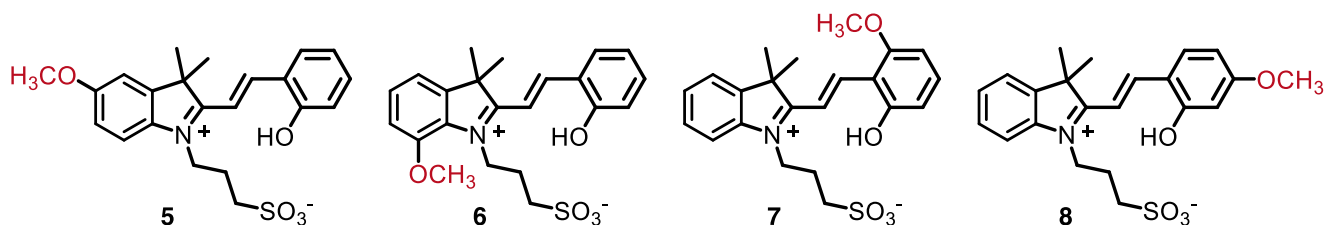
where [HA] and [A] are the concentrations of the acid and its conjugated base, respectively.

The capability of a buffer to resist pH changes – defined to as buffer capacity^[119] – is maximized

when the pH equals the pK_a . Since BIPS are weak acids and display a significant photochemical pK_a shift, we wonder whether BIPS can operate, instead, as “light-switchable buffers”. The extent of proton release (ΔpH) that a given BIPS can achieve in solution results from a delicate interplay between its photoacidity ($\Pi = pK_a^{GS} - pK_a^{MS}$), quantum yield (Φ) and solubility. In this chapter we expand our experimental and theoretical approaches to methoxy-substituted MCHs, dissecting the possibility of achieving reversible pH changes as high as Π (from pK_a^{GS} down to pK_a^{MS}) by using buffered solutions – *i.e.*, aqueous solutions of BIPS whose dark equilibrium composition is not quantitatively shifted towards the undissociated form. Moreover, a detailed description of how to prepare, screen and select the best candidate from a library of differently substituted compounds will be outlined.

5.2 Preliminary screening

As mentioned in previous chapters, working with MCHs in aqueous environments can be problematic due to their tendency to hydrolyze irreversibly.



Scheme 5.1. Library of compounds investigated in this study.

We reasoned that *ortho*- or *para*-substitution of either the indolium or the chromene moiety with electron-donating groups might increase the chemical stability of BIPS by disfavoring water nucleophilic attack.

Therefore, we decided to quest for favorable mesomeric effects by screening a library of four different compounds bearing a methoxy group directly conjugated to the ene-iminium core. Compounds **5-8** were prepared following standard literature procedures and characterized by means of ^1H and ^{13}C NMR, HR-MS and single-crystal X-ray diffraction (see Experimental Section for more details). Initially, to probe the hydrolysis kinetics of compound **5-8**, we adopted the protocols already described in Chapter 3 and 4^[113,120]: we dissolved each photoswitch in aqueous phosphate buffers and monitored its hydrolysis kinetics at different pH values by means of UV-Vis spectroscopy.

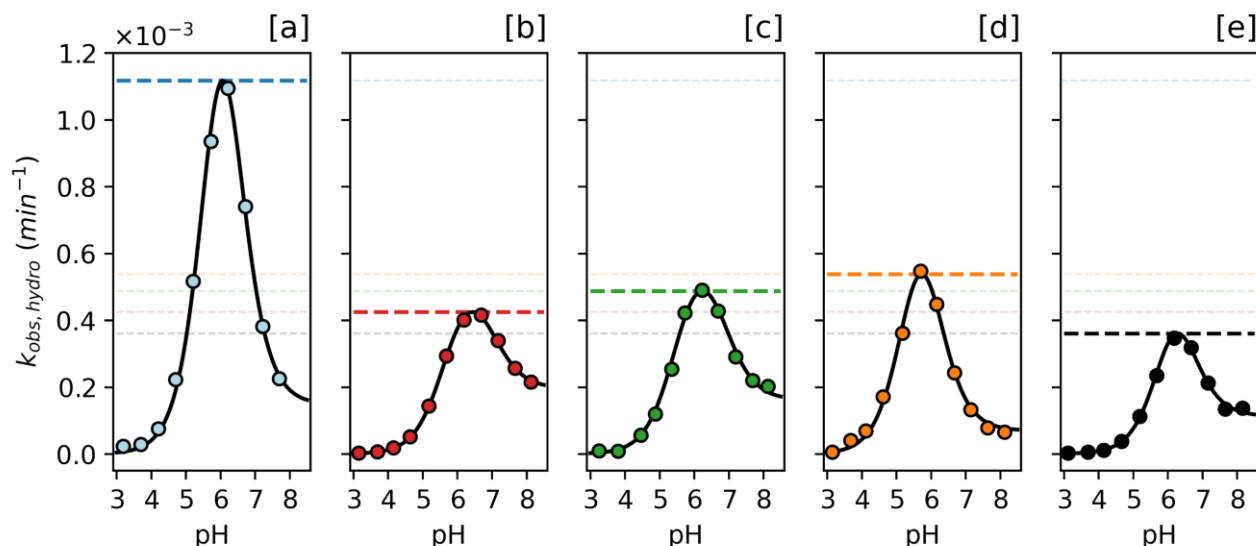


Figure 5.2. The profiles against the pH of $k_{\text{obs,hydro}}$ for compounds **1**, **5**, **6**, **7** and **8** are represented in panel [a],[b],[c],[d] and [e], respectively. The dashed lines represent a visual help to distinguish the maximum $k_{\text{obs,hydro}}$ of each compound. Conditions: [**5-8**] = 25 μM , [buffer] = 20 mM (pH 3 - 8), $T = 298\text{ K}$.

Apparent rate constants of hydrolysis ($k_{\text{obs,hydro}}$) were calculated from the corresponding linearized absorbance profiles and plotted against the pH. In all cases, the obtained bell-shaped profiles fit well the model equation for the hydrolysis derived in Chapter 3 (solid lines, Figure 5.2). To visually help comparison with Liao's merocyanine (which we take as reference), all the obtained hydrolysis profiles are reported in Figure 5.2 sharing the same y axis. The horizontal

lines represent the maximum $k_{\text{obs,hydro}}$ and are color-coded according to the respective experimental points. As can be seen at first glance from Figure 5.2, the compounds displaying the slowest hydrolysis rates are compounds **5** and **8** (Figure 5.2 b and e). A comparison of the microscopic rate constants associated to the evoked mechanism of hydrolysis is given in Figure 5.3.

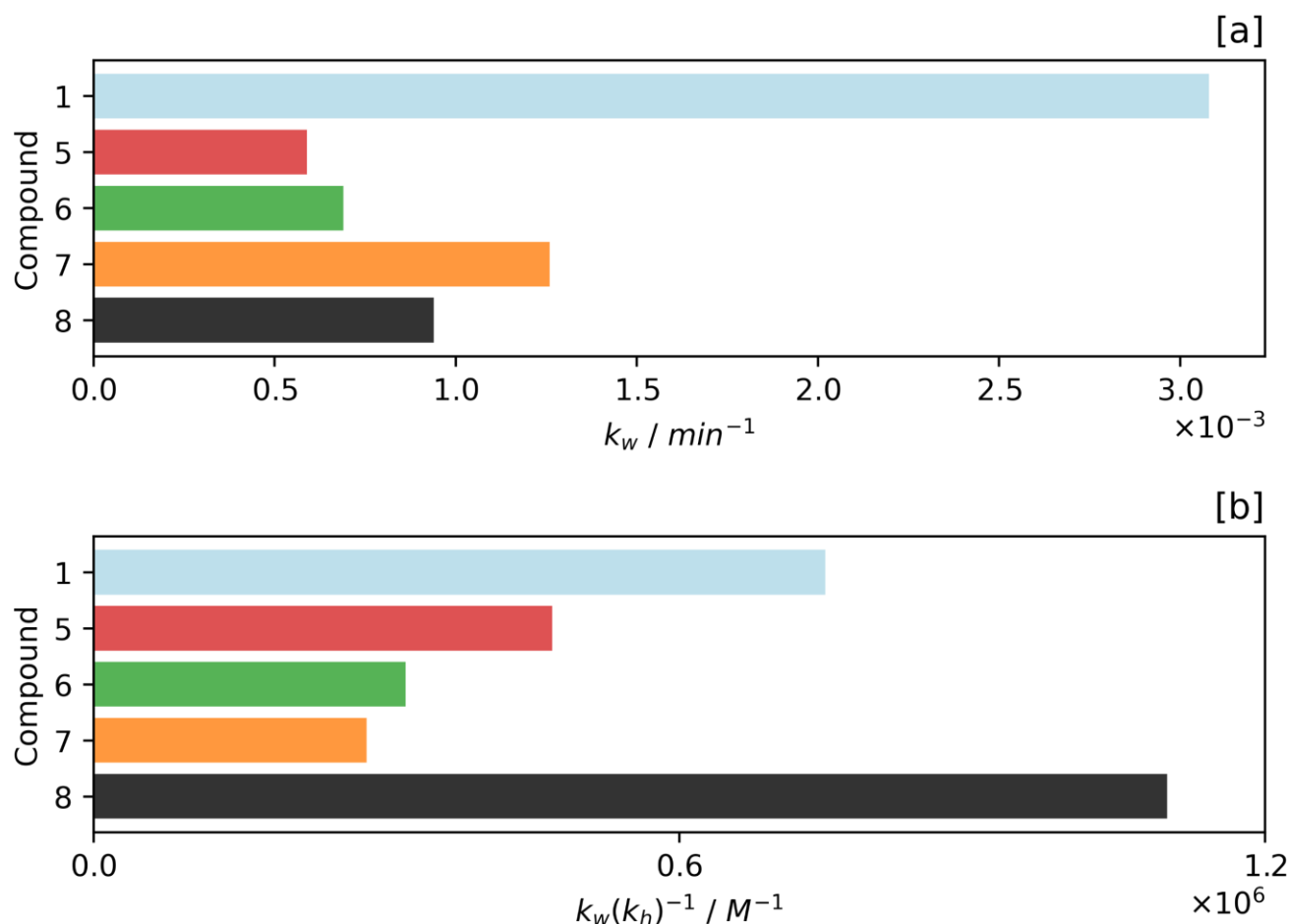


Figure 5.3. In [a] the comparison between compounds **1,5-8** in terms of magnitude of k_w . in [b] comparison of the same compounds in terms of magnitude of the ratio k_w/k_h . The color code is maintained identical to Figure 5.3.

As compared to **1**, it is possible to notice that the nucleophilic addition of water (k_w) is always slower in the presence of a methoxy group (Figure 5.3 a), and that compound **5** has the lowest kinetic tendency to react with water. On the other hand, the carbinol tetrahedral intermediate

(k_w/k_h) react favorably (either backward or forward) only in the case of compound **8** (Figure 5.3 b). These preliminary findings suggest that the compounds having the highest resistance to hydrolysis are **5** and **8**. Our analysis continued determining which between compounds **5-8** had the best set of parameters for maximizing the photochemical ΔpH . First, we went on by determining the $\text{MC} \rightleftharpoons \text{SP}$ equilibration and the K_c values by measuring UV-Vis kinetics.

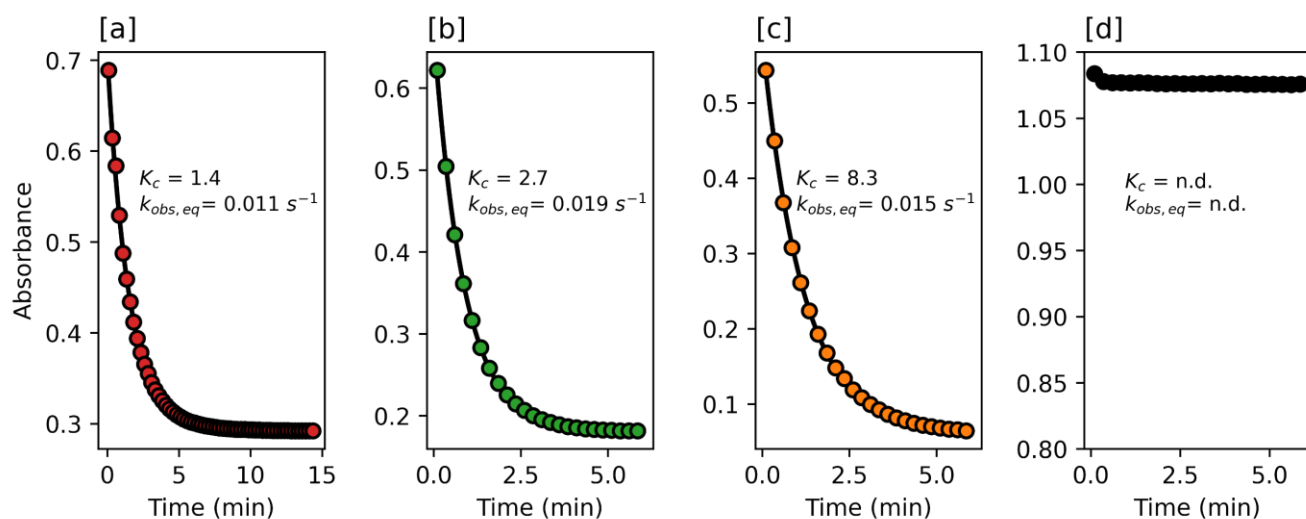


Figure 5.4. Equilibration kinetics experiment for compounds **5-8**. In each panel is reported the K_c and the $k_{obs,eq}$ resulting from the best fit to first-order kinetics. For compound **8**, in [d], it was impossible to fit any parameters due to the fast and small absorbance excursion. Conditions: $[\mathbf{5-8}] = 25 \mu\text{M}$, $[\text{buffer}] = 20 \text{ mM}$ ($\text{pH} = 9.5$), $T = 298 \text{ K}$.

The experiment is analogue to the ones described in Chapter 3 and 4: an aqueous solution of MCH is injected in a potassium phosphate solution at high pH value and the decay of the transiently formed MC is followed until equilibration occurs (Figure 5.4). From this analysis it has been possible to determine that **5** has the lowest K_c value in the series (1.46 ± 0.06) and, strikingly, that compound **8** shows an extremely fast equilibration kinetics. Indeed, with our equipment, it was not possible to extract any reliable parameter from the collected data due to the rapid equilibration reaction (Figure 5.4 d). This is also a sign that the SP form of **8** might be relatively unstable with respect to the MC form and we had to turn towards other experimental

approaches to understand better if **8** was still a good candidate in our screening. To do so, we determined the pK_a^{GS} of each compound by spectrophotometry (Figure 5.5). The results are in line with the values reported by Zhang and co-workers for **5** and **8** (7.05 and 6.51, respectively).^[85] Of note, compound **5** and **6** (substitution on the indolium side) have the lowest dark acidity (Figure 5.5 e,f), while **7** and **8** (substitution on the phenolic moiety) display a markedly increased acidic behavior (Figure 5.5 g,h).

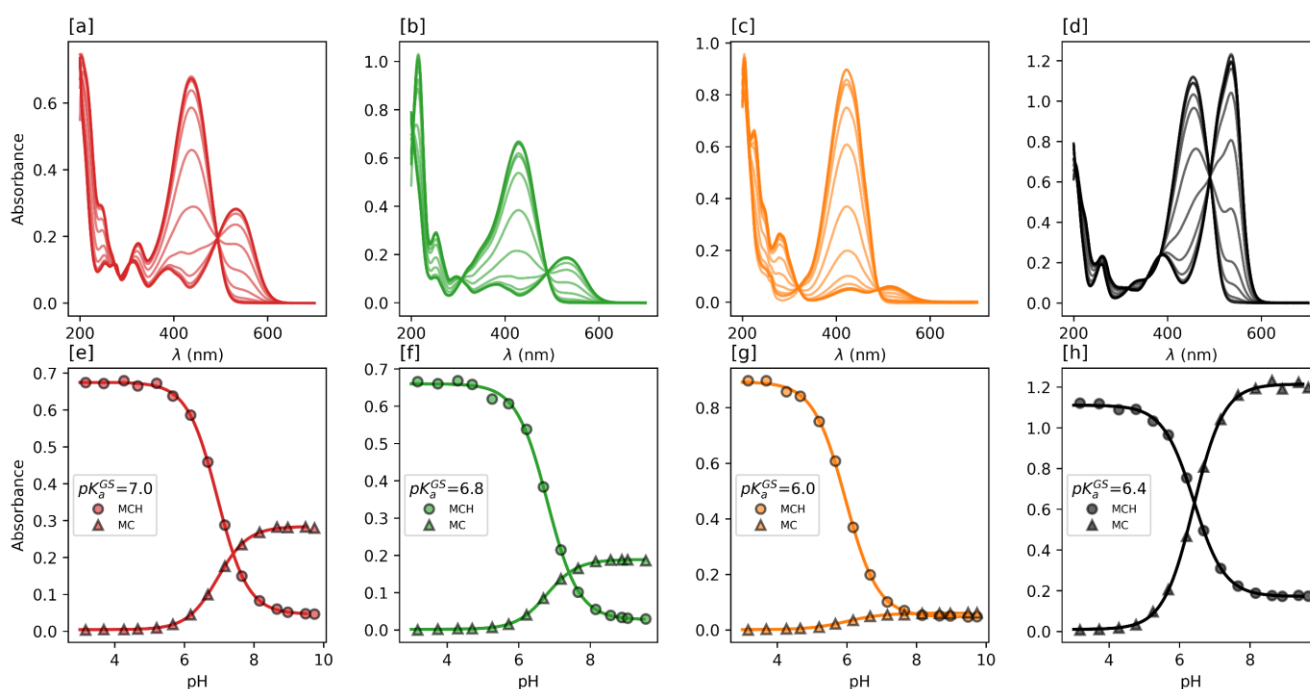


Figure 5.5. UV-Vis titrations of compounds **5-8** in dark conditions. The absorbance of the MCH and MC forms is detected at increasing pH values which were measured *in-situ* using a pH meter. Conditions: [**5-8**]= 25 μ M, [buffer]= 20 mM (pH = 3-10), T = 298 K.

This experiment confirms that the fast equilibration kinetics observed for **8** (Figure 5.4 d) is due to a relatively low stability of the SP form with respect to MC form. As matter of fact, it is possible to observe from Figure 5.5 h that the absorbance of the MC at the end of the titration is the most intense of the whole series of compounds, and points towards a situation in which the amount of SP form present is very small. Overall, these preliminary experiments showed that

compound **5** features the best hydrolytic stability and the lowest dark acidity, consequently we moved on analyzing exclusively this compound.

5.3 Narrowing the focus

As discussed in the previous paragraph, compound **5** displays the best compromise between low dark acidity and the slow hydrolysis, consequently, we decided to focus our efforts on this compound.

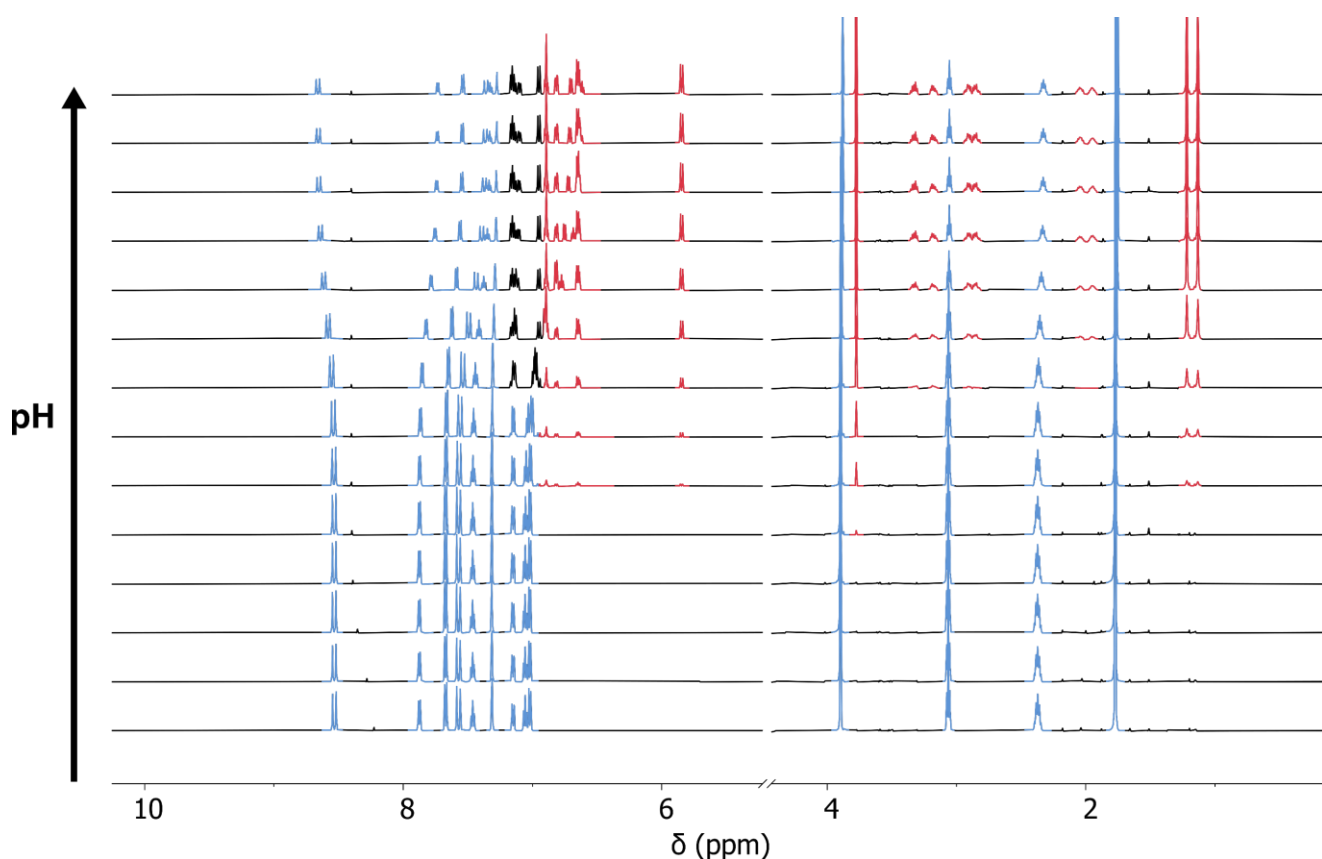


Figure 5.6. ^1H NMR (600 MHz, 298 K, $\text{H}_2\text{O}:\text{D}_2\text{O}$ [6:4]) titration of compound **5** at increasing pH values (from bottom pH = 3.0 to top pH = 9.5 every 0.5 units). Conditions: $[\text{5}] = 0.1$ mM, $[\text{buffer}] = 20$ mM (pH = 3-10), $T = 298$ K. The blue signals are attributed to the MCH/MC couple and the red signals to the SP compound. The black signals are left unattributed due to the overlap of MC and SP signals.

First, we used ^1H NMR spectroscopy to confirm the thermodynamic constants found so far for **5**. As it can be seen in Figure 5.6, the system behaves similarly to compounds **1-3** as described

in Chapter 3. In fact, the MCH form is abundant at low pH values (bottom of Figure 5.6) and, as the pH increases, it undergoes a chemical shift perturbation because of the exchange with MC. At the same time, a new set of signals belonging to the SP form appears at pH values close to the pK_a^{GS} . By applying the same protocol introduced in Chapter 3, it was possible to determine pK_a and K_c independently with one titration (Figure 5.7).

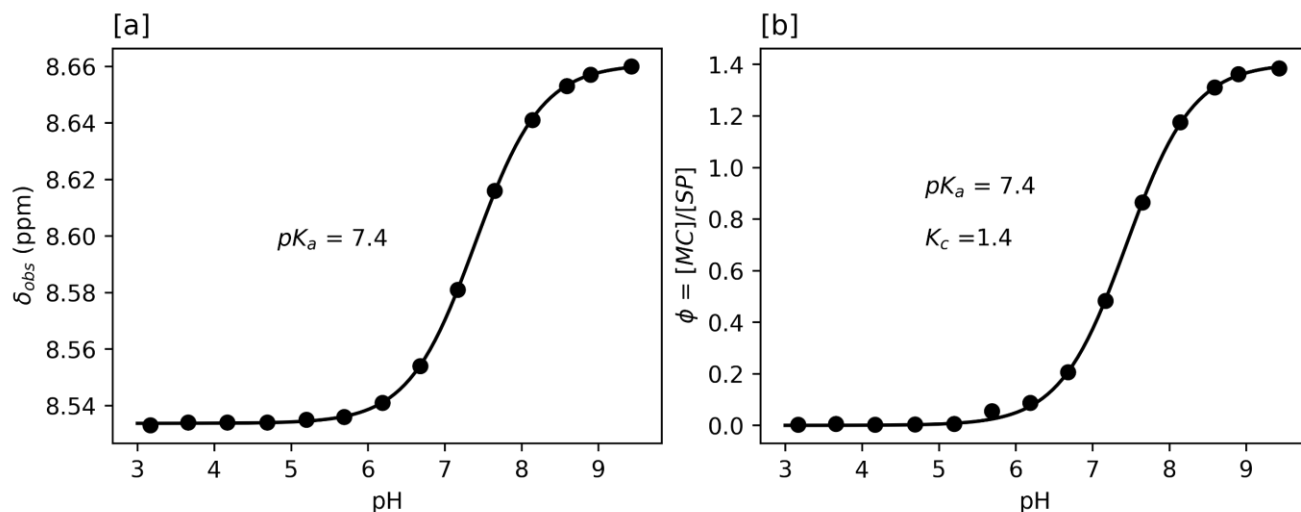


Figure 5.7. In [a] chemical shift perturbation of the doublet located at 8.55 ppm, in [b] integral ratio between the doublet located around 5.8 ppm (SP) and the doublet at 8.55 ppm (MCH/MC).

As it can be seen in Figure 5.7, the chemical shift perturbation of the doublet in the 8.5 ppm region allows to directly determine the pK_a value (which was found to be 7.4 ± 0.1 , Figure 5.7a), while the integral ratio between the same signal and the doublet at around 5.7 ppm (i.e., the ϕ value) allows to confirm the pK_a value while simultaneously determining the K_c (Figure 5.7b represents the NMR value, found in good agreement with that obtained by UV-Vis spectroscopy which is $K_c = 1.4 \pm 0.1$). We then moved on to characterize the acidity of the metastable state of **5** by UV-Vis titration under light illumination. In this case, we probed two different LED-light sources in order to see whether we could trigger the photoswitch with a more

red-shifted light source. First, the experiment was conducted under 425 nm light irradiation (Figure 5.8) to provide consistency with the protocol adopted in Chapter 3. The pK_a^{MS} determined with this method resulted to be 3.43 ± 0.04 , which is around one pK unit higher than the one of compound **1** (2.47 ± 0.04).^[113]

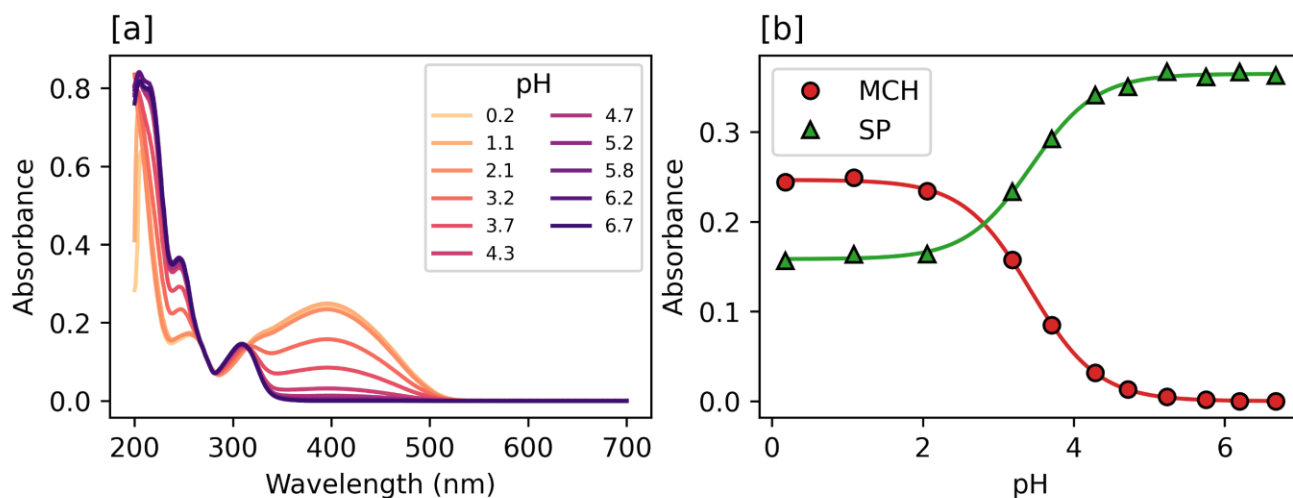


Figure 5.8. UV-Vis titration of compound **5** under 425 nm light irradiation [a]. The absorbance of the *cis*-MCH and SP forms is detected at increasing pH values which were measured *in-situ* using a pH meter [b]. Conditions: [5] = 25 μ M, HCl dilutions or [buffer] = 20 mM (pH = 0 - 6.5), T = 298 K.

After the experiment with the 425 nm LED-light source, we performed another titration under 500 nm illumination. From this experiment, we could observe that the tail suppression of the *cis*-MCH band is more effective (Figure 5.9 a) and we could calculate a pK_a^{MS} value (3.31 ± 0.03) which is 0.1 pK units lower than with 425 nm. This result can be readily explained in terms of overlap between the bands of MCH, *cis*-MCH and the emission spectrum of the light sources. Indeed, the 425 nm LED-light emission spectrum superimposes more with both MCH and *cis*-MCH (Figure 5.10 a) as compared to the 500 nm LED-light source (Figure 5.10 b). Thus, the higher pK_a^{MS} detected under 425 nm may be ascribed to the higher overlap of the light source emission with the *cis*-MCH band, which in turn promotes back-isomerization to MCH. This is

partially prevented by using a 500 nm light which, as shown in Figure 5.10 b, revealed to be a better compromise for obtaining a high overlap with the MCH band (orange curve) and a low overlap with the *cis*-MCH band (purple curve). With these experiments, we assessed that the LED source at 500 nm was our best available option to maximize the photoacidity of compound **5** and for potentially increasing its photochemical ΔpH .

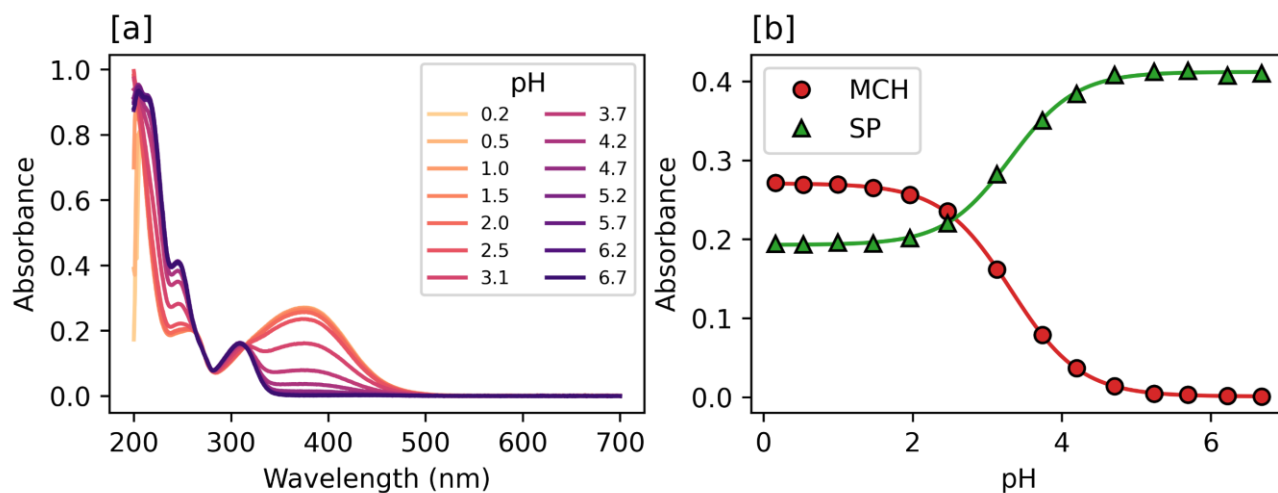


Figure 5.9. UV-Vis titration of compound **5** under 500 nm light irradiation [a]. The absorbance of the *cis*-MCH and SP forms is detected at increasing pH values which were measured *in-situ* using a pH meter [b]. Conditions: $[\mathbf{5}] = 25 \mu\text{M}$, HCl dilutions or $[\text{buffer}] = 20 \text{ mM}$ (pH = 0 - 6.5), $T = 298 \text{ K}$.

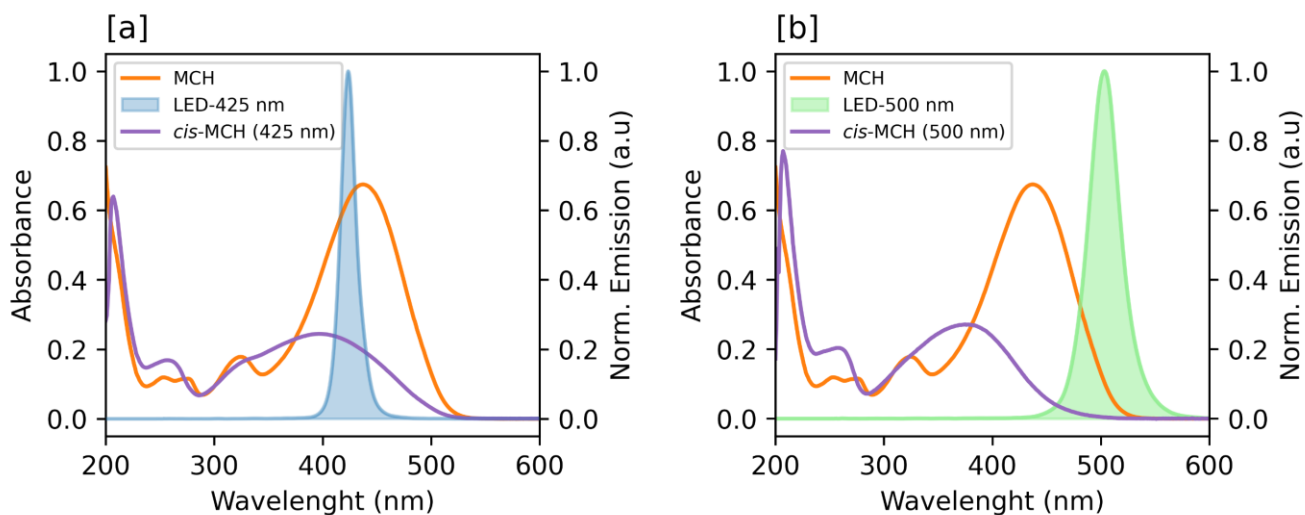


Figure 5.10. In [a]: comparison of the UV-Vis spectrum of MCH (orange), *cis*-MCH (purple) and the 425 nm LED emission spectrum (solid blue). In [b]: the same as [a] with 500 nm LED emission spectrum (solid green).

Finally, we measured the rate constants of relaxation from the metastable state as function of the pH. This was done by illuminating samples of **5** in water at increasing pH values and by subsequent calculation of the apparent rate constant of relaxation from the obtained kinetic traces (Figure 5.11).

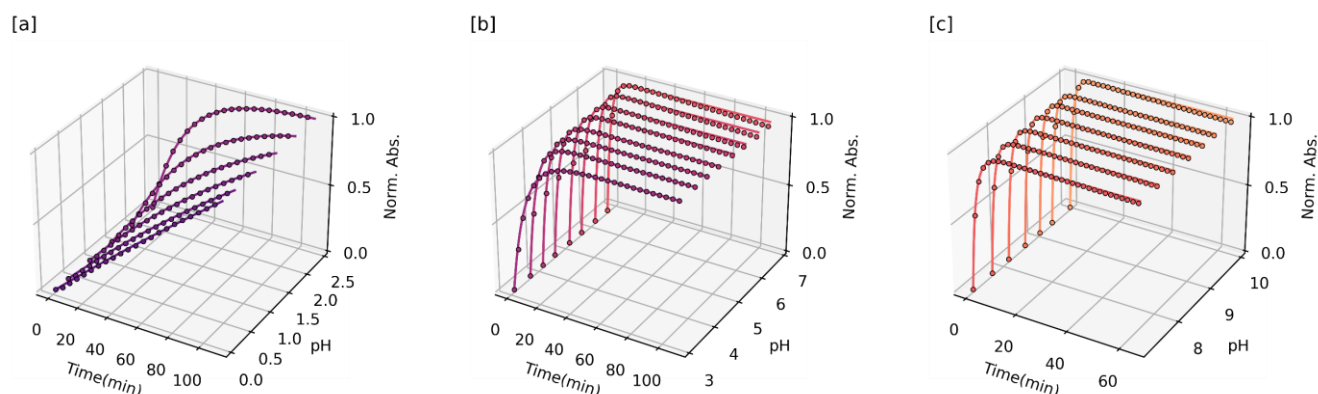


Figure 5.11. Kinetics experiment for the determination of $k_{\text{obs,relax}}$ vs. pH profile for compound **5**. The absorbance values are normalized between 0 and 1 to aid visual comparison. In panel [a] the kinetic traces for $0 < \text{pH} < 3$, [b] $3 < \text{pH} < 7$ and [c] $7 < \text{pH} < 10$. Conditions: $[\mathbf{5}] = 25 \mu\text{M}$, HCl dilutions or $[\text{buffer}] = 20 \text{ mM}$ ($\text{pH} = 0 - 6.5$), $T = 298 \text{ K}$, illumination source: LED 500 nm. Notice the progressive increase of the steepness of the initial points passing from [a] to [c].

The recovery rate is slow at acidic pH values (Figure 5.11 a), increases at intermediate values (Figure 5.11 b) and then reaches the maximum at alkaline pH (Figure 5.11 c). The obtained kinetic constants were then plotted against the pH and the resulting double-sigmoidal profile analyzed as described in Chapter 3. The parameters calculated with this approach match closely the NMR and UV-Vis values (see Experimental Section for more details). In the next section, we will focus on how to achieve the highest possible pH excursion by studying the solubility of **5** as a function of the neutralization extent (a).

5.4 pH photoswitching

In this section we will analyze the pH switching behaviour of compound **5**. As described in Chapter 3, we ran the first experiments on compound **5** in aqueous 20 mM KCl for ensuring a quick and reliable response of the pH meter. The solutions were saturated by stirring an excess of solid **5** for 15 minutes at 298 K, followed by filtration.

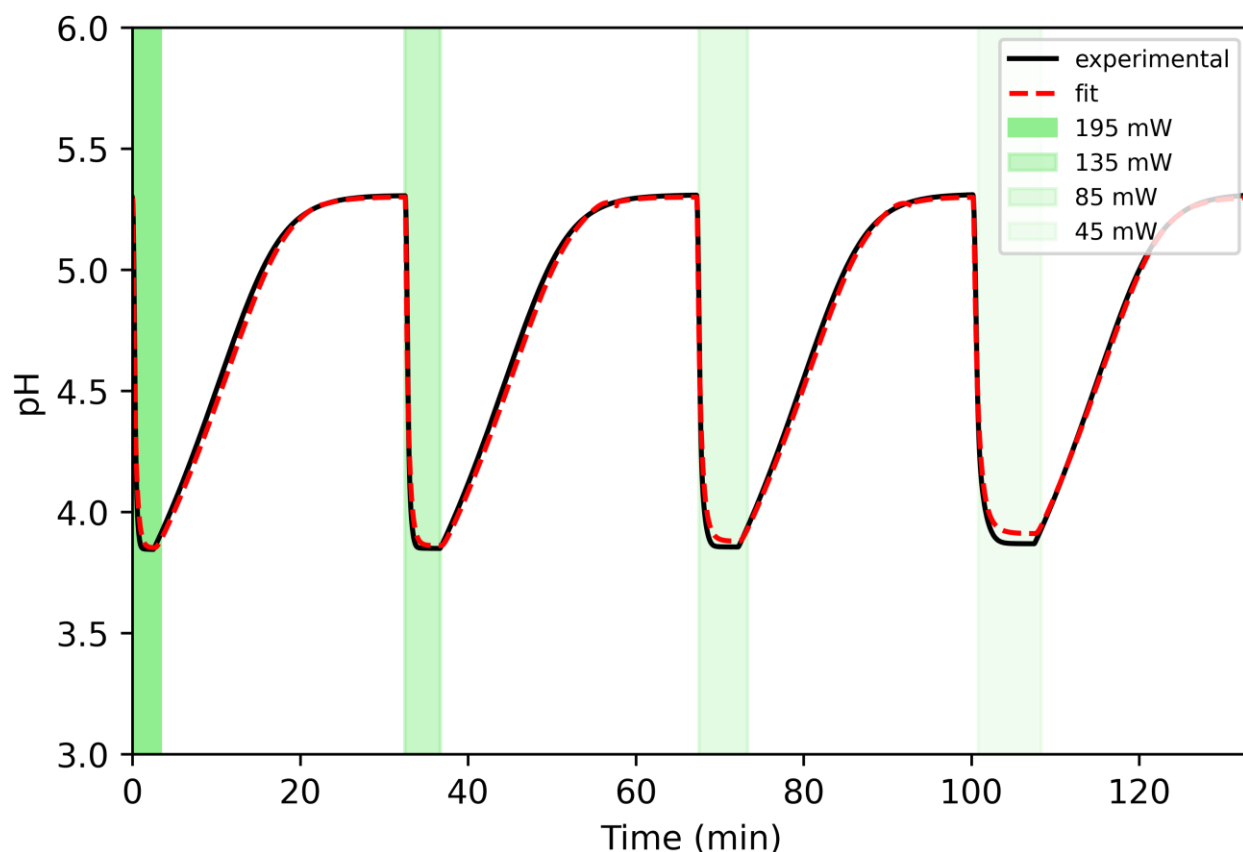


Figure 5.12. Variable power pH jumps. The power of the illumination is represented in the legend of the picture. The black solid line are the experimental data, the red dashed line is the best fit data and the areas in green represent the power and the time of illumination.

The measured pH at equilibrium in the dark agrees with the value predicted by the weak acids law using pK_a^{GS} and the experimentally determined solubility at 298 K. The pH jumps were carried out at four different powers and the observed pH dynamics fit to our four-state model

(Figure 5.13). By adopting this approach, we could calculate the quantum yield which was estimated to be 0.40 ± 0.03 (see Experimental Section for more details). We then moved on by artificially increasing the pH value in the dark using increasing aliquots of NaOH. Upon equilibration of the partially neutralized solutions of **5** in the dark, we observed that the pH trace would stabilize at values that follow the Henderson-Hasselbalch equation (Figure 5.14 a). Moreover, another important feature was how the solubility was influenced by the quantity of base added to the system (Figure 5.15 b).

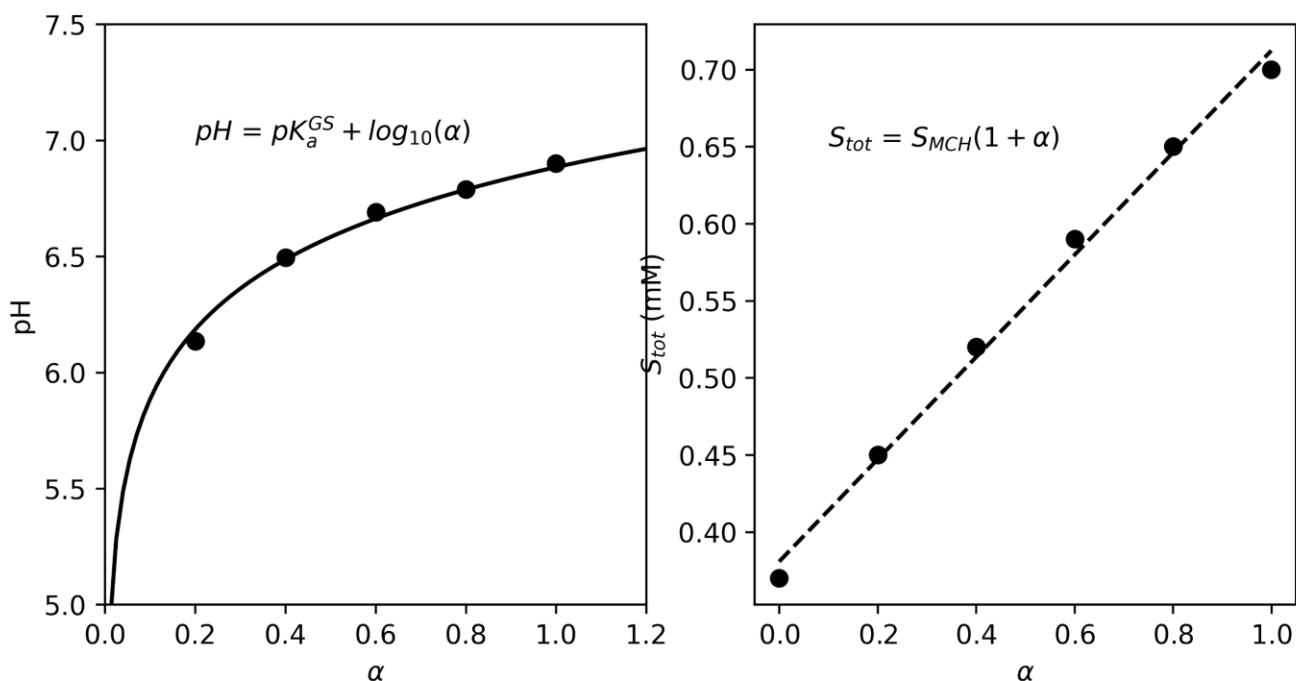


Figure 5.16 In [a] best fit to the Henderson-Hasselbalch equation to the experimental pH of **5** after partial neutralization. In [b] the dependency of the total solubility ($[MCH] + [MC] + [SP]$) of **5** against the equivalents of strong base.

Indeed, this was following a linear trend with respect to the equivalents of base (α in Eq. 5.2) that were added to the saturating solution, and such an effect finds explanation in the higher solubility of the MC and SP anions respect to MCH (see Experimental Section for more details).

Both the slope and the intercept of this linear trend are the intrinsic solubility of MCH at 298 K in absence of other equilibria (S_{MCH} in Eq. 5.2).

$$S_{tot} = S_{MCH}(1 + \alpha) \quad \text{Eq. 5.2}$$

The partially neutralized solutions of **5** are buffer solutions. Hence, we went on to probe the photochemical properties of the solution containing solid **5** neutralized at $\text{pH} = \text{p}K_a^{\text{GS}}$.

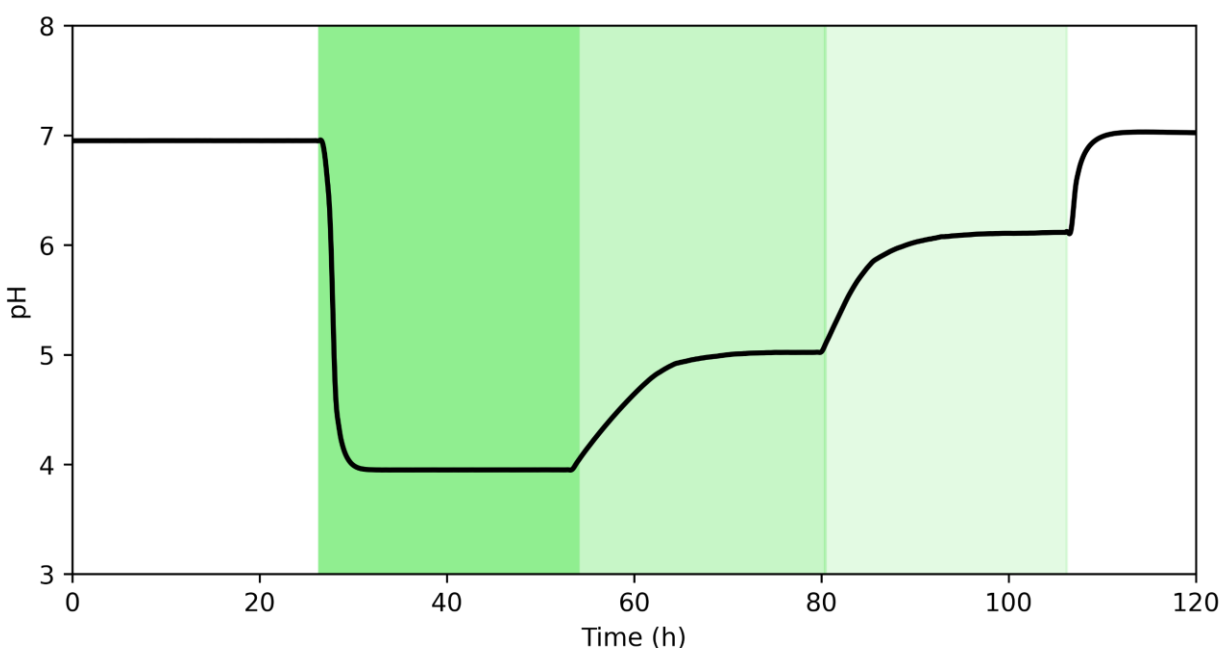


Figure 5.17 Experimental pH jump with different illumination intensities. In the first section the light was tuned so to arrive at $\text{pH} = 4$. In the following sections the light was tuned to reach pH values of 5, 6 and then 7 again in the dark.

After filtration and equilibration at 298 K, the sample was irradiated with 500 nm light: at relatively high output power (40 mW) we observe a deep pH switch down to pH 4. By modulating the light intensity, it was possible to tune the pH value of the solution. In other words, regulation of the light intensity can be used to carefully control the pH of our buffer solution (Figure 5.17). In addition, we found that the fatigue resistance of our system is very high, as we reached pH jumps up to 3 pH units which can be triggered repeatedly for more than two hours using 500

nm light irradiation (Figure 5.18). Importantly, the observed pH dynamics fit very well our four-state model (see Experimental Section for more details).

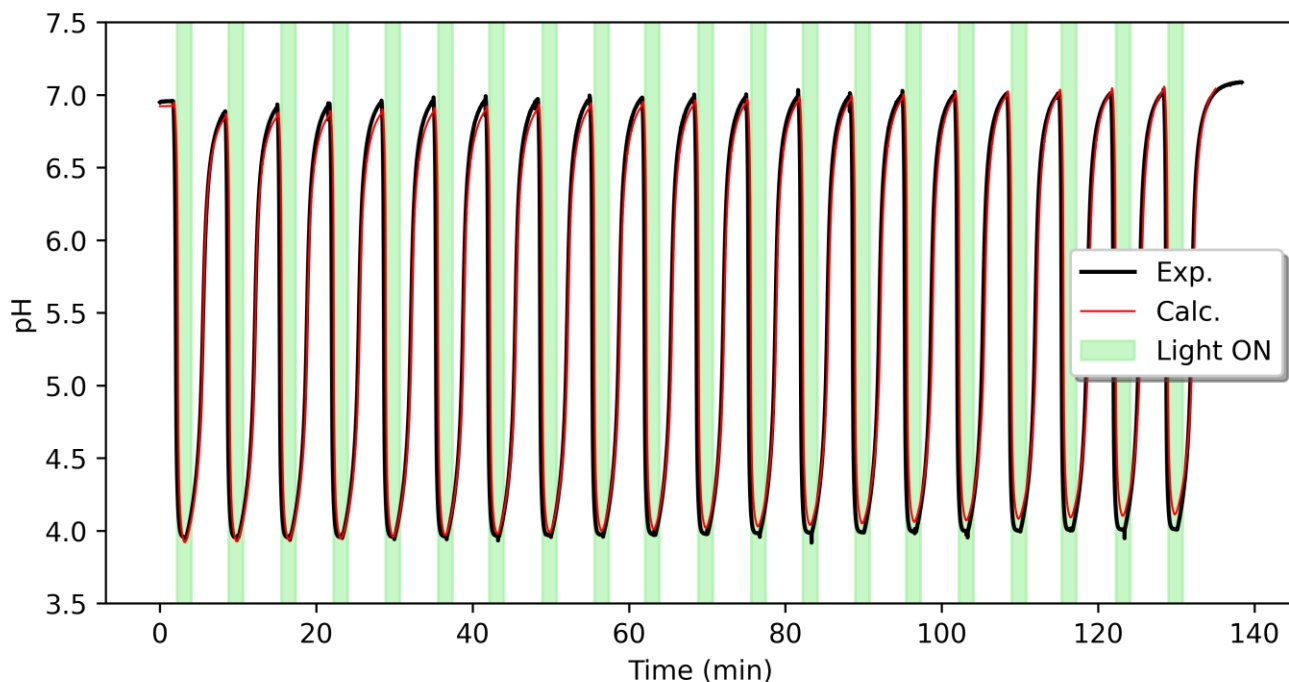


Figure 5.19. Repeated pH jump experiment using compound **5**. The illumination was stopped until no pH variation was observable and turned on at a fixed time delay.

5.5 Conclusions

The findings presented in this chapter highlight how the library of compounds **5-8** demonstrates a lower tendency to hydrolyze with respect to the prototype **1** designed by Liao. A first screening on this aspect allowed us to determine which compound had the slowest hydrolysis and, in these terms, **5** and **8** showed the slowest rate of nucleophilic addition of water. An ulterior filter was applied to the set of compounds based on their dark acidity. As a matter of fact, **5** is the most basic having the highest pK_a^{GS} and the lowest measurable K_c . The runner-up, **8**, demonstrates signs of unstable SP form that can compromise the photoactivity and, in addition,

has high dark acidity despite K_c being virtually negligible. In the photochemical pH switching section was demonstrated how the system comprising **5** and a sub-stoichiometric amount of strong base acts as a buffer solution with photochemical capabilities. Finally, the pH switching behavior has been analyzed and the endurance of the system has been put to test. The photoswitch demonstrated very good stability and resistance to hydrolysis and photochemical fatigue over a timespan of about two hours starting from a pH of physiological and biological interest.

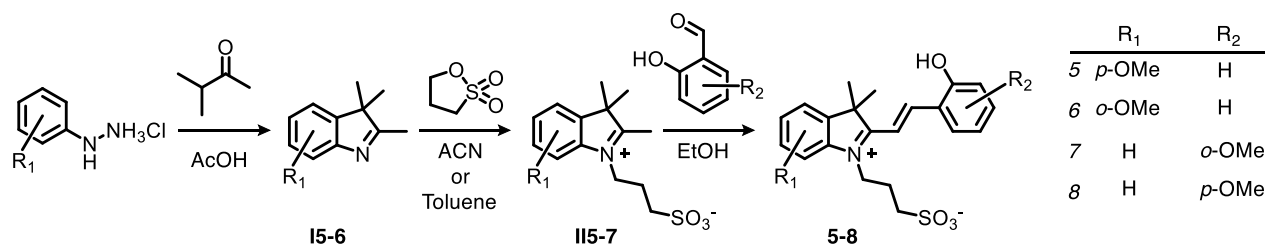
5.6 Experimental section

5.6.1 General Remarks

All reagents and solvents were purchased from commercial suppliers (Sigma-Aldrich, TCI, Acros Organics, Fluorochem, Abcr) and used without further purification. Compound **117** was synthesized and purified as described previously.^[113] H₂O used in all preparations was filtered with a MilliQ-Integral5 purification system (mQ H₂O). NMR spectra were recorded at 298 K on the following spectrometers: Bruker Avance III-400 equipped with a BBFO_z probe, Bruker Avance 400 equipped with a BBI_z probe, Bruker Avance NEO-400 equipped with a BBFO probe (characterization), and on a Bruker Avance III HD-600 equipped with a CPPBO_z ATMA probe (pH titrations). Chemical shifts (δ) are reported in parts per million (ppm), while coupling constants (J) are given in Hertz (Hz). Solvent residual signals are used as internal reference for spectra alignment (CDCl₃: δ = 7.26 ppm, DMSO-*d*₆: δ = 2.50 ppm, D₂O: δ = 4.87 ppm). Electrospray-ionization HRMS analyses were run (positive mode/direct injection) on a Waters XEVO G2-S GTOF spectrometer interfaced with Acquity UPLC pumps and sample manager system. UV-

Vis spectra and kinetics were acquired on an Agilent Cary 60 spectrometer equipped with an 18-cell holder coupled to a Huber thermostat, using Suprasil quartz cuvettes (114-QS) from Hellma Analytics. pH measurements were performed using Metrohm pH module 867 or Titrando 888 coupled with Unitrode Pt1000 or Biotrode glass electrodes; pH data were processed using the software Metrohm Tiamo Light. Samples photoirradiation was carried out using a Prizmatix FC-LED-425Z or FC-LED-500Z high-power LED light sources ($\lambda = 425$ or 500 nm, respectively). The light beam was delivered by polymer optical fibers (core $1500\ \mu\text{M}$) i) positioned orthogonally to and just below the liquid/air interface of sample solutions (UV-Vis) or ii) connected to an FCM1-06 collimator coupled with a 45° mirror cage, resulting in a $25\ \text{mm}$ light beam tilted by 90° (pH jumps). Power measurements of the fiber-coupled LED output were made with Thorlabs S142C integrating sphere photodiode power sensor; the uncertainty is within 3-5%. Potassium phosphate buffers from pH 3 to 10 were prepared titrating a solution of H_3PO_4 (100 mM, 1L) with KOH 10 M. Diluted stocks of H_3PO_4 or HCl were used below pH 3. All buffer stocks were stored at room temperature. In order to account for the pH change in sample preparations, the pH of each buffer stock is measured again after dilution (1/5, 20 mM) in mQ H_2O . Unless stated otherwise, UV-Vis, ^1H NMR and pH jump analyses were carried out and analysed as described previously.^[113] In the case of UV-Vis titrations the error on pH values results from multiple reading before and after the experiments ($\leq \pm 0.04$), whereas in the case of NMR samples we account for an uncertainty of ± 0.1 pH units.

5.6.2 Synthetic Procedures

Scheme S 5.1. Synthetic route for the synthesis of **5-8**.*Synthesis of 2,3,3-trimethylindolenines, I5-6*

I5: In a 250-ml round bottom flask, *p*-methoxyphenylhydrazine hydrochloride (5.12 g, 29.3 mmol) and isopropyl methyl ketone (3.8 ml, 35.0 mmol) were dissolved in glacial AcOH (85 mL) and the mixture was heated to reflux under N₂ atmosphere for 24 h. After evaporation of the solvent under reduced pressure, the residues were dissolved in DCM and the resulting organic layer washed with brine (3 × 100 mL), satd. Na₂CO₃ (3 × 100 mL) and dried over anhydrous MgSO₄. Solvent was removed under reduced pressure and the crude product purified by flash chromatography (SiO₂, hexane/EtOAc 2:1). Fractions containing the product were kept dry by rotary evaporation. The obtained yellow oily residue was further purified by sublimation under vacuum, yielding **I1** as a white crystalline solid (3.49 g, 62.8 %). ¹H NMR (400 MHz, DMSO-*d*₆) δ (ppm): 7.30 (d, *J* = 8.4 Hz, 1H), 7.03 (d, *J* = 2.5 Hz, 1H), 6.80 (dd, *J* = 8.4, 2.5 Hz, 1H), 3.76 (s, 3H), 2.15 (s, 3H), 1.22 (s, 6H). ¹³C NMR (101 MHz, DMSO-*d*₆) δ (ppm): 185.22, 157.37, 147.52, 147.11, 119.45, 112.16, 108.15, 55.41, 53.29, 22.63, 14.88.

I6: The same procedure above is applied. It was noted, however, that compound **I6** is rather unstable as compared to **I5**. Thus, the oily residue obtained after flash chromatography was used in the next step without further purification. ¹H NMR (400 MHz, CDCl₃) δ (ppm): 7.10 (t, *J*

= 7.8 Hz, 1H), 6.83 (d, J = 7.8 Hz, 1H), 6.79 (d, J = 7.8 Hz, 1H), 3.90 (s, 3H), 2.22 (s, 3H), 1.22 (s, 7H). ^{13}C NMR (101 MHz, CDCl_3) δ (ppm): 186.36, 150.91, 147.67, 141.48, 126.24, 113.58, 110.05, 55.59, 53.98, 22.95, 15.27. HRMS (ESI/QTOF) m/z : $[\text{M} + \text{H}]^+$ Calcd for $\text{C}_{12}\text{H}_{16}\text{NO}^+$ 190.1226; Found 190.1228.

Synthesis of 2,3,3-trimethylindolium-propyl-1-sulfonates, II5-6

II5: In a 100-mL round bottom flask **I5** (1.10 g, 5.8 mmol) and 1,3-propanesultone (1.21 g, 9.9 mmol) of were dissolved in MeCN (20 mL) and the solution heated to reflux for 16 h. The resulting mixture was cooled down to room temperature and added dropwise to EtOAc under stirring, leading to a white-green precipitate. The solid was separated by vacuum filtration, washed with EtOAc (3 \times 10 mL) and recrystallized from hot MeCN, yielding **II5** as a purple solid (1.07 g, 59.1%). ^1H NMR (400 MHz, $\text{DMSO}-d_6$) δ (ppm): 7.95 (d, J = 8.8 Hz, 1H), 7.45 (d, J = 2.5 Hz, 1H), 7.15 (dd, J = 8.8, 2.5 Hz, 1H), 4.61 (t, J = 7.5 Hz, 2H), 3.86 (s, 3H), 2.76 (s, 3H), 2.60 (t, J = 6.6 Hz, 2H), 2.13 (p, J = 7.1 Hz, 3H), 1.51 (s, 6H). ^{13}C NMR (101 MHz, DMSO) δ (ppm): 193.54, 160.56, 144.00, 134.38, 116.42, 114.30, 109.37, 56.05, 53.91, 47.33, 46.54, 23.86, 22.12, 13.50.. HRMS (ESI/QTOF) m/z : $[\text{M} + \text{H}]^+$ Calcd for $\text{C}_{15}\text{H}_{22}\text{NO}_4\text{S}^+$ 312.1264; Found 312.1266.

II6: In a 50-mL round bottom flask **I6** (0.80 g, 4.2 mmol) and 1,3-propanesultone (0.52 g, 4.2 mmol) were added and the flask sealed with a septum under N_2 atmosphere. The mixture was heated up at 120 $^\circ\text{C}$ under stirring for 15 minutes. The dark brown mixture was treated with MeCN (20 mL) and the resulting precipitate filtered, washed with MeCN (3 \times 20 mL) and dried, yielding **II6** a beige solid (0.27 g, 20%). ^1H NMR (400 MHz, $\text{DMSO}-d_6$) δ (ppm) 7.57 (t, J = 7.9 Hz, 1H), 7.36 (d, J = 7.4 Hz, 1H), 7.29 (d, J = 8.1 Hz, 1H), 4.67 (m, 1H), 4.00 (s, 3H), 2.79 (s,

3H), 2.59 (t, $J = 6.9$ Hz, 2H), 2.16 (p, $J = 7.1$ Hz, 2H), 1.50 (s, 6H). ^{13}C NMR (101 MHz, DMSO) δ 194.99, 148.50, 144.60, 131.00, 128.34, 115.27, 112.96, 56.75, 53.99, 50.05, 47.76, 24.66, 22.30, 13.61.

General procedure for the synthesis of compounds 5-8

In a 50-mL round-bottom flask 2,3,3-trimethylindolium-propyl-sulfonates (**II5-7**) were dissolved in absolute EtOH (ca. 20 mL/g). The corresponding salicylaldehyde (2 equivalents) was added, the flask sealed with a septum and the solution degassed by gentle N_2 bubbling (10 min) prior to heating it up to 90 °C under stirring for 24 h. The resulting orange precipitate was filtered, washed thoroughly with EtOH to remove unreacted materials and recrystallized from hot MeOH. Crystals were collected, washed with cold MeOH and dried under vacuum (isolated yield $\leq 50\%$). X-ray quality crystals can grow also using EtOH as co-solvent or by slow evaporation of NMR samples.

5. ^1H -NMR (400 MHz, DMSO- d_6) δ 10.92 (s, 1H), 8.50 (d, $J = 16.4$ Hz, 1H), 8.24 (d, $J = 7.9$ Hz, 1H), 7.95 (d, $J = 8.8$ Hz, 1H), 7.81 (d, $J = 16.4$ Hz, 1H), 7.51 (d, $J = 2.5$ Hz, 1H), 7.44 (m, 1H), 7.17 (dd, $J = 8.8, 2.5$ Hz, 1H), 7.02 (d, $J = 8.3$ Hz, 1H), 6.97 (t, $J = 7.6$ Hz, 1H), 4.77 (t, $J = 6.8$ Hz, 2H), 3.89 (s, 3H), 2.63 (t, $J = 6.8$ Hz, 2H), 2.16 (p, $J = 6.8$ Hz, 2H), 1.76 (s, 6H). ^{13}C -NMR (101 MHz, DMSO- d_6) δ 179.48, 160.72, 158.62, 146.73, 145.70, 135.17, 134.18, 129.53, 121.41, 119.99, 116.54, 116.23, 114.86, 111.56, 108.84, 56.13, 51.82, 47.31, 45.58, 26.43, 24.71. HRMS (ESI/QTOF) m/z : $[\text{M} + \text{H}]^+$ Calcd for $\text{C}_{22}\text{H}_{26}\text{NO}_5\text{S}^+$ 416.1532; Found 416.1528.

6. ^1H NMR (400 MHz, DMSO- d_6) δ 10.96 (s, 1H), 8.57 (d, $J = 16.3$ Hz, 1H), 8.31 (d, $J = 7.9$ Hz, 1H), 7.88 (d, $J = 16.4$ Hz, 1H), 7.57 (t, $J = 7.9$ Hz, 1H), 7.49 – 7.38 (m, 2H), 7.29 (d, $J = 8.4$ Hz, 1H), 7.02 (d, $J = 8.3$ Hz, 1H), 6.96 (t, $J = 7.5$ Hz, 1H), 4.89 (t, $J = 7.9$ Hz, 2H), 4.02 (s, 3H), 2.63

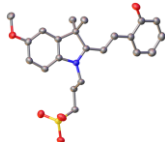
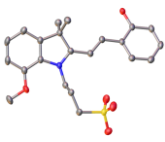
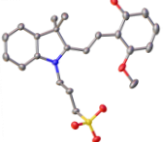
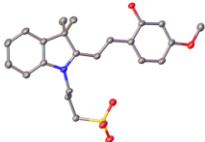
(t, $J = 6.6$ Hz, 2H), 2.21 (p, $J = 6.1$ Hz, 3H), 1.75 (s, 6H). ^{13}C NMR (101 MHz, DMSO- d_6) δ 180.91, 158.80, 148.65, 147.90, 146.06, 135.45, 130.67, 129.69, 128.27, 121.41, 120.05, 116.51, 114.92, 112.95, 111.30, 56.80, 51.70, 48.78, 47.46, 40.15, 39.94, 39.73, 39.52, 39.31, 39.10, 38.89, 26.83, 25.46. HRMS (ESI/QTOF) m/z : $[\text{M} + \text{H}]^+$ Calcd for $\text{C}_{22}\text{H}_{26}\text{NO}_5\text{S}^+$ 416.1532; Found 416.1533.

7. ^1H NMR (400 MHz, DMSO- d_6) δ (ppm) 11.34 (s, 1H), 8.64 (d, $J = 16.3$ Hz, 1H), 8.01 (d, $J = 7.6$ Hz, 1H), 7.95 (d, $J = 16.3$ Hz, 1H), 7.85 (d, $J = 7.0$ Hz, 1H), 7.61 (m, 2H), 7.43 (t, $J = 8.3$ Hz, 1H), 6.65 (dd, $J = 8.4, 3.5$ Hz, 2H), 4.64 (t, $J = 7.2$ Hz, 2H), 2.66 (t, $J = 6.8$ Hz, 2H), 2.17 (p, $J = 7.2$ Hz, 2H), 1.76 (s, 6H). ^{13}C NMR (101 MHz, DMSO) δ (ppm) 182.32, 161.48, 160.64, 145.85, 143.19, 141.04, 136.62, 129.11, 128.82, 122.93, 114.87, 112.85, 110.91, 108.66, 102.50, 56.50, 51.55, 47.92, 45.87, 26.77, 24.25. HRMS (ESI/QTOF) m/z : $[\text{M} + \text{H}]^+$ calcd for $\text{C}_{22}\text{H}_{26}\text{NO}_5\text{S}^+$, 416.1532 found 415.1534.

8. ^1H NMR (400 MHz, DMSO- d_6) δ 11.29 (s, 1H), 8.54 (d, $J = 16.1$ Hz, 1H), 8.29 (d, $J = 9.0$ Hz, 1H), 7.93 (d, $J = 7.8$ Hz, 1H), 7.82 (d, $J = 7.3$ Hz, 1H), 7.71 (d, $J = 16.1$ Hz, 1H), 7.57 (m, 2H), 6.63 (dd, $J = 8.8, 2.4$ Hz, 1H), 6.55 (d, $J = 2.5$ Hz, 1H), 4.73 (t, $J = 7.9$ Hz, 2H), 2.64 (t, $J = 6.4$ Hz, 2H), 2.15 (p, $J = 7.7$ Hz, 2H), 1.74 (s, 6H). ^{13}C NMR (101 MHz, DMSO- d_6) δ 181.06, 166.21, 161.70, 148.78, 143.02, 141.02, 131.92, 129.03, 128.40, 122.87, 115.33, 114.44, 108.41, 108.13, 100.63, 55.75, 51.36, 47.37, 44.94, 26.76, 24.35. HRMS (ESI/QTOF) m/z : $[\text{M} + \text{H}]^+$ Calcd for $\text{C}_{22}\text{H}_{26}\text{NO}_5\text{S}^+$ 416.1532; Found 416.1528

5.6.3 Crystallographic data summary

Table S 5.1 ^a crystals structures are illustrated with thermal ellipsoids at 50% probability; solvent molecules and hydrogens omitted for clarity.

Structure ^a				
Compound	5 (CSB-27)	6 (CP-14)	7 (CSB-25)	8 (CSB-13)
CCDC Deposition Number	2082614	2082821	2082822	2081810
Empirical formula	C ₂₆ H ₃₇ NO ₇ S	C ₂₄ H ₃₁ NO ₆ S ₂	C ₂₃ H ₃₁ NO ₇ S	C ₂₂ H ₂₇ NO ₆ S
Formula weight	507.62 (1·2EtOH)	493.62 (2·DMSO)	465.55 (3·MeOH;H ₂ O)	433.50 (4·H ₂ O)
Temperature/K	140.00(10)	140.00(10)	140.00(10)	139.99(10)
Crystal system	triclinic	triclinic	monoclinic	monoclinic
Space group	P-1	P-1	P2 ₁ /c	P2 ₁ /n
a/Å	9.6537(6)	11.3019(4)	12.49106(8)	12.2487(5)
b/Å	10.4763(8)	15.8376(8)	14.34171(9)	10.7396(3)
c/Å	13.9528(8)	16.1235(7)	13.24822(8)	16.1896(5)
α/°	105.581(6)	61.256(5)	90	90
β/°	100.221(5)	89.549(3)	97.5924(5)	92.984(3)
γ/°	101.036(6)	73.392(3)	90	90
Volume/Å ³	1294.45(16)	2395.8(2)	2352.52(3)	2126.79(13)
Z	2	4	4	4
ρ _{calc} /g/cm ³	1.302	1.368	1.314	1.354
μ/mm ⁻¹	1.488	2.357	1.591	1.686
F(000)	544.0	1048.0	992.0	920.0
Crystal size/mm ³	0.247 × 0.167 × 0.117	0.767 × 0.162 × 0.136	0.24 × 0.16 × 0.126	0.355 × 0.261 × 0.028
Radiation	CuKα (λ = 1.54184)	CuKα (λ = 1.54184)	Cu Kα (λ = 1.54184)	CuKα (λ = 1.54184)
2θ range for data collection/°	9.462 to 146.898	6.722 to 147.42	7.14 to 152.034	8.836 to 152.376
Index ranges	-11 ≤ h ≤ 8, -12 ≤ k ≤ 12, -14 ≤ l ≤ 17	-14 ≤ h ≤ 14, -19 ≤ k ≤ 19, -18 ≤ l ≤ 19	-15 ≤ h ≤ 15, -17 ≤ k ≤ 17, -16 ≤ l ≤ 16	-15 ≤ h ≤ 14, -13 ≤ k ≤ 12, -19 ≤ l ≤ 20
Reflections collected	5215	9772	26172	20471
Independent reflections	5215 [R _{sigma} = 0.0557]	9772 [R _{sigma} = 0.0265]	4894 [R _{int} = 0.0153, R _{sigma} = 0.0104]	4438 [R _{int} = 0.0504, R _{sigma} = 0.0385]
Data/restraints/parameters	5215/68/356	9772/0/642	4894/82/320	4438/0/286
Goodness-of-fit on F ²	0.929	0.989	1.066	1.039
Final R indexes [I > 2σ(I)]	R ₁ = 0.0472, wR ₂ = 0.1175	R ₁ = 0.0373, wR ₂ = 0.0977	R ₁ = 0.0334, wR ₂ = 0.0887	R ₁ = 0.0504, wR ₂ = 0.1363
Final R indexes [all data]	R ₁ = 0.0704, wR ₂ = 0.1253	R ₁ = 0.0468, wR ₂ = 0.1014	R ₁ = 0.0343, wR ₂ = 0.0894	R ₁ = 0.0575, wR ₂ = 0.1448
Largest diff. peak/hole / e Å ⁻³	0.57/-0.28	0.33/-0.41	0.28/-0.32	0.48/-0.51

5.6.4 Hydrolysis

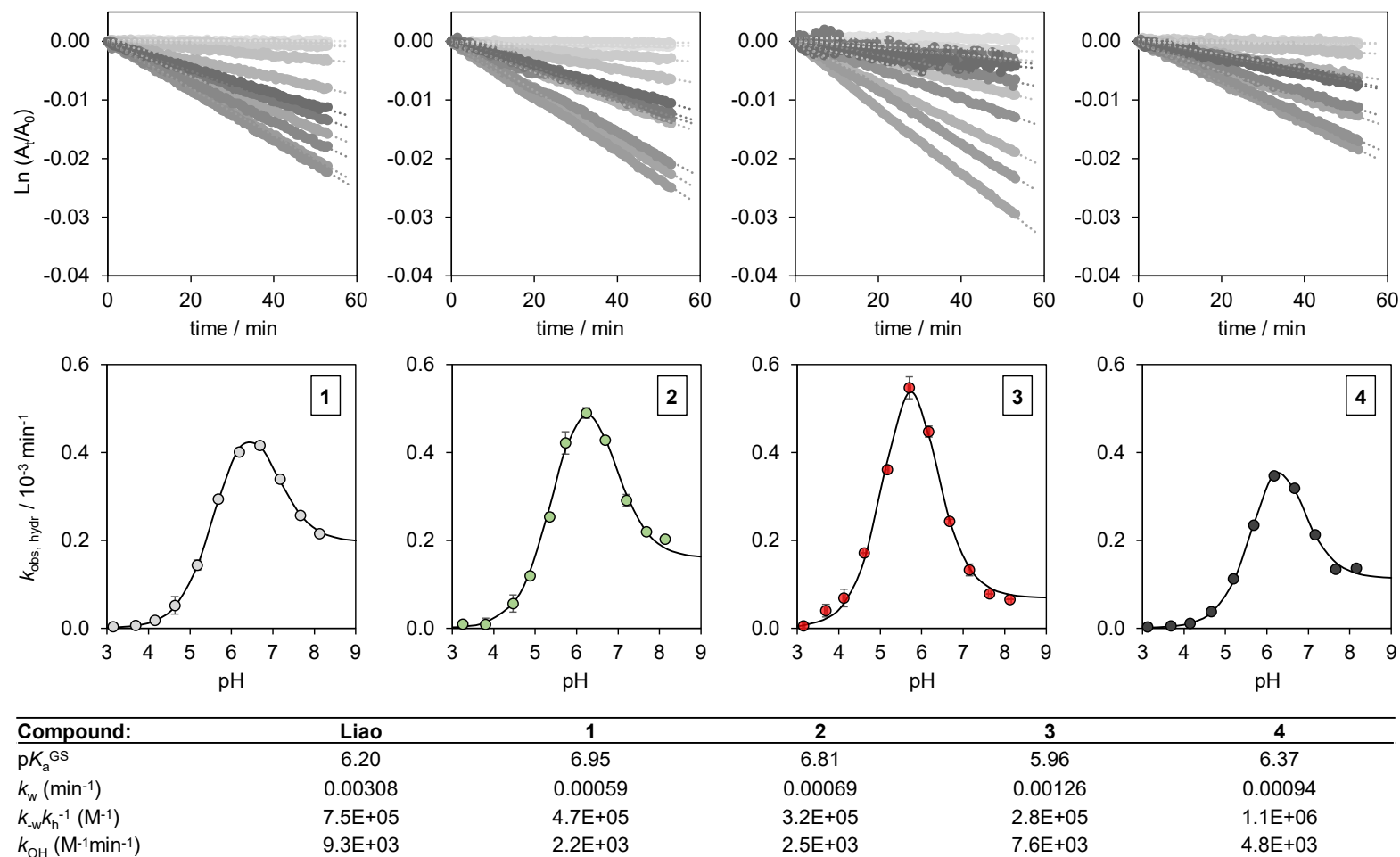


Figure S 5.1. Top: linearized kinetic profiles for the hydrolysis of **5**, **6**, **7** and **8** at different pH in the dark (duplicate experiments). Middle: plots of the obtained apparent first order rate constant of hydrolysis as a function of the pH and relative fitting; solid black lines represent the best fit to eq 3.10 above. Bottom: Comparison of the obtained kinetic parameters with those of Liao's photoacid. Experimental conditions: $[\mathbf{5-8}] = 25 \pm 2 \mu\text{M}$, [phosphate buffers] = 20 mM ($3 < \text{pH} < 8$), $T = 25^\circ\text{C}$; data collected the maximum of the corresponding MCH ($3 < \text{pH} < 7$) and MC form ($\text{pH} > 7$).

5.6.5 MC-to-SP equilibration in the dark

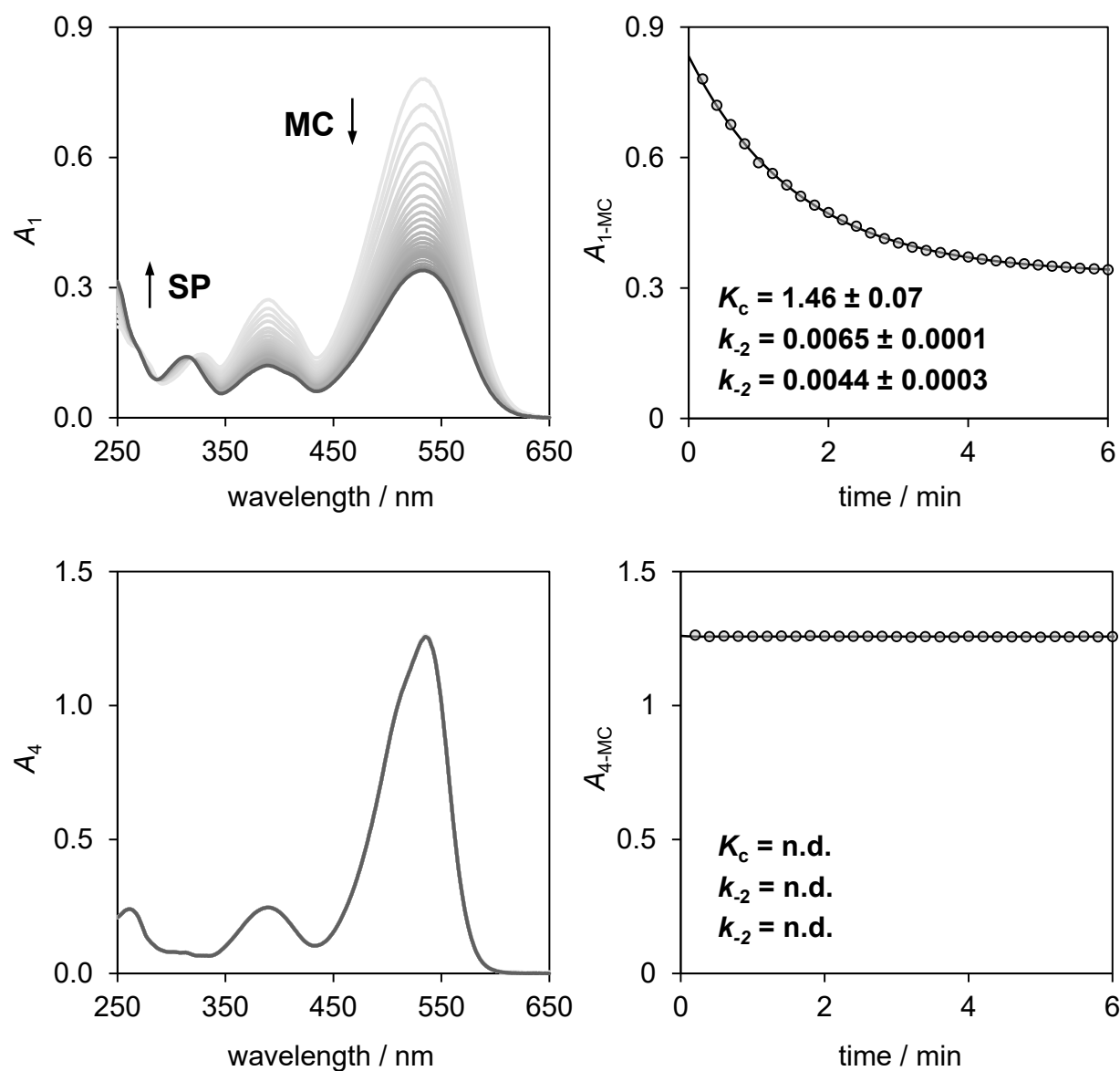


Figure S 5.2.. Representative UV-Vis spectra as a function of time (left) and corresponding kinetic profile (right) after on-site addition and rapid mixing of an aliquot (50 μL) of a solution (0.5 mM in mQ water) of compound **5** (top) and **8** (bottom) into a cuvette containing the buffer solution (950 μL); in the case of **5**, the solid black line represents the best fit to a first-order model equation. K_c , k_{-2} and k_{-2} values and relative error refer to the same experiment performed in duplicate. Experimental conditions: $[\mathbf{5-8}] = 25 \pm 2 \mu\text{M}$, [phosphate buffer] = 20 mM, pH 9.5, $T = 25^\circ\text{C}$.

5.6.6 SP-to-MC(H) relaxation in the dark

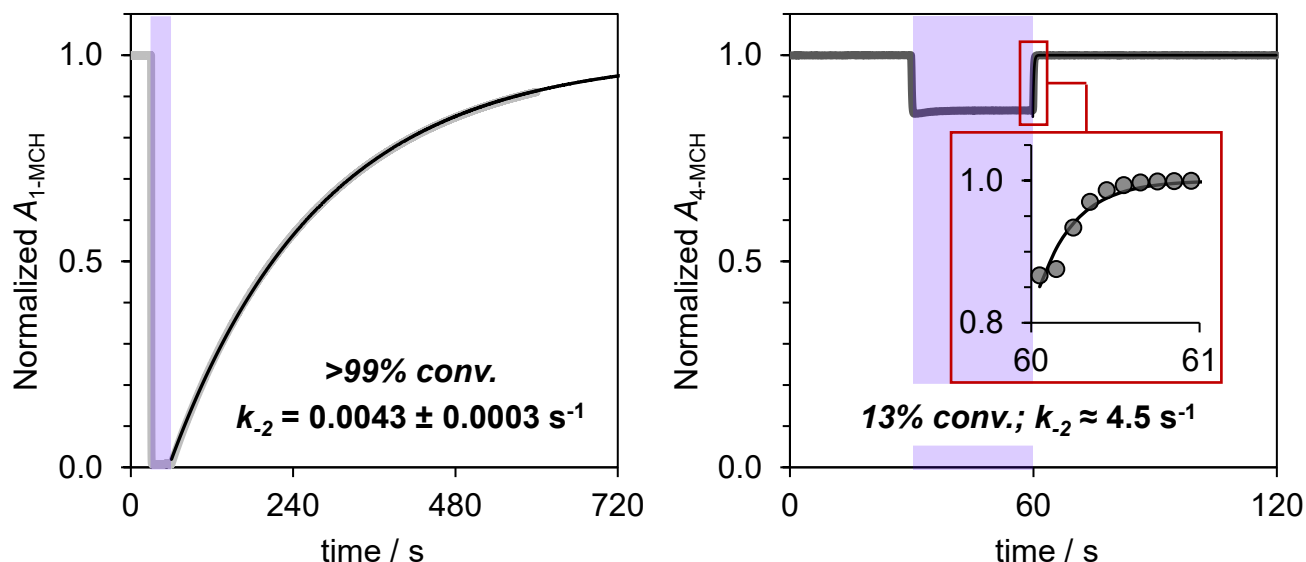


Figure S 5.3. Kinetic profiles for the relaxation of **5** and **8** at pH 5.2 after light irradiation (425 nm, 100 mW); solid black lines represent the best fit to a first-order model equation. In the case of **5**, the k_2 value and relative error refers to the same experiment performed in triplicate. Experimental conditions: $[5-8] = 25 \pm 2 \mu\text{M}$, [phosphate buffer] = 20 mM, pH 5.2, $T = 25^\circ\text{C}$

The data treatment is identical to the one described in Chapter 3, paragraph 3.9.6. For compound **8** it was very difficult to obtain photoisomerization even at the maximum power of our light sources (Figure S 5.3, right inset). The recovery profile was very fast and we could only have a rough estimate of the k_2 value.

For compound **5** the analysis of the SP-to-MC(H) kinetics was performed as for the compounds in Chapter 3 and 4 (see paragraph 3.9.6 for the full description). The guided graphics in Figure S 5.4 result from these considerations.

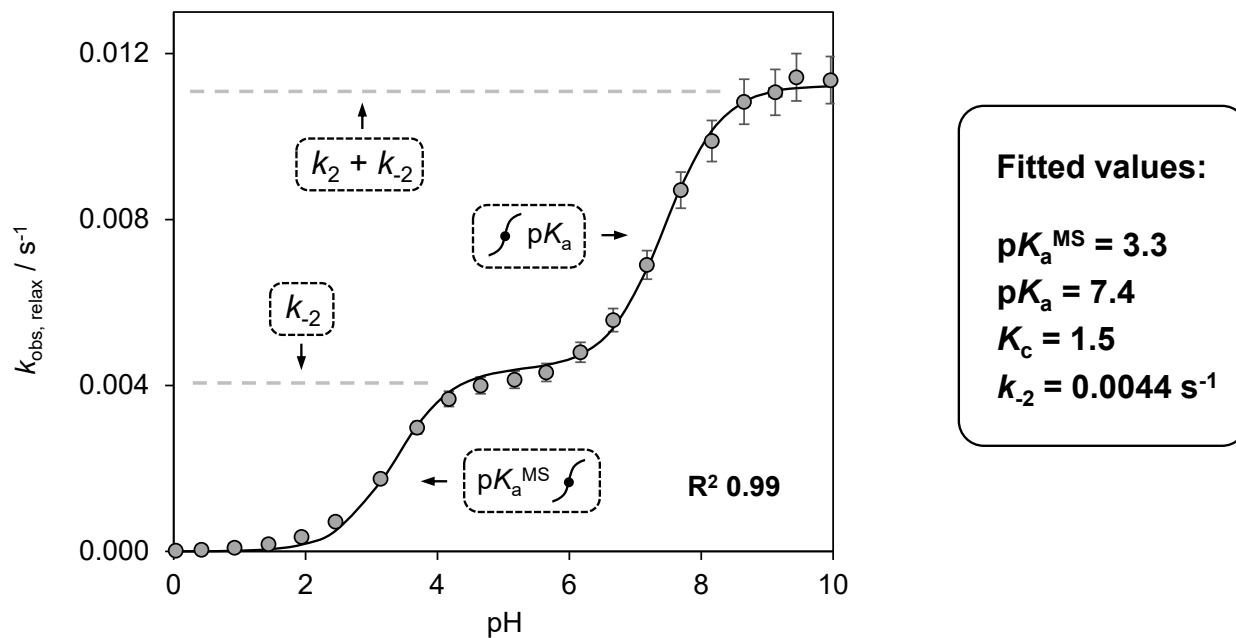


Figure S 5.4. In the case of compound **5**, the same experiment above is repeated as a function of the pH in duplicate; the solid black line represents the best fit. Fitted values are in good agreement with those determined independently through UV-Vis and ^1H NMR measurements. Together with the corresponding one of hydrolysis (see Figure S1), this profile is used to fit the pH jumps obtained with **5** below.

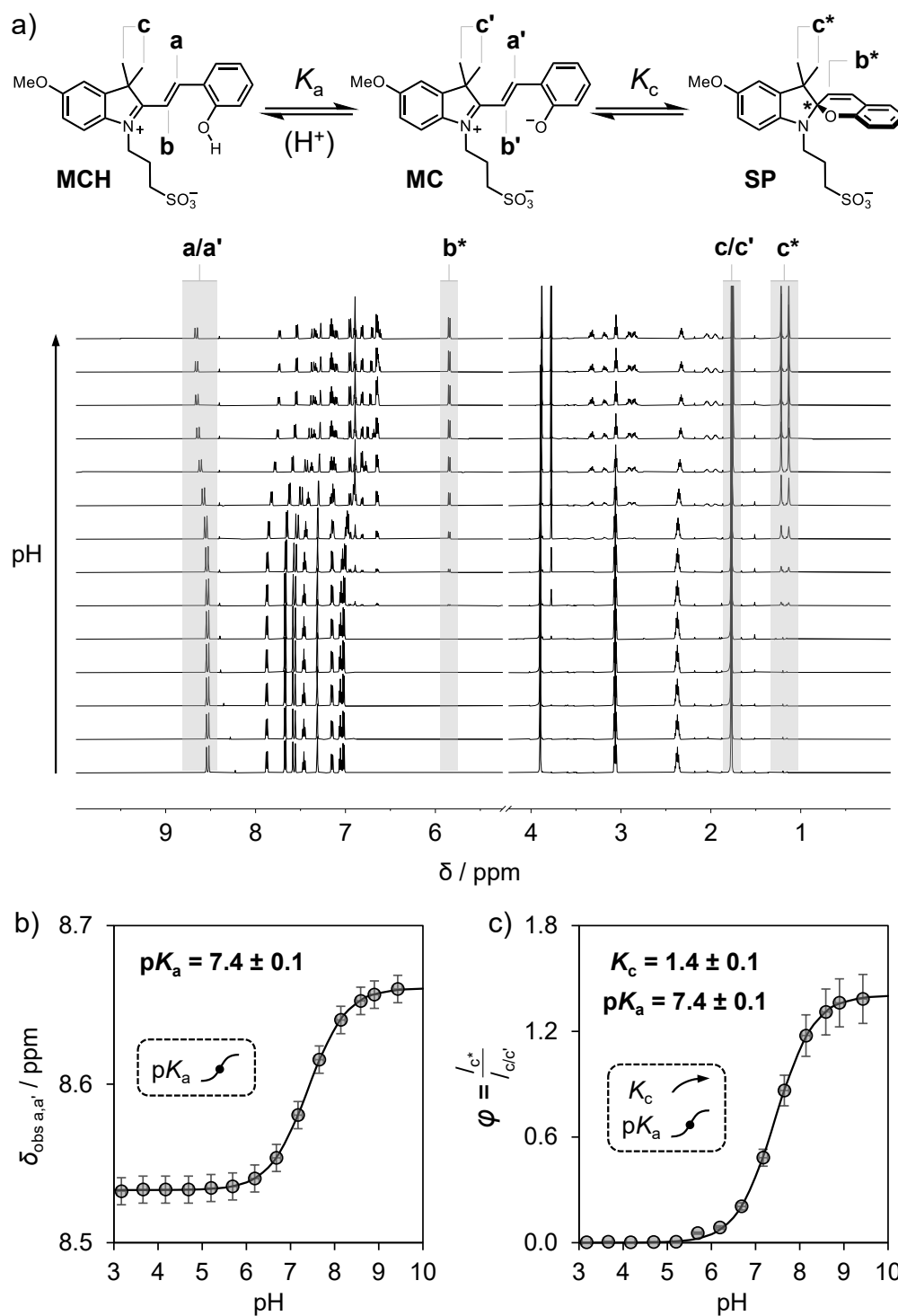
5.6.7 ^1H NMR titration of **5** in the dark

Figure S 5.5. (a) Three-component equilibrium system describing the ground state of **5** (top) and ^1H NMR (600 MHz) spectra at increasing pH values (bottom). Profiles of the chemical shift of a,a' (b) and the integral ratio between c* and c,c' (c) as a function of the pH; solid black lines represent the best fit to the corresponding model equation. Experimental conditions: $[\mathbf{5}] = 0.1 \text{ mM}$, $[\text{phosphate buffers}] = 20 \text{ mM}$ ($3 < \text{pH} < 10$) in $\text{H}_2\text{O}/\text{D}_2\text{O}$ 6:4, $T = 25^\circ\text{C}$

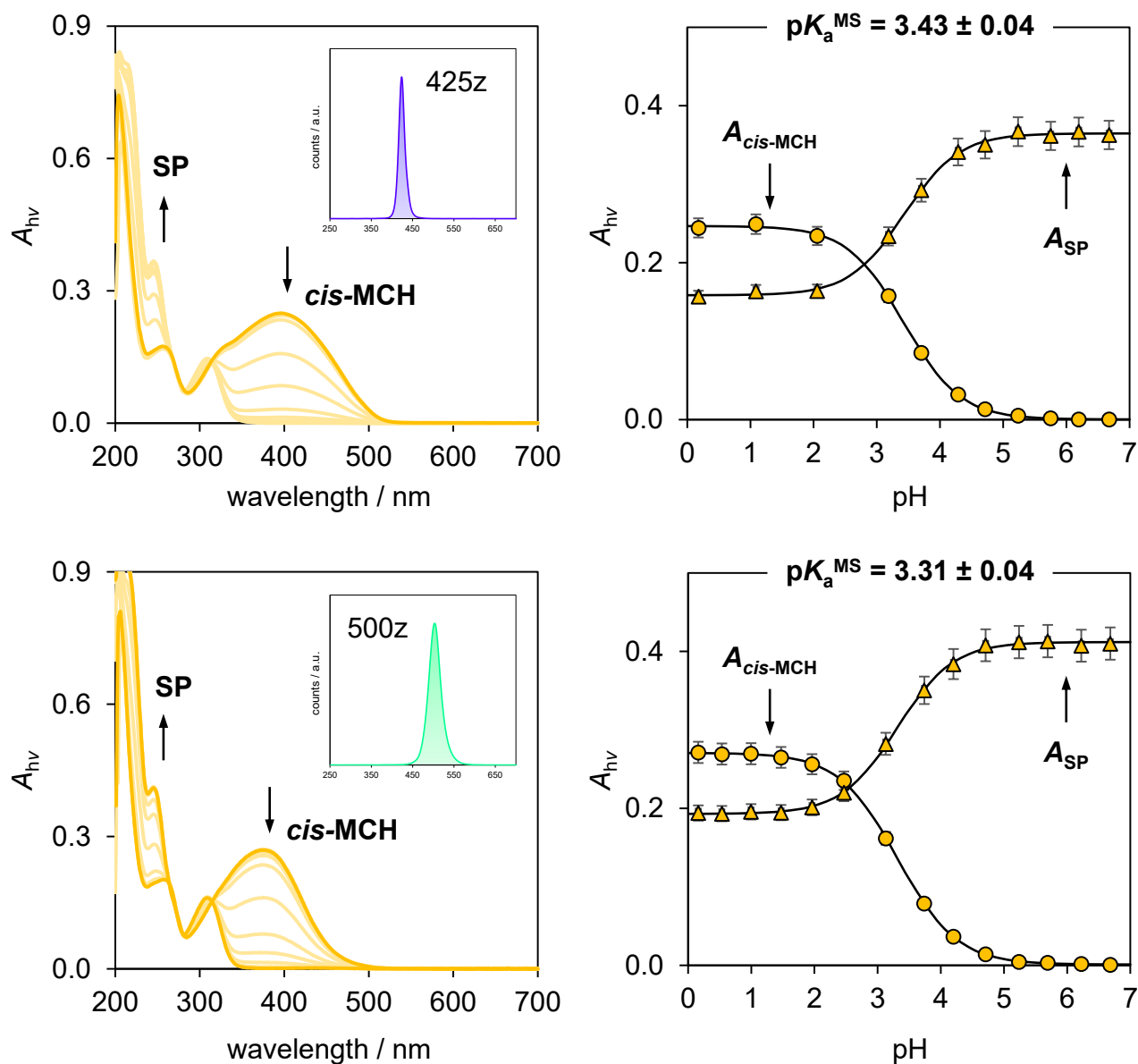
5.6.8 Apparent acid dissociation constants of **5** under light irradiation

Figure S 5.6. UV-Vis pH titration (left) and corresponding elaboration (right) obtained using 425 nm (top) and 500 nm (bottom) LED light sources (100 mW). Experimental conditions: $[5] = 25 \pm 2 \mu\text{M}$, $[\text{buffers}] = 20 \text{ mM}$ ($\text{pH} > 3$), $T = 25 \text{ }^\circ\text{C}$.

5.6.9 Molar extinction coefficient of **5**-MCH (ϵ_{MCH})

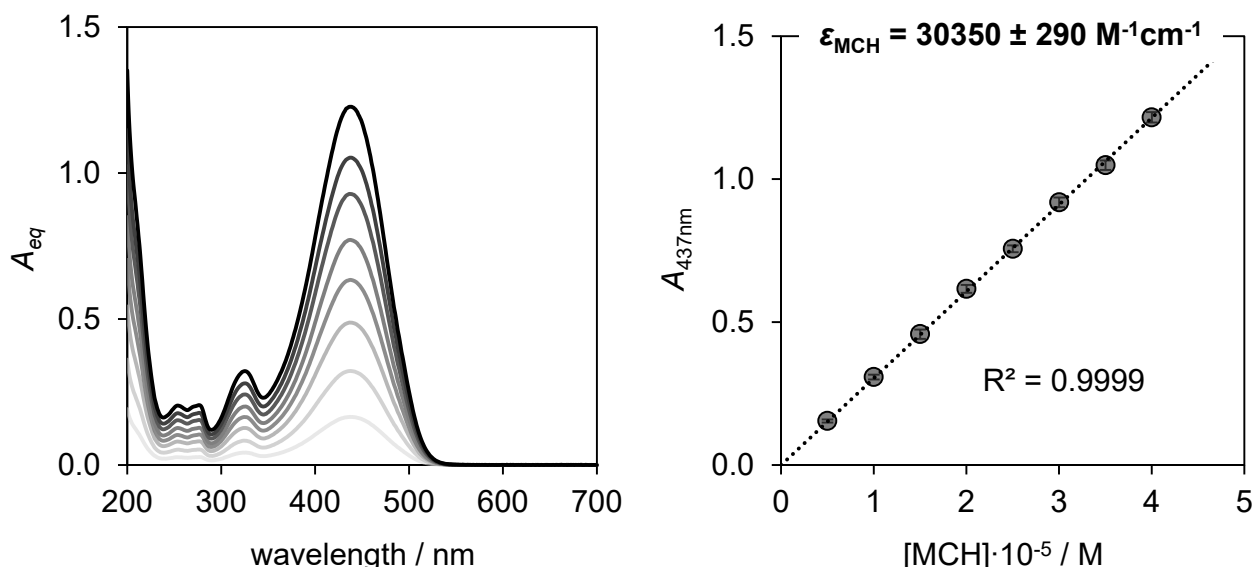


Figure S 5.7. Representative spectra as a function of the concentration of **5** at equilibrium in the dark (left) and calibration curve (right). The obtained value and relative error result from five independent experiments. Experimental conditions: [buffer] = 20 mM, pH = 3, $T = 25^\circ\text{C}$.

5.6.10 pH-jump studies

Saturated solutions of **5** in aqueous KCl (30 mL, 20 mM) were prepared by sonication as described in the Experimental Section of Chapter 3. Each experiment is run independently, transferring the resulting solution into a 50-mL jacketed beaker kept at 25°C , equipped with a 2.5 cm cross-shaped stir bar and mounted above a 45° mirror cage. pH data acquisition is carried out under stirring (250 rpm) and inert atmosphere (gentle N_2 bubbling) with a pre-calibrated Unitrode Pt1000 glass electrode. The setup is identical to the one described in Chapter 3, paragraph 3.9.7 and Chapter 3, Figure 3.8.

Concomitantly, the concentration of each satd. solution is determined from optical readings at pH 3 knowing ϵ_{MCH} (see Figure S 5.10).

Note: solubility is extremely sensitive to preparation time, position of the sample in the sonicator, sonicator type, as well as temperature. For this reason we developed an alternative way to determine S_{MCH} (see sections below). For the following pH jumps, however, each solution was prepared with the procedure described in Chapter 3.

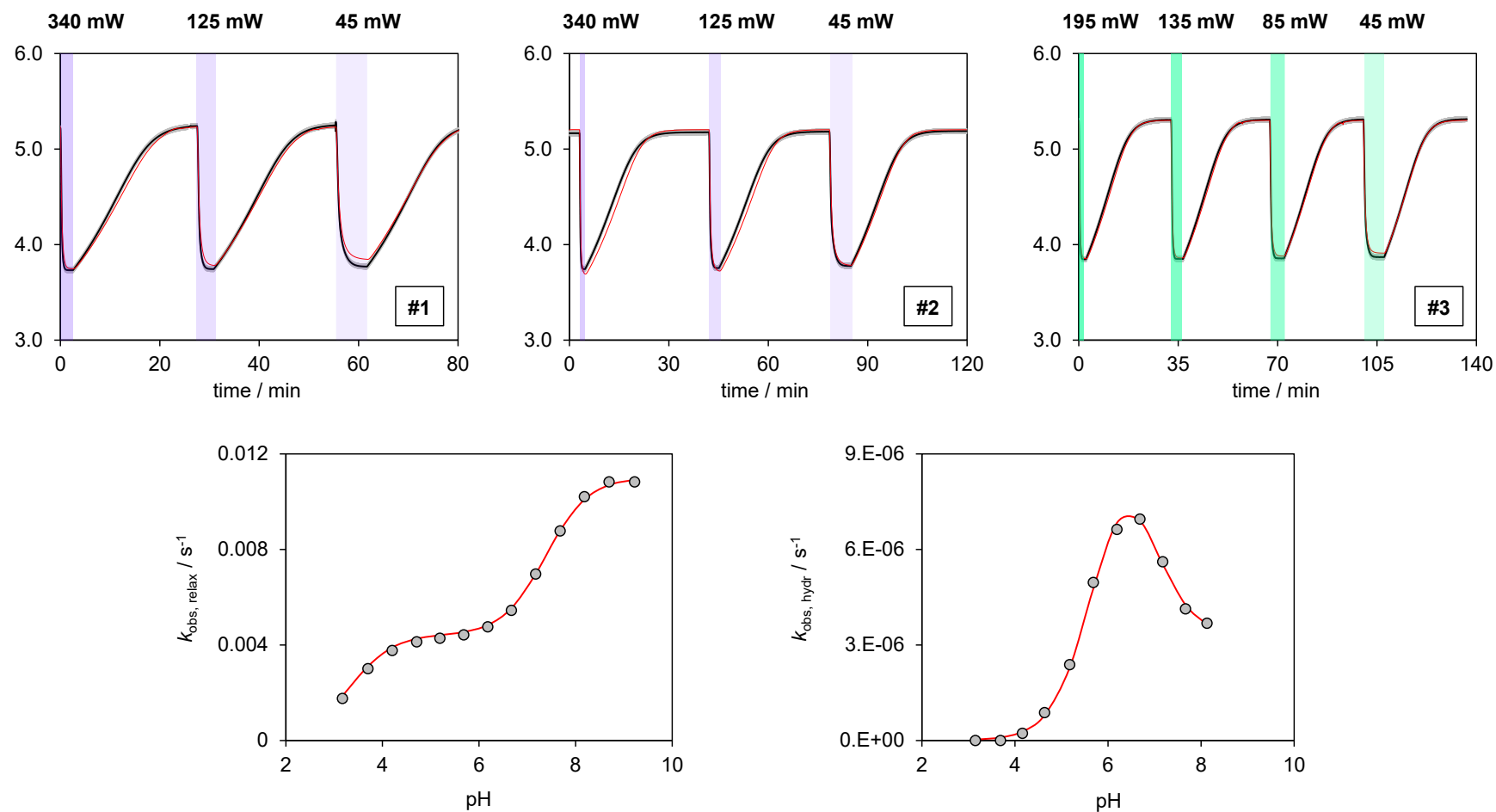


Figure S 5.8. Simultaneous fit of three independent variable-power pH jump experiments (top) together with the pH-dependent profiles of relaxation (Figure S6) and hydrolysis (Figure S1) (bottom). Fitting curves are highlighted in red, the resulting Monte-Carlo validation analysis is reported on the bottom right corner. Fitted parameters are listed in Table S1-3 below for comparison.

Table S 5.2. Fitted parameters for experiment #1 (425 nm light irradiation)

Parameter	Predicted value	Experimental value ^a	Deviation (σ)
C	0.000282 M	0.000287 M	0.17
$pK_a = -\log_{10} K_a$	7.32	7.4	0.5
$pK_c = -\log_{10} K_c$	-0.17	-0.17	0
$pK_a^{MS} = -\log_{10} K_a^{MS}$	3.29	3.31	0.06
k_1	0.061 s^{-1}	n/a	n/a
k_2	0.0066 s^{-1}	0.0065 s^{-1}	0.15
k_3	66.7 s^{-1}	n/a	n/a
k_4	$4.87 \times 10^{-5} s^{-1}$	n/a	n/a
k_v (340 mW)	0.0557 s^{-1}	n/a	n/a
k_v (125 mW)	0.0199 s^{-1}	n/a	n/a
k_v (45 mW)	0.00836 s^{-1}	n/a	n/a
k_{OH}	40.9 s^{-1}	n/a	n/a
k_{-OH}	0.00486 s^{-1}	n/a	n/a
k_h	0.239 s^{-1}	n/a	n/a
k_{-h}	$3.3 \times 10^{-11} s^{-1}$	n/a	n/a
k_w	$1.04 \times 10^{-5} s^{-1}$	$9.83 \times 10^{-6} s^{-1}$	ok ^b
k_{-w}	$123.6 \times 10^3 M^{-1} s^{-1}$	n/a	n/a
k_{-w}/k_h	$4.7 \times 10^5 M^{-1}$	$4.7 \times 10^5 M^{-1}$	ok ^b
pH _{dark}	5.24	5.25	0.04
pH _{light} (340 mW)	3.74	3.73	0.05
pH _{light} (125 mW)	3.78	3.74	0.11
pH _{light} (45 mW)	3.84	3.77	0.19
Φ_{425} (340 mW)	0.39	n/a	n/a
Φ_{425} (125 mW)	0.38	n/a	n/a
Φ_{425} (45 mW)	0.44	n/a	n/a
Φ_{425} (Mean \pm St. Dev.)	0.40 ± 0.03	n/a	n/a

- a. average values obtained considering both UV-Vis and ¹H NMR, or pH jump experiments. In all cases, error stays within 10%.
- b. kinetic constants for hydrolysis are optimized esteems resulting from fitting, so checked for the order of magnitude to be consistent.

Table S 5.3. Fitted parameters for experiment #2 (425 nm light irradiation)

Parameter	Predicted value	Experimental value	Deviation (σ)
C	0.000336 M	0.000291 M	1.55 ^c
k_v (340 mW)	0.0469 s^{-1}	n/a	n/a
k_v (125 mW)	0.0165 s^{-1}	n/a	n/a
k_v (45 mW)	0.00672 s^{-1}	n/a	n/a
pH _{dark}	5.20	5.18	0.04
pH _{light} (340 mW)	3.69	3.74	0.13
pH _{light} (125 mW)	3.72	3.75	0.08
pH _{light} (45 mW)	3.80	3.78	0.05
Φ_{425} (340 mW)	0.39	n/a	n/a
Φ_{425} (125 mW)	0.37	n/a	n/a
Φ_{425} (45 mW)	0.42	n/a	n/a
Φ_{425} (Mean \pm St. Dev.)	0.40 \pm 0.02	n/a	n/a

c. This deviation was likely due to a pipetting error during UV-Vis concentration check.

Table S 5.4. Fitted parameters for experiment #3 (500 nm light irradiation)

Parameter	Predicted value	Experimental value	Deviation (σ)
C	0.000210 M	0.000216 M	0.28
k_v (195 mW)	0.049 s^{-1}	n/a	n/a
k_v (135 mW)	0.0347 s^{-1}	n/a	n/a
k_v (85 mW)	0.0218 s^{-1}	n/a	n/a
k_v (45 mW)	0.013 s^{-1}	n/a	n/a
pH _{dark}	5.31	5.31	0
pH _{light} (195 mW)	3.85	3.85	0
pH _{light} (135 mW)	3.86	3.85	0.03
pH _{light} (85 mW)	3.88	3.86	0.05
pH _{light} (45 mW)	3.91	3.87	0.1
Φ_{500} (195 mW)	0.38	n/a	n/a
Φ_{500} (135 mW)	0.39	n/a	n/a
Φ_{500} (85 mW)	0.39	n/a	n/a
Φ_{500} (45 mW)	0.43	n/a	n/a
Φ_{500} (Mean \pm St. Dev.)	0.40 \pm 0.03	n/a	n/a

5.6.11 Preparation of buffered solutions

Saturated solutions of **5** are prepared by stirring (250 rpm) an excess amount of grinded crystals into aqueous KCl (15 mL, 20 mM) containing HCl ($C_{\text{HCl}} = 1 \text{ mM}$; S_{MCH}) or increasing amounts of NaOH ($C_{\text{NaOH}} = \alpha \cdot S_{\text{MCH}}$; $0 < \alpha \leq 1$). We used the same apparatus described above in Chapter 3 to keep the temperature constant ($T = 25 \text{ }^{\circ}\text{C}$) and monitor the pH during dissolution in the dark. In all cases, the pH stabilizes within 20 minutes (Figure S 5.9). The resulting mixtures are then microfiltered (H-PTFE-45/25) and subjected to UV-Vis (Figure S 5.10) prior to pH jump analyses (Figure S 5.11).

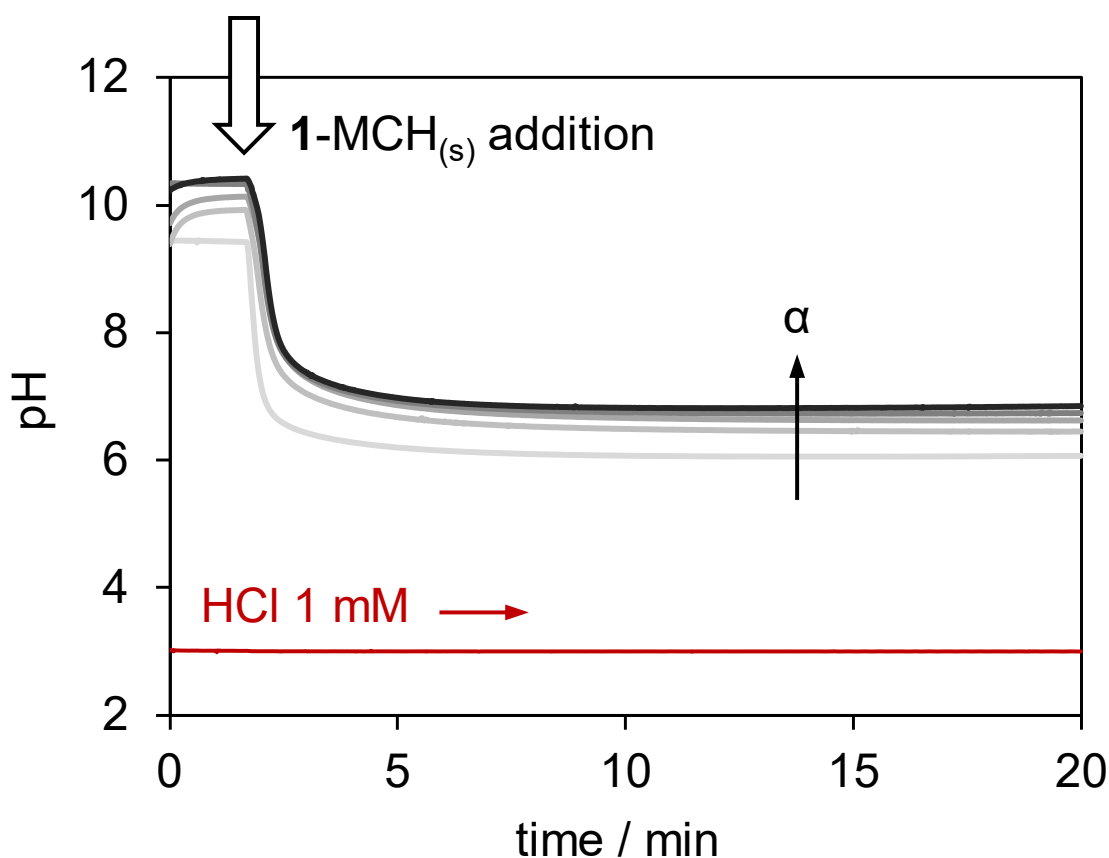


Figure S 5.9. Time course of pH upon solubilization of compound **5** in aqueous KCl containing HCl (red trace) or increasing amounts of NaOH (0.1 N, 11, 22, 33, 44 and 55 μL , from bottom to top respectively). The amount of NaOH was calculated with respect to S_{MCH} in order to cover the range $0 < \alpha \leq 1$. Grounded crystals of **1** were added after 100 seconds.

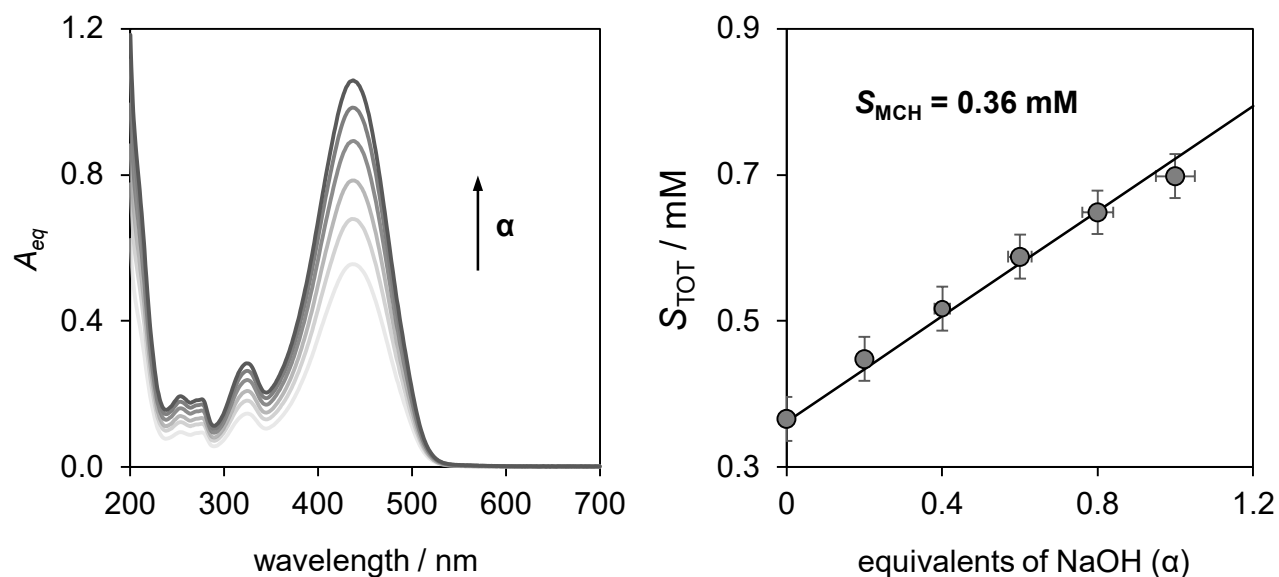
5.6.12 Solubility vs. α 

Figure S 5.10. Representative spectra as a function of α after equilibration (20 min) in the dark (left); dilution factor was 20: 50 μ L of PTFE-filtered sample solution, final volume = 1.0 mL; Absorbances at 437 nm are converted into concentration knowing ϵ_{MCH} (see Figure S7). Solubility of **5** vs. α (right); solid black line represents the best linear fit. The resulting S_{MCH} value is in agreement with the one obtained after solubilization in HCl 1 mM: 0.37 ± 0.3 mM (triplicate experiment). Experimental conditions: [buffer] = 20 mM, pH = 4.5, $T = 25$ °C.

5.6.13 pH jumps vs. α

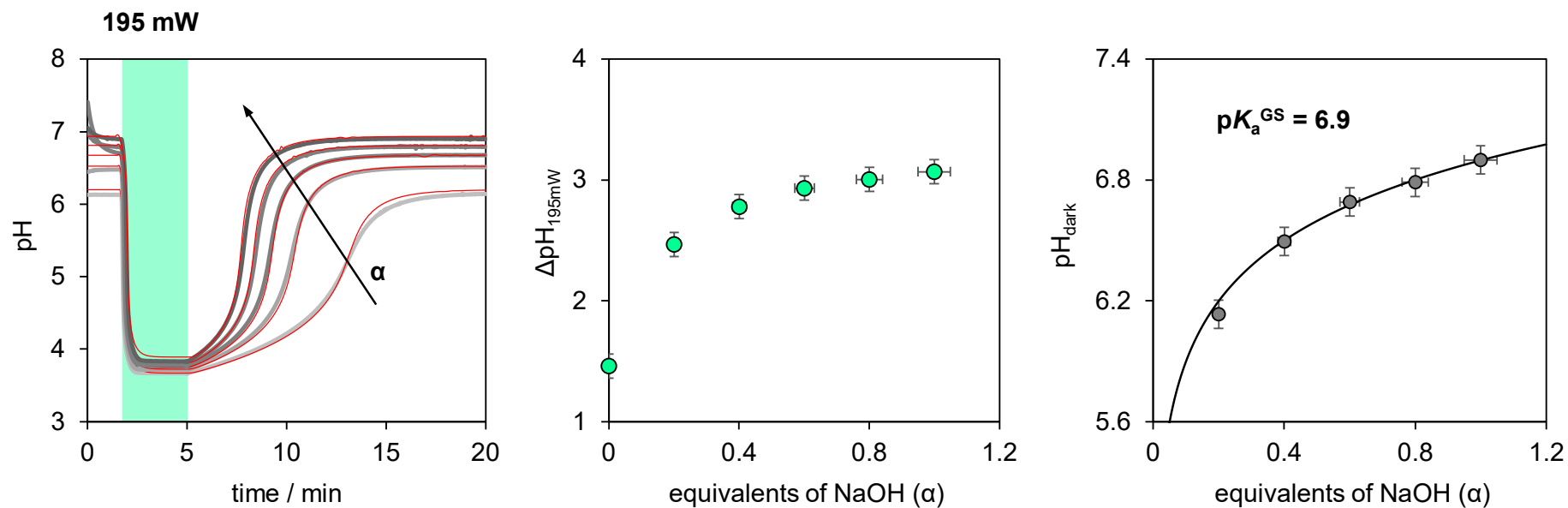
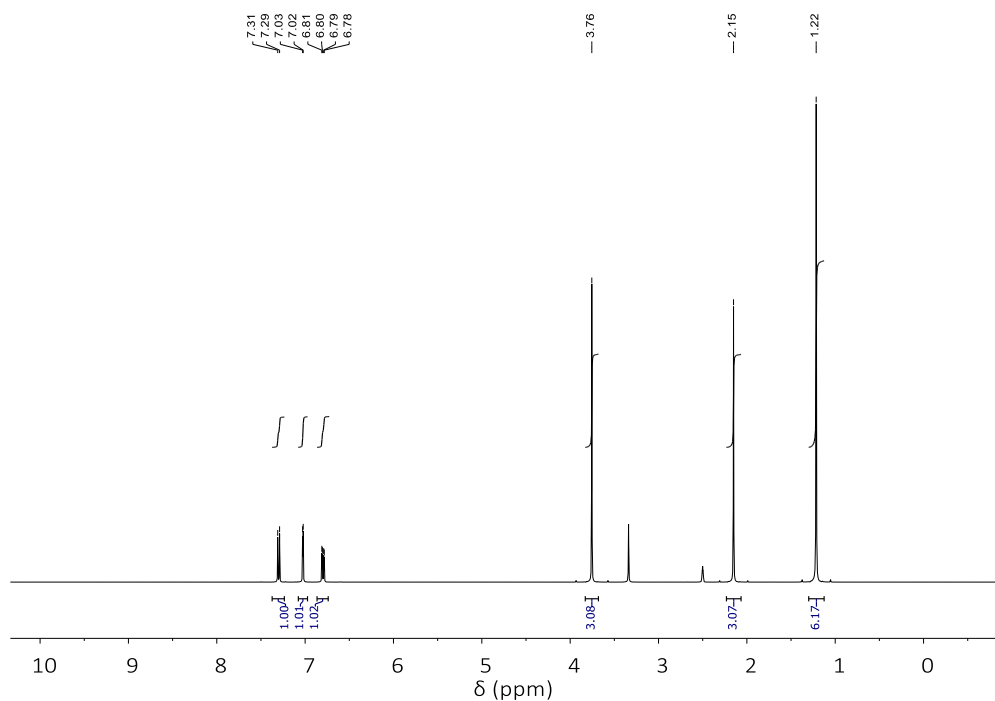
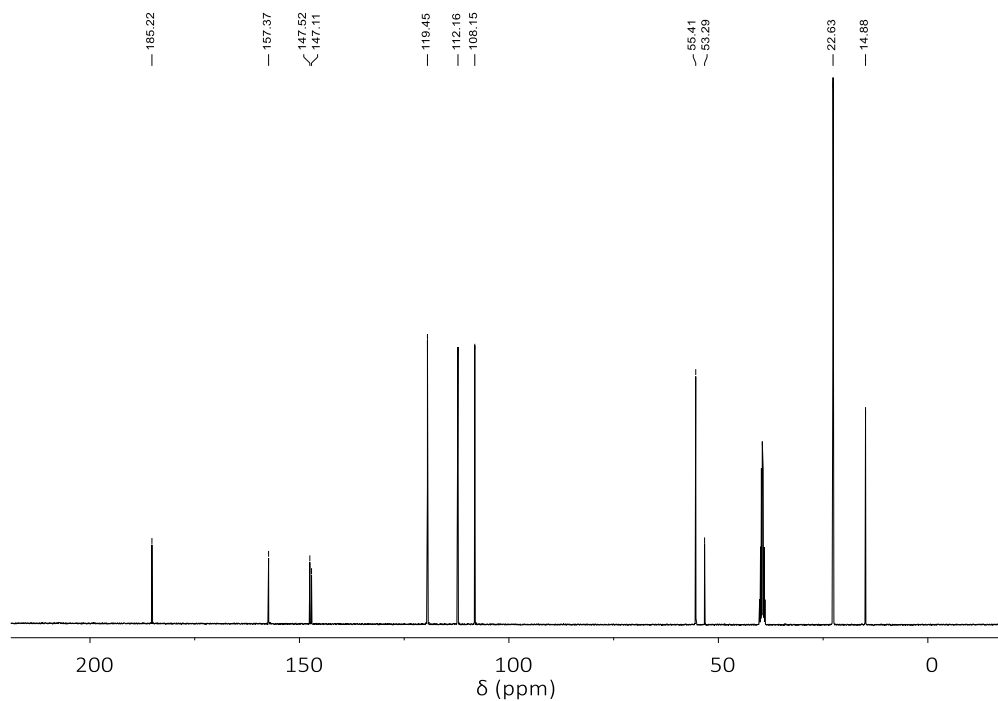
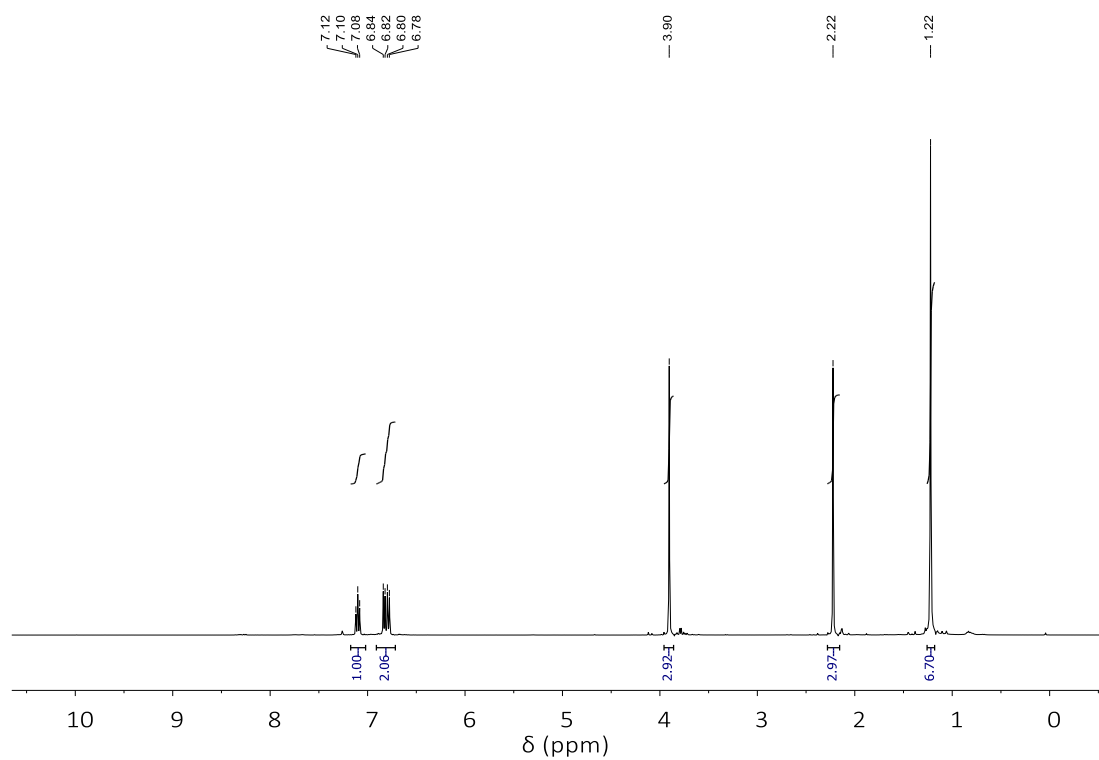
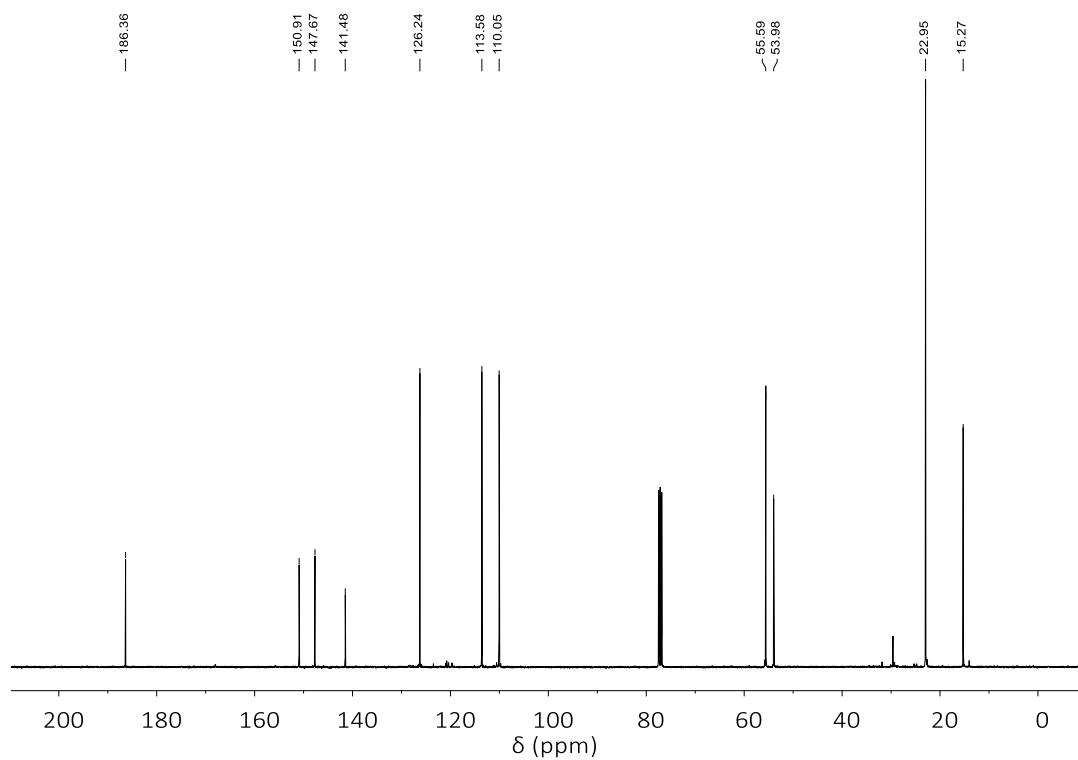
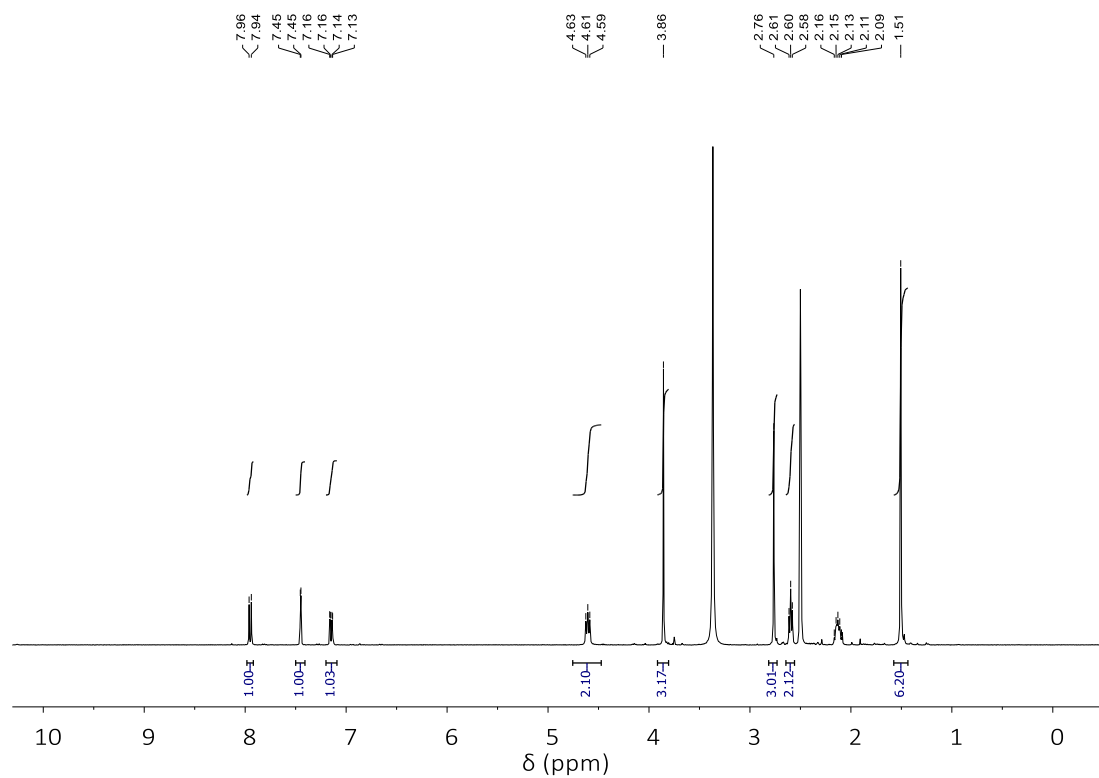
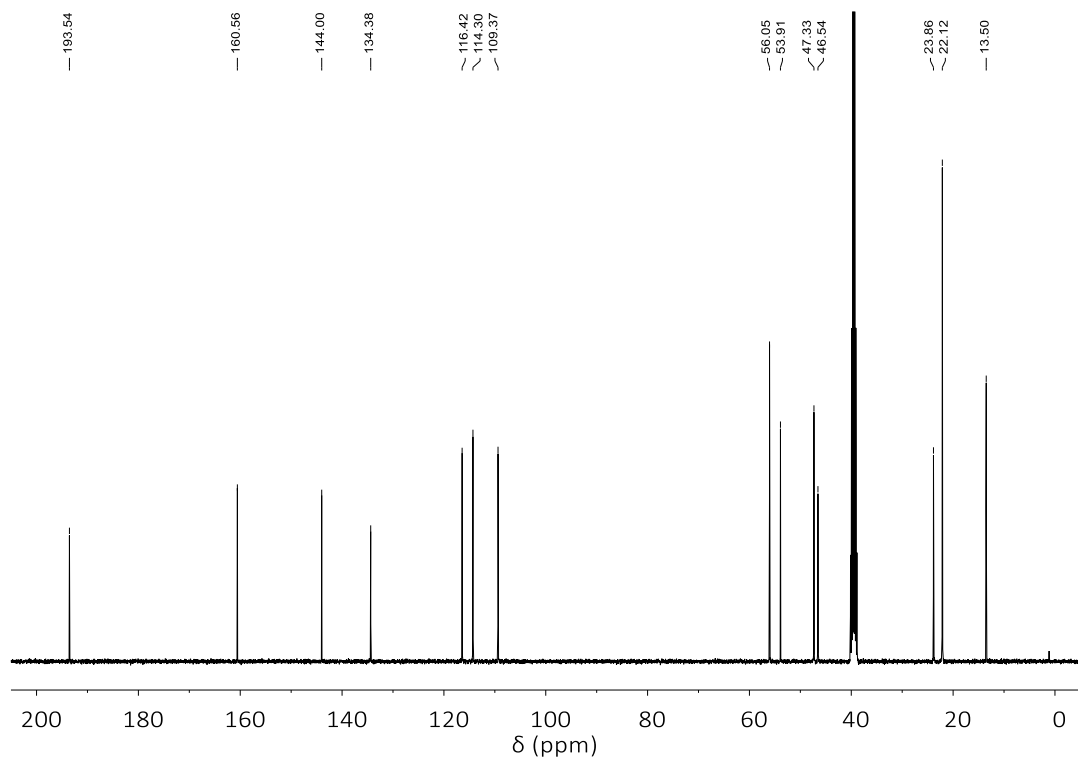
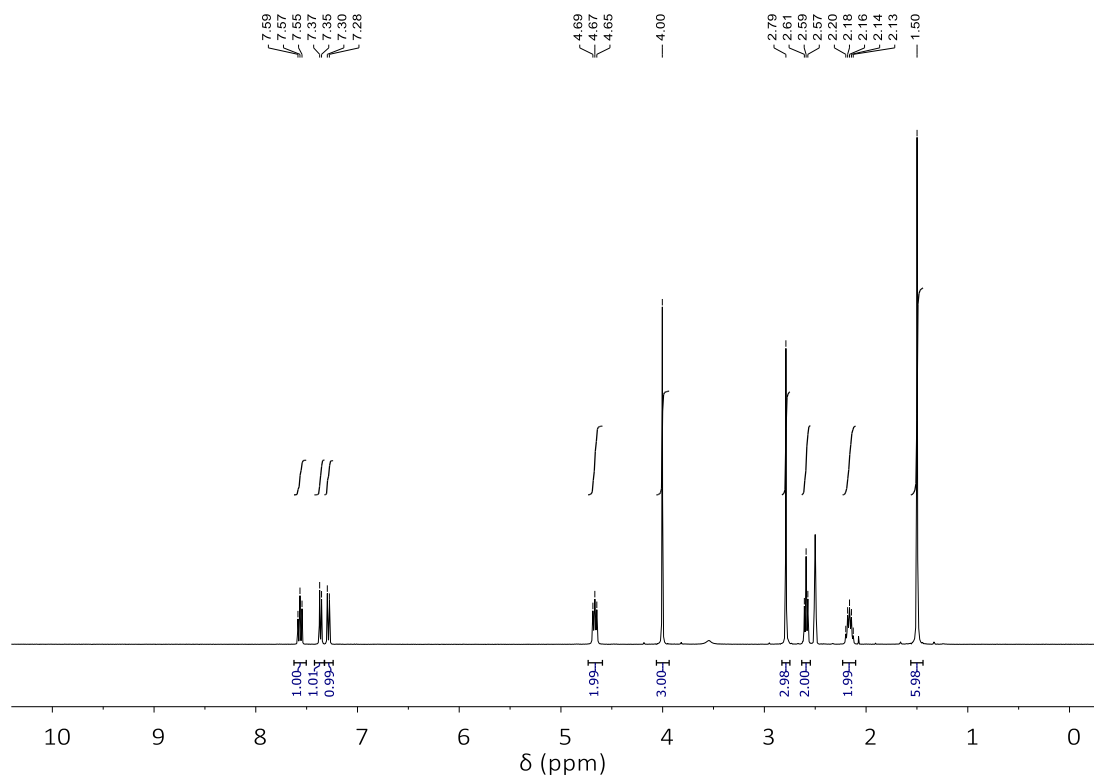
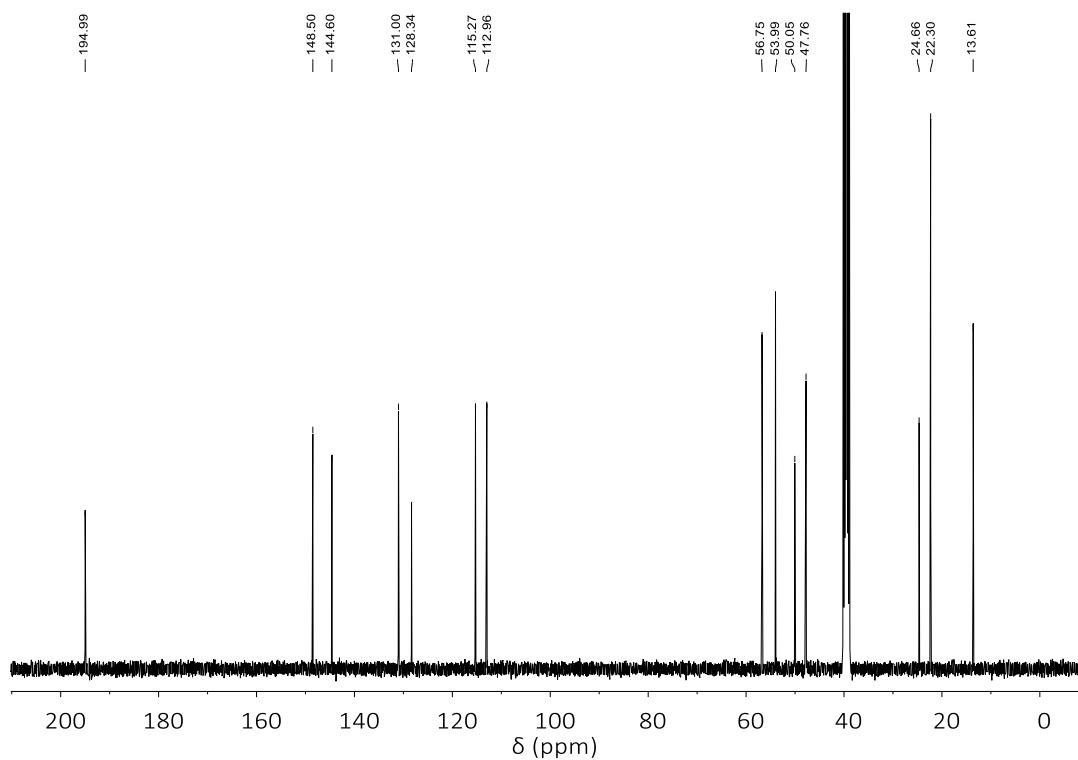


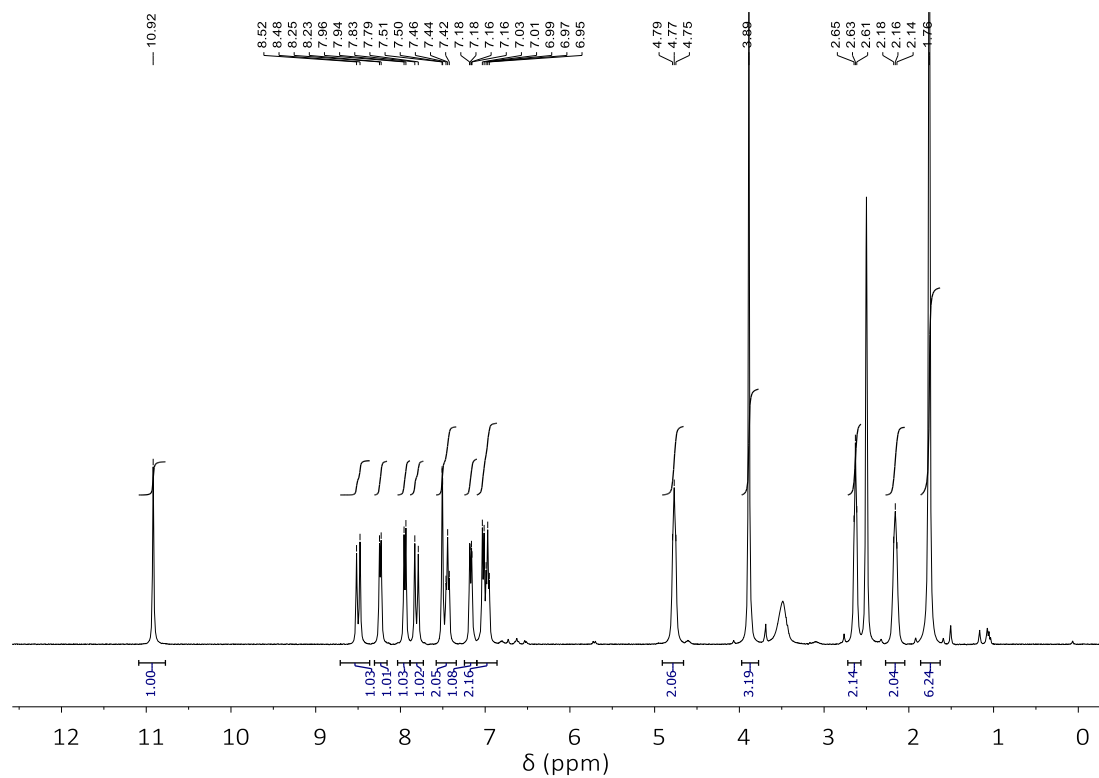
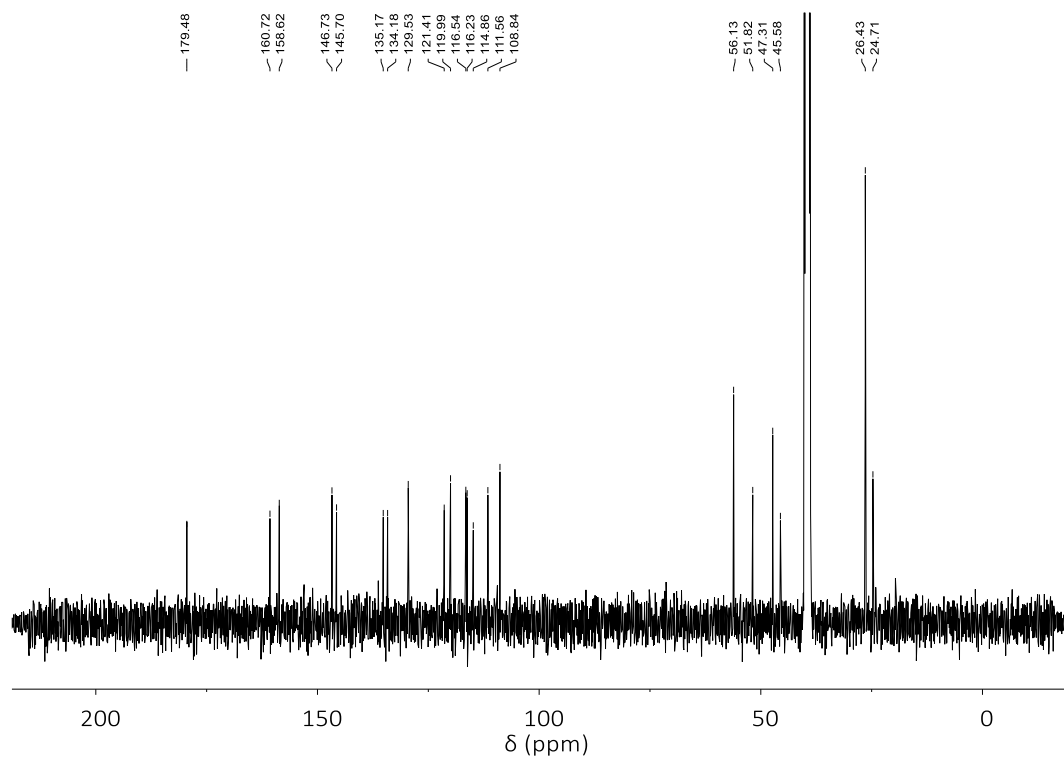
Figure S 5.11. From left to right: pH jumps experiments, $\Delta\text{pH} = \text{pH}_{\text{dark}} - \text{pH}_{\text{light}}$ and pH_{dark} as a function of α . Solid red lines represent model predictions of our four-state cycle taking into account the degree of neutralization in the dark, whereas the solid black lines represent the best fit to the Henderson-Hasselbalch equation. Experimental conditions: $[\mathbf{5}]_0$ = see Figure S10, $T = 25^\circ\text{C}$.

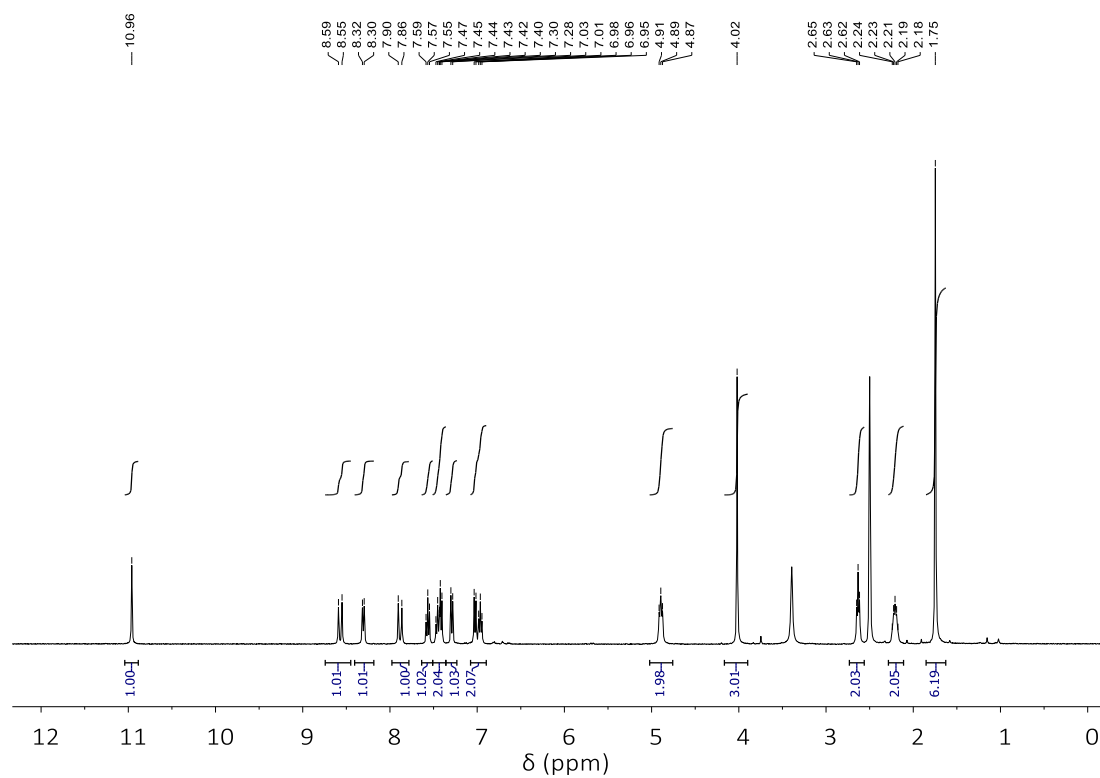
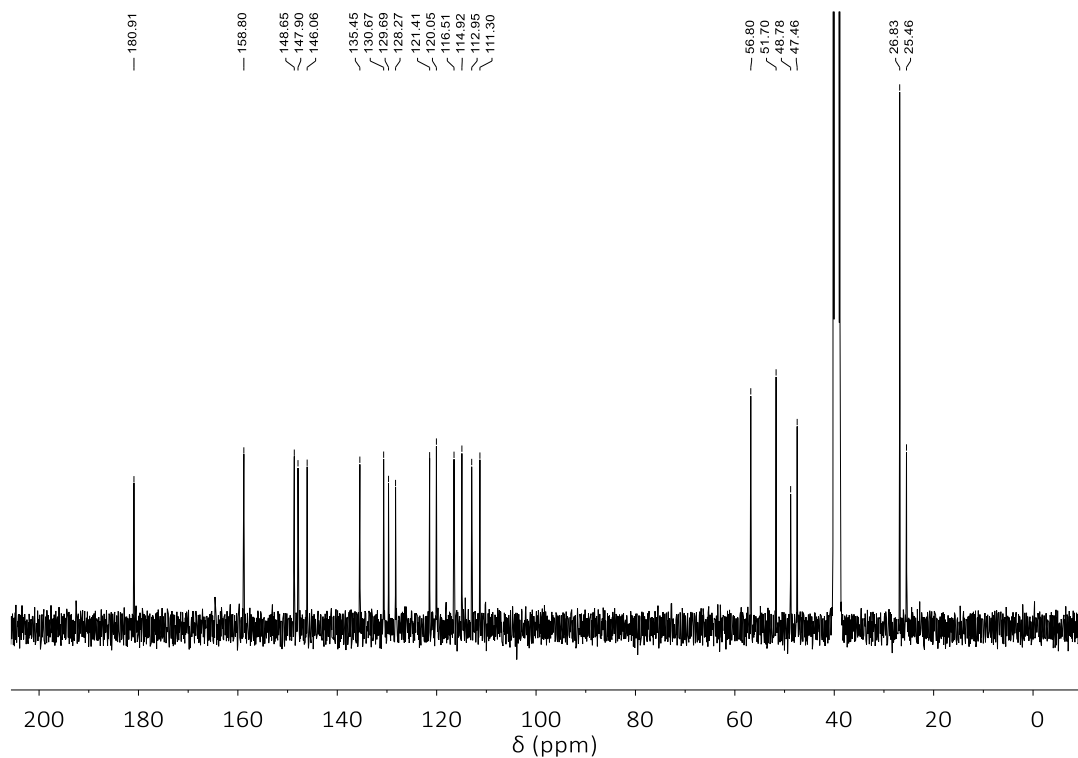
5.6.14 ^1H and ^{13}C NMR spectraFigure S 5.12. ^1H NMR spectrum (400 MHz, $\text{DMSO}-d_6$) of **15**.Figure S 5.13. ^{13}C NMR spectrum (101 MHz, $\text{DMSO}-d_6$) of **15**.

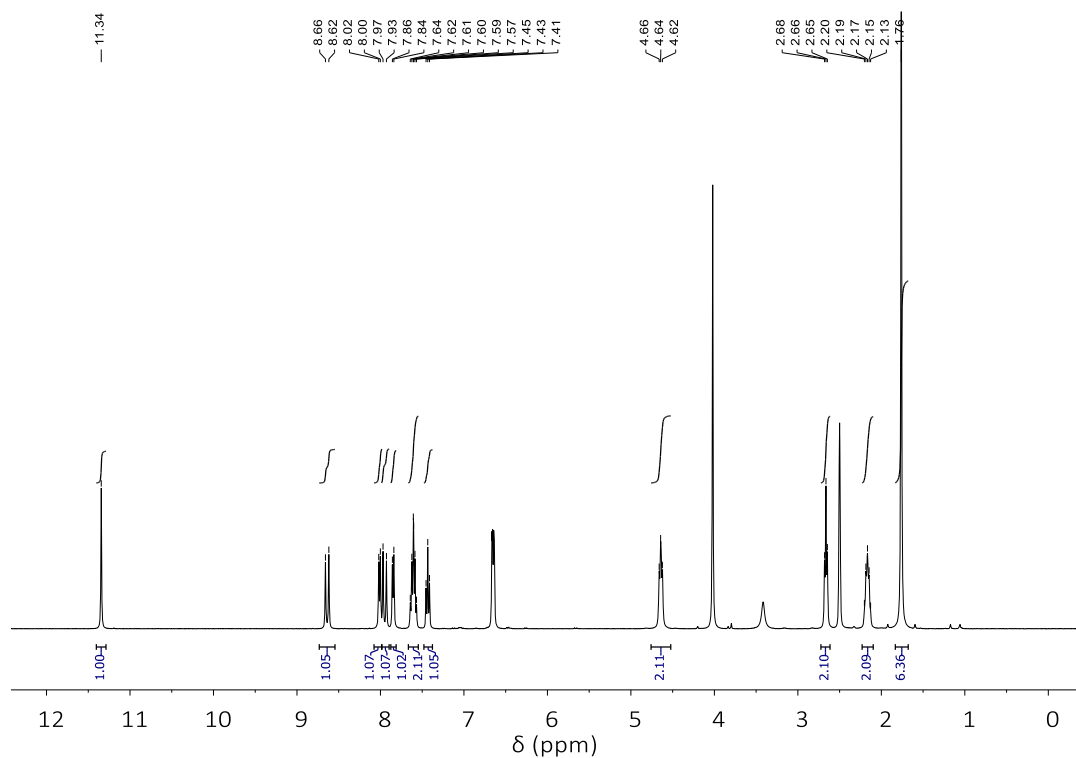
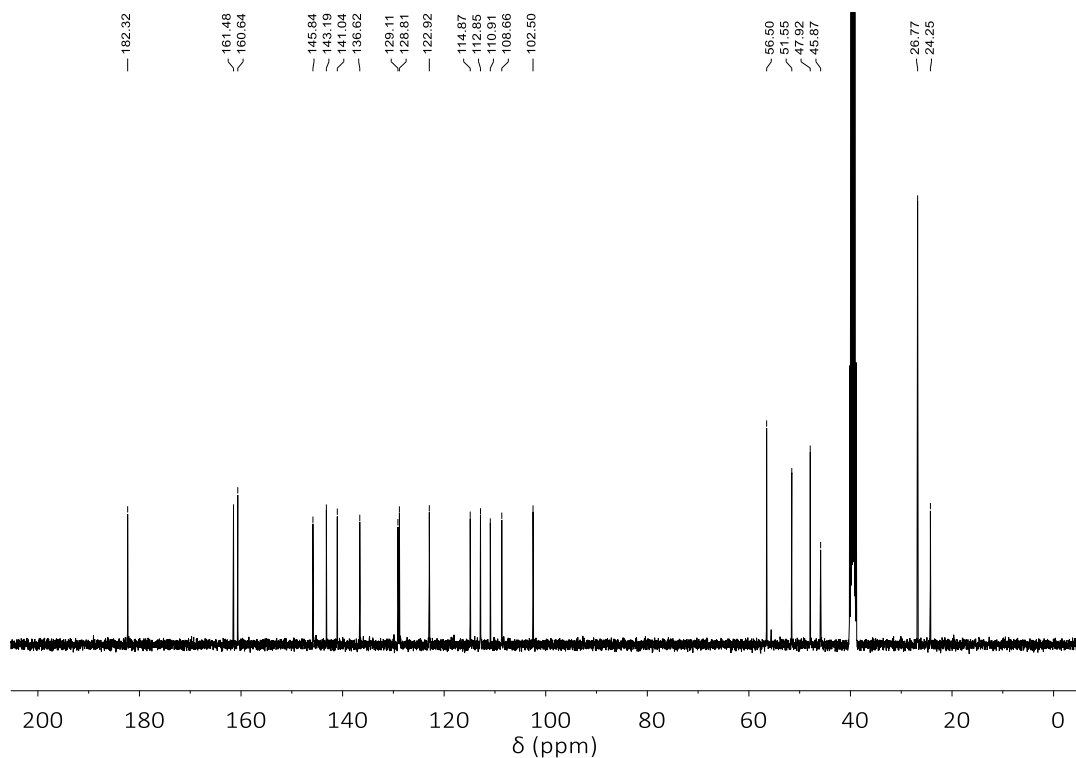
Figure S 5.14. ^1H NMR spectrum (400 MHz, CDCl_3) of **16**.Figure S 5.15. ^{13}C NMR spectrum (101 MHz, CDCl_3) of **16**.

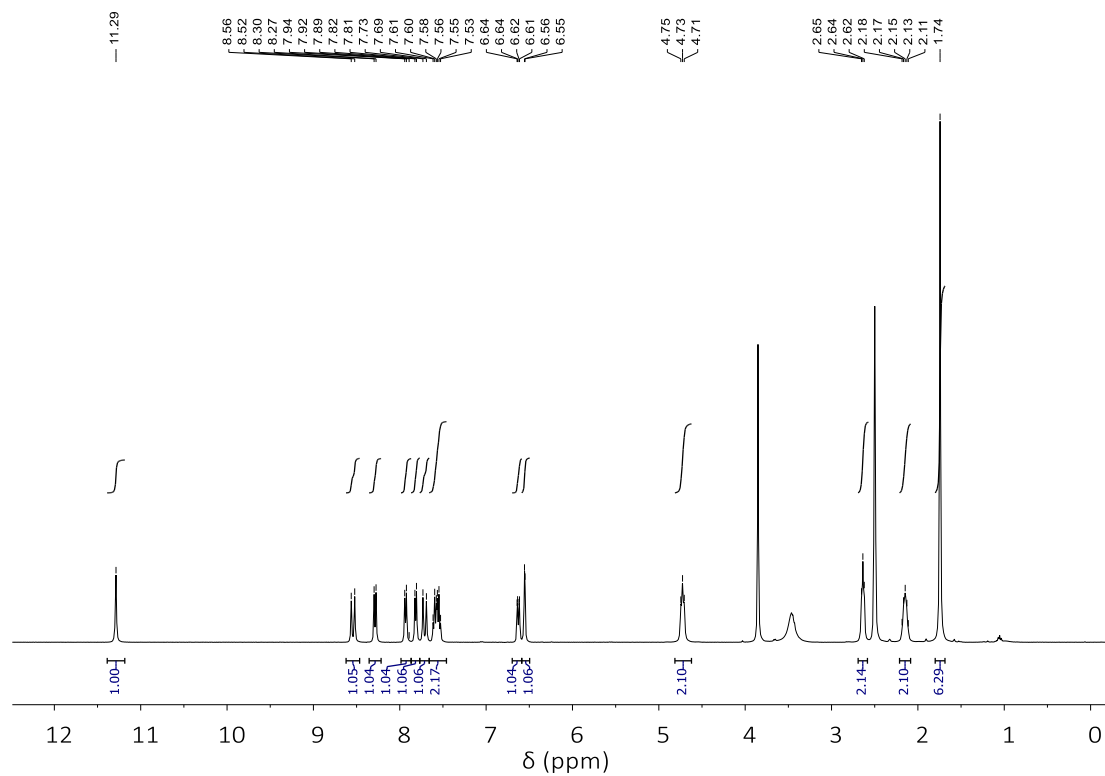
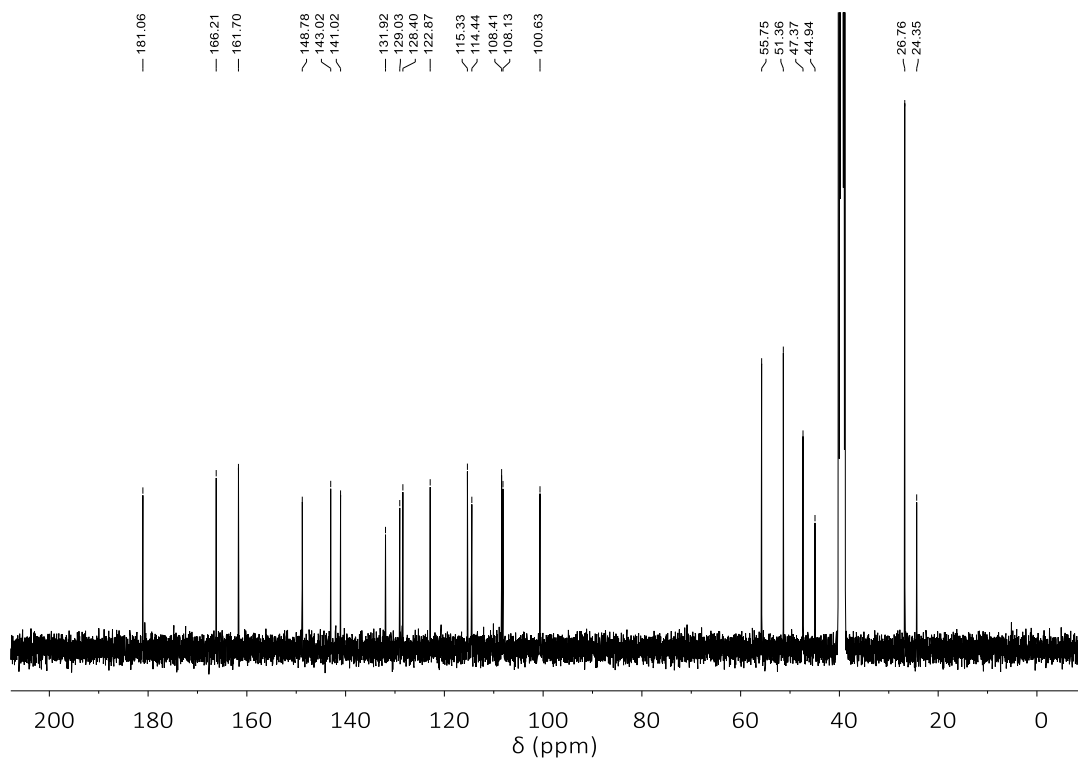
Figure S 5.16. ¹H NMR spectrum (400 MHz, DMSO-*d*₆) of **II5**.Figure S 5.17. ¹³C NMR spectrum (101 MHz, DMSO-*d*₆) of **II5**.

Figure S 5.18. ¹H NMR spectrum (400 MHz, DMSO-*d*₆) of **II6**.Figure S 5.19. ¹³C NMR spectrum (101 MHz, DMSO-*d*₆) of **II6**.

Figure S 5.20. ^1H NMR spectrum (400 MHz, $\text{DMSO}-d_6$) of 5.Figure S 5.21. ^{13}C NMR spectrum (101 MHz, $\text{DMSO}-d_6$) of 5.

Figure S 5.22. ¹H NMR spectrum (400 MHz, DMSO-*d*₆) of 6.Figure S 5.23. ¹³C NMR spectrum (101 MHz, DMSO-*d*₆) of 6.

Figure S 5.24. ¹H NMR spectrum (400 MHz, DMSO-*d*₆) of 7.Figure S 5.25. ¹³C NMR spectrum (101 MHz, DMSO-*d*₆) of 7.

Figure S 5.26. ¹H NMR spectrum (400 MHz, DMSO-*d*₆) of **8**.Figure S 5.27. ¹³C NMR spectrum (101 MHz, DMSO-*d*₆) of **8**.

Chapter 6

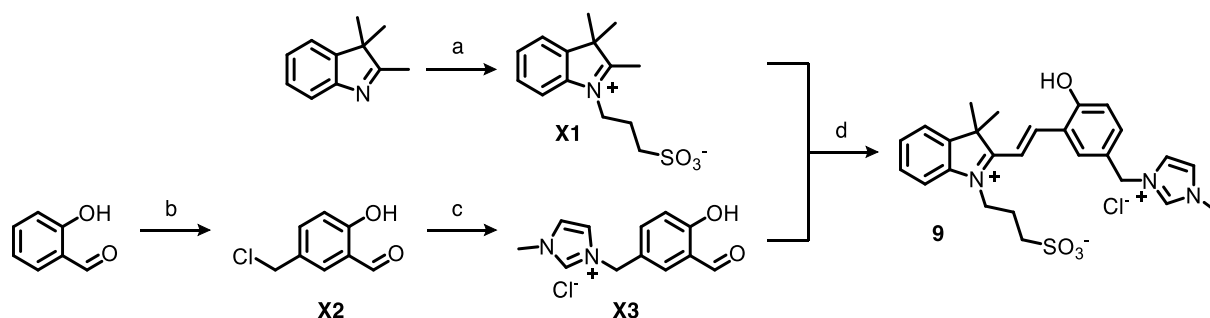
Integrating photoacidity and host-guest chemistry in water

6.1 Introduction

Changing the acidity of functional groups by means of intermolecular interaction or host-guest complexations is an event which is widespread in natural systems, where enzymes tune and modify their own acid-base properties to carry out their reactivity.^[121–125] In synthetic systems, achieving large pK_a variations on demand can be challenging and supramolecular chemistry has proven to be a viable option to stabilize selectively one of the conjugated acid or base. Many supramolecular receptors are available nowadays for this type of task and most of them such as cyclodextrins^[126,127], calixarenes^[128–131] and cucurbiturils^[132–135] have been studied extensively. The capability to influence the thermodynamics of proton release of their guest molecules^[135–141] can happen in two ways^[142]: either the non-ionized form of the acid/base is stabilized by hydrophobic interactions or the ionized form is stabilized by ion-dipole or dipole-dipole interactions with the host molecule. Specifically, cucurbiturils display a high affinity for cations^[143] and consequently they can act as stabilizers for the protonated and charged form of guest molecules. This feature emerges clearly considering the large positive pK_a shifts observed for amines upon host-guest complexation.^[135,137,144–150] Another important consequence of the encapsulation-induced pK_a shifts can be addressed to the solubility of the guests. Indeed, many protic compounds display a broad spectrum of conditional solubilities

where the most important parameter that influences their dissolution is their pK_a . Significant enhancements of water solubility have been demonstrated for a wide range of pharmaceutically relevant guests including albendazole, carbendazim, fuberidazole, to name a few.^[151] The influence of the pocket of the host molecule, does not limit only to solubility and acidity effects. Indeed, many examples have been published on the stabilization of reactive molecules towards both nucleophiles^[152–154], electrophiles^[155] and physical effectors such as light^[151,156–158] and temperature^[159,160]. The following chapter covers the design, synthesis and characterization of a cationic merocyanine guest for cucurbit-[7]-uril, with the aim of obtaining a robust host-guest system featuring improved pH photoswitching properties. This encompasses the enhancement of the photochemical ΔpH and the stabilization of the photoswitch against hydrolysis.

6.2 Synthesis and characterization of the photoswitch



Scheme 6.1. Synthesis of photoswitch **9**. a) 1,3-propanesultone, toluene, 24h reflux (95%), b) HCl 32%, (HCHO)_n, r.t., 8 h (79%), c) 1-methylimidazole, toluene ,r.t., 30 min (89%), d) EtOH, reflux, 12 h (76%).

In Chapter 4 we discussed the aqueous chemistry of compound **4**, whose high water solubility was attributed to the introduction of a sodium sulfonate group on the phenolic moiety. Here, instead, we decided to investigate the possibility to introduce a cationic

group that imparts high solubility to the photoswitch. After optimization, the synthesis has been streamlined making the preparation of the photoswitch very simple and modular. The indolium salt, **X1**, was prepared as described in the previous chapters. Salicylaldehyde, which is an inexpensive and abundant building block, is easily derivatized by treatment with hydrochloric acid and formaldehyde to yield the chloromethyl-salicylaldehyde, **X2**, which is reactive towards a broad spectrum of nucleophiles. We chose 1-methylimidazole as the nucleophile for the lack of relevant acid-base properties of the corresponding imidazolium salts, and for the biocompatibility of the potential degradation products of hydrolysis. Adding 1-methylimidazole to a toluene solution of **X2** yields the corresponding imidazolium chloride salt **X3** with high yield and purity. As described in the previous chapters, the final step is a Knoevenagel condensation between **X1** and **X3** that yields compound **9** (see Experimental Section for the full ^1H , ^{13}C -NMR, HR-MS and X-Ray characterization). The solubility in acidic water of **9** is very high (ca. 30 mM) as compared to previous generations of BIPS, and is above any photoacid characterized in this thesis, except **4** which displays comparable solubility by virtue of the additional anionic sulfonate group.

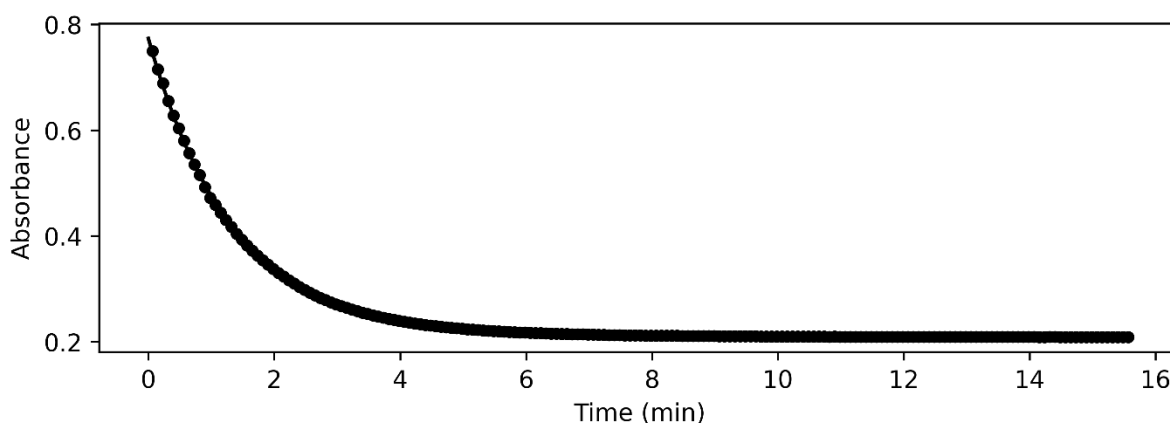


Figure 6.1. Absorbance profile at 532 nm for the MC-to-SP equilibration at pH 10.

The first characterization we conducted was the measurement of the K_c value by means of UV-Vis kinetics. Indeed, this allows for identifying the equilibration time that is necessary to calculate all the thermodynamic parameters as described previously.^[113,115] The experiment consists in injecting an aqueous solution of the MCH form of **9** in a buffered solution at alkaline pH values. Monitoring the time evolution of the *in-situ* formed MC, allows for quantifying in a fast and precise way the forward and backward rate constants of the equilibrium between MC and SP, along with the K_c value. As can be seen from Figure 6.1, the decay of MC is complete within 15 minutes at 25 °C. The K_c value was found to be 2.73, which is lower than that of compound **1** but almost twice the one of compound **5**. The MC-to-SP rate (k_2 , see Experimental Section) was found to be approximatively two times the one of **5** and one quarter with respect to Liao's photoacid **1**. On the other hand, k_{-2} was found to be slightly lower than those of the other two. In other words, the MC ring-closure reaction becomes faster in the order **5** < **9** < **1**, while the rate of the ring opening of SP remains similar. This trend can be rationalized by considering the substituent effects in *para* with respect to the hydroxyl group of the phenol. Indeed, the decreasing EDG character in the series -OMe, -CH₂(mim)Cl, -H is compatible with a decreasing nucleophilicity of the phenolate, this in turn slows down the MC-to-SP kinetics. On the other hand, the invariance of k_{-2} finds explanation on the polarization of the spiro carbon which in this series of compounds is rather similar. In fact, for compounds **1**, **2**, and **3** ($n = 2, 1, 3$), the inversely proportional trend for k_{-2} is a clue for the importance of the electron density supplied to the spiro carbon. This must pass from a sp³ hybridization (in the SP form) to a sp² (in the MC form) which is favored in case of higher the electron density on the nitrogen; moreover, in the reaction from SP to MC, the expulsion of the phenolate leaving group is presumably faster if the spiro carbon is electron-rich. We

then moved on to study the acid-base properties of the ground state. We determined $pK_a^{GS} = 5.83$ (Figure 6.2), which is less acidic than **2**, **4**, and, for analogy to cationic photoacids, all the compounds bearing an alkylammonium sidechain reported by Beves and co-workers.^[114] We then probed the metastable state acidity of **9** under 500 nm irradiation. We determined a pK_a^{MS} of 2.00 (Figure 6.3), which means the photoacidity of **9** is $\Delta = 3.8$ pK units.

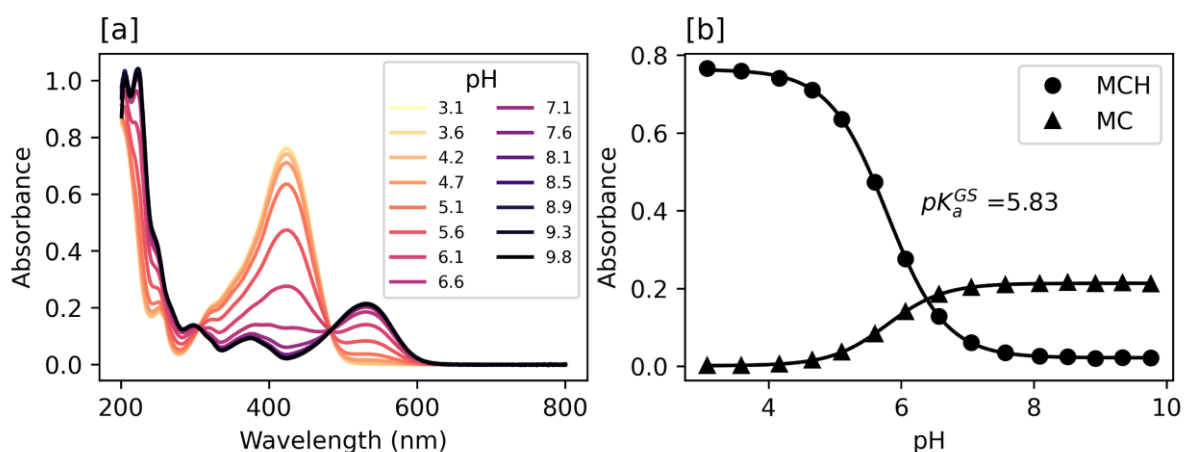


Figure 6.4. UV-Vis titration of compound **9** in the dark. In [a] the spectra as function of pH, in [b] the absorbance profiles.

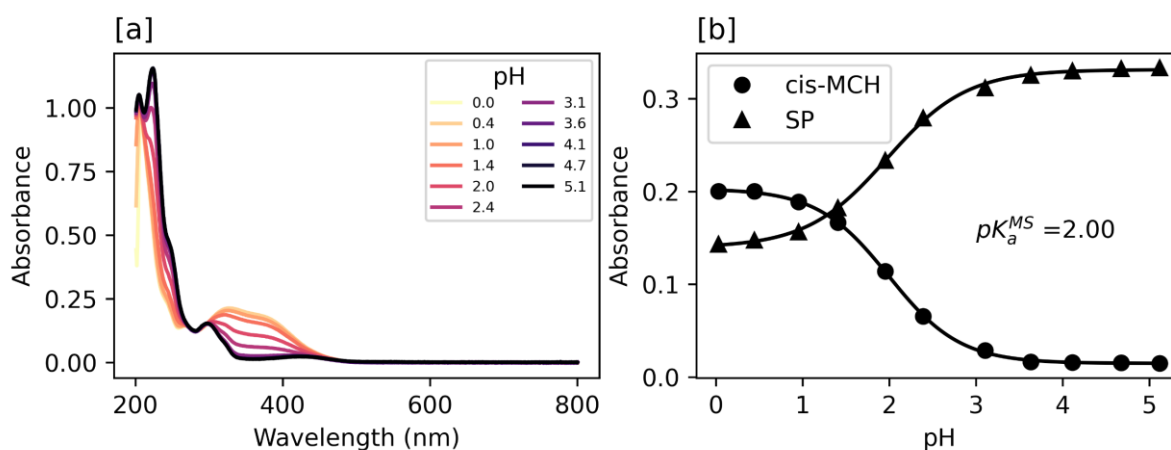


Figure 6.5. UV-Vis titration of compound **9** under 500 nm irradiation. In [a] the spectra as function of pH, in [b] the absorbance profiles.

The hydrolysis and recovery from the metastable state of **9** were then tested with the same methods described in Chapters 3 and 4. As mentioned previously, it was

possible to obtain both the hydrolysis (Figure 6.6) and relaxation kinetics profiles (Figure 6.7) with a single experiment (see Experimental Section for more details). The photoacid **9** displays hydrolysis kinetics similar to **1** while having high dark acidity as compared to **1** and **5**. Consequently, we decided to explore the supramolecular chemistry of **9** with the aim of spreading the ΔpH and stabilizing the photoswitch respect to hydrolysis.

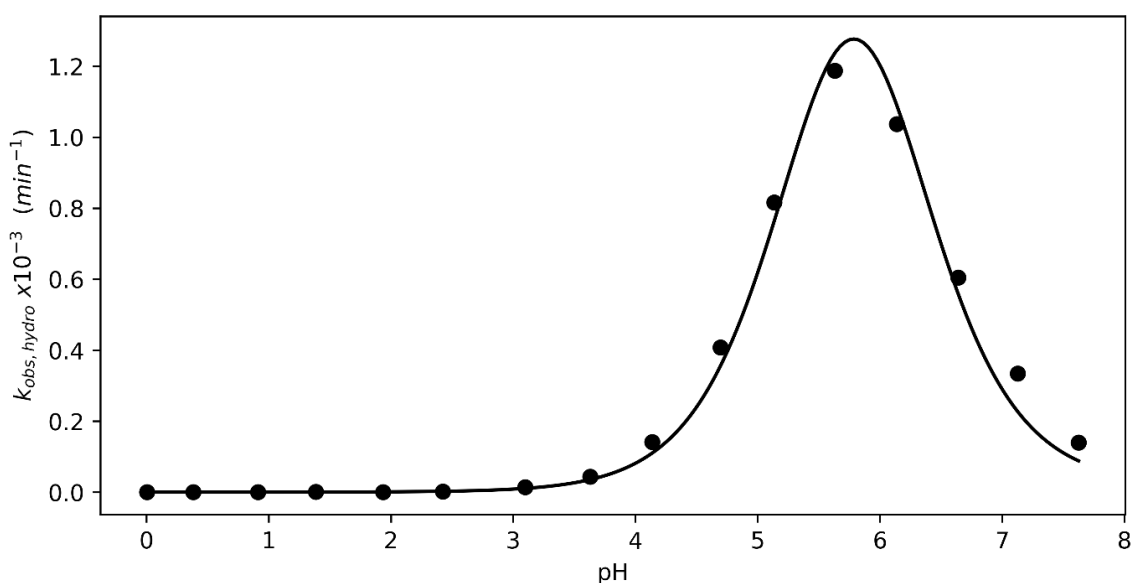


Figure 6.6. Hydrolysis rate constants as function of the pH value for **9**.

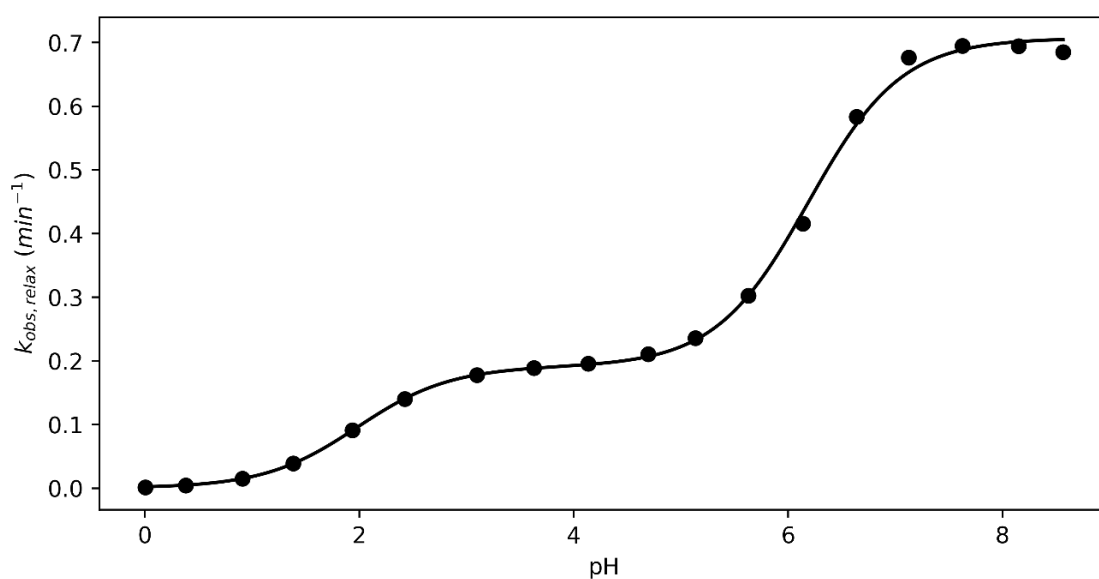


Figure 6.7. Relaxation rate constants as function of the pH value for **9**.

6.3 Supramolecular chemistry with cucurbit-[7]-uril

Cucurbit-[n]-urils are a class of macrocyclic compounds firstly reported in 1905 by Behrend^[161] who experimented the acidic condensation between glycourils and formaldehyde resulting in insoluble polymeric materials. These cyclic condensates demonstrated exceptional chemical stability and it was possible to isolate co-crystals with KMnO_4 , AgNO_3 and many dyes.^[132]

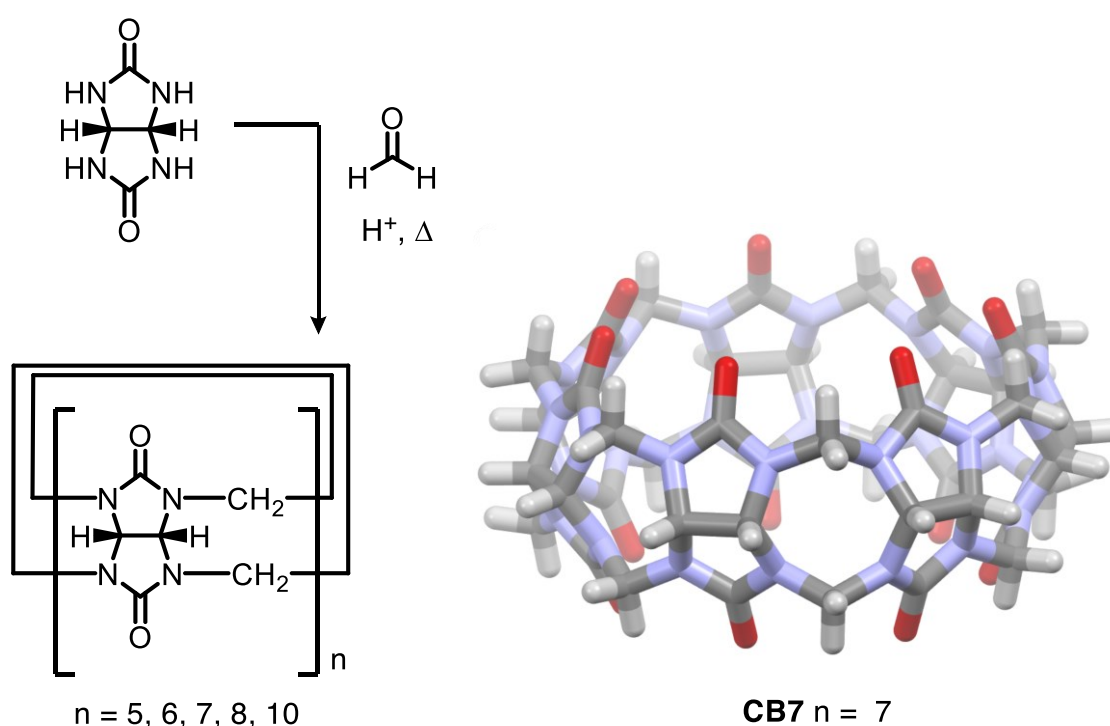


Figure 6.8. Synthesis and structure of cucurbit-[n]-urils. On the right the crystal structure of cucurbit-[7]-uril.

The synthesis of these compounds was not developed for decades until Mock^[162] in the 1980s managed to isolate the calcium complex of the six-membered ring. This was interacting with the calcium cations through the carbonyl rims. The name of this class of macrocyclic hosts derives from the apparent resemblance of the macrocycle to pumpkins belonging to the family of *cucurbitaceae*. The first crystallographic characterizations of these compounds was reported by Kim and co-workers, who managed to isolate and crystallize cucurbit-[n]-urils with $n = 5, 7$ and 8 .^[133] Over the

years, the preparation methods improved considerably and nowadays robust protocols for obtaining CB[n] with $n=5, 6, 7, 8, 10$ are widely adopted.^[163–165] These species are sparingly soluble in almost all organic solvents, while in water only **CB5** and **CB7** show solubilities up to 30 mM.^[132] Among all of them, **CB7** (Figure 6.8) is the one displaying the highest affinity towards organic cations.^[132,143] For our scopes, a relevant example is found in the report of Andréasson on the possibility to capture ammonium-SPs with this macrocycle.^[134] Motivated by these facts, we decided to explore the host-guest chemistry of **9** with **CB7**.

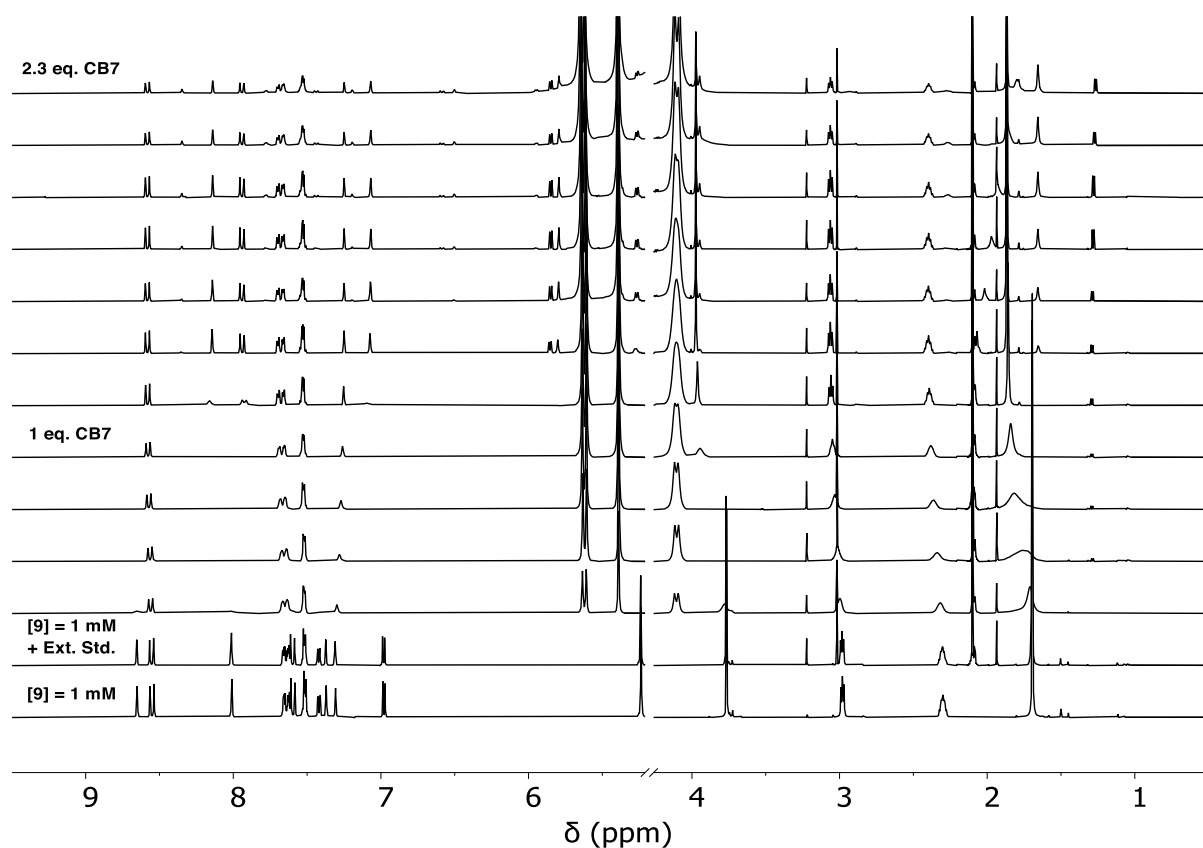


Figure 6.9. ^1H NMR (600 MHz, 298K, $\text{H}_2\text{O}:\text{D}_2\text{O}$ [95:5]) titration of **9** at pH 3 with increasing concentration of CB7. $[\text{9}] = 1 \text{ mM}$, $[\text{buffer}] = 2 \text{ mM}$. The external standard is dimethylsulfone in pure D_2O located in a coaxial insert.

We began our evaluation by measuring the ^1H NMR spectra while titrating aliquots of **CB7** in potassium phosphate solutions of **9** at pH 3 (Figure 6.9). These conditions ensure that **9** is completely in the MCH form, consequently the events deriving from

the dark acidity of **9** can be disregarded. From the titration experiment we had a first insight on the formation of the 1:1 host-guest complex between **9** and **CB7**. In fact, consecutive additions of **CB7** caused severe broadening of many of the signals belonging to **9**. The signals become sharp again as soon as the first stoichiometric equivalent of **CB7** is exceeded, nevertheless, the chemical shift of each signal at the end of the titration is significantly different than for free **9**. The exchange between **9** and **9@CB7** is in the intermediate regime respect to the NMR timescale at 25 °C and at the magnetic field in which the experiment was conducted. This, unfortunately, complicates the calculation of the affinity constant (K_B), so we opted for other techniques.

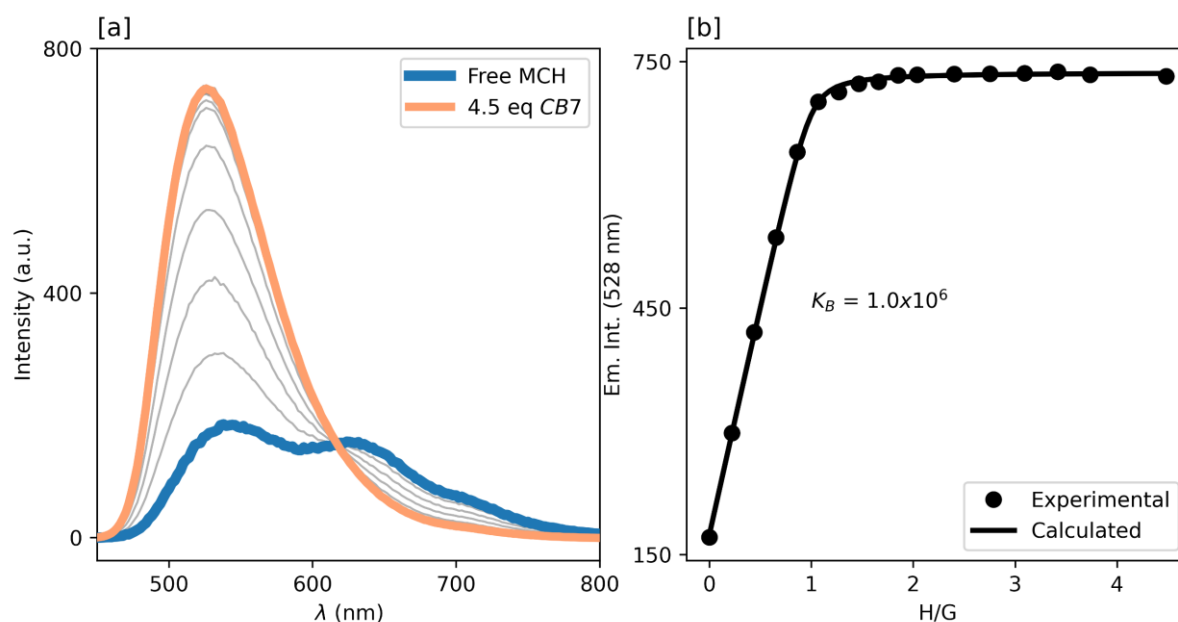


Figure 6.10. Fluorescence titration of **9** with **CB7**, in [a] the excitation spectrum at 423 nm, in [b] the emission profile at 528 nm and the fitting to a 1:1 binding isotherm.

The 1:1 binding found additional confirmation by HR-MS, as we were able to observe the molecular ion of the host-guest complex **9@CB7** (see Experimental Section for more details). From this we moved on based on the well-known fact that **CB7** can alter

the photophysical properties of dyes included in its pocket^[135,166,167], and that some BIPS can bind to CB[n]s with important changes to their photonics.^[145,146] Consequently, we continued our investigation by means of fluorescence spectroscopy. Determining the stoichiometry of binding events requires careful calibration of the reagents used in the experiment. CB[n]s are optically transparent in the UV-Vis region in water, hygroscopic in the solid state, non-luminescent and have no analytical standards for chromatography. This makes their quantification complicated and, to circumvent this problem, it is possible to exploit their high affinity towards chromophores. The protocol of Kaifer and co-workers allows easy quantifications of **CB7** stock solutions by taking advantage of the high affinity towards cobaltocenium hexafluorophosphate ($K_B > 10^8$, see Experimental Section).^[168] Once concentrations of **CB7** and **9** were determined with accuracy, fluorescence titrations between **9** and **CB7** were performed at 25 °C in pH 3 potassium phosphate buffers. Excitation of the 423 nm band of the free MCH form of **9** yields a modest fluorescence intensity that undergoes progressive enhancement upon addition of **CB7** (Figure 6.10 a). The experimental points fit well to a 1:1 binding isotherm giving a K_B of 1.0×10^6 (Figure 6.10 b). To have ulterior confirmations over the binding stoichiometry and on the magnitude of the affinity constant, we performed ITC experiments for the determination of the binding enthalpy, entropy, stoichiometry and affinity constant. In this experiment, a solution of **9** in potassium phosphate buffer at pH 3 and 25 °C, is placed in the measuring cell of the instrument. A **CB7** solution with the same solvent/buffer composition is placed in the titrant burette and added in aliquots to the measuring cell. Analysis of the thermogram (Figure 6.11 a) and the calculation of the integrated powers allows to graph the heat generated from the reaction against the ratio between the nominal molarity of **9** and **CB7**. The 1:1 binding isotherm fits

optimally the experimental points and it is possible to calculate the binding thermodynamic parameters. The calculated binding constant for the formation of **9@CB7** is $K_B = 9.5 \times 10^5$ which is very close to the value determined by fluorescence, giving a binding Gibbs free energy $\Delta_r G^0 = -8.2$ kcal/mol. The enthalpy calculated from the isotherm fitting is $\Delta_r H^0 = -5.3$ kcal/mol and the standard reaction entropy is $\Delta_r S^0 = 9.5$ cal/(K mol).

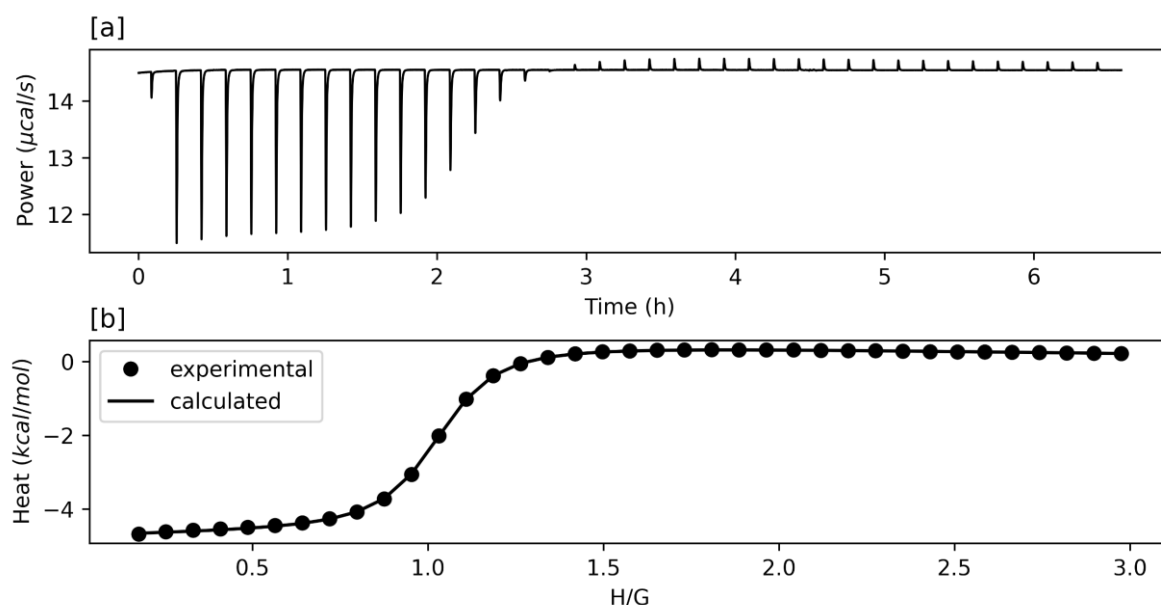


Figure 6.11. ITC titration of **9** with CB7. In [a] the raw thermogram, in [b] the integrated power and the 1:1 binding isotherm.

The titration reveals that the binding is highly exothermic and entropically favored. All the previous facts are in line with the chemistry of CB[n]s towards organic cations, indeed the encapsulation of a guest molecule bearing hydrophobic moieties – *e.g.*, photoacid **9** – leads to the expulsion of hydrogen bond deficient and highly structured water molecules from the cavity CB[n]s.^[169–172] This tendency has been calculated in MD simulations of CB[n]s by putting explicitly water molecules within the cavity. The energy gained from the extrusion of water molecules follows a trend that depends on

the number of hydrogen bonds and water molecules contained in the CB[n]s cavity, the net gain has been calculated to be maximum for **CB7** in the family of CB[n]s.^[171]

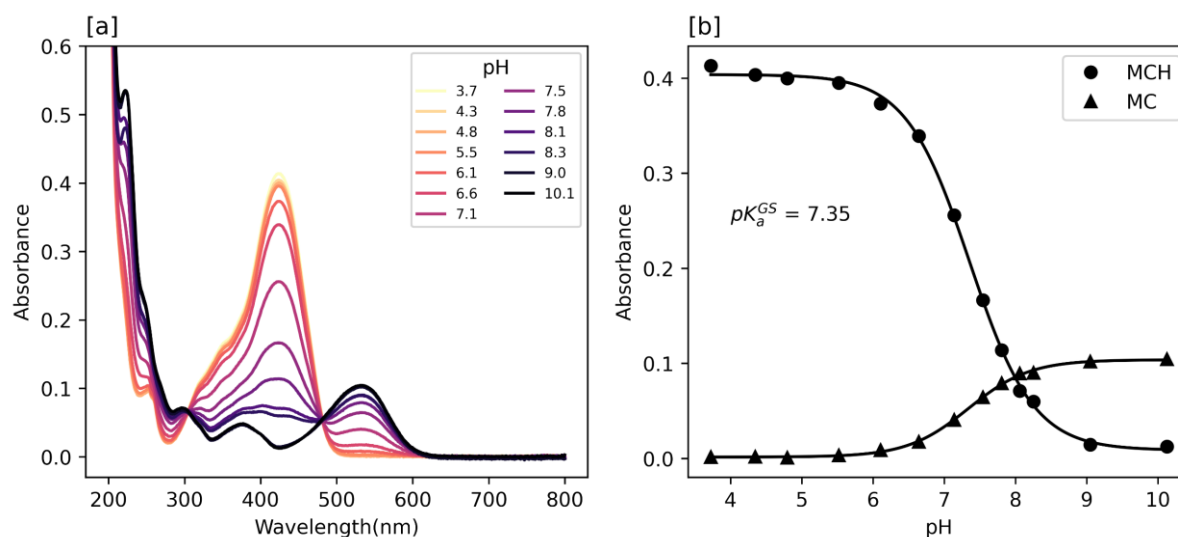


Figure 6.12. UV-Vis titration of compound **9** in the dark with 4 equivalents of CB7. In [a] the spectra as function of pH, in [b] the absorbance profiles.

The affinity between **9** and **CB7** drove our interest in exploring whether there were any beneficial effects in terms of pK_a shifts and hydrolytic stability. We went on and probed the pK_a^{GS} of **9** by saturating its population by **CB7**, thus analyzing the properties of **9@CB7**. The inclusion complex **9@CB7** demonstrated a significant pK_a^{GS} shift respect to the free **9** passing from 5.83 to 7.35 (Figure 6.12 a and b). The K_c was then determined on the same samples, revealing the absence of significant variations on the parameters of the MC-to-SP equilibration (Figure 6.13). These first observations on the acidity and equilibration kinetics imply a stabilization of the MCH form, while the equilibria of the conjugated bases MC and SP are negligibly influenced by the presence of **CB7**. As last experiment in the dark we probed the hydrolysis kinetics in presence of **CB7** to determine whether there were any effects in stabilizing the photoswitch. From the data represented in Figure 6.14 it is possible to observe a dramatic reduction of approximately six times of the peak hydrolysis rate.

To summarize the exploration of the **CB7** effects on the ground state of **9**, it is possible to state that the presence of **CB7** is beneficial both on the dark acidity and hydrolytic stability aspects.

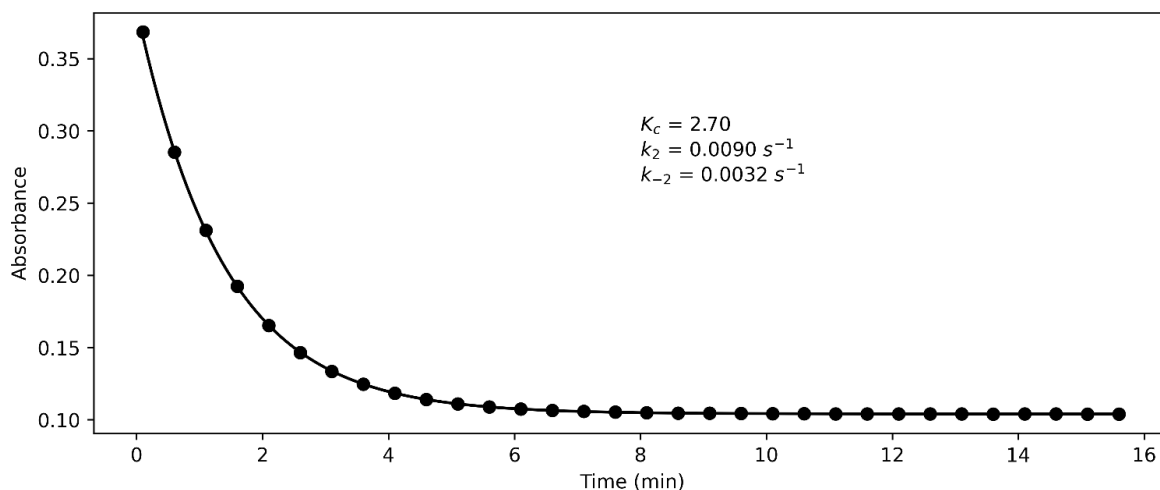


Figure 6.13. Absorbance profile at 532 nm for the MC-to-SP equilibration at pH 10 in presence of 4 equivalents of CB7.

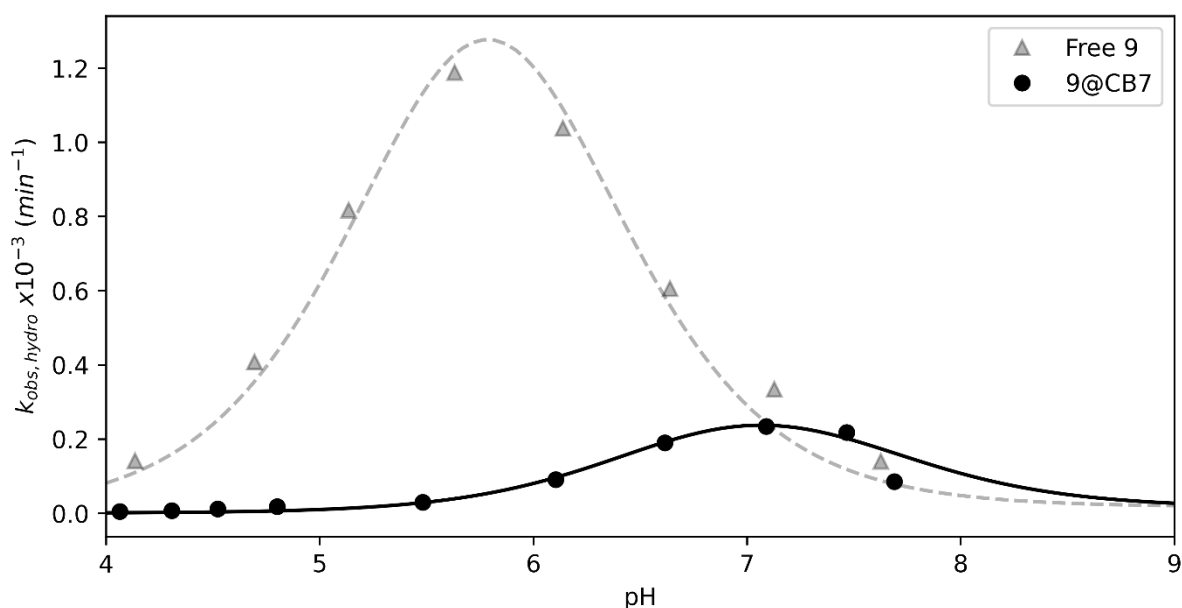


Figure 6.14. Hydrolysis rate constants as function of the pH value for **9** (triangles and dashed line) and for **9@CB7** (circles and solid line).

We then probed the metastable state properties in presence of **CB7**. These involved, at first, the measurement of the pK_a^{MS} with **CB7** in solution. Using 500 nm light and UV-Vis spectroscopy we could determine that the pK_a^{MS} is 3.12 (Figure 6.15).

Considering the parameters calculated in this last section, we can summarize and compare the effects of **CB7**. The photoacidity in absence of **CB7** is 3.8 while the addition of the macrocycle brings this value to 4.2, thus, bringing an indication that the pH excursion between light and dark is likely to be wider ($\Delta\text{pH} = +0.4$, Figure 6.16).

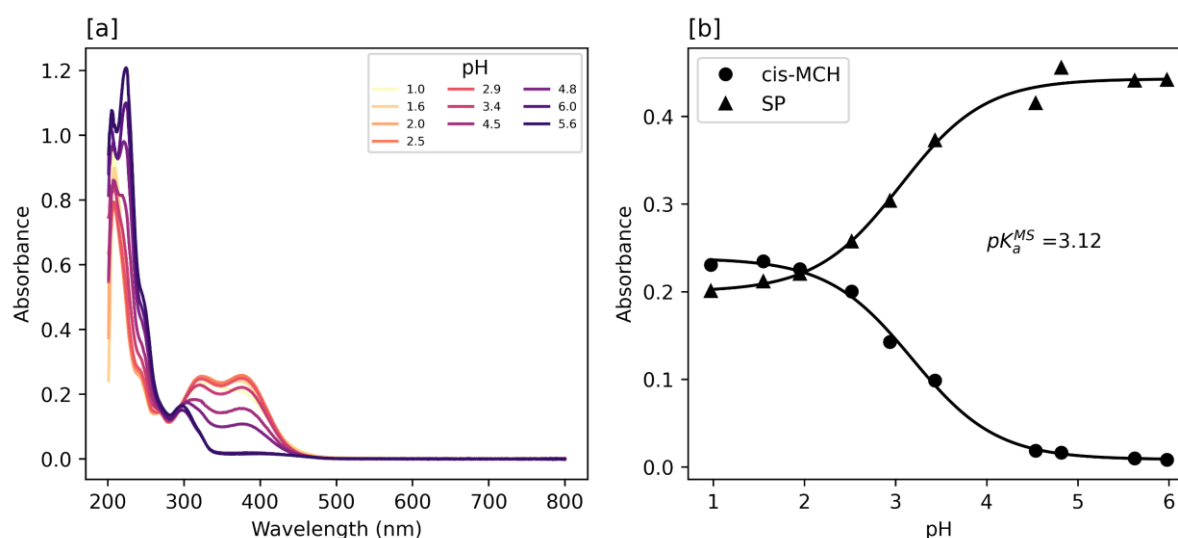


Figure 6.15. UV-Vis titration of compound **9** under 500 nm illumination with 4 equivalents of **CB7**. In [a] the spectra as function of pH, in [b] the absorbance profiles.

Additionally, the $\text{p}K_a^{\text{GS}}$ with **CB7** is very close to biologically relevant values and, consequently, the supramolecular adduct **9@CB7** becomes a stable photoswitch capable to trigger acidity variations starting from physiological pH. The only experiment left to perform was the relaxation from the metastable state in presence of **CB7**. This experiment would highlight any significant differences in terms of relaxation mechanisms. Samples of **9@CB7** in phosphate buffers at increasing pH values were irradiated with 500 nm light until no significant absorbance variation was noticeable, then the light was switched off and the absorbance was traced as function of time. The traces were fit to a first-order rate law and the resulting $k_{\text{obs,relax}}$ has been fit to the models described in Chapter 3. From Figure 6.17 it is possible to observe that the

general shape of the curves is similar, and the most important difference happens at the two inflection points, corresponding to pK_a^{MS} and pK_a^{GS} respectively.

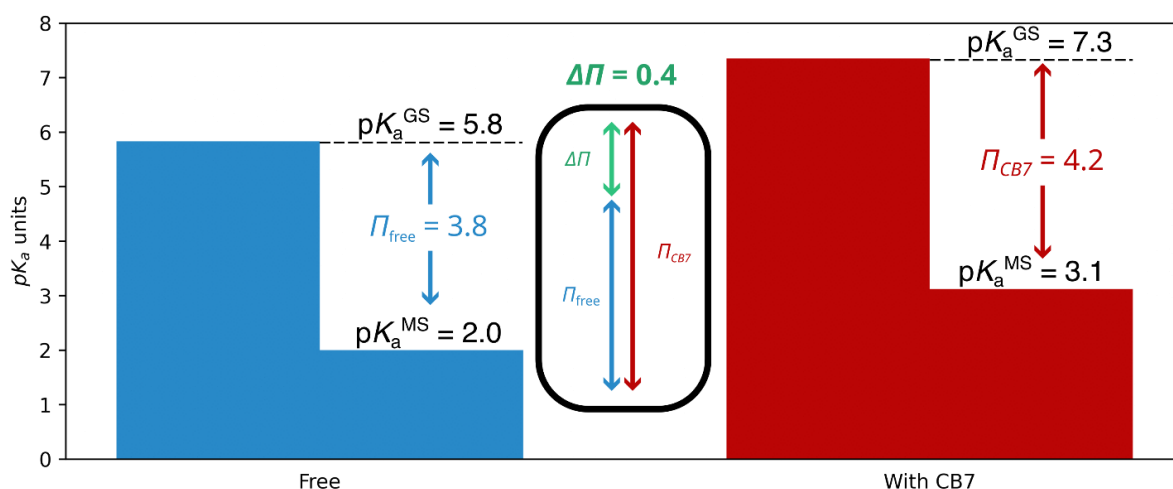


Figure 6.16. Photoacidity difference between free **9** (in blue) and **9@CB7** (in red), The green arrow represents the differential photoacidity between the free and the bound state.

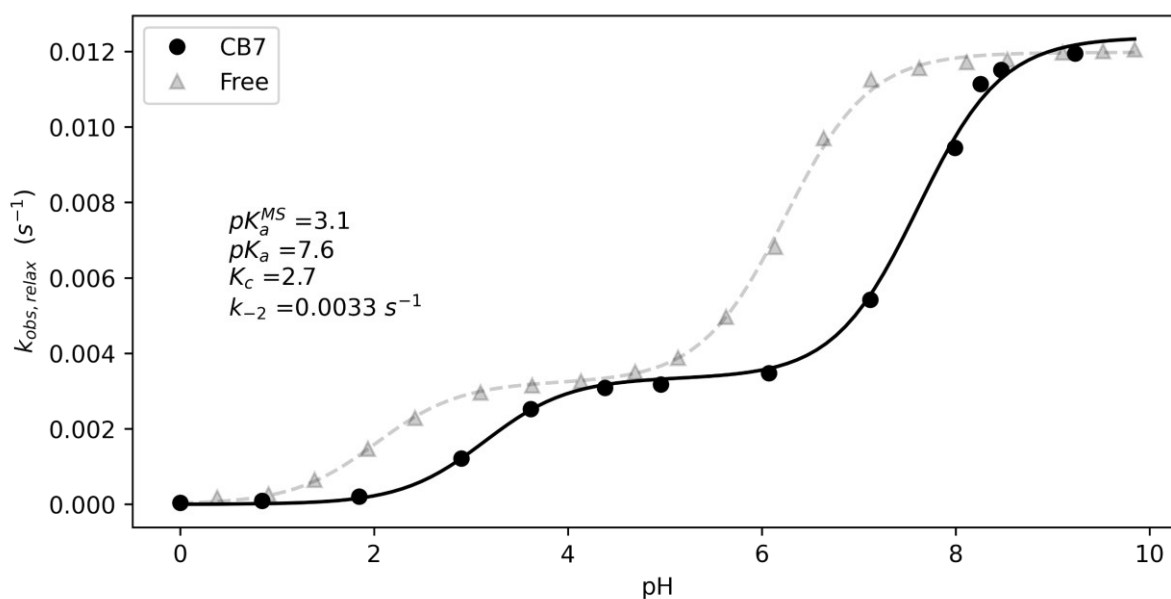


Figure 6.17. Relaxation rate constants as function of the pH value for free **9** (dashed line) and **9@CB7** (solid line).

Moreover, the magnitude of k_{-2} does not change upon formation of **9@CB7** supporting the hypothesis on the invariance of the relaxation mechanism in presence of **CB7**. In other words, the relaxation mechanism of **9** is the same despite its encapsulation, the

main differences can be ascribed to the pK_a shifts. After the preliminary characterizations, we then performed pH switching experiments for **9@CB7** with partial neutralization using a strong base to pH close to pK_a^{GS} so to obtain the maximum ΔpH possible. Illumination with 500 nm light of the sample, triggered the proton release that was detected as a deep pH excursion from 7.4 to 3.4. We ran the experiment for as long as possible to obtain information about the durability of the system and it was possible to switch continuously for more than one day. The durability of the photoswitch in these conditions is significantly superior as compared to the initial generations – *i.e.*, the photoacids of Chapter 3 and 4 – and it is comparable to the methoxylated adducts of Chapter 5 with lower dark-acidity and higher aqueous solubility.

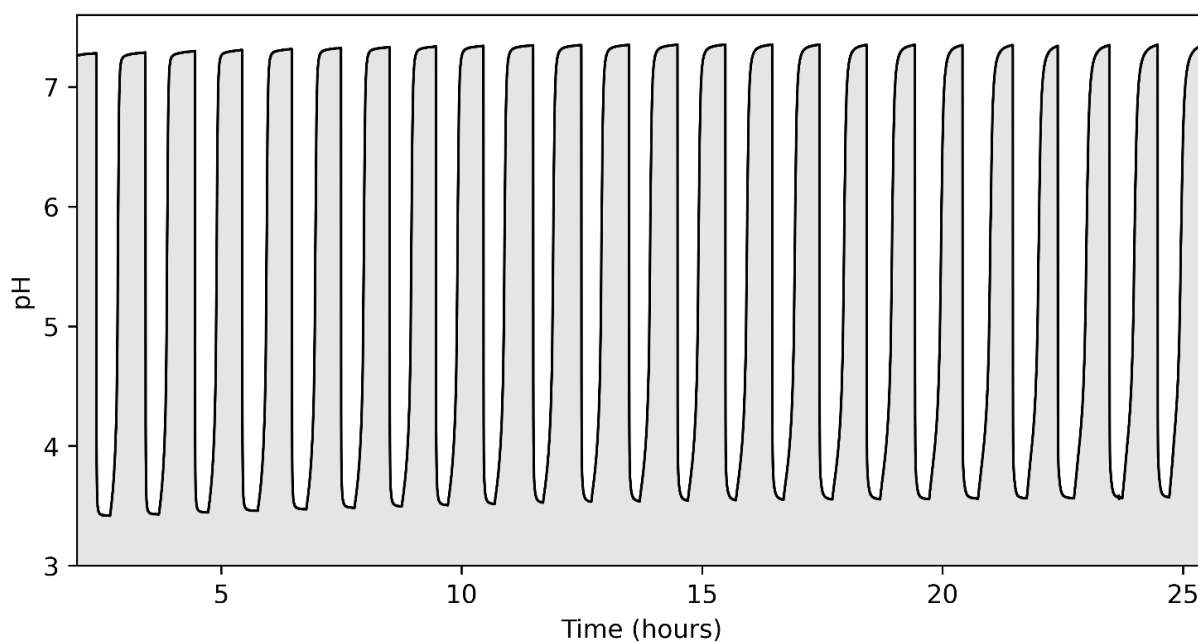


Figure 6.18. Photochemical pH-jump profiles for 1 mM of **9** and 2 mM **CB7** under 500 nm irradiation.

6.4 Conclusions

The collection of experiments presented in this chapter allows for the preparation of a new and highly water soluble photoacid. This has been possible starting from commonly available, inexpensive and nontoxic starting materials enabling also to prepare intermediates that are modular and can allow for the exploration of vast libraries of substituents with relatively low synthetic efforts. We concentrated our efforts on **9** that had poor stability towards hydrolysis and high dark acidity, nonetheless it demonstrated high affinity towards **CB7**. After preliminary characterizations, the experiments lead to the conclusion that **CB7** has beneficial effects by means of encapsulation forming **9@CB7**. The supramolecular interaction has been tested with many techniques yielding the binding stoichiometry and the binding thermodynamic parameters. The newly discovered **9@CB7** was then tested with the standard protocol for BIPS developed in Chapter 3, displaying a significant and beneficial difference in dark-acidity and hydrolytic stability. Additionally, many observations give value to the hypothesis of a selective binding towards the MCH form of **9** as can be seen from the invariance of the parameters of the MC-to-SP equilibration. Once completed the preliminary characterization our study concluded with a repetitive pH jump of 4 units for more than one full day of cycling (24 cycles). This confirms the high stability of the system and unlocks the potential of BIPS in physiologically relevant conditions.

6.5 Experimental section

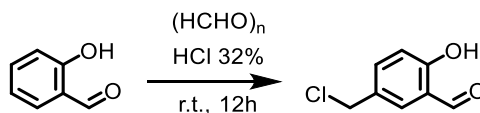
6.5.1 General Remarks

For the spectrophotometric titrations were used potassium phosphate buffers which were prepared by titration of a solution 0.1 M in H_3PO_4 with 10 M aqueous KOH. The pH was measured with a Metrohm Unitrode Pt 1000 combined pH electrode. The buffer concentration used for the following spectra is 20 or 2 mM, the concentration of compound 1 in the cells is 25 or 12.5 μM and the spectra were acquired after 15 minutes from the preparation of the samples to allow enough time for equilibration. After the spectral acquisition the pH was checked using a pre-calibrated Metrohm Biotrode to measure the pH directly inside the cells. The resulting profiles were then fitted to the Boltzmann sigmoidal function with the aid of the Excel Solver. Salicylaldehyde (99%) was purchased from Abcr, 1-methylimidazole from Fluorochem (98%), paraformaldehyde from Roth (99%). H_3PO_4 85% and standard HCl 1 N from Merck, while KOH was purchased from Reactolab. All reagents and solvents were used without further purification, whereas H_2O used in all preparations was filtered with a MilliQ-Integral5 purification system, degassed by N_2 bubbling (1h under vigorous stirring) and stored at 4 °C. NMR spectra were recorded at on a Bruker Avance III spectrometer (^1H : 400 MHz; ^{13}C : 101 MHz) equipped with a 5 mm BBFOz ATMA probe (characterization), and on a Bruker Avance III HD spectrometer (^1H : 600 MHz) equipped with a 5 mm CPPBBOz ATMA probe (pH titrations). Chemical shifts (δ) are reported in parts per million (ppm), while coupling constants (J) are given in Hertz (Hz). Solvent residual signals are used as internal reference for spectra alignment ($\text{DMSO}-d_6$: δ = 2.50 ppm, D_2O : δ = 4.87 ppm, CDCl_3 : δ = 7.26 ppm). Electrospray-ionization HRMS analyses were run (positive mode/direct injection) on a

Waters XEVO G2-S GTOF spectrometer interfaced with Acquity UPLC pumps and sample manager system. UV-Vis spectra and kinetics were acquired on an Agilent Cary 60 spectrometer equipped with an 18-cell holder coupled to a Huber thermostat, using Suprasil quartz cuvettes (114-QS) from Hellma Analytics. pH measurements were performed using Metrohm pH module 867 or Titrand 888 coupled with Unitrode Pt1000 or Biotrode glass electrodes; pH data were processed using the software Metrohm Tiamo Light. Samples photoirradiation was carried out using a Prizmatix FC-LED-500Z high-power LED light source ($\lambda = 500 \text{ nm}$). Unless stated otherwise, the light beam was delivered by polymer optical fibers (core $1500 \text{ }\mu\text{m}$) i) positioned orthogonally to and just below the liquid/air interface of sample solutions (UV-Vis) or ii) connected to an FCM1-06 collimator coupled with a 45° mirror cage, resulting in a 25 mm light beam tilted by 90° (pH jumps). Power measurements of the fiber-coupled LED output were made with Thorlabs S142C integrating sphere photodiode power sensor; the uncertainty is within 3-5%. Potassium phosphate buffers from pH 3 to 10 were prepared titrating a solution of H_3PO_4 (100 mM, 1L) with KOH 10 M. Diluted stocks of standard HCl 0.1 N were used below pH 4. All buffer stocks were stored at room temperature. In order to account for the pH change in sample preparations, the pH of each buffer stock is measured again after dilution (1/5, 20 mM) in mQ water. In the UV-Vis experiments the error on pH values results from multiple readings before and after the experiments ($\leq \pm 0.04$). Unless stated otherwise, curve fitting is performed in Excel, using the Solver add-in for minimizing the sum of the square deviations from the corresponding model curve.

6.5.2 Synthetic Procedures

Synthesis of compound **X2**



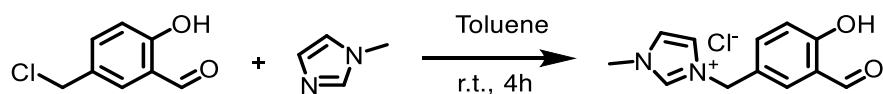
Scheme S6.1. Synthesis of compound **X1**.

In a 250 ml Erlenmeyer flask were added 150 ml of concentrated hydrochloric acid (32%) followed by 12.3 g of powdered paraformaldehyde (410 mmol, 10.0 eq) and 5.00 g of salicylaldehyde (41.0 mmol, 1.00 eq). The mixture appeared pale yellow upon addition of the salicylaldehyde and was vigorously stirred overnight. After 12 h a white precipitate had formed, this was filtered and the solid was washed with water (4 x 50ml), dissolved in 50 ml of DCM, dried over MgSO_4 and the solvent removed by rotary evaporation. At this point the solid was of very pale pink color and the purification was done by dissolving the compound in the minimal amount of boiling petroleum ether followed by hot filtration. The so-obtained petroleum ether solution then spontaneously crystallizes upon passive cooling yielding white, large, needle-like crystals. These were filtered, washed with petroleum ether (3x20 ml) and air dried on the filter. The purity of the compound can be checked by silica TLC in pure dichloromethane ($R_f = 0.48$). The final yield of **X2** is 5.53 g (32.2 mmol, 78.8 %).

^1H NMR (600 MHz, CDCl_3) δ (ppm): 11.07 (s, 1H), 9.90 (s, 1H), 7.59 (d, $J = 2.4$ Hz, 1H), 7.56 (dd, $J = 8.6, 2.4$ Hz, 1H), 7.00 (d, $J = 8.6$ Hz, 1H), 4.59 (s, 2H).

^{13}C NMR (151 MHz, CDCl_3) δ (ppm) 196.33, 161.78, 137.50, 133.79, 129.35, 120.48, 118.49, 45.38.

HRMS (Sicrit plasma/LTQ-Orbitrap) m/z: $[M + H]^+$ Calcd for $C_8H_8ClO_2^+$ 171.0207;
Found 171.0207.

Synthesis of compound X3

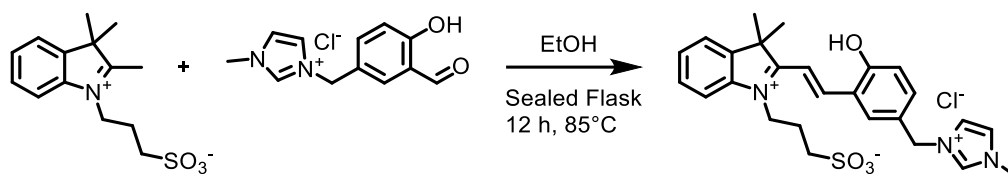
Scheme S6.2. Synthesis of compound X3.

In a 100 ml round-bottomed flask were added 25 ml of toluene and 1.00 g of compound 1a (5.86 mmol, 1.00 eq). Upon dissolution was added dropwise and under strong stirring a solution composed by 10 ml of toluene and 0.51 g of 1-methylimidazole (6.16 mmol, 1.05 eq). Immediately a white, crystalline precipitate forms and the stirring was continued for 4 h at room temperature. The mixture was filtered and the solid was washed with toluene (3 x 10 ml), petroleum ether (3 x 20 ml) and dried in air. The so-obtained white crystalline solid is of high purity and can be used in the next steps without further processing. The final yield of X3 is 1.32 g (5.86 mmol, 89.1 %).

^1H NMR (400 MHz, D_2O) δ (ppm): 9.94 (s, 1H), 8.74 (s, 1H), 7.77 (d, $J = 2.4$ Hz, 1H), 7.61 (dd, $J = 8.6, 2.4$ Hz, 1H), 7.46 (dt, $J = 8.4, 2.4$ Hz, 2H), 7.06 (d, $J = 8.4$ Hz, 1H), 5.38 (s, 2H), 3.88 (s, 3H).

^{13}C NMR (101 MHz, D_2O) δ (ppm): 196.84, 160.35, 137.42, 135.99, 133.65, 125.52, 123.84, 122.08, 121.16, 118.15, 51.76, 35.70.

HRMS (ESI/QTOF) m/z : $[\text{M}]^+$ Calcd for $\text{C}_{12}\text{H}_{13}\text{N}_2\text{O}_2^+$ 217.0972; Found 217.0976.

Synthesis of compound **9**Scheme S 6.3. Synthesis of photoswitch **9**.

The synthesis of 3-(2,3,3-trimethyl-3H-indol-1-ium-1-yl)propane-1-sulfonate was carried out as described in previous works.^[113,115] In a 100 ml round-bottomed flask were added 15 ml of absolute ethanol, 0.75 g of 3-(2,3,3-trimethyl-3H-indol-1-ium-1-yl)propane-1-sulfonate (2.67 mmol, 1.00 eq) and 0.67 g of compound **X3** (2.67 mmol, 1.00 eq). The flask was sealed with a rubber septum and the system cycled three times between vacuum and nitrogen. The temperature was increased to 85° C under stirring for 12 hours. After this time, the mixture had turned to dark red and this was added dropwise to 250 ml of diethyl ether under strong stirring. A bright orange solid precipitates immediately as a powder in the diethyl ether mixture which is filtered and washed with more diethyl ether (3 x 25 ml). The solid was dried under vacuum before proceeding with the next step. The orange powder was added to 150 ml of *i*-PrOH, suspended in it and brought to boiling temperature, to this was added dropwise the minimal amount of absolute ethanol to completely dissolve the powder. The so-obtained mixture was then allowed to passively cool down to room temperature and then transferred in a 3° C refrigerator overnight. The next day red-orange flake-like crystals had formed which were filtered and washed with -19°C *i*-PrOH (3 x 15 ml). The crystals were ground on a mortar and the residues of *i*-PrOH were removed by azeotropic distillation with DCM in a rotary evaporator (25 ml of DCM x 5 cycles). The solid was grinded and dried *in-vacuo* at 120 °C for 24 h yielding a dark orange crystalline powder of high purity. The final yield was 1.05 g (2.03 mmol, 76.3%).

^1H NMR (600 MHz, $\text{DMSO}-d_6$) δ (ppm) 11.40 (s, 1H), 9.47 (s, 1H), 8.63 (s, 1H), 8.55 (d, $J = 16.4$ Hz, 1H), 8.07 – 7.93 (m, 3H), 7.93 – 7.83 (m, 1H), 7.74 – 7.54 (m, 4H), 7.13 (d, $J = 8.4$ Hz, 1H), 5.33 (s, 2H), 4.89 (t, $J = 7.8$ Hz, 2H), 3.88 (s, 3H), 2.87 – 2.68 (m, 2H), 2.32 – 2.18 (m, 2H), 1.76 (s, 6H).

^{13}C NMR (151 MHz, DMSO) δ (ppm) 181.53, 159.09, 147.02, 143.64, 140.92, 136.56, 136.06, 129.79, 129.32, 129.20, 126.66, 124.02, 123.12, 121.97, 121.74, 117.22, 115.06, 112.21, 51.86, 51.36, 46.95, 45.30, 35.88, 26.34, 24.46.

HRMS (nanochip-ESI/LTQ-Orbitrap) m/z : $[\text{M}]^+$ Calcd for $\text{C}_{26}\text{H}_{30}\text{N}_3\text{O}_4\text{S}^+$ 480.1952; Found 480.1973.

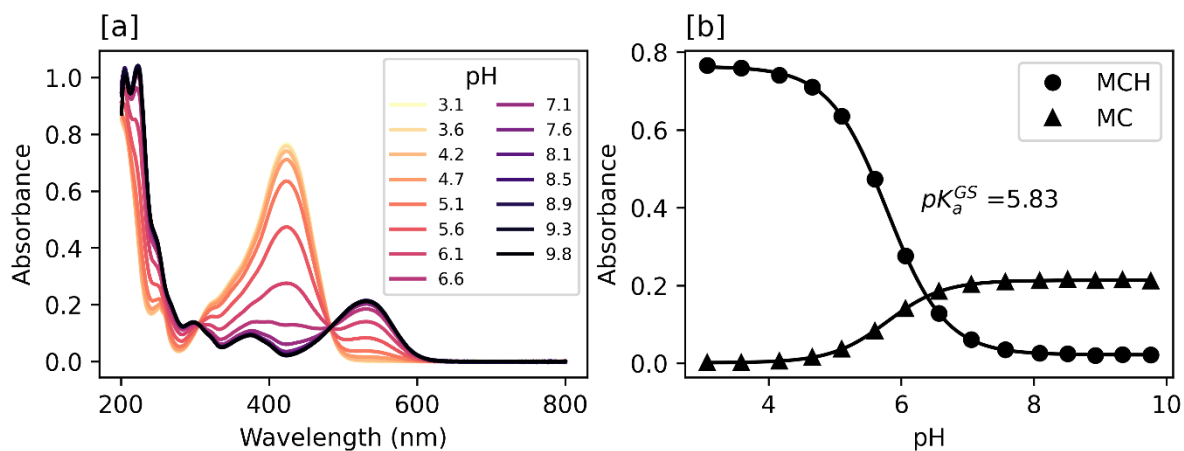
6.5.3 pH titration for the pK_a^{GS} determination of compound **9**

Figure S 6.1. UV-Vis spectra of compound **9** between pH 3 and 10 in 20 mM potassium phosphate buffer solutions. Temperature 298 K, $[9] = 25 \mu\text{M}$.

Table S 6.1. Parameters for MCH curve fit, absorption data at 423 nm

Abs (low pH)	0.719
Abs (high pH)	0.0220
pK_a	5.78
dx	-0.436
R^2	0.9998

Table S 6.2. Parameters for MC curve fit, absorption data at 532 nm

Abs (low pH)	0.213
Abs (high pH)	0.001
pK_a	5.79
dx	0.423
R^2	0.9998

6.5.4 pH titration for the pK_a^{MS} determination of compound 9

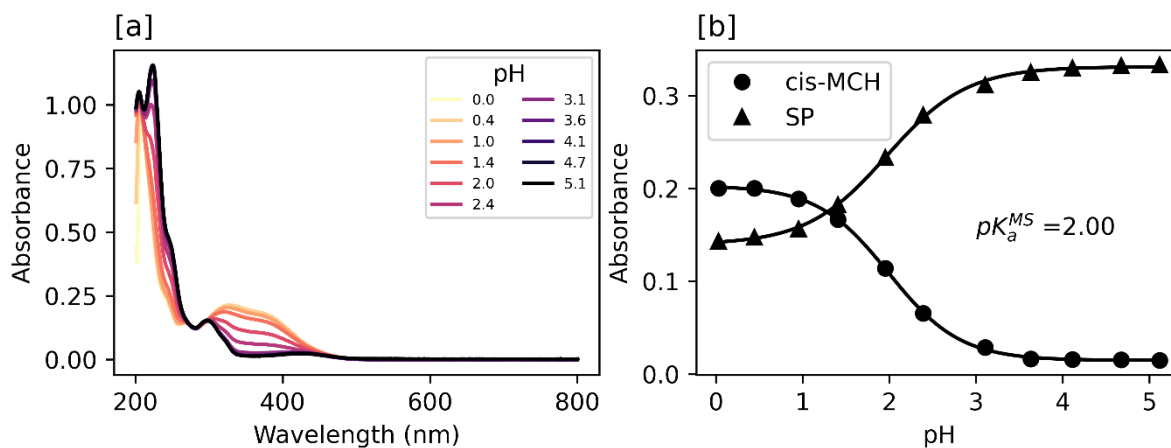


Figure S 6.2. UV-Vis spectra of compound 9 between pH 3 and 10 in 20 mM potassium phosphate buffer solutions. Temperature 298 K, [9] = 25 μ M, light source LED 500 nm.

Table S 6.3. Parameters for cis-MCH curve fit, absorption data at 350 nm

Abs (low pH)	0.203
Abs (high pH)	0.0147
pK_a	1.99
dx	-0.410
R^2	0.9998

Table S 6.4. Parameters for SP curve fit, absorption data at 250 nm

Abs (low pH)	0.139
Abs (high pH)	0.331
pK_a	1.97
dx	0.461
R^2	0.9998

6.5.5 Kinetic determination of K_c

The determination of the MC to SP equilibrium constant is performed by means of kinetics measurements of the concentration of the MC form generated *in-situ* by injecting a solution of MCH into an alkaline aqueous solution as described previously (Chapter 3).^[113,115,120] In these experiments a solution 20 mM in potassium phosphate at pH 10 was prepared in the UV-Vis cell, to this was added (and mixed for 6 seconds) MCH so to have a concentration of 25 μM in the cell.

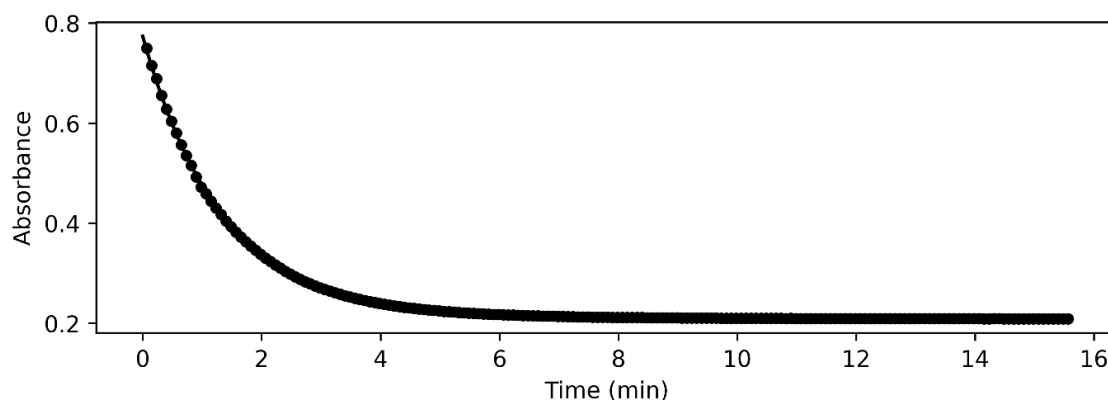


Figure S6.3. Absorbance profile at 532 nm after injecting **9** in pH 10 buffer 20 mM. Temperature 298 K, $[\mathbf{9}] = 25 \mu\text{M}$.

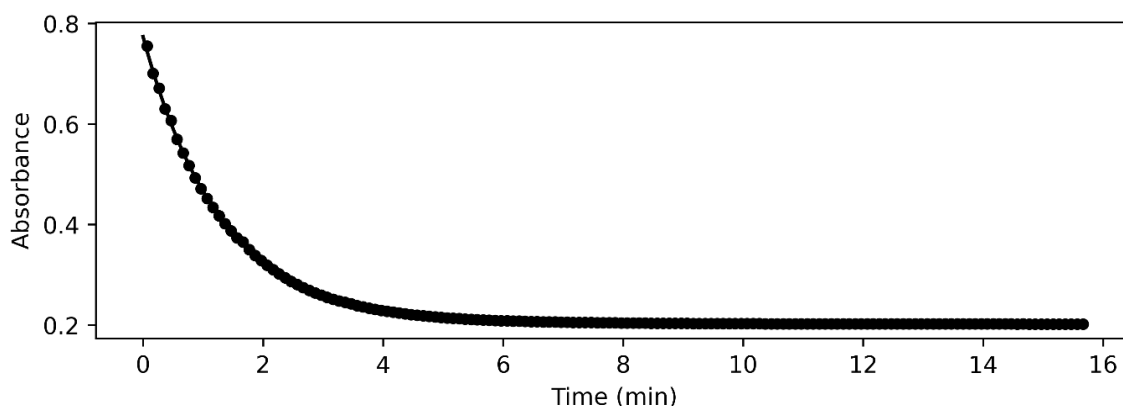


Figure S 6.4. Absorbance profile at 532 nm after injecting **9** in pH 10 buffer 20 mM. Temperature 298 K, $[\mathbf{9}] = 25 \mu\text{M}$.

The decay of the MC form was followed by monitoring the absorbance at 532 nm every 3 seconds and fitted to a first-order decay kinetics. At the completion of the experiment

the pH was checked directly in the cell using a MetrOhm Biotrode. The error was calculated as maximum semidispersion between the two experiments.

Table S 6.5. Parameters for MC curve fit, absorption data at 532 nm.

	Exp. 1	Exp. 2	Average	Error
Abs (time 0)	0.759	0.773	0.766	0.01
Abs (equilibrium)	0.202	0.210	0.203	0.001
k_{obs} (s^{-1})	0.0125	0.0128	0.0126	0.0002
K_{c}	2.75	2.68	2.71	0.04
k_2 (s^{-1})	0.00944	0.00912	0.0093	0.0002
k_{-2} (s^{-1})	0.00343	0.00339	0.0034	0.0002
R^2	0.9999	0.9999		

6.5.6 Relaxation kinetics

The experiment is performed as described previously, the kinetics of recovery from the metastable state are followed by monitoring the absorbance of either the MCH form or the MC form. In the experiments were used potassium phosphate buffers which were prepared by titration of a solution 0.1 M in H_3PO_4 with 10 M aqueous KOH. The pH was measured with a MetrOhm Unitrode Pt 1000 combined pH electrode. For the first four samples (between pH 0 and 2.5 included) the pH was regulated by appropriate dilutions of HCl 1 M, 0.1 M and 0.01 M respectively. The buffer concentration used for the following profiles (above pH 2.5) is 20 mM, the concentration of compound 1 in the cells is 25 μM . For pH between 0 and 7.5 was followed every 30 seconds the absorbance at 423 nm, corresponding to the MCH peak

absorption. For the pH values above 7.5 was followed the absorbance at 532 nm corresponding to the MC form absorption. At the end of each experiment, the pH was measured with a freshly calibrated MetrOhm Biotrode directly in the optical cells.

Relaxation kinetics fitting

The data was truncated at time zero which corresponds to the switching-off of the light source. The recovery profile was then fit to a first-order rate law yielding the parameters: A_0 the initial absorbance of the sample, A_{eq} the equilibrium. The initial guesses for the parameters were obtained as follows: for A_0 was used the first experimental point, for A_{eq} was used the maximum experimental point, for $k_{obs,relax}$ was calculated the slope of the first five points. The equation used to fit the data is:

$$A(t) = A_{eq} + (A_0 - A_{eq}) \exp(-k_{obs,relax}t)$$

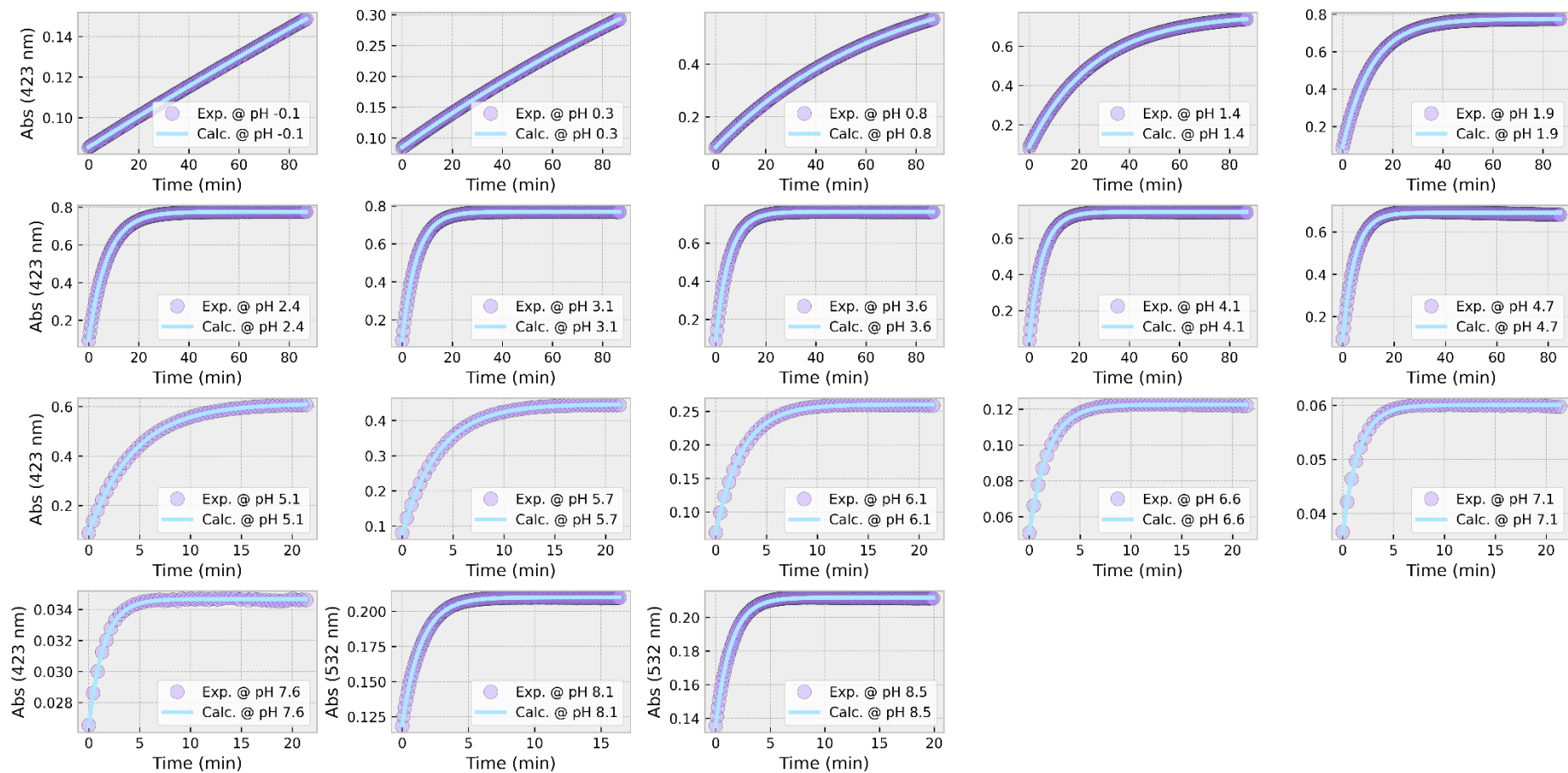


Figure S 6.5. Absorbance at 532 nm after irradiation of **9** in either diluted HCl or potassium phosphate buffer 20 mM regulated at pH 3-10. Temperature 298 K, [9] = 25 μ M, light source LED 500 nm. The purple bullets represent the experimental points and the light-blue line the best fit to the first-order rate equation.

Table S 6.6. Parameters for first order kinetics curve fit from Figure S 6.5.

pH	k (min ⁻¹)	A_0	A_{eq}	R^2
-0.15	0.0014	0.0855	0.6402	0.999986
0.34	0.0044	0.0851	0.7426	0.999997
0.83	0.0144	0.0853	0.7660	0.999997
1.36	0.0382	0.0859	0.7641	0.999995
1.87	0.0867	0.0887	0.7753	0.999993
2.39	0.1367	0.0952	0.7757	0.999992
3.08	0.1741	0.0931	0.7691	0.999995
3.61	0.1855	0.0924	0.7643	0.999987
4.15	0.1946	0.0364	0.7460	0.999859
4.66	0.2140	0.0879	0.6908	0.997687
5.10	0.2247	0.0890	0.6122	0.999979
5.65	0.2795	0.0801	0.4463	0.999911
6.11	0.3901	0.0682	0.2604	0.999736
6.64	0.5414	0.0509	0.1226	0.999636
7.12	0.6428	0.0364	0.0600	0.999200
7.64	0.6752	0.0265	0.0347	0.998563
8.12	0.7009	0.1192	0.2099	0.999713
8.53	0.7055	0.1355	0.2118	0.999256

The rate constant is itself a function of pH and this can be fit with the following equation where: k_2 is the rate constant of ring-opening for the $SP \rightarrow MC$ reaction, K_a , K_c and K_a^{MS} are respectively the acidity constant of the phenol OH, the self-cyclization constant and the metastable state acidity constant. The initialization of all the parameters for the fitting is done by using the values calculated in the previous experiments.

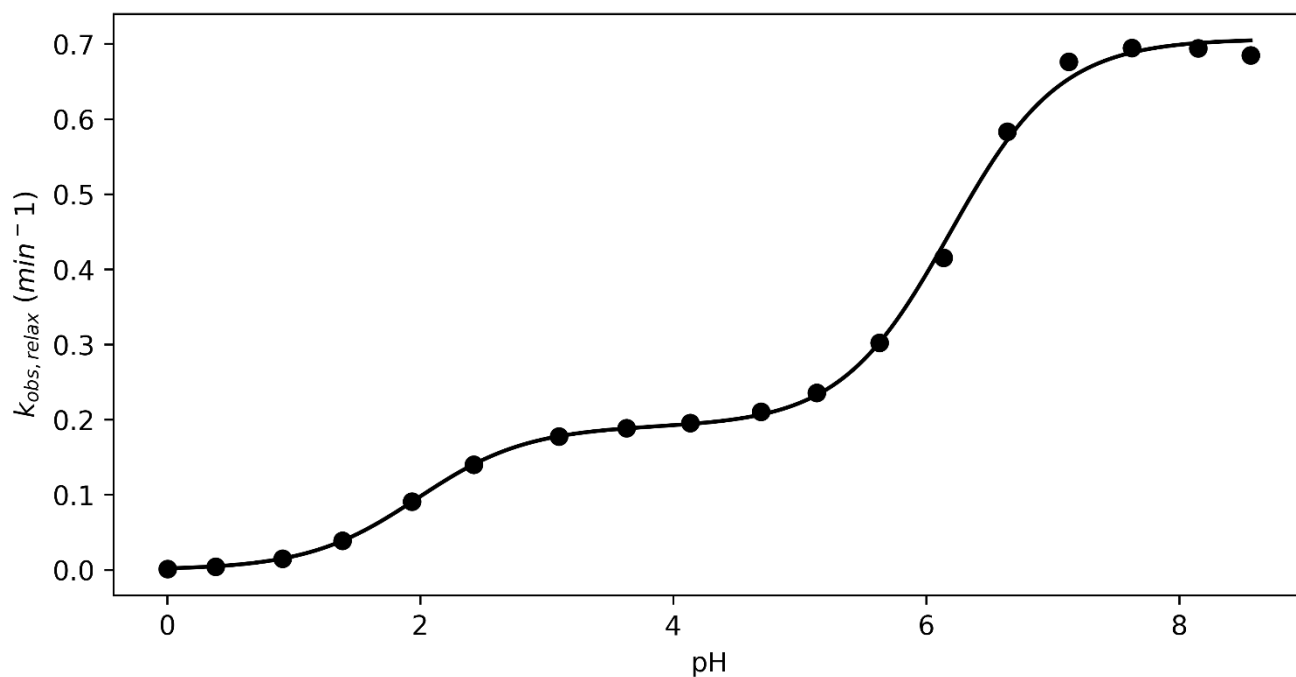


Figure S 6.6. Relaxation rate constant profile against the pH. The black solid line represents the best fit as described in Chapter 3.

Table S 6.7. Best fit parameters.

$k_2 (min^{-1})$	0.195
pK_a^{MS}	1.98
pK_a	6.19
K_c	2.70
R^2	>0.998

6.5.7 Hydrolysis

The hydrolysis of **9** as function of the pH has been followed by preparation of solutions 25 μM of **9** in potassium phosphate buffers 20 mM at pH between 3 and 10. These solutions were subject to 500 nm irradiation for obtaining the results presented in paragraph 6.5.6, in this case the samples were monitored by UV-Vis spectroscopy while thermostatted at 25 °C for much longer than the relaxation timeframe. The absorbance profile fit to a double exponential equation as presented in Chapter 4. The observed hydrolysis rate constants were then graphed as function of the experimental pH and fit as explained in Chapter 3 and 4.

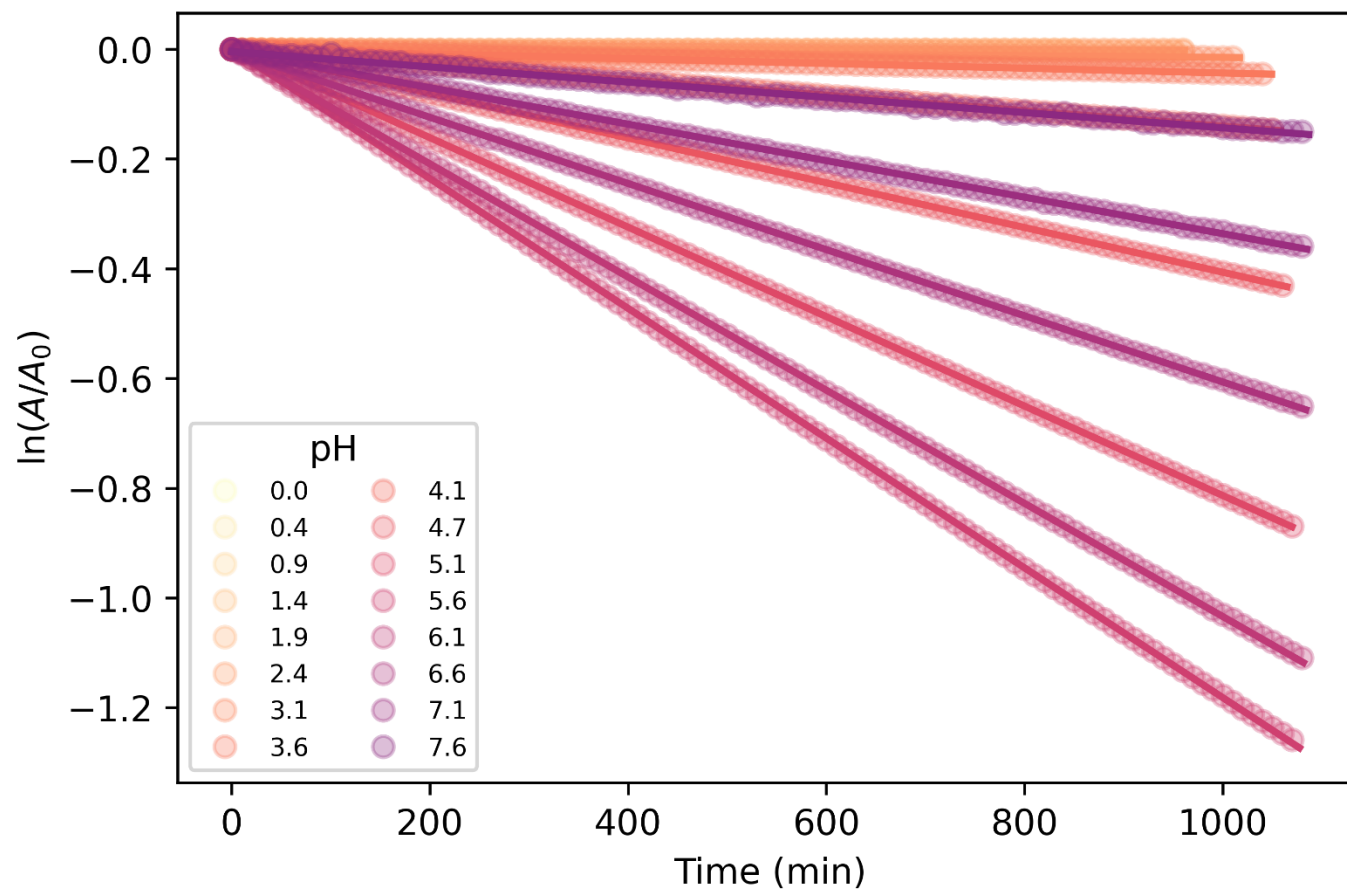


Figure S 6.7. Hydrolysis kinetics of **9** against the pH. The solid lines represents the best fit as described in Chapter 3. Temperature 298 K, $[9] = 25 \mu\text{M}$,.

Table S 6.8. Best fit parameters

pH	$k_{\text{obs,hydro}} \text{ (min}^{-1}\text{)}$	R^2
-0.15	0 ^a	0.999999
0.34	0 ^a	0.999997
0.83	0 ^a	0.999988
1.36	0 ^a	0.999991
1.87	0 ^a	0.999982
2.39	1.79E-06	0.999965
3.08	1.42E-05	0.999928
3.61	4.31E-05	0.999972
4.15	0.000141	0.999937
4.66	0.000408	0.999993
5.10	0.000816	0.999988
5.65	0.001187	0.999967
6.11	0.001037	0.999918
6.64	0.000605	0.999897
7.12	0.000334	0.999664
7.64	0.000139	0.996622

^a: artificially put to zero, the slope value was negligible (below 10^{-8} min^{-1}).

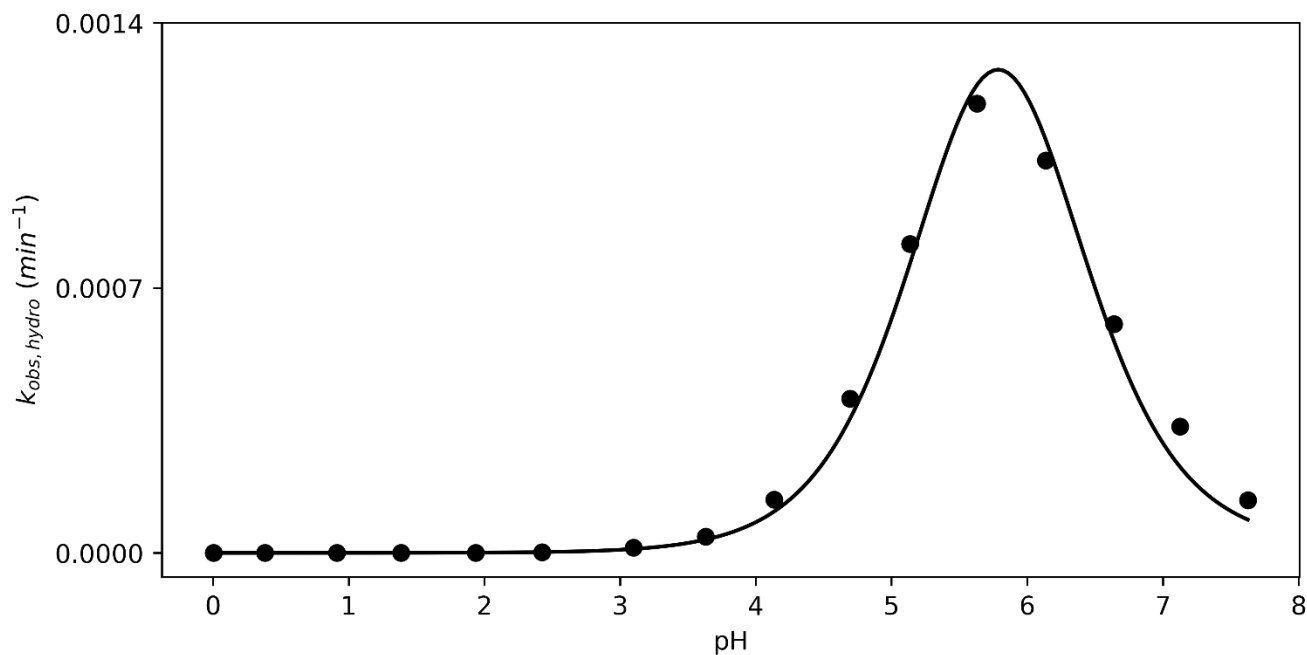


Figure S 6.8. Hydrolysis rate constants of **9** against the pH. The solid line represents the best fit as described in Chapter 3. Temperature 298 K, $[9] = 25 \mu M$.

Table S 6.9. Best fit parameters

$k_w (min^{-1})$	4.90×10^{-3}
$k_{OH} (min^{-1})$	2.73×10^3
pK_a^{GS}	1.00×10^6
$k_w/k_h (M^{-1})$	5.80×10^6
R^2	>0.988

6.5.8 Molar extinction coefficient determination

The determination of the molar extinction coefficient has been carried out in two steps: *i*) potentiometric titration of the stock solution of compound **1**, *ii*) spectrophotometric calibration of compound **9**.

Potentiometric titration

For the potentiometric titration 2 mL of a methanol stock solution approximatively 5 mM in compound **9** was diluted to 20 mL using KCl 2mM to guarantee a rapid response of the electrode, then this was titrated with freshly prepared 0.10 N NaOH standard solution (Merck Titrisol) with the aid of a MetrOhm Titrimo connected to a calibrated MetrOhm Unitrode Pt 1000. The equivalence point has been calculated with the second derivative method.

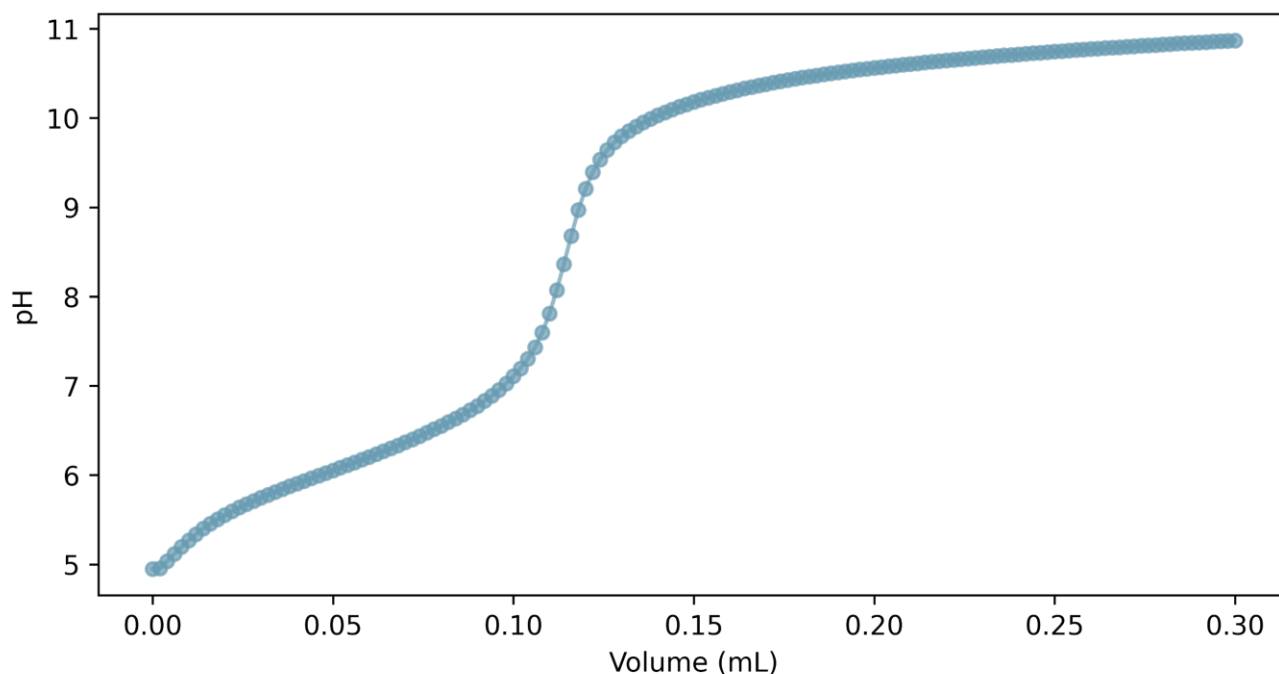


Figure S 6.9. Potentiometric titration of **9** for the determination of the title of the methanolic solution.

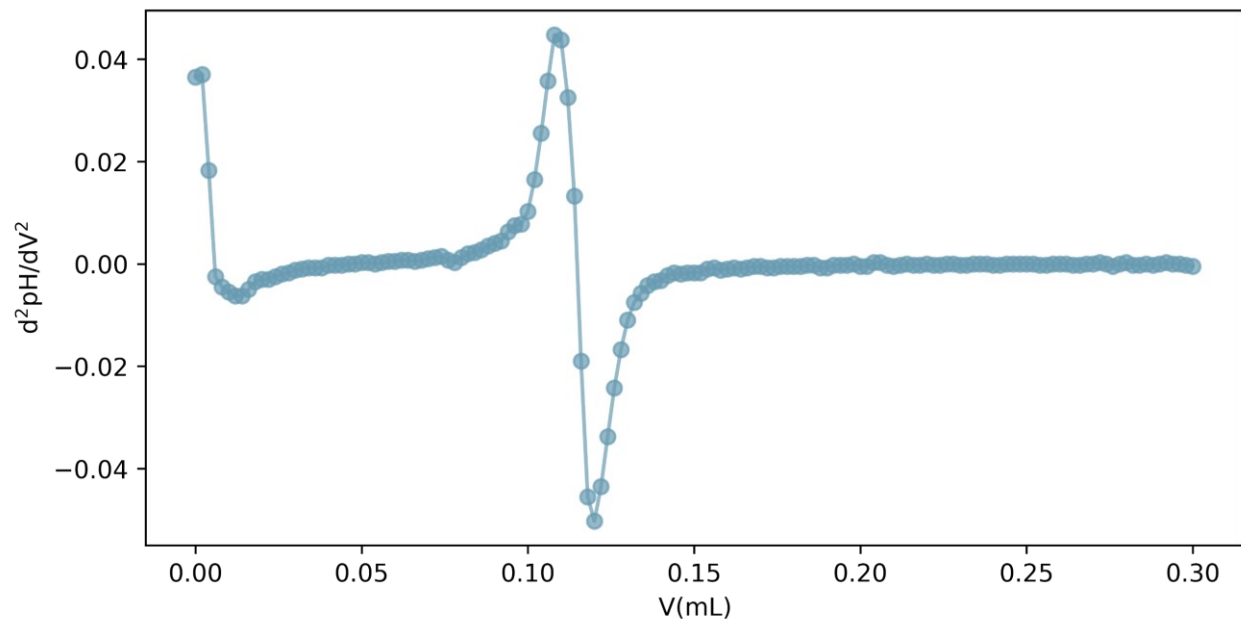


Figure S 6.10. Second derivative of the titration experiment in Figure S 6.9.

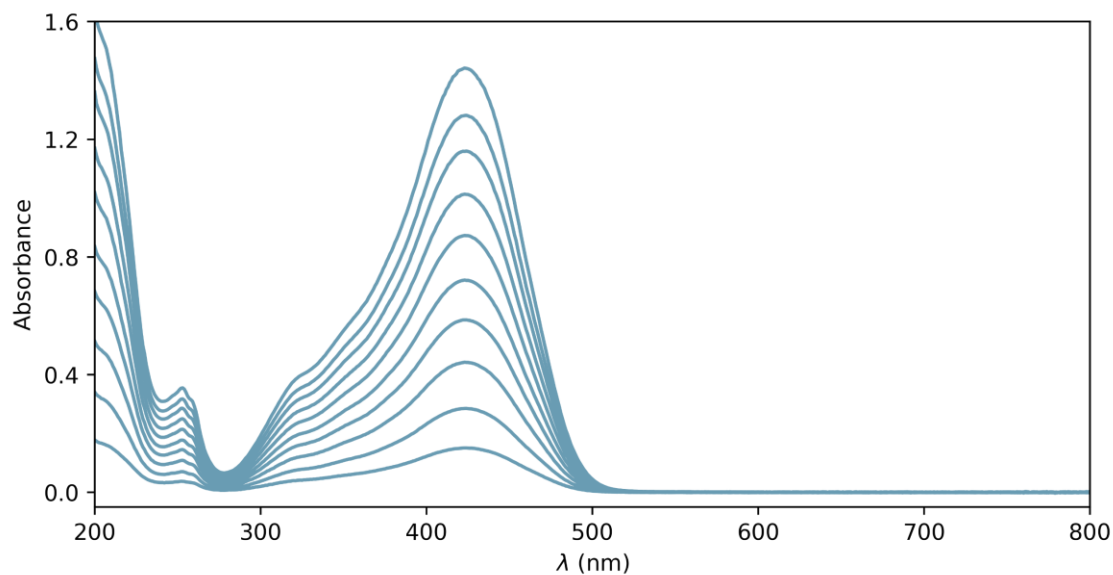
The equivalence point is reached at 0.116 mL of NaOH 0.10 N, corresponding to a concentration of the methanolic stock solution of 5.80 mM.

Spectrophotometric calibration

For this experiment the methanolic stock solution titrated in the previous section was diluted to a substock by adding 100 μ L of compound **9** solution to 900 μ L of mQ water. This was thoroughly mixed and added in different aliquots to 1 cm UV-Vis cells containing 20 mM potassium phosphate buffer adjusted to pH = 3. The sample was thermostatted at 25° C and the spectra were acquired after 15 minutes of equilibration.

Table S 6.10. UV-Vis spectroscopy data for the determination of the molar extinction coefficient of **9**.

Volume (μL) substock	Cell conc. (μM) Compound 1	Absorbance 423 nm
10	5.80	0.151
20	11.6	0.285
30	17.4	0.442
40	23.2	0.586
50	29.0	0.721
60	34.8	0.872
70	40.6	1.013
80	46.4	1.158
90	52.2	1.280
100	58.0	1.442

Figure S 6.11. UV-Vis spectra of compound **9** at the concentrations reported in Table S 6.10 in potassium phosphate buffer 20 mM at pH 3.

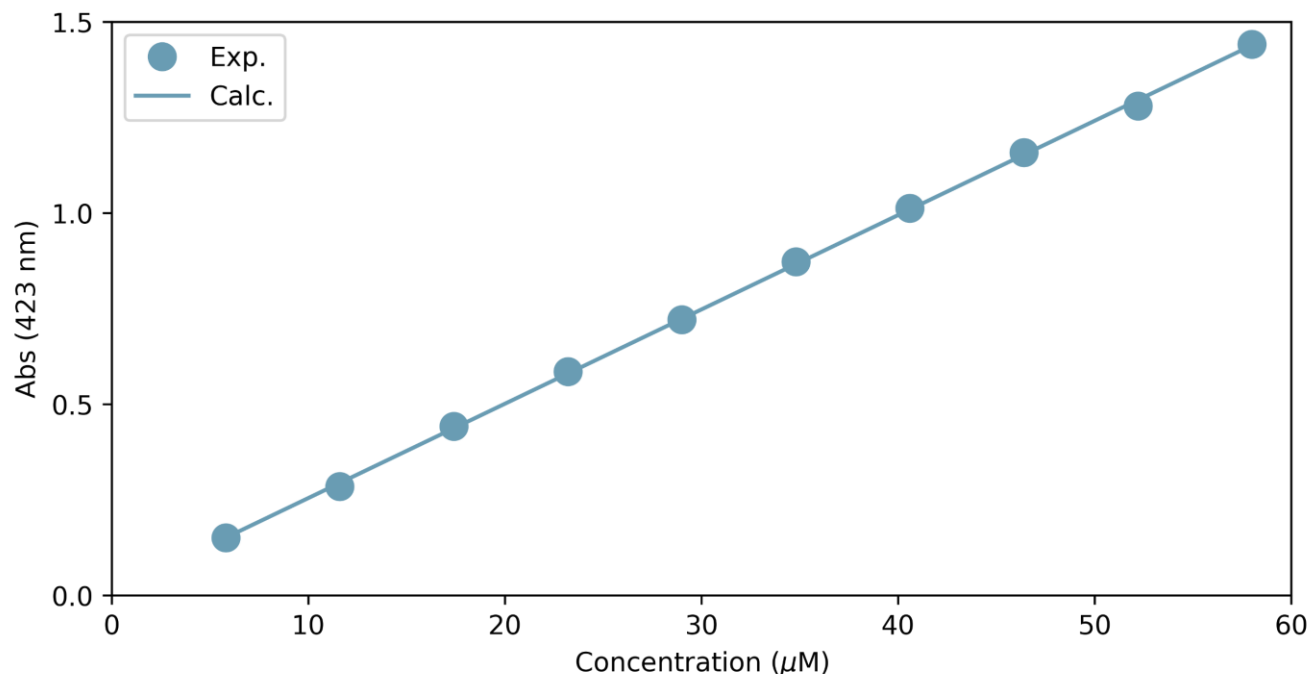


Figure S 6.12. Absorbance at 423 nm and correspondent linear fit to obtain the molar extinction coefficient of **9**.

The molar extinction coefficient so calculated is $2.46 \times 10^5 \text{ (M cm)}^{-1}$ with an intercept value of 0.008 and a determination coefficient R^2 of 0.999.

6.5.9 Calibration of the cucurbit-[7]-uril concentration

Cucurbit-[7]-uril is usually found as hydrate in ambient conditions, therefore, a careful titration of its solutions is in order for obtaining quantitative results in binding experiments involving this host. To do so we adopted the method developed by Yi and Kaifer^[168] which exploits the formation of a very stable complex between cobaltocenium hexafluorophosphate (COBPF_6) and cucurbit-[7]-uril. Due to the high association constant, the reaction can be considered

quantitative and it is useful as analytical reference for the quantification of the title of aqueous cucurbit-[7]-uril solutions. Moreover, the molar extinction coefficient of COBPF₆ in water is known, the chemical is air stable and the shelf-life of its solutions is long making the preparation of the experiment straightforward.

The COBPF₆ solution has been prepared by weighting 10.73 mg of solid COBPF₆ (MW=334.09), dissolving it in 20.0 mL of mQ water with the aid of an ultrasound bath prior to bring the volumetric flask to volume. The concentration of this solution is 1.61 mM. From this, 186.8 μ L were transferred to a 20.0 mL volumetric flask and topped up with mQ water. The new solution is 14.4 μ M.

Titrant preparation (Solution A): The titrant has been prepared by mixing 980 μ L of 14.4 μ M COBPF₆ with 20 μ L of aqueous cucurbit-[7]-uril determined by weighting to be approximatively 9 mM.

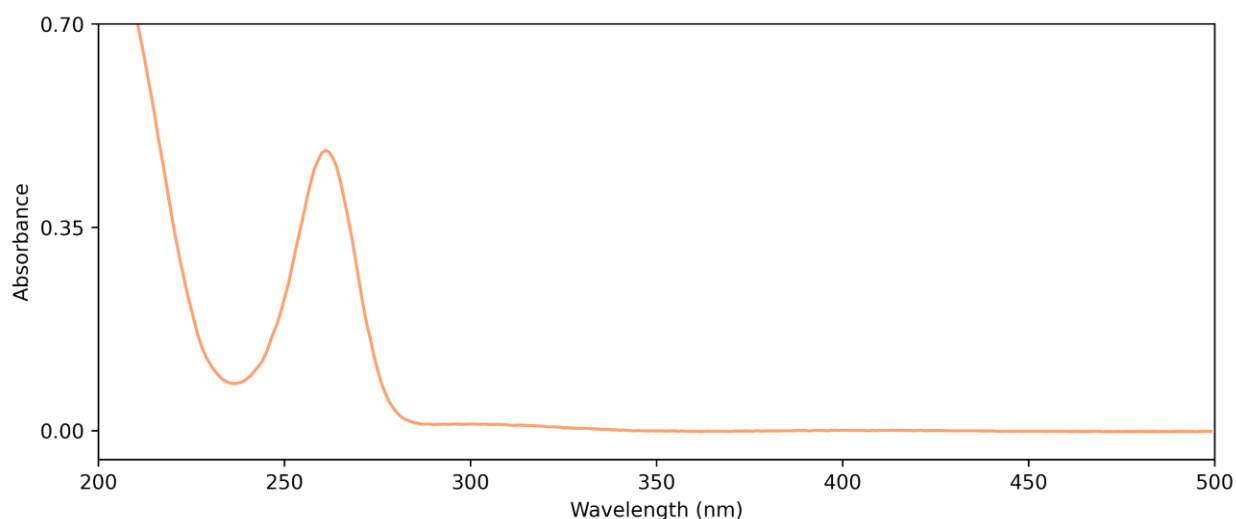


Figure S 6.13. UV-Vis spectrum of the initial point of the titration for the determination of the content of COBPF₆.

Titrand preparation (Solution B): In a 1 cm UV-Vis thermostatted at 25 ° C cell were added 980 μL of 14.4 μM COBPF₆ and 20 μL of mQ water.

The initial point of the titration represents the spectrum of COBPF₆ at the concentration used for the titration. From here it is possible to extract the effective concentration of COBPF₆ in both the titrand and the titrant. The molar extinction coefficient is reported in literature for the peak at 261 nm and is 34200 (M cm)⁻¹.^[168] The absorbance at this point is 0.457 and, thus, the corrected concentration of COBPF₆ is 13.4 μM .

Once quantified the title of Solution A, the titration occurs by adding 20 μL aliquots of Solution A to the cell containing Solution B, thoroughly mixing and allowing 5 minutes of equilibration time at 25 °C to the sample prior to spectral acquisition.

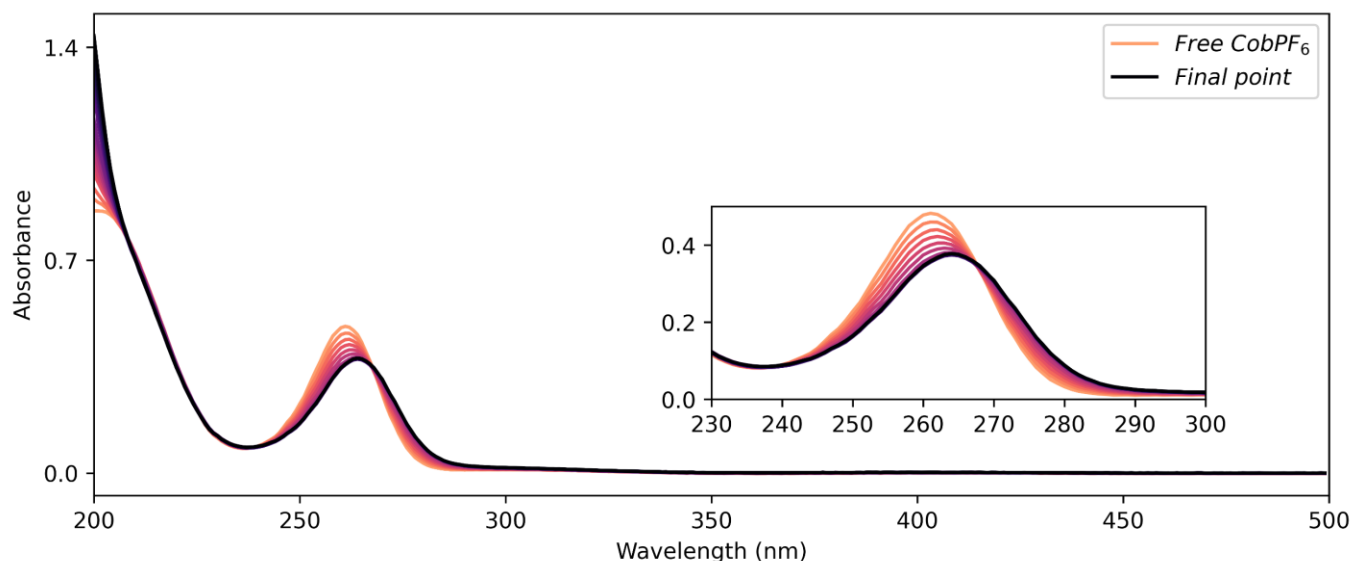


Figure S 6.14. UV-Vis spectra of the titration of CB7 with COBPF₆. The titration progresses from orange to black.

The absorbance at 261 nm is extracted from each spectrum and plotted against the titrant volume. The dataset is shaped like a broken line with the discontinuity at the equivalence point. The experimental points have been fit to two different lines as reported by Yi and Kaifer^[168] and

the intersection abscissa calculated by using the following equation where b and b' are the intercepts of the lines, a and a' are the slopes.:

$$x_{eq} = \frac{b' - b}{a - a'}$$

The calculated equivalence point is at 79 μL which corresponds to a stock solution of cucurbit-[7]-uril of 9.1 mM. This concentration is used throughout the other experiments as the nominal title of the cucurbit-[7]-uril solution.

Table S 6.11. Data for the determination of the title of the **CB7** solution.

Volume (μL)	Absorbance 261 nm	Slope 1 (μL) ⁻¹	Intercept 1	Slope 2 (μL) ⁻¹	Intercept 2
0	0.458	-0.00144	0.456		
20	0.426				
40	0.396				
60	0.369				
80	0.344				
100	0.342			4.25 x 10 ⁻⁵	0.339
120	0.345				
140	0.345				
160	0.346				
180	0.347				
200	0.347				

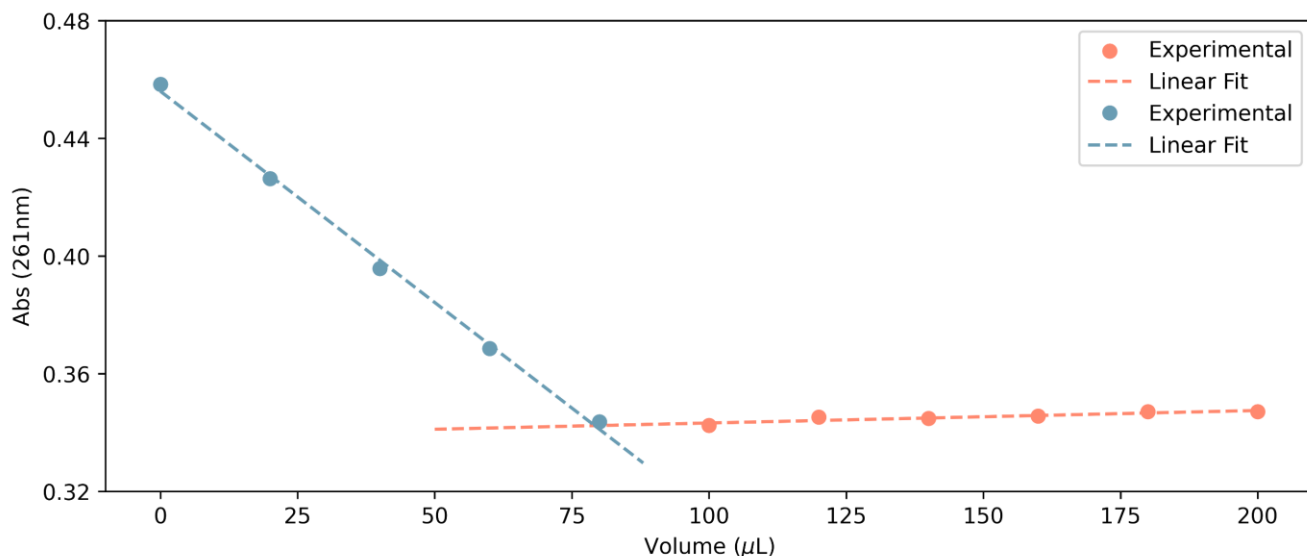


Figure S 6.15. Results of the titration experiment. The intersection between the orange and the blue line represents the equivalence point.

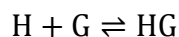
6.5.10 K_B determination by fluorescence titration

The titration experiments have been carried out on a Varian Cary 50 Eclipse equipped with a multi-cell holder and a thermostat set at 25° C. The PMT voltage has been set at the predefined level 'Medium' corresponding to 600 V. The excitation slit was set to 2.5 nm while the emission to 20 nm. The titration was performed in its entirety in aqueous potassium phosphate buffer 2 mM set at pH = 3. The selected excitation wavelength is 423 nm, corresponding to the maximum absorption of compound 1. Before every acquisition the instrument was zeroed against air. At the end of the titration the pH was checked with a calibrated MetrOhm Biotrode and resulted to be unvaried at pH = 3.

In a 1 cm optical pathway fluorescence cell were added 1000 μL of a solution 0.11 mM in compound **9** and 2 mM potassium phosphate set at pH = 3. To this were added aliquots of a solution 0.11 mM in compound 1 and 2.4 mM in cucurbit-[7]-uril. Between points the system

was allowed to equilibrate for 15 minutes at 25 °C. The emission intensity at 528 nm was extracted from each spectrum and plotted against the ratio between concentrations of cucurbit-[7]-uril and compound **9**. The so-obtained data were fit to a 1:1 binding isotherm. The equation describing the equilibrium concentration of the host-guest complex and its correlation with the fluorescence intensity is derived as described below.

The equilibrium under investigation is the 1:1 association reaction between cucurbit-[7]-uril (host, H) and compound **9** (guest, G) described as follows:



The equilibrium equations are defined as follows, mass balance for the cucurbit-[7]-uril :

$$C_H = [H] + [HG]$$

Mass balance for compound **9**:

$$C_G = [G] + [HG]$$

Association constant:

$$K_B = \frac{[HG]}{[H][G]}$$

From these definitions, it is possible to solve the system and to calculate the equilibrium concentration of the [HG] complex:

$$[HG] = \frac{C_G K_B + C_H K_B + 1 - \sqrt{C_G^2 K_B^2 - 2C_G C_H K_B^2 + 2C_G K_B + C_H^2 K_B^2 + 2C_H K_B + 1}}{2K_B}$$

While for the free guest [G] the equation is:

$$[G] = \frac{C_G K_B - C_H K_B - 1 + \sqrt{C_G^2 K_B^2 - 2C_G C_H K_B^2 + 2C_G K_B + C_H^2 K_B^2 + 2C_H K_B + 1}}{2K_B}$$

The experimental observable in this case is the fluorescence intensity, cucurbit-[7]-uril is known to not have any significant luminescence properties in the visible excitation region, therefore the total fluorescence intensity is:

$$F = k_G [G] + k_{HG} [HG]$$

Where k_G and k_{HG} are the molar fluorescence efficiencies of the free guest and of the host-guest complex respectively. In absence of H the fluorescence intensity assumes the value F_0 and it is proportional to the concentration of G.

$$\lim_{C_H \rightarrow 0} (F) = F_0 = k_G [G] = k_G C_G$$

When the system is saturated by H then the fluorescence intensity assumes the value F_{inf} . The maximum concentration of HG, by experimental design, is the initial concentration of G present in solution, this can be rewritten in the limit form for clarity:

$$\lim_{C_H \rightarrow +\infty} (F) = F_{inf} = k_{HG} [HG] = k_{HG} C_G$$

Using the mass balance equation of the guest allows to rewrite the total fluorescence in two different forms based on the previous limit conditions:

$$F - F_0 = (k_{HG} - k_G) [HG]$$

$$F - F_{inf} = (k_G - k_{HG}) [G]$$

Taking the ratio (and knowing that [HG] can also be zero) we obtain the operative equation:

$$\frac{F - F_0}{F_{inf} - F} = \frac{[HG]}{[G]}$$

Which when solved for F gives the direct relationship between the observed fluorescence and the host-guest ratio.

$$F = \frac{C_G K_B (F_0 + F_{inf}) - C_H K_B (F_0 - F_{inf}) + (F_0 - F_{inf}) \cdot \sqrt{C_G^2 K_B^2 - 2C_G C_H K_B^2 + 2C_G K_B + C_H^2 K_B^2 + 2C_H K_B + 1} - F_0 + F_{inf}}{2C_G K_B}$$

In the equation C_G is a fixed parameter determined by experimental design, C_H is the independent variable (which can be simply interchanged with the H/G ratio for clarity in the titration plots). The parameters to be fit to the experimental data are F_0 , F_{inf} and K_B .

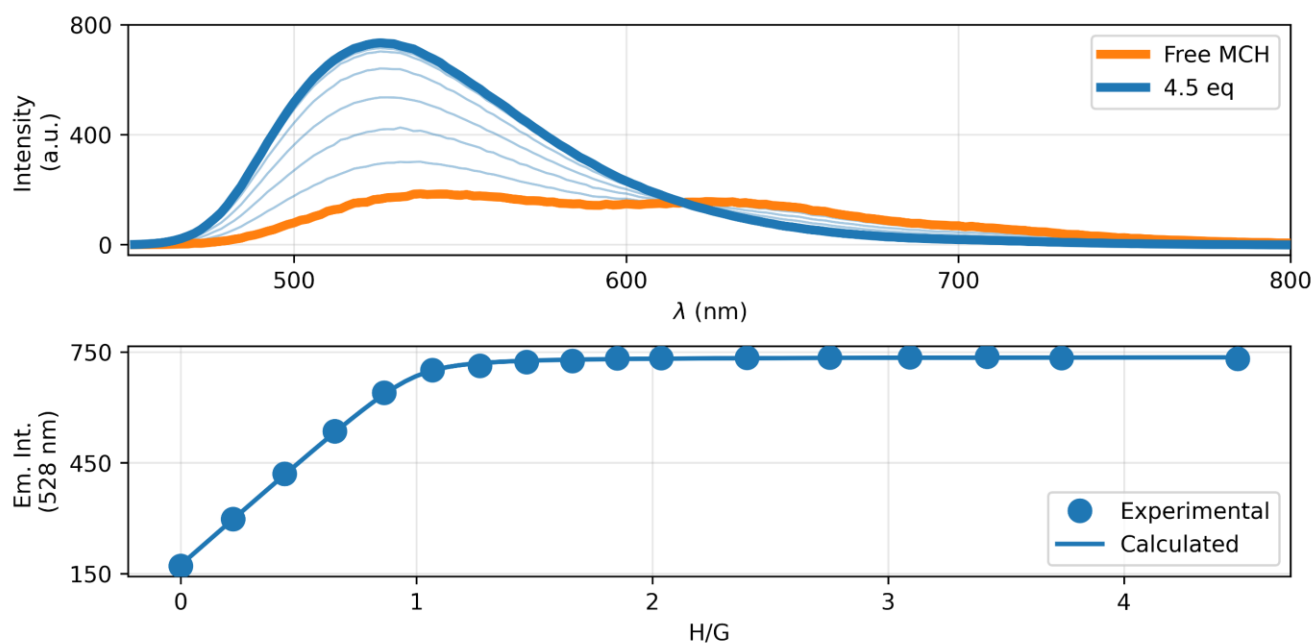


Figure S 6.16. On top: fluorescence titration of **9** at increasing amounts of CB7 (excitation 423 nm). On the bottom: fluorescence profile at 528 nm at increasing amounts of CB7 and best fit to a 1:1 isotherm (solid line).

Table S 6.12. Best fit parameters.

F₀	174.1
F_{inf}	737.0
K_B	1.00 x 10 ⁶
R²	>0.999

6.5.11 Titration experiment kinetics

To check for the stability of the system and to confirm the equilibration time, the same titration described previously was repeated with excitation slit 1.5 nm and the instrument zeroed against the free guest to confirm the absence of interferences from the excitation source (*i.e.*: photobleaching or photoswitching). The experiment was conducted by monitoring the time evolution of the emission intensity at 528 nm by exciting the sample at 423 nm. Every point was acquired with a time interval of 5 seconds between points; for the rest the protocol was the same as the full-scan titration. The negative spikes correspond to the points in time in which the addition of the volumes of the titration took place plus the time necessary to mix thoroughly the contents of the cell. At the end of the titration the pH was checked with a calibrated MetrOhm Biotrode and resulted to be unvaried pH = 3. The emission intensities were calculated as the time-average between different additions (red dots in Figure S 6.17). As shown in the time-evolution of the emission intensity, the binding takes place immediately and the last addition with prolonged acquisition highlights how the final plateau is stable in time. The fit parameters are calculated on the extracted experimental points with a 1:1 binding isotherm as derived in the previous paragraph.

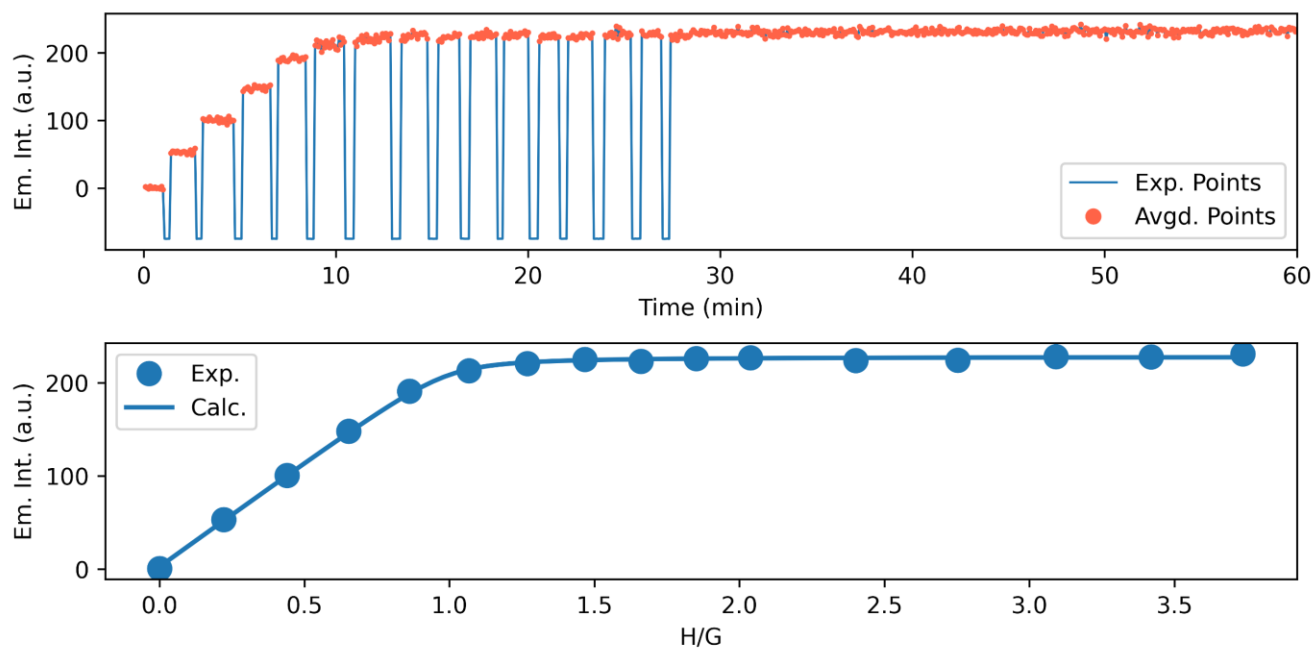


Figure S 6.17. On top: time-dependent fluorescence profile of the titration of **9** at increasing amounts of CB7, the red dots represent the averaged points used for the isotherm fitting (excitation: 423 nm, detection: 528 nm). On the bottom: fluorescence profile at 528 nm and 1:1 binding isotherm fitting (blue solid line).

Table S 6.13. Best fit parameters.

F_0	2.585
F_{inf}	228.1
K_B	1.13×10^6
R^2	>0.999

6.5.12 Cucurbit-[7]-uril ITC affinity titrations

The affinity constant and thermodynamic parameters of binding between compound **9** and cucurbit-[7]-uril have been determined with a Microcal VP-ITC machine which was controlled by the dedicated software implemented in Origin 7. The measurements have been carried out in aqueous potassium phosphate buffer 2 mM regulated at pH = 3, the buffered solutions containing compound **9** and cucurbit-[7]-uril were kept in the dark during the whole length of the experiment and were degassed for 10 minutes under stirring at 25° C using the Thermovac accessory of the calorimeter. The titrant (in the syringe) was cucurbit-[7]-uril 2.4 mM while in the cell was placed a solution 0.155 mM in compound **9**. The titrations were carried out at 298 K with instrumental feedback set to 'high', the delay between injections has been set to 600 s to ensure a flat baseline. In the reference cell, was added the same aqueous buffer as used for the titrant and the analyte, reference solution was degassed in the same conditions as for the other components and allowed to equilibrate in the instrument for 1 hour before the experiment. The stirring rate of the injector was set to 400 rpm, the filter period to 2 s, the first injection consisted in 2.5 µL injected in 15 s and was discarded from the fitting, all the other injections were set to 7.5 µL injected in 15 s. Once obtained, the raw thermogram was integrated with the software NITPIC^[173] and the integrated heat points were fit to a 1:1 binding model found in the program SEDPHAT.^[174,175] The blank titrations of CB7 in buffer and **9** in buffer were subtracted from the integrated heats yielding no variations on the parameters. The experiment was repeated two times.

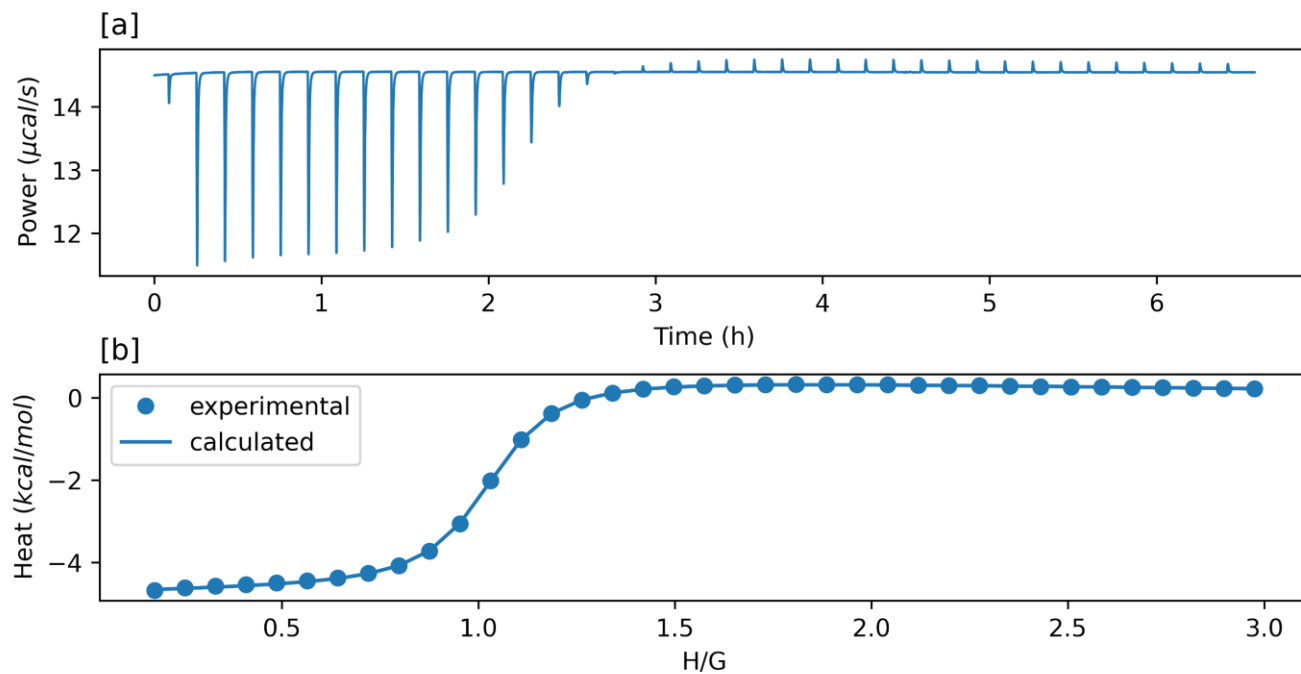


Figure S 6.18. ITC titration (experiment 1) of **9** with CB7. In [a] the raw thermogram, in [b] the elaborated reaction heat profile and 1:1 binding isotherm.

Table S 6.14. Best fit parameters for the ITC titration (experiment 1).

ΔH_{rxn} (298K) kcal/mol	-5.33
$\text{Log}_{10}(K_{\text{B}})$	5.98
ΔG_{rxn} (298K) kcal/mol	-8.14
ΔS_{rxn} (298K) cal (K mol)^{-1}	9.43
R^2	>0.999

Table S 6.15. Best fit parameters for the ITC titration (experiment 2).

ΔH_{rxn} (298K) kcal/mol	-5.23
$\text{Log}_{10}(K_B)$	6.01
ΔG_{rxn} (298K) kcal/mol	-8.19
ΔS_{rxn} (298K) cal (K mol) ⁻¹	9.20
R^2	>0.999

6.5.13 HR-MS of the HG complex

The solution deriving from the titration in fluorescence monitoring (*vide supra* paragraph 6.5.11) was subject to HRMS analysis at the end of the titration, the sample was not manipulated further, the measurement was carried out on a Thermo Orbitrap Elite with ion source nanochip-ESI and mass analyzer LTQ-Orbitrap. The experimental spectrum displays the presence of ions which confirm the presence of HG complex. HRMS (nanochip-ESI/LTQ-Orbitrap) m/z: [9 - Cl + H]⁺² Calcd for C₆₈H₇₃N₃₁O₁₈S⁺² 821.7730; Found 821.7764.

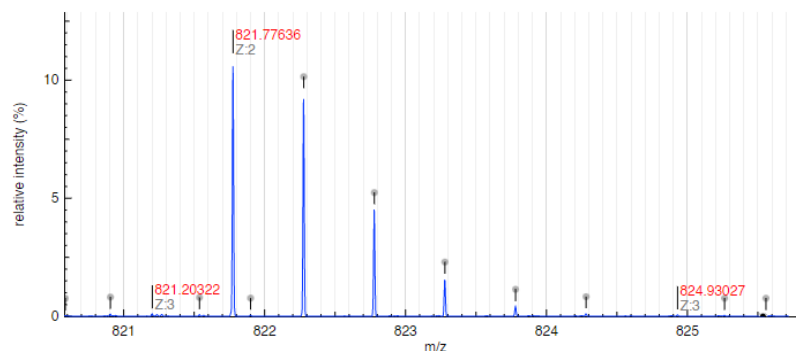


Figure S 6.19. HR-MS (orbitrap) spectrum of 9@CB7 from the solution used in the experiment of Figure S 6.17.

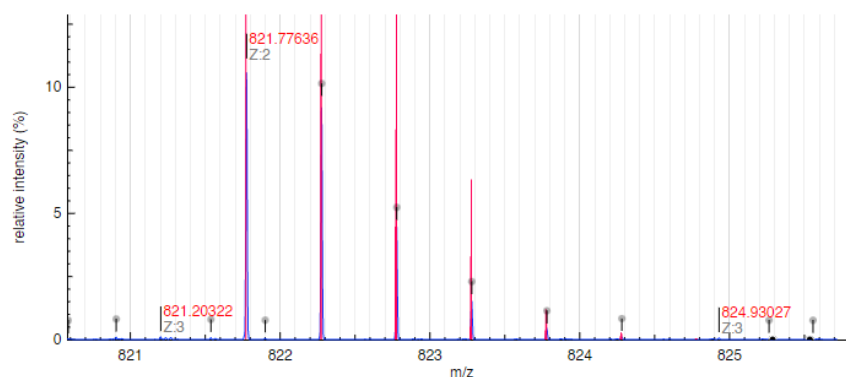


Figure S 6.20. HR-MS (orbitrap) spectrum of **9@CB7** from the solution used in the experiment of Figure S 6.17. The red lines represent the calculated mass for the ion $[9 - \text{Cl}^- + \text{H}^+]^{2+}$.

6.5.14 pH titration for the pK_a^{GS} of compound **1** (4.0 eq CB[7])

For the spectrophotometric titration were used potassium phosphate buffers which were prepared by titration of a solution 0.1 M in H_3PO_4 with 10 M aqueous KOH. The pH was measured with a MetrOhm Unitrode Pt 1000 combined pH electrode. The buffer concentration used for the following spectra is 2 mM, the concentration of compound **1** in the cells is 12.5 μM and 4.0 equivalents of cucurbit-[7]-uril; the spectra were acquired after 15 minutes from the preparation of the samples to allow enough time for equilibration. After the spectral acquisition the pH was checked using a pre-calibrated MetrOhm Biotrode to measure the pH directly inside the cells. The resulting profiles were then fitted to the Boltzmann sigmoidal function with the aid of the Excel Solver.

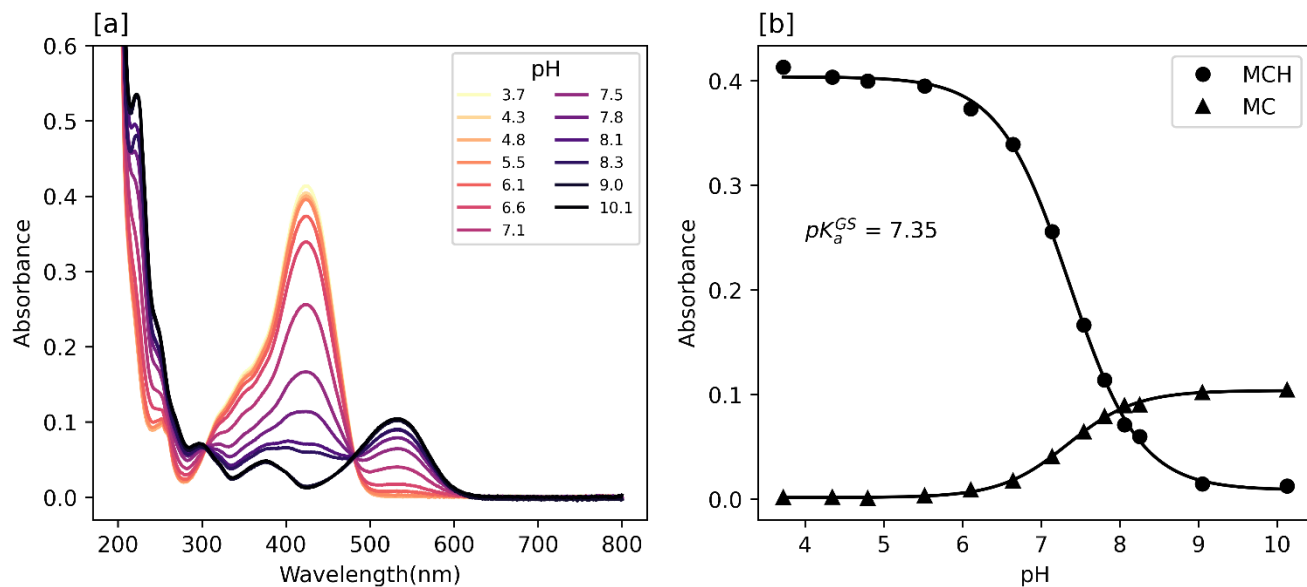


Figure S 6.21. UV-Vis spectra of compound **9** between pH 3 and 10 in 2 mM potassium phosphate buffer solutions. Temperature 298 K, $[9] = 12.5 \mu\text{M}$, $[\text{CB7}] = 50 \mu\text{M}$.

Table S 6.16. Parameters for MCH curve fit

Abs (low pH)	0.404
Abs (high pH)	0.0086
pK_a	7.36
dx	-0.446
R^2	0.9997

Table S 6.17. Parameters for MC curve fit

Abs (low pH)	0.0015
Abs (high pH)	0.104
pK_a	7.34
dx	0.429
R^2	0.9995

6.5.15 pH titration for the pK_a^{MS} of compound **9** (4.0 eq CB[7])

For the spectrophotometric titration were used potassium phosphate buffers which were prepared by titration of a solution 0.1 M in H_3PO_4 with 10 M aqueous KOH. The pH was measured with a MetrOhm Unitrode Pt 1000 combined pH electrode. For the first four samples (between pH 0 and 2.5 included) the pH was regulated by appropriate dilutions of HCl 1 M, 0.1 M and 0.01 M respectively. The buffer concentration used for the following spectra (above pH 2.5) is 2 mM, the concentration of compound **9** in the cells is 12.5 μ M and 4.0 equivalents of cucurbit-[7]-uril the spectra were acquired after 5 minutes of irradiation with 500 nm light. After the spectral acquisition the pH was checked using a pre-calibrated MetrOhm Biotrode to measure the pH directly inside the cells under 500 nm light irradiation. The resulting profiles were then fitted to the Boltzmann sigmoidal function with the aid of the Excel Solver.

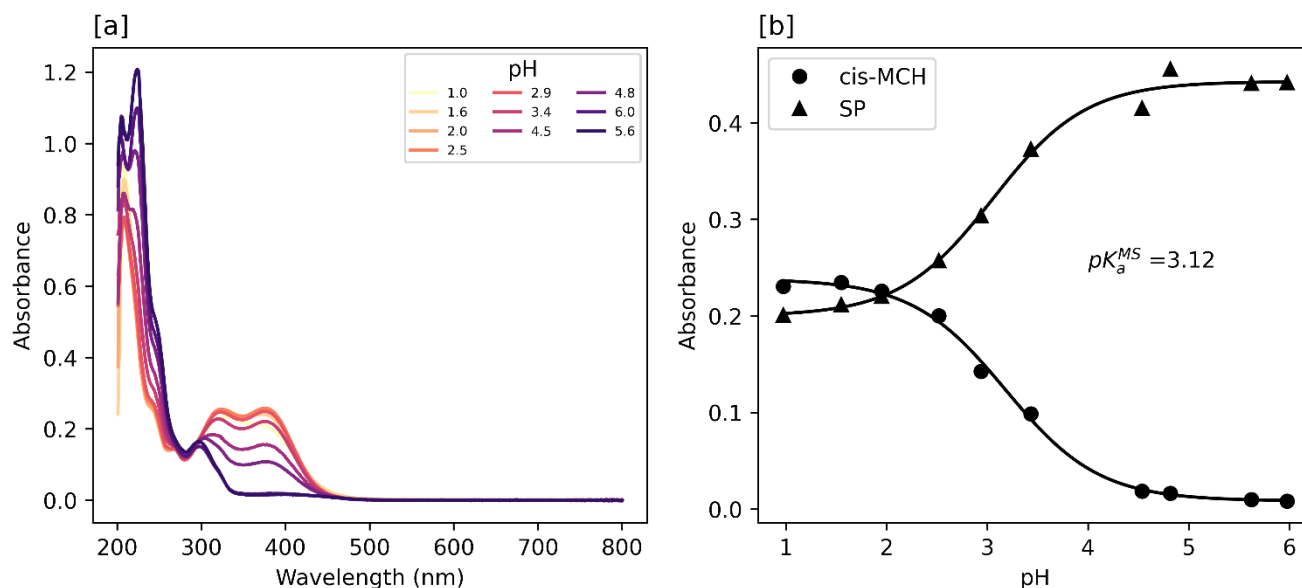


Figure S 6.22. UV-Vis spectra of compound **9** between pH 3 and 10 in 2 mM potassium phosphate buffer solutions. Temperature 298 K, $[9] = 12.5 \mu$ M, $[CB7] = 50 \mu$ M, light source LED 500 nm.

Table S 6.18. Parameters for MC curve fit, data for 350 nm absorption

Abs (low pH)	0.232
Abs (high pH)	0.0084
pK_a	3.18
dx	-0.463
R²	0.9993

Table S 6.19. Parameters for SP curve fit, data for 250 nm absorption

Abs (low pH)	0.200
Abs (high pH)	0.443
pK_a	3.10
dx	-0.462
R²	0.9990

6.5.16 Kinetic determination of K_c (4.0 equivalents of CB7)

The determination of the MC to SP equilibrium constant is performed by means of kinetics measurements of the concentration of the MC form generated *in-situ* by injecting a solution of MCH into an alkaline aqueous solution as described previously^[1–3]. In these experiments a solution 2 mM in potassium phosphate at pH 10 and 50 μ M of cucurbit-[7]-uril was prepared in the UV-Vis cell, to this was added (and mixed for 6 seconds) MCH so to have a concentration of 12.5 μ M in the cell. The decay of the MC form was followed by monitoring the absorbance

at 532 nm every 3 seconds and fitted to a first-order decay kinetics. At the completion of the experiment the pH was checked directly for variation in the cell using a MetrOhm Biotrode and resulted the same as the beginning of the experiment. The error was calculated as maximum semidispersion between the two experiments.

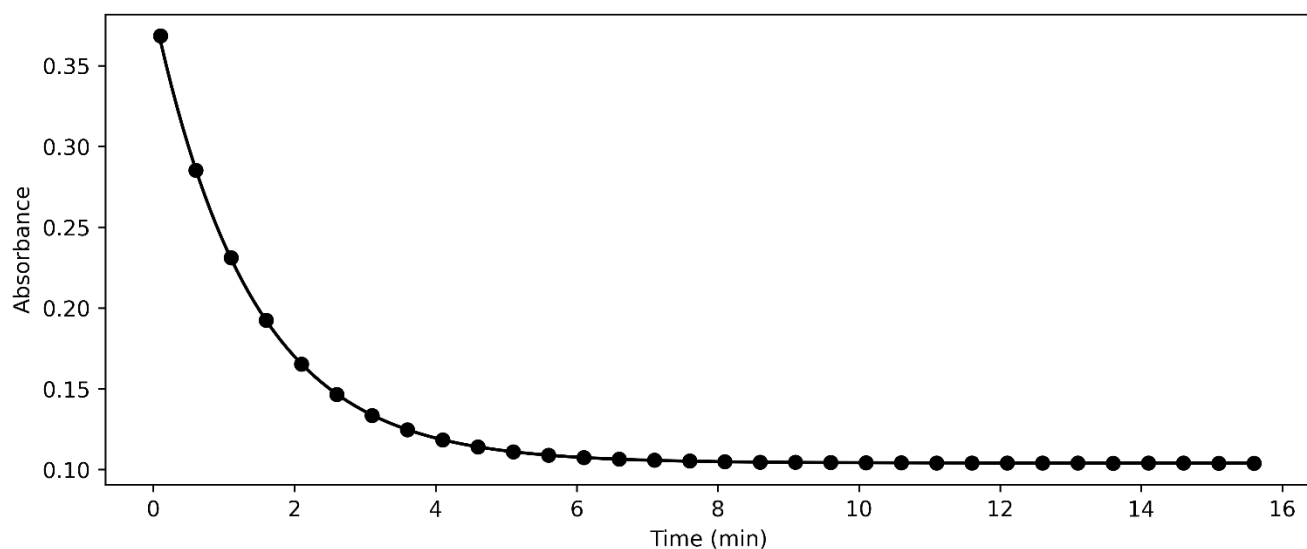


Figure S 6.23. Absorbance profile at 532 nm after injecting **9** in pH 10 buffer 2 mM. Temperature 298 K, $[9] = 12.5 \mu\text{M}$, $[\text{CB7}] = 50 \mu\text{M}$.

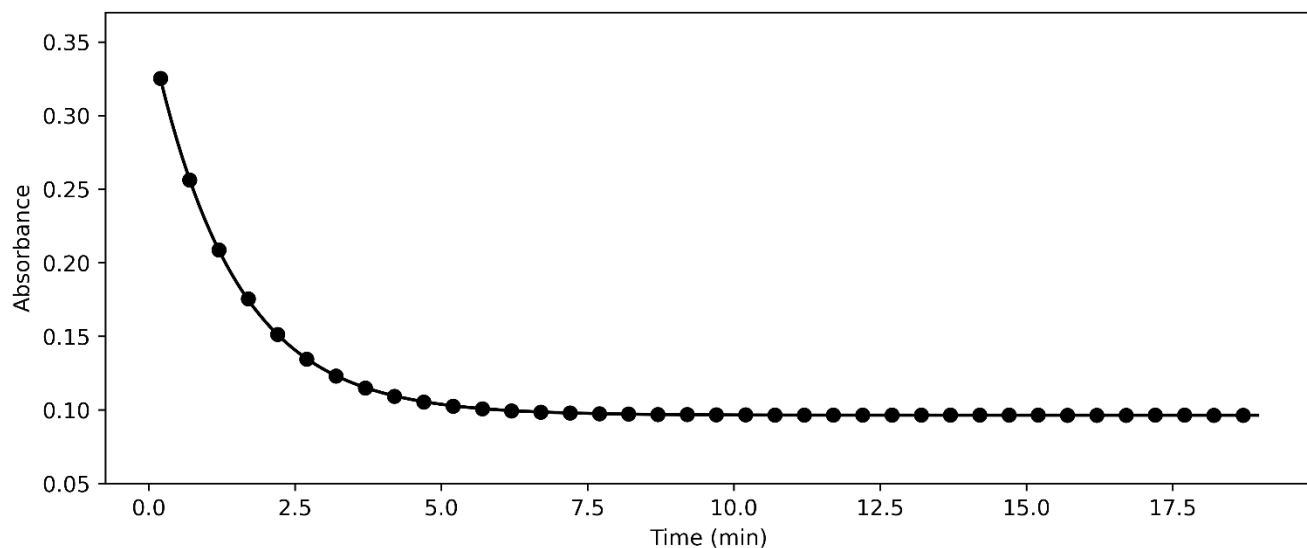


Figure S 6.24. Absorbance profile at 532 nm after injecting **9** in pH 10 buffer 2 mM. Temperature 298 K, $[9] = 12.5 \mu\text{M}$, $[\text{CB7}] = 50 \mu\text{M}$.

Table S 6.20. Parameters for SP curve fit, data for 250 nm absorption

	Exp. 1	Exp. 2	Average	Error
Abs (time 0)	0.385	0.356	0.37	0.01
Abs (equilibrium)	0.104	0.0963	0.100	0.004
$k_{\text{obs}} (\text{s}^{-1})$	0.0125	0.0119	0.0122	0.0003
K_c	2.69	2.70	2.70	0.01
$k_2 (\text{s}^{-1})$	0.00881	0.00868	0.0087	0.0007
$k_{-2} (\text{s}^{-1})$	0.00326	0.00321	0.0032	0.0003
R^2	0.9999	0.9999		

6.5.17 Relaxation kinetics with CB7

The experiment is performed as described previously, the kinetics of recovery from the metastable state are followed by monitoring the absorbance of either the MCH form or the MC form. In the experiments were used potassium phosphate buffers which were prepared by titration of a solution 0.1 M in H_3PO_4 with 10 M aqueous KOH. The pH was measured with a Metrohm Unitrode Pt 1000 combined pH electrode. For the first four samples (between pH 0 and 2.5 included) the pH was regulated by appropriate dilutions of HCl 1 M, 0.1 M and 0.01 M respectively. The buffer concentration used for the following profiles (above pH 2.5) is 20 mM, the concentration of compound 1 in the cells is 12.5 μM and CB7 50 μM .

For pH between 0 and 7.5 was followed every 30 seconds the absorbance at 423 nm, corresponding to the MCH peak absorption. For the pH values above 7.5 was followed the absorbance at 532 nm corresponding to the MC form absorption. At the end of each experiment, the pH was measured with a freshly calibrated Metrohm Biotrode directly in the optical cells.

The data was truncated at time zero which corresponds to the switching-off of the light source. The recovery profile was then fit to a first-order rate law yielding the parameters: A_0 the initial absorbance of the sample, A_{eq} the equilibrium. The initial guesses for the parameters were obtained as follows: for A_0 was used the first experimental point, for A_{eq} was used the maximum experimental point, for $k_{obs,relax}$ was calculated the slope of the first five points.

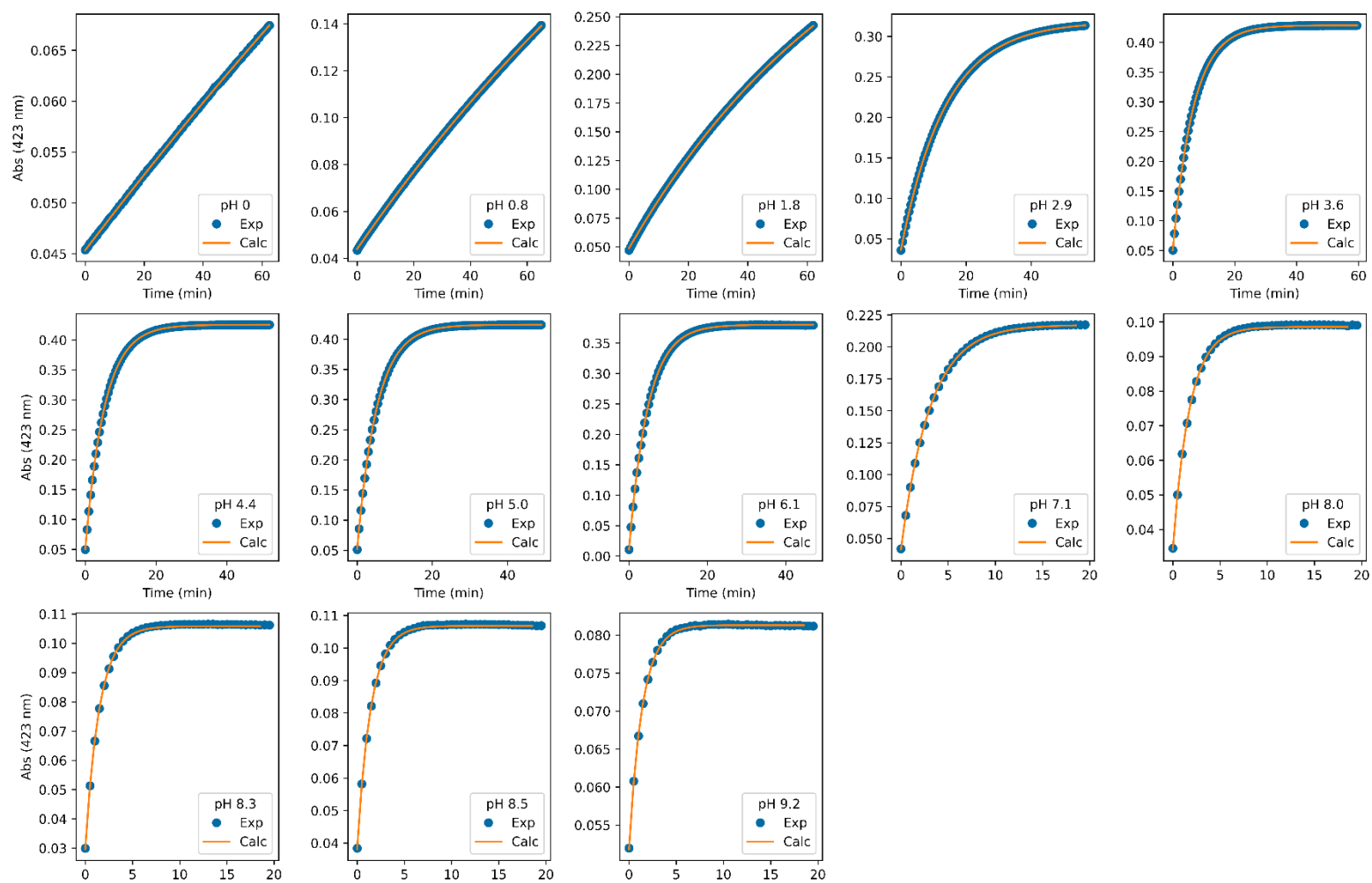


Figure S 6.25. Absorbance profile at 423 nm after irradiation of **9** with 500 nm light in pH 0-10 buffer 2 mM. Temperature 298 K, $[9] = 12.5 \mu\text{M}$, $[\text{CB7}] = 50 \mu\text{M}$. The best fit profiles are represented with an orange solid line.

Table S 6.21. First-order best fit parameters and the pH value of the experiment.

pH	k (min ⁻¹)	A_0	A_{eq}	R^2
0.0	0.002315	0.045346	0.209411	0.999962
0.844	0.005609	0.044041	0.355273	0.999982
1.845	0.012388	0.048874	0.409359	0.999958
2.899	0.072698	0.036465	0.318297	0.999997
3.616	0.151518	0.050503	0.428752	0.999997
4.382	0.184979	0.049785	0.425418	0.999999
4.958	0.190537	0.05149	0.424	0.999996
6.075	0.208689	0.010779	0.380074	0.99996
7.120	0.32525	0.041311	0.217178	0.999775
7.992	0.566878	0.034184	0.098568	0.997423
8.257	0.668487	0.02967	0.105841	0.997654
8.471	0.690635	0.038165	0.106799	0.99869
9.232	0.717	0.05184	0.081312	0.999426

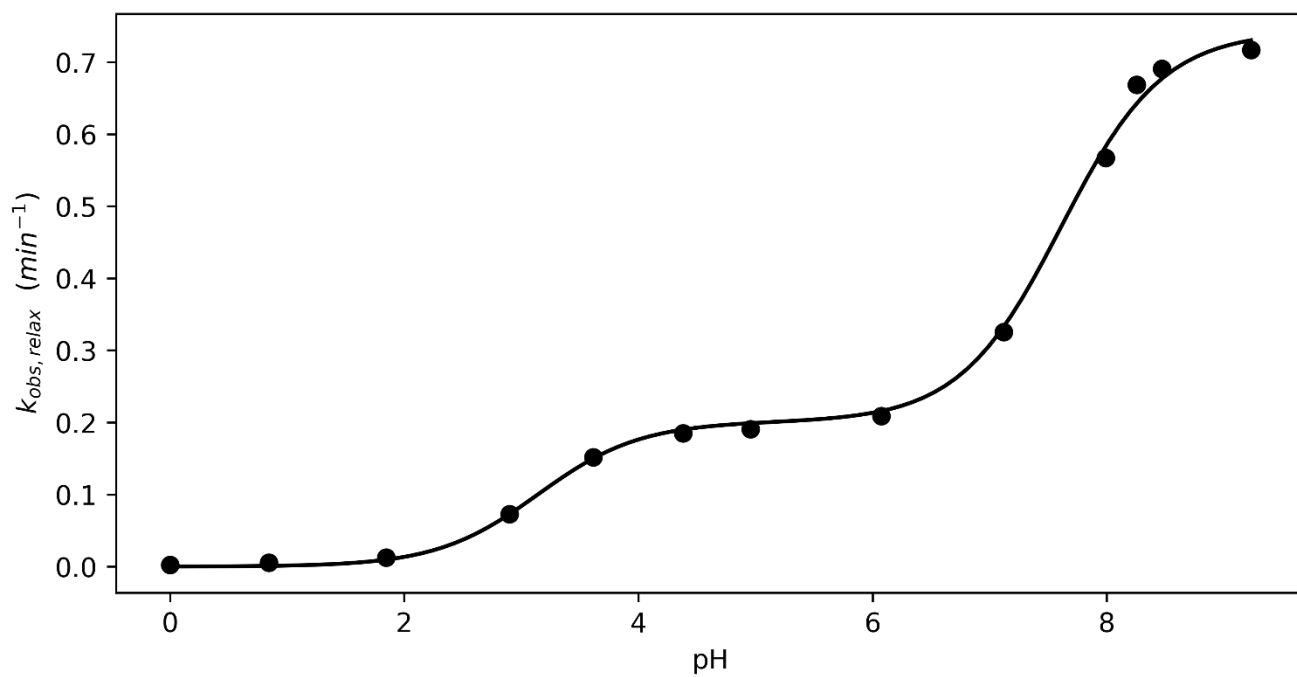


Figure S 6.26. Relaxation rate constant profile against the pH in presence of CB7. The black solid line represents the best fit as described in Chapter 3.

Table S 6.22. Best fit parameters

$k_{-2} \text{ (min}^{-1}\text{)}$	0.201
pK_a^{MS}	3.144
pK_a	7.62
K_c	2.70
R^2	>0.998

6.5.18 Hydrolysis with CB7

The hydrolysis of **9** as function of the pH has been followed by preparation of solutions 12.5 μM of **9** and 50 μM in CB7 in potassium phosphate buffers 20 mM at pH between 4 and 8. These solutions were subject to 500 nm irradiation for obtaining the results presented in paragraph 6.5.6, in this case the samples were monitored by UV-Vis spectroscopy while thermostatted at 25 °C for much longer than the relaxation timeframe. The absorbance profiles were linearized and the observed rate constant extracted from the slope of the linear fit. The observed hydrolysis rate constants were then graphed as function of the experimental pH and fit as explained in Chapter and 4. The pH was measured with a MetrOhm Biotrode before and after the experiment and presented as an averaged value

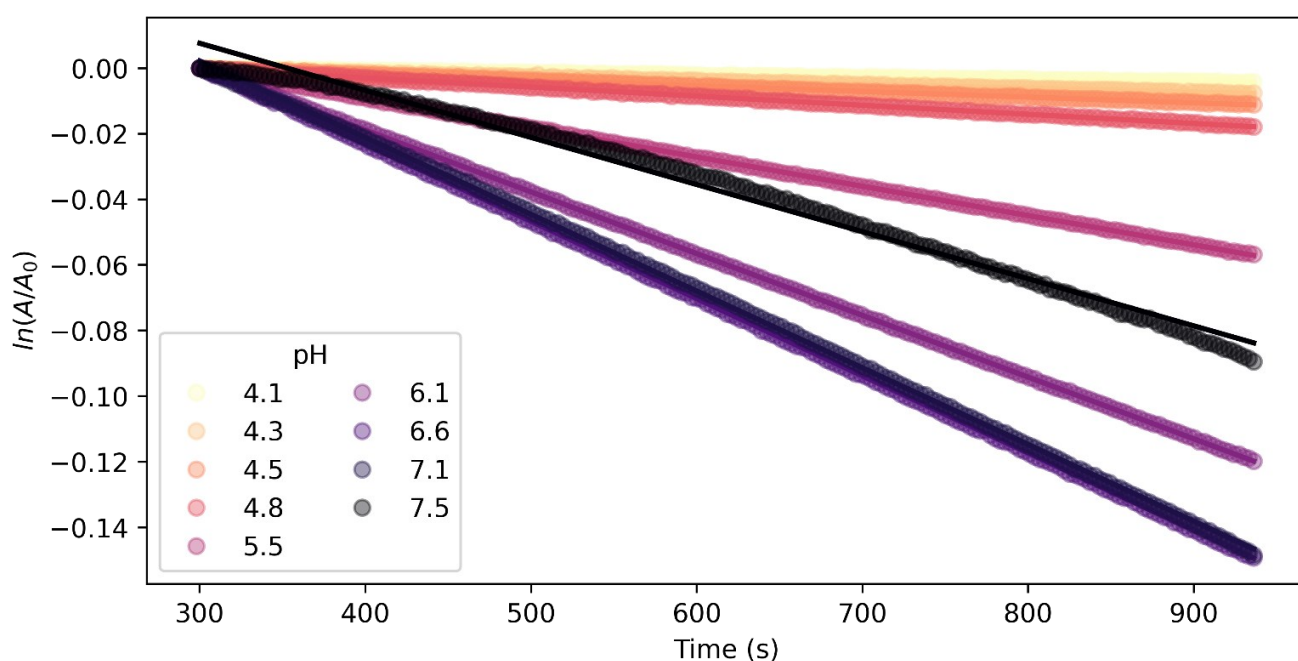


Figure S 6.27. Hydrolysis kinetics of **9** against the pH. The solid lines represent the best fit as described in Chapter 3. Temperature 298 K, $[\mathbf{9}] = 12.5 \mu\text{M}$, $[\text{CB7}] = 50 \mu\text{M}$.

Table S 6.23. Hydrolysis best fit parameters.

pH	$k_{\text{obs,hydro}} \text{ (s}^{-1}\text{)}$	R^2
4.065	4.25E-06	0.990147
4.308	6.86E-06	0.994669
4.523	1.20E-05	0.998084
4.801	1.77E-05	0.999013
5.483	2.90E-05	0.999877
6.110	9.08E-05	0.999975
6.616	0.00019	0.999963
7.09	0.000234	0.999651
7.466	0.000217	0.989159
7.69	8.53E-05	0.971567

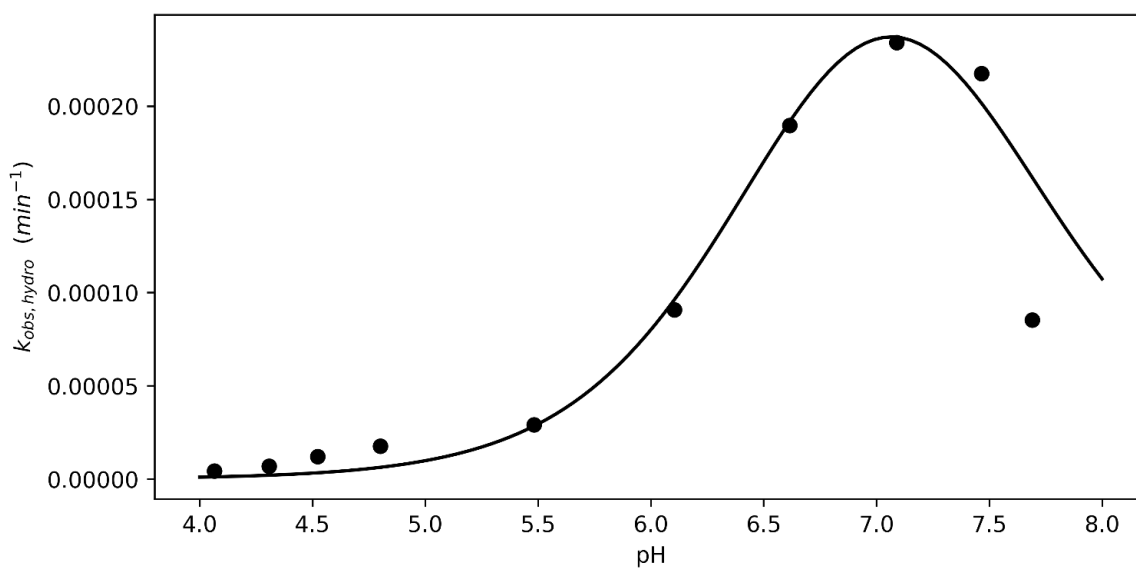


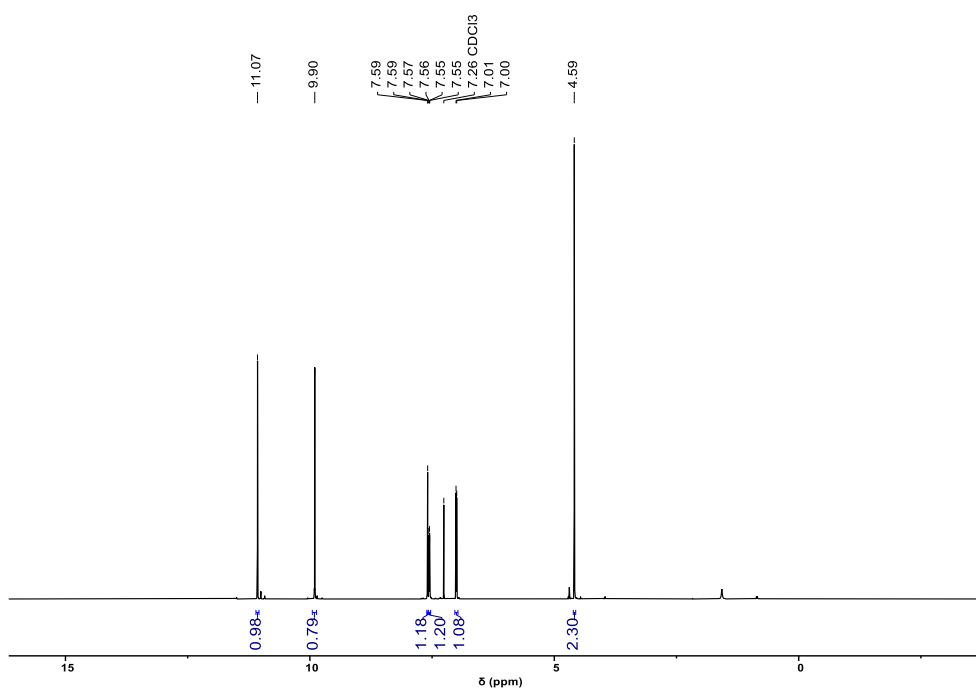
Figure S 6.28. Hydrolysis rate constants of **9** against the pH. The solid line represents the best fit as described in Chapter 3. Temperature 298 K, $[\mathbf{9}] = 12.5 \mu\text{M}$, $[\text{CB7}] = 50 \mu\text{M}$.

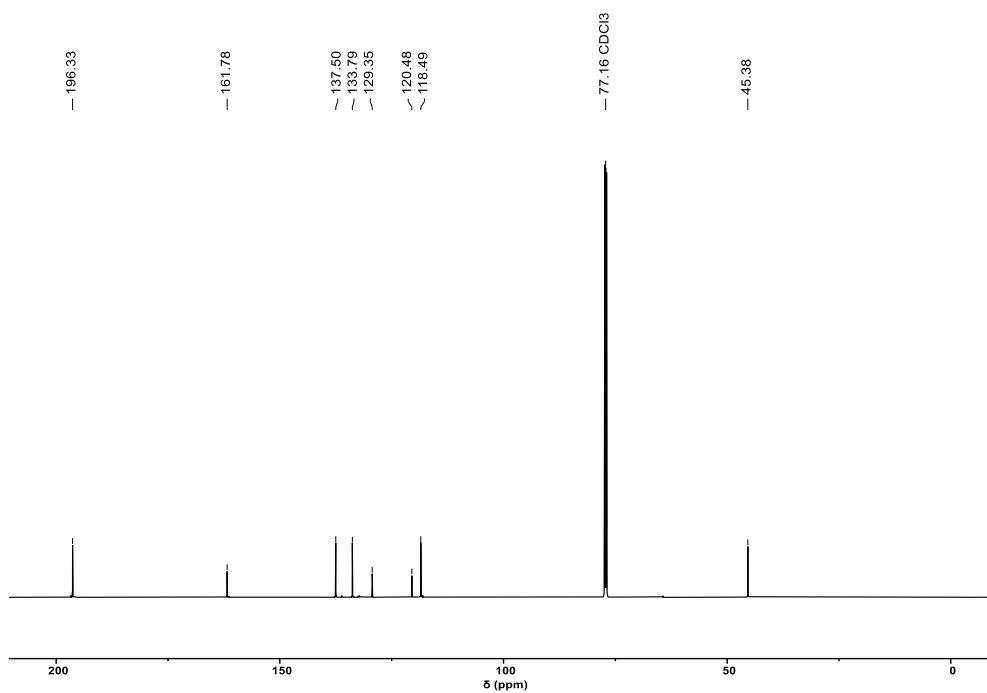
Table S 6.24. Best fit parameters

k_w (min^{-1})	4.63×10^{-4}
k_{OH} (min^{-1})	5.34×10^2
$\text{p}K_a^{\text{GS}}$	7.44
k_w/k_h (M^{-1})	4.58×10^6
R^2	>0.989

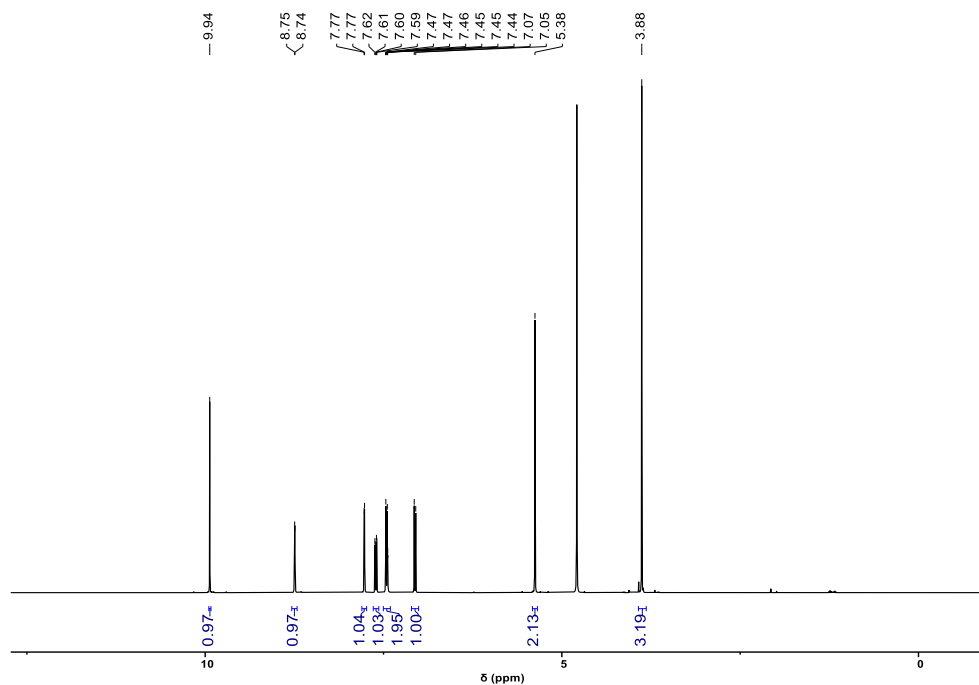
6.5.19 NMR spectra of synthesized compounds

Spectra of compound X1

Figure S 6.29. ^1H NMR (400 MHz, 298 K, CDCl_3) of compound **X1**.

Figure S 6.30. ^{13}C NMR (101 MHz, 298 K, CDCl_3) of compound **X1**.

Spectra of compound **X2**

Figure S 6.31. ^1H NMR (400 MHz, 298 K, D_2O) of compound **X2**.

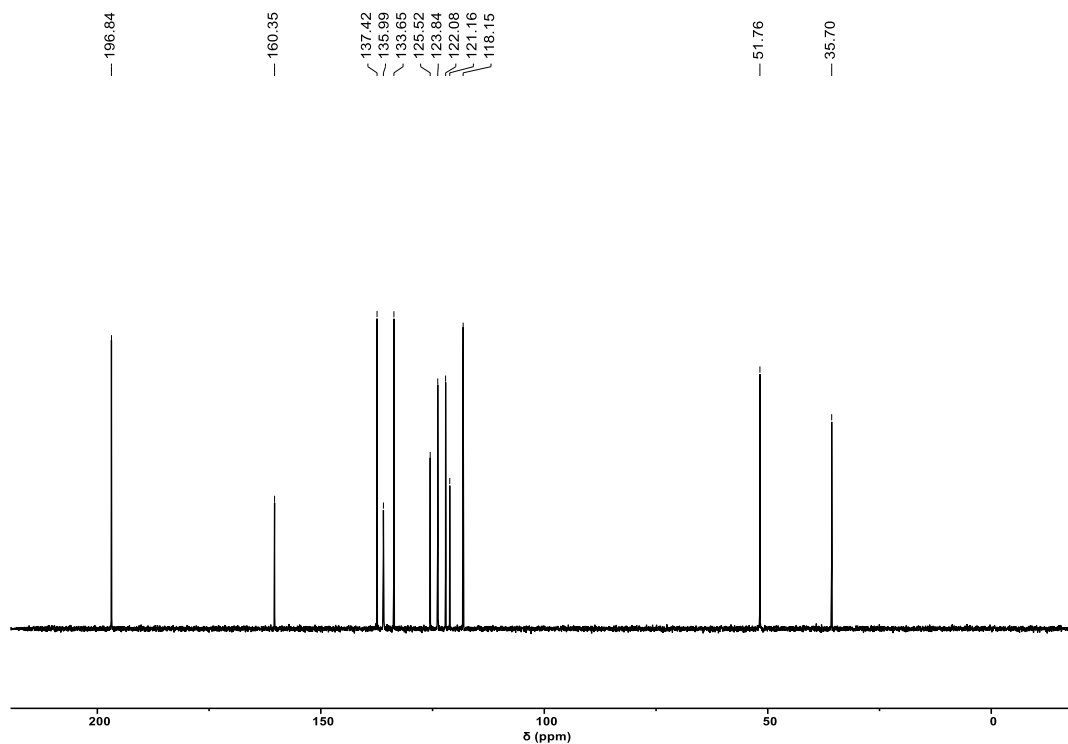


Figure S 6.32. ^{13}C NMR (101 MHz, 298 K, D_2O) of compound **X2**.

Spectra of compound **9**

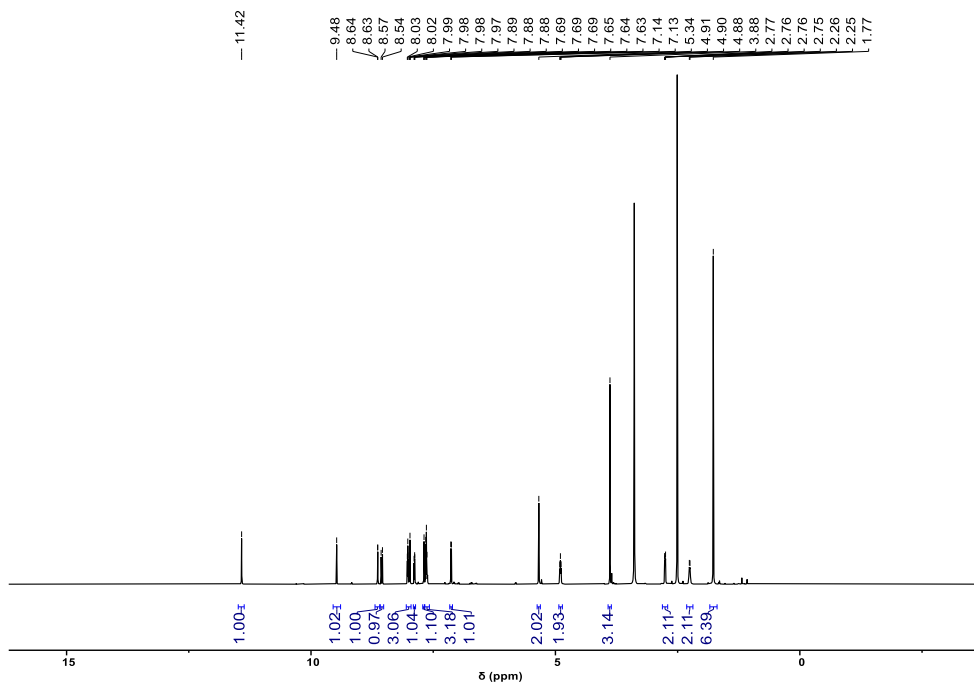


Figure S 6.33 ^1H NMR (600 MHz, 298 K, $\text{DMSO}-d_6$) of compound **9**

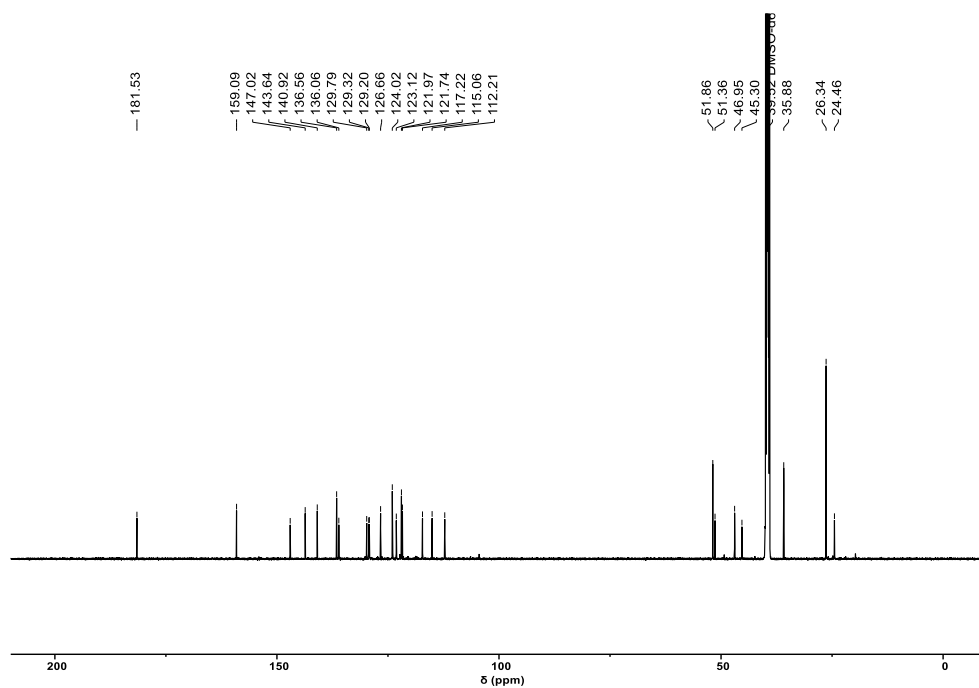


Figure S 6.34. ^{13}C NMR (125 MHz, 298 K, $\text{DMSO}-d_6$) of compound **9**.

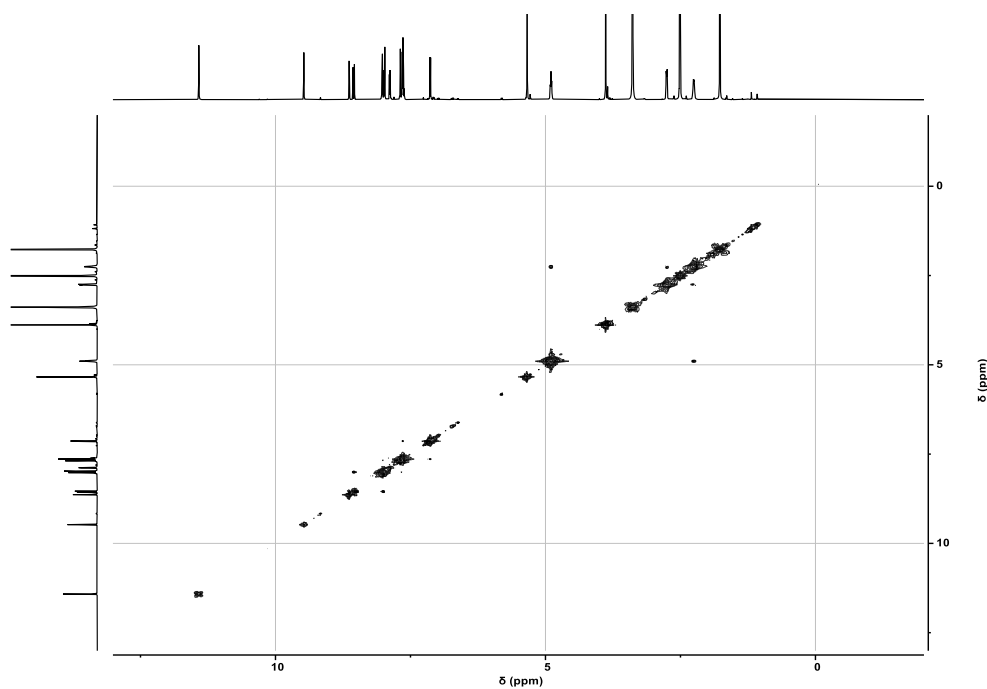


Figure S 6.35. $(^1\text{H}-^1\text{H})$ COSY NMR (600 MHz, $\text{DMSO}-d_6$, 298K) of compound **9**.

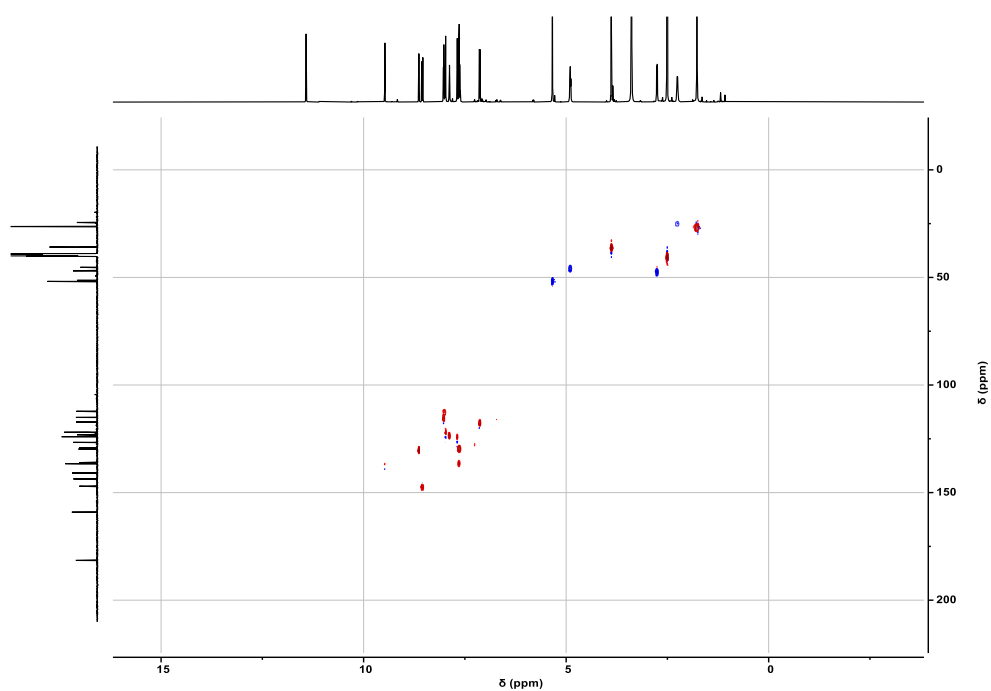


Figure S 6.36. Multiplicity edited (^1H - ^{13}C) HSQC NMR (600 MHz, $\text{DMSO}-d_6$, 298K) of compound 9. The positive peaks are represented in red, while the negative ones in blue.

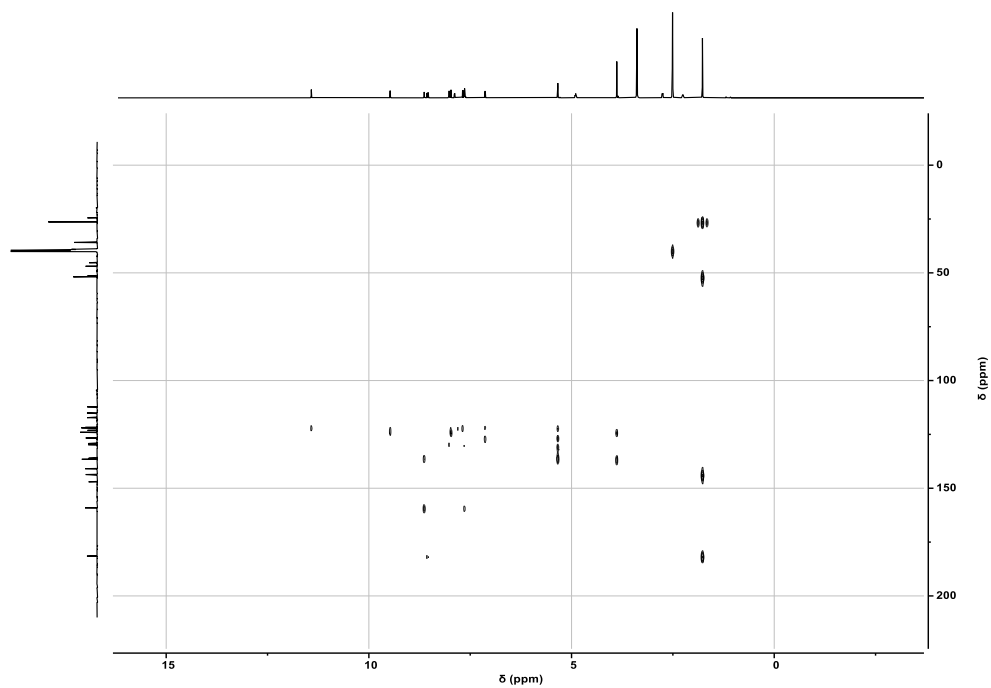


Figure S 6.37. (^1H - ^{13}C) HMBC NMR (600 MHz, $\text{DMSO}-d_6$, 298K) of compound 9.

Chapter 7

Conclusions and perspectives

In this thesis I have dissected several operational aspects of BIPS photoacidity in water. As demonstrated in Chapter 3, their aqueous (photo)chemistry can be fully described by a four-state dynamic model, which was applied to three different compounds and revealed to be of general applicability.

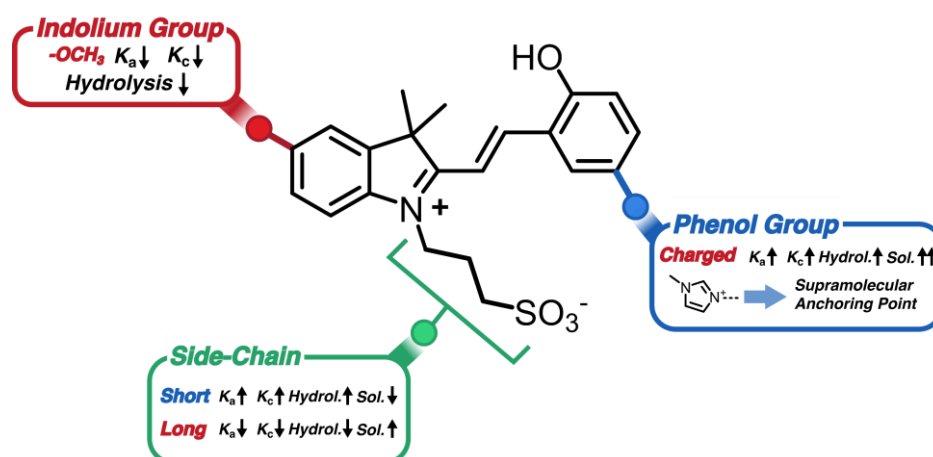


Figure 7.1. The structural aspects of BIPS investigated in this thesis and their repercussions on the chemistry of these compounds. In red is reported the effect of EDGs in *para* position respect to the nitrogen of the indolium. In green the effects observed by extending or shortening the alkylsulfonate sidechain. In blue the effect of substitution of the phenol moiety with a charged group.

In Chapter 4, a more detailed analysis on BIPS photoacidity was carried out, showing for the first time its inverse relationship with the temperature: the photoacidity of BIPS increases as the temperature decreases. In Chapter 5, structure-function relationship studies we carried out on a library of four different methoxy-substituted compounds, showing that *para*-substitution of the indolium side significantly stabilizes the open protonated form from hydrolysis and allows for actuating the pH switch with red-shifted light. In addition, the solubility equilibria were also studied, leading to the development

of “light-switchable buffers” featuring enhanced pH jumps and fatigue resistance. Finally, in Chapter 6 we investigated the selective encapsulation of a highly water-soluble cationic photoacid by cucurbit-[7]-uril, showing that the chemical stability can be increased further and that pH switches of up to 4 units can be promoted over at least one day without significant loss of efficiency. These last results are promising, as they open up a set of new (supramolecular) design principles for enhancing the photoacidic properties of BIPS. We believe the opportunity to trigger deep and reversible proton gradients with visible light outlined in this thesis may open new horizons in the development of novel devices for solar energy harvesting.

Bibliography

- [1] L. Kortekaas, W. R. Browne, in *Mol. Photoswitches*, John Wiley & Sons, Ltd, **2022**, pp. 131–149.
- [2] L. Kortekaas, W. R. Browne, *Chem. Soc. Rev.* **2019**, *48*, 3406–3424.
- [3] R. Klajn, *Chem. Soc. Rev.* **2013**, *43*, 148–184.
- [4] H. Durr, H. Bouas-Laurent, *Pure Appl Chem* **2001**, *73*, 639–665.
- [5] R. Wizinger, H. Wenning, *Helv. Chim. Acta* **1940**, *23*, 247–271.
- [6] Y. Hirshberg, E. Fischer, *J. Chem. Soc. Resumed* **1952**, 4522.
- [7] A. Samat, D. De Keukeleire, R. Guglielmetti, *Bull Soc Chim Belg* **1991**, *100*, 679–700.
- [8] K. K. Kalninsk, *J. Struct. Chem.* **1998**, *39*, 642–650.
- [9] Y. Hirshberg, E. Fischer, *J. Chem. Soc. Resumed* **1953**, 629–636.
- [10] H. Chen, Y. Liao, *J. Photochem. Photobiol. Chem.* **2015**, *300*, 22–26.
- [11] I. Shimizu, H. Kokado, E. Inoue, *Bull. Chem. Soc. Jpn.* **2006**, *42*, 1726–1729.
- [12] S. Aiken, R. J. L. Edgar, C. D. Gabbutt, B. M. Heron, P. A. Hobson, *Dyes Pigments* **2018**, *149*, 92–121.
- [13] G. Liu, Y. Li, C. Cui, M. Wang, H. Gao, J. Gao, J. Wang, *J. Photochem. Photobiol. Chem.* **2022**, *424*, 113658.
- [14] L. Wu, R. Chen, Z. Luo, P. Wang, *J. Mater. Sci.* **2020**, *55*, 12826–12835.
- [15] V. K. Johns, P. K. Patel, S. Hassett, P. Calvo-Marzal, Y. Qin, K. Y. Chumbimuni-Torres, *Anal. Chem.* **2014**, *86*, 6184–6187.
- [16] O. Oms, K. Hakouk, R. Dessapt, P. Deniard, S. Jobic, A. Dolbecq, T. Palacin, L. Nadjo, B. Keita, J. Marrot, P. Mialane, *Chem. Commun.* **2012**, *48*, 12103–12105.
- [17] J. D. Steen, D. R. Duijnste, A. S. Sardjan, J. Martinelli, L. Kortekaas, D. Jacquemin, W. R. Browne, *J. Phys. Chem. A* **2021**, *125*, 3355–3361.
- [18] E. Ando, J. Hibino, T. Hashida, K. Morimoto, *Thin Solid Films* **1988**, *160*, 279–286.
- [19] H. Görner, *Phys. Chem. Chem. Phys.* **2001**, *3*, 416–423.
- [20] S.-R. Keum, K.-B. Lee, P. M. Kazmaier, E. Buncel, *Tetrahedron Lett.* **1994**, *35*, 1015–1018.
- [21] S.-R. Keum, S.-J. Roh, S.-M. Ahn, S.-S. Lim, S.-H. Kim, K. Koh, *Dyes Pigments* **2007**, *74*, 343–347.
- [22] P. Joseph, K. Kundu, P. K. Kundu, *ChemistrySelect* **2018**, *3*, 11065–11070.
- [23] A. R. Boyd, P. G. Jessop, J. M. Dust, E. Buncel, *Org. Biomol. Chem.* **2013**, *11*, 6047–6055.
- [24] D. E. Wetzler, P. F. Aramendía, M. L. Japas, R. Fernández-Prini, *Phys. Chem. Chem. Phys.* **1999**, *1*, 4955–4959.
- [25] H. Kagel, M. Frohme, J. Glöckler, *J. Cell. Biotechnol.* **2019**, *4*, 23–30.
- [26] Y. Liao, *Acc. Chem. Res.* **2017**, *50*, 1956–1964.
- [27] Y. Liao, *Phys. Chem. Chem. Phys.* **2022**, *24*, 4116–4124.
- [28] N. Klikovits, P. Knaack, D. Bomze, I. Krossing, R. Liska, *Polym. Chem.* **2017**, *8*, 4414–4421.
- [29] C. J. Martin, G. Rapenne, T. Nakashima, T. Kawai, *J. Photochem. Photobiol. C Photochem. Rev.* **2018**, *34*, 41–51.
- [30] N. A. Kuznetsova, G. V. Malkov, B. G. Gribov, *Russ. Chem. Rev.* **2020**, *89*, 173.
- [31] N. Agmon, W. Rettig, C. Groth, *J. Am. Chem. Soc.* **2002**, *124*, 1089–1096.

- [32] R. M. D. Nunes, M. Pineiro, L. G. Arnaut, *J. Am. Chem. Soc.* **2009**, *131*, 9456–9462.
- [33] Z. Shi, P. Peng, D. Strohecker, Y. Liao, *J. Am. Chem. Soc.* **2011**, *133*, 14699–14703.
- [34] M. Emond, T. Le Saux, S. Maurin, J.-B. Baudin, R. Plasson, L. Jullien, *Chem. – Eur. J.* **2010**, *16*, 8822–8831.
- [35] S. Samanta, A. Babalhavaeji, M. Dong, G. A. Woolley, *Angew. Chem. Int. Ed.* **2013**, *52*, 14127–14130.
- [36] V. K. Johns, P. Peng, J. DeJesus, Z. Wang, Y. Liao, *Chem. - Eur. J.* **2014**, *20*, 689–692.
- [37] S. Silvi, A. Arduini, A. Pochini, A. Secchi, M. Tomasulo, F. M. Raymo, M. Baroncini, A. Credi, *J. Am. Chem. Soc.* **2007**, *129*, 13378–13379.
- [38] S. Silvi, E. C. Constable, C. E. Housecroft, J. E. Beves, E. L. Dunphy, M. Tomasulo, F. M. Raymo, A. Credi, *Chem. - Eur. J.* **2009**, *15*, 178–185.
- [39] R.-J. Li, C. Pezzato, C. Berton, K. Severin, *Chem. Sci.* **2021**, *12*, 4981–4984.
- [40] S. M. Jansze, G. Cecot, K. Severin, *Chem. Sci.* **2018**, *9*, 4253–4257.
- [41] S. Silvi, E. C. Constable, C. E. Housecroft, J. E. Beves, E. L. Dunphy, M. Tomasulo, F. M. Raymo, A. Credi, *Chem. Commun.* **2009**, 1484–1486.
- [42] W. Renè M., K. Gudrun, S. E. Braslavsky, *Helv. Chim. Acta* **2001**, *85*, 2557–2576.
- [43] D. Balogh, R. Tel-Vered, R. Freeman, I. Willner, *J. Am. Chem. Soc.* **2011**, *133*, 6533–6536.
- [44] K. Sumaru, M. Kameda, T. Kanamori, T. Shinbo, *Macromolecules* **2004**, *37*, 4949–4955.
- [45] F. J. Rizzuto, C. M. Platnich, X. Luo, Y. Shen, M. D. Dore, C. Lachance-Brais, A. Guarné, G. Cosa, H. F. Sleiman, *Nat. Chem.* **2021**, *13*, 843–849.
- [46] A. Koçer, M. Walko, W. Meijberg, B. L. Feringa, *Science* **2005**, *309*, 755–758.
- [47] O. S. Shafaat, J. R. Winkler, H. B. Gray, D. A. Dougherty, *ChemBioChem* **2016**, *17*, 1323–1327.
- [48] H. Bao, F. Li, L. Lei, B. Yang, Z. Li, *RSC Adv.* **2014**, *4*, 27277–27280.
- [49] Y. Xu, J. Fei, G. Li, T. Yuan, Y. Li, C. Wang, X. Li, J. Li, *Angew. Chem. Int. Ed.* **2017**, *56*, 12903–12907.
- [50] Y. Luo, C. Wang, P. Peng, M. Hossain, T. Jiang, W. Fu, Y. Liao, M. Su, *J. Mater. Chem. B* **2013**, *1*, 997–1001.
- [51] C. Ash, M. Dubec, K. Donne, T. Bashford, *Lasers Med. Sci.* **2017**, *32*, 1909–1918.
- [52] R. Han, S. Wu, K. Tang, Y. Hou, *Adv. Powder Technol.* **2020**, *31*, 3860–3866.
- [53] C. Wang, P. Zhao, G. Yang, X. Chen, Y. Jiang, X. Jiang, Y. Wu, Y. Liu, W. Zhang, W. Bu, *Mater. Horiz.* **2020**, *7*, 1180–1185.
- [54] S.-F. Zhou, G.-M. Wu, C.-X. Zhang, Q.-L. Wang, S.-F. Zhou, Q.-L. Wang, G.-M. Wu, C.-X. Zhang, *Adv. Mater. Interfaces* **2022**, 2101247.
- [55] A. Elgattar, N. Abeyrathna, Y. Liao, *J. Phys. Chem. B* **2019**, *123*, 648–654.
- [56] D. Go, D. Rommel, Y. Liao, T. Haraszti, J. Sprakel, A. J. C. Kuehne, *Soft Matter* **2018**, *14*, 910–915.
- [57] H. Zhang, H. Zeng, A. Priimagi, O. Ikkala, *Nat. Commun.* **2019**, *10*, 1–8.
- [58] X.-M. Chen, X.-F. Hou, H. K. Bisoyi, W.-J. Feng, Q. Cao, S. Huang, H. Yang, D. Chen, Q. Li, *Nat. Commun.* **2021**, *12*, 4993.

- [59] M. P. M. Dicker, P. M. Weaver, J. M. Rossiter, I. P. Bond, C. F. J. Faul, *Bioinspiration Biomim. Bioreplication* **2016**, 9797, 97970.
- [60] J. Guo, H. Y. Zhang, Y. Zhou, Y. Liu, *Chem. Commun.* **2017**, 53, 6089–6092.
- [61] J. Ryssy, A. K. Natarajan, J. Wang, A. J. Lehtonen, M.-K. Nguyen, R. Klajn, A. Kuzyk, *Angew. Chem. Int. Ed.* **2021**, 60, 5859–5863.
- [62] H. Qian, S. Pramanik, I. Aprahamian, *J. Am. Chem. Soc.* **2017**, 139, 9140–9143.
- [63] P. K. Patel, K. Y. Chumbimuni-Torres, *Analyst* **2016**, 141, 85–89.
- [64] R. Bennett, S. Clifford, K. Anderson, G. Puxty, *Energy Procedia* **2017**, 114, 1–6.
- [65] J. Bae, H. Lim, J. Ahn, Y. H. Kim, M. S. Kim, I.-D. Kim, J. Bae, H. Lim, J. Ahn, Y. H. Kim, M. S. Kim, I. -d Kim, J. A. B. J. Paulson, *Adv. Mater.* **2022**, 34, 2201734.
- [66] V. K. Johns, Z. Wang, X. Li, Y. Liao, *J. Phys. Chem. A* **2013**, 117, 13101–13104.
- [67] L. A. Tatum, J. T. Foy, I. Aprahamian, *J. Am. Chem. Soc.* **2014**, 136, 17438–17441.
- [68] L. P. Yang, F. Jia, J. S. Cui, S. B. Lu, W. Jiang, *Org. Lett.* **2017**, 19, 2945–2948.
- [69] X. Li, J. Fei, Y. Xu, D. Li, T. Yuan, G. Li, C. Wang, J. Li, *Angew. Chem. Int. Ed.* **2018**, 57, 1903–1907.
- [70] C. Maity, W. E. Hendriksen, J. H. V. Esch, R. Eelkema, *Angew. Chem. Int. Ed.* **2015**, 54, 998–1001.
- [71] P. K. Kundu, D. Samanta, R. Leizrowice, B. Margulis, H. Zhao, M. Börner, T. Udayabhaskararao, D. Manna, R. Klajn, *Nat. Chem.* **2015**, 7, 646–652.
- [72] D. Samanta, R. Klajn, *Adv. Opt. Mater.* **2016**, 4, 1373–1377.
- [73] S. Mahvidi, S. Takeuchi, S. Kusumoto, H. Sato, T. Nakagawa, Y. Yokoyama, *Org. Lett.* **2016**, 18, 5042–5045.
- [74] M. S. Zayas, N. D. Dolinski, J. L. Self, A. Abdilla, C. J. Hawker, C. M. Bates, J. R. de Alaniz, *ChemPhotoChem* **2019**, 3, 467–472.
- [75] M. J. Feeney, S. W. Thomas, *Macromolecules* **2018**, 51, 8027–8037.
- [76] L. Yang, L. C. da Silva, H. Thérien-Aubin, M. B. Bannwarth, K. Landfester, *Macromol. Rapid Commun.* **2019**, 40, 1800713.
- [77] C. Li, A. Iscen, L. C. Palmer, G. C. Schatz, S. I. Stupp, *J. Am. Chem. Soc.* **2020**, 142, 8447–8453.
- [78] N. Abeyrathna, Y. Liao, *J. Am. Chem. Soc.* **2015**, 137, 11282–11284.
- [79] N. Abeyrathna, Y. Liao, *J. Phys. Org. Chem.* **2017**, 30, e3664.
- [80] J. Vallet, J. C. Micheau, C. Coudret, *Dyes Pigments* **2016**, 125, 179–184.
- [81] T. Khalil, A. Alharbi, C. Baum, Y. Liao, *Macromol. Rapid Commun.* **2018**, 39, 1800319.
- [82] M. D. Liptak, K. C. Gross, P. G. Seybold, S. Feldgus, G. C. Shields, *J. Am. Chem. Soc.* **2002**, 124, 6421–6427.
- [83] Y. Shiraishi, M. Itoh, T. Hirai, *Phys. Chem. Chem. Phys.* **2010**, 12, 13737–13745.
- [84] J. T. C. Wojtyk, A. Wasey, P. M. Kazmaier, S. Hoz, E. Buncel, *J. Phys. Chem. A* **2000**, 104, 9046–9055.
- [85] J. Liu, W. Tang, L. Sheng, Z. Du, T. Zhang, X. Su, S. X. A. Zhang, *Chem. – Asian J.* **2019**, 14, 438–445.
- [86] T. Stafforst, D. Hilvert, *Chem. Commun.* **2009**, 287–288.
- [87] M. Hammarson, J. R. Nilsson, S. Li, T. Beke-Somfai, J. Andréasson, *J. Phys. Chem. B* **2013**, 117, 13561–13571.
- [88] R. L. Reeves, *J. Am. Chem. Soc.* **1962**, 84, 3332–3337.

- [89] E. H. Cordes, W. P. Jencks, *J. Am. Chem. Soc.* **1963**, *85*, 2843–2848.
- [90] F. M. Raymo, S. Giordani, *J. Am. Chem. Soc.* **2001**, *123*, 4651–4652.
- [91] L. Kortekaas, J. Chen, D. Jacquemin, W. R. Browne, *J. Phys. Chem. B* **2018**, *122*, 6423–6430.
- [92] M. Rae, M. N. Berberan-Santos, *J. Chem. Educ.* **2004**, *81*, 436–440.
- [93] D. Moldenhauer, F. Gröhn, *Chem. – Eur. J.* **2017**, *23*, 3966–3978.
- [94] M. Dong, Y. W. Wang, Y. Peng, *Supramol. Chem.* **2013**, *25*, 116–120.
- [95] S. Kusumoto, T. Nakagawa, Y. Yokoyama, *Adv. Opt. Mater.* **2016**, *4*, 1350–1353.
- [96] M. Schnurbus, M. Kabat, E. Jarek, M. Krzan, P. Warszynski, B. Braunschweig, *Langmuir* **2020**, *36*, 6871–6879.
- [97] P. Nitschke, N. Lokesh, R. M. Gschwind, *Prog. Nucl. Magn. Reson. Spectrosc.* **2019**, *114–115*, 86–134.
- [98] K. A. Robinson, *Anal. Methods* **2017**, *9*, 2744–2750.
- [99] J. Zhou, Y. Li, Y. Tang, F. Zhao, X. Song, E. Li, *J. Photochem. Photobiol. Chem.* **1995**, *90*, 117–123.
- [100] C. L. Fleming, S. Li, M. Grøtli, J. Andréasson, *J. Am. Chem. Soc.* **2018**, *140*, 14069–14072.
- [101] N. Abeyrathna, Y. Liao, *J. Photochem. Photobiol. Chem.* **2017**, *332*, 196–199.
- [102] T. Galaon, V. David, *J. Sep. Sci.* **2011**, *34*, 1423–1428.
- [103] H. Görner, *Chem. Phys.* **1997**, *222*, 315–329.
- [104] B. Razavi, A. Abdollahi, H. Roghani-Mamaqani, M. Salami-Kalajahi, *Mater. Sci. Eng. C* **2020**, *109*.
- [105] D. Dulić, T. Kudernac, A. Pužys, B. L. Feringa, B. J. van Wees, *Adv. Mater.* **2007**, *19*, 2898–2902.
- [106] M. Milek, F. W. Heinemann, M. M. Khusniyarov, *Inorg. Chem.* **2013**, *52*, 11585–11592.
- [107] J. M. Cox, I. M. Walton, D. G. (Dan) Patel, M. Xu, Y.-S. Chen, J. B. Benedict, *J. Phys. Chem. A* **2015**, *119*, 884–888.
- [108] T. Kudernac, T. Kobayashi, A. Uyama, K. Uchida, S. Nakamura, B. L. Feringa, *J. Phys. Chem. A* **2013**, *117*, 8222–8229.
- [109] E. Fischer, *J. Am. Chem. Soc.* **1960**, *82*, 3249–3252.
- [110] N. Eleya, S. Ghosh, E. Lork, A. Staubitz, *J. Mater. Chem. C* **2021**, *9*, 82–87.
- [111] H. Zhou, C. Xue, P. Weis, Y. Suzuki, S. Huang, K. Koynov, G. K. Auernhammer, R. Berger, H.-J. Butt, S. Wu, *Nat. Chem.* **2017**, *9*, 145–151.
- [112] T. Gebretsadik, Q. Yang, J. Wu, J. Tang, *Coord. Chem. Rev.* **2021**, *431*, 213666.
- [113] C. Berton, D. M. Busiello, S. Zamuner, E. Solari, R. Scopelliti, F. F. Tirani, K. Severin, C. Pezzato, *Chem. Sci.* **2020**.
- [114] L. Wimberger, S. K. K. Prasad, M. D. Peeks, J. Andréasson, T. W. Schmidt, J. E. Beves, *J. Am. Chem. Soc.* **2021**, *143*, 20758–20768.
- [115] C. Berton, D. M. Busiello, S. Zamuner, R. Scopelliti, F. Fadaei-Tirani, K. Severin, C. Pezzato, *Angew. Chem. - Int. Ed.* **2021**, *60*, 21737–21740.
- [116] V. S. Stoll, J. S. Blanchard, in *Guide Protein Purif. Methods Enzymol.*, Academic Press, New York, **1990**, pp. 24–38.
- [117] S. P. L. Sørensen, in *Enzym. II Über Mess. Bedeut. Wasserstoffionenkonzentration Bei Enzym. Prozessen*, Springer-Verlag, **1909**, pp. 131–304.
- [118] N. V. Bhagavan, in *Med. Biochem. Fourth Ed.* (Ed.: N.V. Bhagavan), Academic Press, San Diego, **2002**, pp. 1–16.

- [119] E. T. Urbansky, M. R. Schock, *J. Chem. Educ.* **2000**, *77*, 1640.
- [120] V. J. Périllat, C. Berton, C. Pezzato, *Mater. Today Chem.* **2022**, *25*, 100918.
- [121] J. E. Nielsen, J. A. McCammon, *Protein Sci. Publ. Protein Soc.* **2003**, *12*, 1894–1901.
- [122] T. K. Harris, G. J. Turner, *IUBMB Life* **2002**, *53*, 85–98.
- [123] D. G. Isom, C. A. Castañeda, B. R. Cannon, B. García-Moreno E., *Proc. Natl. Acad. Sci.* **2011**, *108*, 5260–5265.
- [124] F. H. Westheimer, *Tetrahedron* **1995**, *51*, 3–20.
- [125] B. Honig, A. Nicholls, *Science* **1995**, *268*, 1144–1149.
- [126] K. A. Connors, *Chem. Rev.* **1997**, *97*, 1325–1358.
- [127] M. V. Rekharsky, Y. Inoue, *Chem. Rev.* **1998**, *98*, 1875–1918.
- [128] D.-S. Guo, V. D. Uzunova, X. Su, Y. Liu, W. M. Nau, *Chem. Sci.* **2011**, *2*, 1722–1734.
- [129] Y. Liu, D.-S. Guo, H.-Y. Zhang, Y.-H. Ma, E.-C. Yang, *J. Phys. Chem. B* **2006**, *110*, 3428–3434.
- [130] Y. Liu, Y.-H. Ma, Y. Chen, D.-S. Guo, Q. Li, *J. Org. Chem.* **2006**, *71*, 6468–6473.
- [131] D.-S. Guo, L.-H. Wang, Y. Liu, *J. Org. Chem.* **2007**, *72*, 7775–7778.
- [132] E. Masson, X. Ling, R. Joseph, L. Kyeremeh-Mensah, X. Lu, *RSC Adv.* **2012**, *2*, 1213–1247.
- [133] J. Kim, I.-S. Jung, S.-Y. Kim, E. Lee, J.-K. Kang, S. Sakamoto, K. Yamaguchi, K. Kim, *J. Am. Chem. Soc.* **2000**, *122*, 540–541.
- [134] J. R. Nilsson, C. P. Carvalho, S. Li, J. P. D. Silva, J. Andréasson, U. Pischel, *ChemPhysChem* **2012**, *13*, 3691–3699.
- [135] A. L. Koner, W. M. Nau, *Supramol. Chem.* **2007**, *19*, 55–66.
- [136] J. Wu, L. Isaacs, *Chem. – Eur. J.* **2009**, *15*, 11675–11680.
- [137] U. Pischel, V. D. Uzunova, P. Remón, W. M. Nau, *Chem. Commun.* **2010**, *46*, 2635–2637.
- [138] H. Bakirci, A. L. Koner, T. Schwarzlose, W. M. Nau, *Chem. – Eur. J.* **2006**, *12*, 4799–4807.
- [139] I. W. Wyman, D. H. Macartney, *Org. Biomol. Chem.* **2010**, *8*, 247–252.
- [140] I. W. Wyman, D. H. Macartney, *Org. Biomol. Chem.* **2010**, *8*, 253–260.
- [141] I. W. Wyman, D. H. Macartney, *J. Org. Chem.* **2009**, *74*, 8031–8038.
- [142] I. Ghosh, W. M. Nau, *Adv. Drug Deliv. Rev.* **2012**, *64*, 764–783.
- [143] M. A. Alnajjar, W. M. Nau, A. Hennig, *Org. Biomol. Chem.* **2021**, *19*, 8521–8529.
- [144] C. P. Carvalho, V. D. Uzunova, J. P. D. Silva, W. M. Nau, U. Pischel, *Chem. Commun.* **2011**, *47*, 8793–8795.
- [145] Z. Miskolczy, L. Biczók, *Photochem. Photobiol.* **2012**, *88*, 1461–1466.
- [146] Z. Miskolczy, L. Biczók, *J. Phys. Chem. B* **2011**, *115*, 12577–12583.
- [147] M. Shaikh, J. Mohanty, P. K. Singh, W. M. Nau, H. Pal, *Photochem. Photobiol. Sci.* **2008**, *7*, 408–414.
- [148] M. Shaikh, S. D. Choudhury, J. Mohanty, A. C. Bhasikuttan, H. Pal, *Phys. Chem. Chem. Phys.* **2010**, *12*, 7050–7055.
- [149] P. Montes-Navajas, H. Garcia, *J. Photochem. Photobiol. Chem.* **2009**, *204*, 97–101.
- [150] R. Wang, L. Yuan, D. H. Macartney, *Chem. Commun.* **2005**, 5867–5869.
- [151] A. L. Koner, I. Ghosh, N. Saleh, W. M. Nau, *Can. J. Chem.* **2011**, *89*, 139–147.
- [152] N. J. Wheate, A. I. Day, R. J. Blanch, A. P. Arnold, C. Cullinane, J. G. Collins, *Chem. Commun.* **2004**, 1424–1425.

- [153] Y. J. Jeon, S.-Y. Kim, Y. H. Ko, S. Sakamoto, K. Yamaguchi, K. Kim, *Org. Biomol. Chem.* **2005**, *3*, 2122–2125.
- [154] J. Grant Collins, N. J. Wheate, *J. Inorg. Biochem.* **2004**, *98*, 1578–1584.
- [155] H. Cong, C.-R. Li, S.-F. Xue, Z. Tao, Q.-J. Zhu, G. Wei, *Org. Biomol. Chem.* **2011**, *9*, 1041–1046.
- [156] Z. Miskolczy, M. Megyesi, G. Tárkányi, R. Mizsei, L. Biczók, *Org. Biomol. Chem.* **2011**, *9*, 1061–1070.
- [157] R. N. Dsouza, U. Pischel, W. M. Nau, *Chem. Rev.* **2011**, *111*, 7941–7980.
- [158] C. Marquez, F. Huang, W. M. Nau, *IEEE Trans. NanoBioscience* **2004**, *3*, 39–45.
- [159] N. J. Wheate, V. Vora, N. G. Anthony, F. J. McInnes, *J. Incl. Phenom. Macrocycl. Chem.* **2010**, *68*, 359–367.
- [160] F. J. McInnes, N. G. Anthony, A. R. Kennedy, N. J. Wheate, *Org. Biomol. Chem.* **2010**, *8*, 765–773.
- [161] R. Behrend, E. Meyer, F. Rusche, *Justus Liebigs Ann. Chem.* **1905**, *339*, 1–37.
- [162] W. A. Freeman, W. L. Mock, N. Y. Shih, *J. Am. Chem. Soc.* **1981**, *103*, 7367–7368.
- [163] A. Day, A. P. Arnold, R. J. Blanch, B. Snushall, *J. Org. Chem.* **2001**, *66*, 8094–8100.
- [164] A. Thangavel, A. M. M. Rawashdeh, C. Sotiriou-Leventis, N. Leventis, *Org. Lett.* **2009**, *11*, 1595–1598.
- [165] R. L. Halterman, J. L. Moore, L. M. Mannel, *J. Org. Chem.* **2008**, *73*, 3266–3269.
- [166] A. Koc, D. Tuncel, *Isr. J. Chem.* **2018**, *58*, 334–342.
- [167] M. A. Rankin, B. D. Wagner, *Supramol. Chem.* **2004**, *16*, 513–519.
- [168] S. Yi, A. E. Kaifer, *J. Org. Chem.* **2011**, *76*, 10275–10278.
- [169] W. M. Nau, M. Florea, K. I. Assaf, *Isr. J. Chem.* **2011**, *51*, 559–577.
- [170] F. Biedermann, M. Vendruscolo, O. A. Scherman, A. De Simone, W. M. Nau, *J. Am. Chem. Soc.* **2013**, *135*, 14879–14888.
- [171] F. Biedermann, V. D. Uzunova, O. A. Scherman, W. M. Nau, A. De Simone, *J. Am. Chem. Soc.* **2012**, *134*, 15318–15323.
- [172] F. Biedermann, W. M. Nau, H.-J. Schneider, *Angew. Chem. Int. Ed.* **2014**, *53*, 11158–11171.
- [173] T. H. Scheuermann, C. A. Brautigam, *Methods* **2015**, *76*, 87–98.
- [174] J. C. D. Houtman, P. H. Brown, B. Bowden, H. Yamaguchi, E. Appella, L. E. Samelson, P. Schuck, *Protein Sci. Publ. Protein Soc.* **2007**, *16*, 30–42.
- [175] H. Zhao, G. Piszczek, P. Schuck, *Methods* **2015**, *76*, 137.

Curriculum Vitae

EDUCATION

EDCH Doctoral Student (Jan. 2019 – Jan. 2023), Prof. K. Severin Group (LCS), EPFL. **Advisors:** Prof. K. Severin, Dr. C. Pezzato. **Characterizing courses:** Basic and Advanced NMR I and II, Scientific Writing, Advanced Mass Spectrometry, Wolfram Mathematica for data analysis in physics, Inorganic chemistry.

Master Degree in Chemistry (Oct. 2016 – Sept. 2018) from the University of Padova (UniPD). **Final mark:** 110/110 *Cum Laude*, **Advisor:** Prof. C. Zonta, **Thesis title:** ‘*Molecular Cage Encapsulation as Versatile Tool for Experimental Quantification of π - π Aromatic Stacking Interaction*’, Description: In the thesis was developed a supramolecular toolbox for the quantification of the free-energy of interaction of aromatic guests encapsulated in a synthetic supramolecular cage (*Chem. Sci*, 2019,1466). The approach used for the extrapolation of the interaction free energies is the Double Mutant Cycle, a method known in biochemistry used to calculate the interaction energy between residues in proteins/peptides. Moreover, the mechanism of formation of the molecular cage has been investigated by kinetic analysis unravelling a complex chemical reaction network. During this project I learnt advanced techniques in organic chemistry under inert conditions, in glovebox, NMR spectroscopy applied to supramolecular chemistry and all the related characterization methods (MS, HPLC, IR). **Characterizing courses:** Organic reaction mechanisms, Advanced stereochemistry, Advanced Organic synthesis and strategies, NMR and MS methods for advanced organic chemistry, (Bio)molecular X-ray crystallography, Synthesis and characterization of surfaces.

Bachelor Degree in Chemistry (Oct. 2013 – Oct. 2016) from the University of Padova. **Final mark** 105/110, **Advisor:** Prof. C. Zonta, **Thesis title:** ‘*Rearrangement Reactions Inside Molecular Containers*’, Description: In the project were explored the confined-space catalysis properties of TPMA-Zn molecular containers over the rearrangement reactions of a well-known mechanophore such as dibromogemcyclopropane. With the proper functionalization, it was possible to bind the cyclopropane to the molecular cage and observe the effects on its reactivity. By means of kinetic measurements, it was possible to detect an increment of the rate of the ring-opening reaction in the presence of the molecular container; the study was extended to two compounds for comparing two differently sized compounds and their interactions with the molecular cage. During this timeframe I learnt the basic skills necessary to perform organic synthesis in inert atmosphere and the basics of supramolecular characterization methods. **Characterizing courses:** Computational chemistry, pharmaceutical chemistry.

SKILLS

- Organic and inorganic synthesis and characterization
- Advanced NMR spectroscopy
- Calorimetric methods
- Supramolecular and computational chemistry
- Optical spectroscopies
- Python, JMP, R, Mathematica, Matlab, GNU Octave
- Mass spectrometry coupled with liquid/gas chromatography

PUBLICATIONS

- [1] “The effect of temperature on the photoacidity of merocyanine photoacids in water” V. J. Périllat, C. Berton, C. Pezzato, *Materials Today Chemistry* **2022**, 25, 100918. doi: doi.org/10.1016/j.mtchem.2022.100918
- [2] “A Mesoionic Diselenolene Anion and the Corresponding Radical Dianion” Z. Dong, A. Sienkiewicz, A. A. Suleymanov, C. Berton, F. Fadaei-Tirani, R. Scopelliti, K. Severin, *Chemistry – A European Journal* **2022**, 28, e202200893. doi : doi.org/10.1002/chem.202200893
- [3] “Light-Switchable Buffers” C. Berton, D. M. Busiello, S. Zamuner, R. Scopelliti, F. Fadaei-Tirani, K. Severin, C. Pezzato, *Angewandte Chemie - International Edition* **2021**, 60, 21737–21740. doi: doi.org/10.1002/anie.202109250
- [4] “Light-induced assembly and disassembly of polymers with Pd_nL_{2n}-type network junctions” R.-J. Li, C. Pezzato, C. Berton, K. Severin, *Chemical Science* **2021**, 12, 4981–4984. doi: doi.org/10.1039/D1SC00127B
- [5] “Thermodynamics and kinetics of protonated merocyanine photoacids in water” C. Berton, D. M. Busiello, S. Zamuner, E. Solari, R. Scopelliti, F. F. Tirani, K. Severin, C. Pezzato, *Chemical Science* **2020**, 11, 8457-8468. doi: doi.org/10.1039/D0SC03152F
- [6] “The photoacidity of indolinobenzopyrans in water” C. Berton, C. Pezzato, *submitted to EurJOC*.
- [7] “Controlling DNA nanodevices with visible light-switchable buffers” V. J. Périllat, E. Del Grosso, C. Berton, F. Ricci, C. Pezzato, *submitted to Chem. Sci*.
- [8] “Performance boost of a merocyanine photoacid by supramolecular encapsulation” C. Berton, C. Pezzato, *in preparation*.

[9] “Synthetic Receptors with Micromolar Affinity for Chloride in Water”, S. Sudan, D. Chen, C. Berton, K. Severin, *Angewandte Chemie - International Edition*, (pages, volume and issue not available yet), doi.org/10.1002/anie.202218072

CONFERENCES AND EVENTS

Swiss Snow Symposium, January 2023, Abstract accepted for a contributed talk.

SCS Photochemistry Symposium June 2022, (Best poster presentation award) attended for short talk and poster session with title: ‘Performance boost of a merocyanine photoacid by supramolecular encapsulation’.

SCS Fall Meeting 2022, Poster exposition entitled: ‘Performance boost of a merocyanine photoacid by supramolecular encapsulation’.

SCS Fall meeting 2020, Poster exposition entitled: ‘Metastable state Photoacids, Comparative Study of Substituent effects’.

TEACHING ACTIVITIES

From 2019 to present:

500+ hours as teaching assistant and organizer for EPFL: Teaching for around 500+ hours for the course ‘TP Chimie Préparative II’ of Prof. Kay Severin and Prof. Xile Hu on the use of inert atmosphere techniques in the preparation, manipulation and characterization of organometallic compounds. For the academic years 2020-2021 and 2021-2022 I oversaw the full organization of the laboratory course and the related exams. For 70 hours in the academic year 2020-2021 I was a teaching assistant in the laboratory of general chemistry for pharmacists and biologists.

Between 2016 and 2018:

100 hours in the PLS project for UniPD: During my time at the University of Padova I was called from the PLS (Progetto Lauree Scientifiche) for the preparation of teaching and support materials (slides, booklets and *vademecum*) for the courses of general chemistry for Biology, Biotechnology and Molecular Biology. The total time spent over this activity amounts to 100 hours.

80 hours in the Organic Chemistry II Laboratory for UniPD: During my last year of master’s degree, I was called as teaching assistant for the laboratory course Organic Chemistry II. In this course were covered the basics of organic synthesis, separation and characterization of organic compounds including chiral compounds.

Students supervision: I supervised at EPFL two students for the full length of their projects 1A (bachelor degree in chemistry, 1 full-time month) and one student for his project 1B (master degree in chemistry, 6 months full-time project). I supervised for two months a student-apprentice in chemistry for 2 full-time months. During my master

thesis project at UniPd I supervised two bachelor students during their thesis project (3 months full-time each).

LANGUAGES

Italian: Mother tongue, full professional proficiency and fluency

English: Full professional proficiency and fluency

French: Intermediate professional proficiency

CERTIFICATIONS

Udemy course certificate: 'Basics of Good Manufacturing Practices (GMPs)' September 2022

Udemy course certificate: 'GUI Development with Python and Tkinter' August 2022

Udemy course certificate: 'Python A-Z: Python for Data Science with real exercises' August 2022

Webinar attendance: "Make better data-based decisions with statistical modelling techniques using JMP" October 2022.

EXTRACURRICULAR ACTIVITIES

Sports Career:

Played rugby for Petrarca Rugby Padova and Rangers Rugby Vicenza with internationally known players.

Played in the Italian Junior national rugby teams between the under-16 to the under-20 categories.

Drafted and participated to the Accademia Nazionale Ivan Francescato (national academy for high-level rugby players) in the sports seasons 2010-11 and 2011-12.

REFERENCES

Ph.D. Advisor: Prof. Kay Severin, LCS, EPFL, kay.severin@epfl.ch

Ph.D. Co-Advisor: Dr. Cristian Pezzato, LCS, EPFL, cristian.pezzato@unipd.it

M.Sc. and B.Sc. Advisor: Prof. Cristiano Zonta, Uni. Padova, cristiano.zonta@unipd.it